MANCHESTER
1824
The University of Manchester

Bayesian inference on microstructural, hyperelastic models of soft tissue deformation.

A thesis submitted to the University of Manchester for the degree of
Doctor of Philosophy
in the Faculty of Science and Engineering

2022

James Haughton
Department of Mathematics
School of Natural Sciences

Contents

Word Count: 44359

List of figures

Abstract

This thesis studies the modelling of soft tissue behaviour and whether Bayesian statistical techniques can be applied to models of soft tissue deformation in order to quantify the level of uncertainty in the values of a model's parameters. Fibrous soft tissues, such as tendon and skin, are ubiquitous in mammals and essential for our daily lives. Changes in the behaviour of these soft tissues, which are associated with changes in their microstructures, have a tremendous impact on people. Understanding how microstructure influences the macroscopic behaviour we observe in experiments is vital, therefore, and advances in our knowledge of soft tissue mechanics have many important applications in wider society. Furthermore, quantifying uncertainty in a model's estimates of parameters is key to understanding how well it can replicate physical behaviour and inform us of the relation between the microscale and the macroscale.

Models of fibrous soft tissues can, broadly, follow one of two approaches. Phenomenological models can fit experimental data well and be versatile in terms of the scientific software they can be implemented in, but the parameters included in these models do not have a physical basis for inclusion. Therefore, while these models can be widely used and replicate observed data well, we do not learn anything about the relationship between microstructure and physical behaviour from their results. Microstructural models, by contrast, can be complex, but they enable us to study the effect that the properties and arrangement of tissue constituents have on mechanical behaviour.

In this thesis, we complement existing work performed in microstructural modelling by developing a new microstructural model that, through realistic assumptions about the nature of tissue constituents, is tractable and contains only parameters that have a physical basis for inclusion. We show that the model fits mechanical experimental data on tendons and skin well when subjected to standard non-linear optimisation. Furthermore, by assuming that independently and identically distributed noise is present during the collection of the experimental data, we derive a Random Walk Metropolis Markov chain Monte Carlo algorithm that can be used to accurately sample from the posterior distribution of the model's parameters. Additionally, we obtain from the algorithm probable values for the parameters that are realistic, when compared with existing literature values.

Declaration of originality

I hereby confirm that no portion of the work referred to in the thesis has been submitted in support of an application for another degree or qualification of this or any other university or other institute of learning.

Copyright statement

i The author of this thesis (including any appendices and/or schedules to this thesis) owns certain copyright or related rights in it (the "Copyright") and s/he has given The University of Manchester certain rights to use such Copyright, including for administrative purposes.

ii Copies of this thesis, either in full or in extracts and whether in hard or electronic copy, may be made *only* in accordance with the Copyright, Designs and Patents Act 1988 (as amended) and regulations issued under it or, where appropriate, in accordance with licensing agreements which the University has from time to time. This page must form part of any such copies made.

iii The ownership of certain Copyright, patents, designs, trademarks and other intellectual property (the "Intellectual Property") and any reproductions of copyright works in the thesis, for example graphs and tables ("Reproductions"), which may be described in this thesis, may not be owned by the author and may be owned by third parties. Such Intellectual Property and Reproductions cannot and must not be made available for use without the prior written permission of the owner(s) of the relevant Intellectual Property and/or Reproductions.

iv Further information on the conditions under which disclosure, publication and commercialisation of this thesis, the Copyright and any Intellectual Property and/or Reproductions described in it may take place is available in the University IP Policy (see `http://documents.manchester.ac.uk/DocuInfo.aspx?DocID=24420`), in any relevant Thesis restriction declarations deposited in the University Library, The University Library's regulations (see `http://www.library.manchester.ac.uk/about/regulations/`) and in The University's policy on Presentation of Theses.

Acknowledgements

I am immensely grateful for the time and effort that my supervisors, Dr Tom Shearer and Prof. William J. Parnell, have afforded me throughout my PhD. I am also immensely thankful to Dr Simon Cotter, who has been an instrumental part of my PhD studies. It is no exaggeration to say that his guidance and expertise have been invaluable to the research performed in this thesis. Finally, I would like to thank my parents, Peter and Tracey, for their unquestioning support of me throughout this PhD.

Chapter 1

Introduction

Fibrous soft tissues such as skin, arteries, and tendons are fundamental components of mammalian life and, without them, we would not be able to function properly. These materials enable us to move, form the first line of defence against impact injuries and any objects coming into contact with us, and allow blood to flow through the body, continually providing oxygenated blood and nutrients to the biological materials that need them to work. During the course of these important everyday tasks, fibrous soft tissues are subjected to many different loads that deform them. Soft tissues must neither break nor be damaged when they are subjected to these physiological loads. Instead, they must exhibit a certain pattern of stress-strain behaviour: they must be compliant for smaller loads, enabling the body to function as normal, but as the load is placed upon them, and the deformation they are subjected to, increases in magnitude, they must stiffen rapidly to protect the integrity of the human body. Advances in our understanding of these highly complex behaviours have applications in a variety of different fields. Physically accurate models of materials such as skin are important for the animation [1] and cosmetics industries [2]. Accurate modelling could also provide surgeons with important information on routine and experimental procedures, as soft tissues can be subjected to much higher stresses and strains when operated upon than they would normally be subjected to [3]. It is vital, therefore, that we attempt to understand quantitatively how a soft tissue deforms when a given load is placed upon it. To do this, we use the field of continuum mechanics and, in particular, the theory of hyperelasticity to construct mathematical models of soft tissues that relate the stress acting on a soft tissue to the strain it is placed under through a strain energy function (SEF).

Fibrous soft tissues are highly complex materials mathematically. As mentioned previously, they exhibit non-linear elasticity, being compliant at small strains, but stiffening rapidly at larger strains. Furthermore, they are anisotropic, as they are stiffer in certain directions than others, and viscoelastic [2], exhibiting creep [4], stress relaxation [5], and hysteresis [6] because energy is dissipated in the soft tissue during a loading-unloading cycle. As we explain later, these complex microscopic phenomena are caused largely by the microstructure, that is, the properties of the tissue's constituents and their arrangement in the material. Consequently, the constitutive modelling of soft tissues is a sophisticated multidisciplinary field that incorporates multiple mathematical, physical, and biological sciences to accurately model these complex materials.

Models of the macroscopic mechanical behaviour of soft tissues broadly fall into two cat-

egories. Firstly, there are phenomenological models, which are designed to fit stress-strain data well with relatively simple, tractable equations. Good fits to experimental data can, and certainly have, been achieved in the literature. However, these models do not provide much information on how a tissue's microstructure affects its behaviour on the macroscale, because they do not, on the whole, contain physically relevant parameters. The second category of soft tissue models is structural modelling. In this approach, we seek to directly incorporate properties of the tissue's constituents in the SEF when describing the stress-strain behaviour that is observed. However, accounting for the physics and biology of a soft tissue in the SEF increases its complexity, potentially limiting its viability to study physical mechanics. In reality, many models incorporate features of both the phenomenological and structural approaches to modelling, explicitly accounting for some microstructural phenomena, while indirectly modelling other phenomena in order to retain the tractability of the model.

The outline for the rest of this chapter is as follows. Firstly, we introduce some key constituents in biological soft tissues. In particular, we explain what each component is, how it is created, and what function it serves in biological tissues. Next, we describe non-linear elasticity, anisotropy, and viscoelasticity in more detail, focusing particularly on how the properties and arrangement of soft tissue constituents cause these macroscopic phenomena. Finally, we introduce the soft tissues that we study in the rest of this thesis –tendons and skin. We describe the microstructure of each tissue and how it is adapted in order to allow the tissue to perform the duties required of it for its normal function. Although ageing, damage, and growth are beyond the scope of this thesis, we also examine these phenomena in order to highlight how changes in the microstructure affect the behaviour of a tissue on the macroscale.

1.1 Soft tissue biology

Although the term soft tissues comprises many distinct biological materials, there are certain constituents that are common to the tissues. These tissues contain cells that help regulate bodily functions and synthesise the building blocks from which other constituents are made, and we shall discuss them in more detail later when we introduce the soft tissues that we aim to analyse in this thesis. However, we focus on the extracellular materials of the tissue for the moment. In terms of a soft tissue's ability to resist a deformation, the most important extracellular materials are fibrils of the stiff protein collagen. In the interfibrillar spaces in the tissue, there is also a non-collagenous matrix (NCM) that contains fibres of the more compliant protein elastin and a ground substance whose components include proteoglycans. We now examine these constituents in more detail.

1.1.1 Collagen

In humans, the collagens are a family of 28 proteins that contain three polypeptide chains, which, for sections of each chain, contain the repeating Glycine-X-Y amino acid sequence, where X and Y are *any* two amino acids, and are wound into a right-handed triple helix with

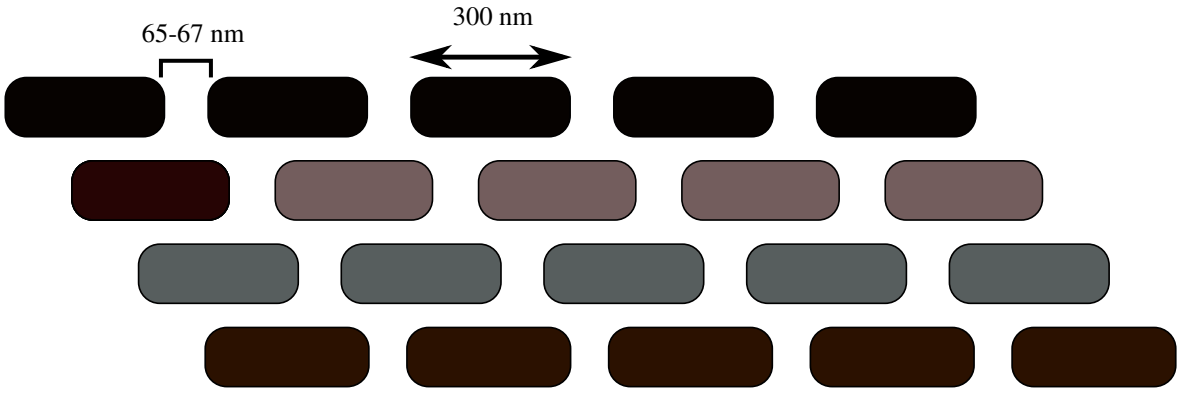

Figure 1.1. A staggered array of collagen molecules, approximately 300 nm in length. The 65-67 nm-long gap between adjacent molecules in a layer is called the d-period. The staggered array allows collagen molecules to fuse with molecules in adjacent layers of the array, conferring strength on collagen. Figure adapted from Gelse *et al*. [11]

glycine residues present in the centre of the helix and residues X and Y exposed on its surface [7]. An amino acid is an organic molecule that contains both an amino ($-NH_2$) and an acidic carboxyl ($-COOH$) group. The basic unit of collagen is the collagen molecule, also known as a tropocollagen molecule, approximately 300 nm in length [8]. Non-helical telopeptides, also known as the N- and C-termini, are situated at both ends of a tropocollagen molecule. The telopeptides are important in the formation of supramolecular collagenous structures because cross-links are formed between neighbouring molecules at the telopeptides [9]. To facilitate the formation of cross-links, collagen molecules aggregate in a staggered array [10], Figure 1.1, ensuring telopeptides in different layers of the array are closer to one another than if the array was not staggered.

Within the family of collagens in the human body, there are distinct subsets of collagen types that aggregate to form different suprastructures. For the purposes of this thesis, we concentrate on the collagen types that aggregate to form subunits known as fibrils, as these collagen types are the most abundant in the biological soft tissues that we study in this thesis. Collagen's primary importance to soft tissues is the strength and stiffness it provides to them. Collagen possesses a high Young's modulus that is usually stated as being approximately equal to 1 GPa, [12], although values of this property stated in the literature have ranged from 32 MPa [13] to 16 GPa [14].

Fibrillar-forming collagen types include types I, II, III, V, and XI [15]. Collagen type I is found in many fibrous soft tissues, where it forms the majority of collagen content and where it confers mechanical strength on the soft tissues. In contrast, other fibril-forming collagen types are found in a more restricted set of soft tissues, and they are less numerous than collagen type I. For example, type II collagen is found in cartilage, and type III collagen is found in more elastic soft tissues such as blood vessels and embryonic skin [16]. In addition to fibrillar-forming collagen types, there are a group of collagen types known as *Fibril-associated collagen with interrupted triple helices* (FACIT) collagens [17]. FACIT collagen types include types IX, XII, and XIV amongst others. Type XII and XIV collagen, for example, play a role in fibrillogenesis, regulating the properties of the collagen fibrils [17], [18].

Not all types of collagen form fibrils, or help in the formation of fibrils. Collagen type IV, for example, is mainly present in basement membranes [15]: specialised structures found at tissue boundaries. These structures underlie epithelial, endothelial, fat, muscle, and nerve cells. Collagen type VI, on the other hand, is found in tissues, where it has been postulated to help in maintaining tissue integrity [16]. Collagen types that do not form fibrils possess further differences compared to ones that do. Collagen type IV does not exist in a precursor form, that is, a molecule, with telopeptides involved in formation. Non-fibrillar-forming collagens are also different lengths compared to fibrillar-forming collagens: collagen type IV is generally longer than fibril-forming collagens; collagen type VII is the longest collagen type; but collagen type VI is shorter than fibrillar-forming collagens [16].

Other differences between collagen types are present too. Type XXIV and XXVII are fibrillar-forming collagens that possess shorter triple-helical regions than collagen type I, II, or III. Furthermore, the length of the ends of the collagen molecule and the composition of the molecule outside its triple-helical region are both different between collagen types. Finally, the three chains that constitute the triple helix of collagen can be the same, producing homotrimeric collagen molecules, or one chain, at least, can be different, creating a heterotrimeric collagen molecule. Some collagen types consist of homotrimeric molecules, while others consist of heterotrimeric molecules [15]. Through these numerous areas of difference, we obtain many different collagen types.

Collagen fibrils in a given soft tissue do not possess a uniform diameter. Instead, soft tissues contain a varied distribution of fibrils [12], with fibrils of a certain diameter possessing unique properties compared to differently sized fibrils. This distribution of collagen fibrils in a soft tissue enables soft tissues to perform all the complex macroscopic mechanical roles required of them. Larger, wider collagen fibrils possess a higher ultimate tensile strength than smaller, thinner fibrils [19]. However, multiple thin fibrils will have a larger surface area than a larger collagen fibril of equivalent volume and form more cross-links. A soft tissue can fail either due to the ultimate tensile strength of the constituents being reached or due to fibrils sliding over one another, which causes constituents to disaggregate [12]. Possessing fibrils of different diameters protects a soft tissue against failure through either of these processes.

Similar to the benefits of soft tissues containing fibrils of different diameters, there are benefits to collagen being distributed into a plethora of smaller subunits. In addition to the aforementioned benefits of collagen fibrils cross-linking with one another, cracks cannot propagate through the tissue as far when collagen is distributed into subunits as opposed to through a single homogeneous structure [12]. Furthermore, the existence of collagenous subunits allows for more flexibility in the tissue.

1.1.2 Elastin

Elastin is another protein found in soft tissues and is a significant component of the elastic fibres that provide soft tissues with elasticity. In the elastic fibres, elastin is situated in the core of the fibre and is surrounded by microfibrils of other glycoproteins such as fibrillin

and fibulins. As with collagen, elastin is first secreted as molecules of tropoelastin, which include hydrophobic domains that contain valine, glycine, and proline, and hydrophilic domains containing lysine [20]. In the soft tissues, these tropoelastin molecules aggregate with one another to form the elastin fibrils that are found in elastic fibres.

The most obvious function of the elastic fibres in soft tissues is to provide recoil and elasticity to the tissue. This is vital because soft tissues are deformed continually and must be able to withstand all of these numerous strains. In aged tissue, where elastic fibres degrade and are not sufficiently replaced, the tissue is stiffer and less adept at recovering from deformations. Elastic fibres also act as signalling molecules, inhibiting the production of smooth muscle cells in the arterial wall, for instance, and regulating the activity of certain growth factors [20].

1.1.3 Proteoglycans

Proteoglycans are a type of glycoprotein that contain polysaccharide chains (chains of carbohydrates whose molecules consist of sugars bonded together) bonded to a protein at the material's core [21]. Examples of proteoglycans found in soft tissues include versican, biglycan, and decorin. Proteoglycans are found between collagen subunits throughout multiple levels in the hierarchy of collagenous structures found in soft tissues. While proteoglycans may not be a significant constituent of soft tissues, they constitute just 1% by dry weight of tendons, for example, they have a significant impact on tissue behaviour [22]. Proteoglycans link one collagen fibril to another. Another function of proteoglycans is in fibrillogenesis, in which collagen molecules synthesised by fibroblasts are aligned and ordered correctly as the molecules mature and aggregate into fibrils. Different proteoglycans play an important role in the earlier and later stages of fibrillogenesis: biglycan and decorin in the early phases of fibrillogenesis, and decorin and fibromodulin during the later phases [21]. During fibrillogenesis, these proteoglycans ensure that collagen and elastic fibrils possess a consistent shape and a range of diameters that ensure soft tissues behave normally [22].

1.2 Macroscopic soft tissue phenomena

We have introduced the core components of soft tissues. Now, we explain how these materials, their individual properties and their distribution in the tissue, in particular, are a key factor in the macroscopic stress-strain behaviour that we observe in experimental testing.

1.2.1 Anisotropy

If the same stretch is applied to a soft tissue in two distinct directions, the tissue will, generally, be more compliant in one direction. This directional dependence is caused by the alignment of collagen fibrils in soft tissues. Collagen fibrils are key to anisotropy because they are significantly stiffer than any component in the NCM. The orientation of collagen

fibrils, thus, has a significant impact on both the degree of anisotropy exhibited by the tissue and both the maximum and minimum stiffness exhibited by a sample across all possible directions that it can be stretched in. When fibrils are predominantly aligned in parallel to one another, the soft tissue is stiff and strong in the same direction as the fibrils are oriented in, but at the cost of being compliant and weak in other directions. Conversely, fibrils in a soft tissue can be oriented in a mesh with fibrils oriented in many directions and fewer fibrils oriented along the modal direction, or directions. Compared to tissues with highly aligned collagen fibrils, tissues that possess a mesh of fibrils are more compliant and weaker when the deformation coincides with the modal alignment of the fibrils, but they are stronger and stiffer when stretched in other directions. For a particular tissue, the distribution of fibril orientations, and hence the degree of anisotropy in the tissue, will be dependent on the profile of loading the tissue is subjected to under regular physiological conditions.

1.2.2 Elasticity theory for viscoelastic soft tissues

Collagenous soft tissues are viscous materials. They exhibit creep, the deformation of a material under a constant load [4]; stress relaxation, a reduction in the stress experienced by a material subjected to a constant deformation [5]; and hysteresis, a change in the mechanical behaviour of a material between the loading and unloading phases of a deformation cycle, as energy is dissipated in the material during the cycle [6]. For example, between 15-20% of the total strain energy input is lost in each cycle of a load when an artery is deformed [23]. How the microstructure exactly induces viscoelasticity is unknown. Potential causes include the dissipation of energy due to the sliding of collagen fibrils over one another during deformations [24], and molecular relaxations in both collagen and the NCM [25]. As soft tissues are viscous materials, we can only apply elasticity theory, including hyperelastic SEFs, to study the stress-strain behaviour of the tissues under certain conditions. Consequently, before experiments are performed, soft tissues are subjected to preconditioning, Figure 1.2. In preconditioning, a cyclic load is applied to a soft tissue until the stress-strain behaviour between adjacent cycles of the load is consistent. At this point, the soft tissue can be treated as pseudoelastic [26]. That is, the soft tissue is assumed to obey one elastic loading path and another elastic path during unloading. Viscous effects are present, but the material is considered as elastic along either path. Therefore, if we restrict ourselves to one loading path, for example, we can model the soft tissue using a hyperelastic SEF. Furthermore, for quasi-static loading, the loading and unloading paths are approximately the same.

At large strains, the yield stresses of microstructural components are reached, resulting in plastic deformation for both collagenous structures in the soft tissue and the NCM. As the strain acting on the tissue is increased still further, the tissue fails and is unable to resist the deformation because its components, which resist the deformation, break. However, damage to the structural components of the tissue and the subsequent impact on its mechanical behaviour are beyond the scope of this thesis. Similarly to plastic deformation, tissue failure is beyond the scope of this project.

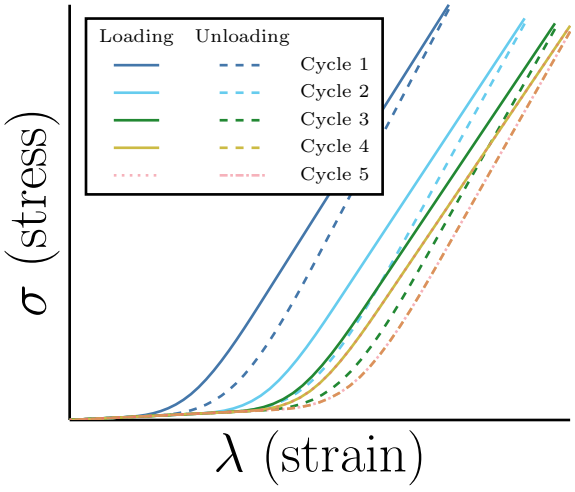

Figure 1.2. An example of the behaviour of a soft tissue when it is subjected to preconditioning. The tissue is viscoelastic, even once it is preconditioned, but we can treat it as pseudoelastic along one loading path once it is preconditioned.

1.2.3 Non-linear elasticity and collagen crimp

When subjected to mechanical testing, fibrous soft tissues exhibit a particular form of non-linear stress-strain behaviour, Figure 1.3. At small strains, soft tissues are compliant and behave like linearly elastic materials. As the stretch is increased, the stress-strain behaviour becomes non-linear. As the stretch is increased still further, however, the tissue returns to exhibiting linear stress-strain behaviour, but is much stiffer than it was at small strains. To explain this pattern, we assume that collagen fibrils are initially crimped [27], i.e. wavy, and subsequently straighten as the tissue is stretched, and that collagen fibrils are slack when they are crimped. In tendons, bundles of collagen fibrils have been observed by imaging techniques such as microscopy to be crimped. Furthermore, the straightening of fibrils in tendons during the initial stretching phase has also been observed. Collagen crimp, and the subsequent straightening of the fibrils as the tissue is deformed, has been observed in skin [28], too.

In order to capture the initial slackness and eventual tautening of collagen fibrils, some constitutive models have employed a tension-compression switch that assumes fibrils become taut and mechanically active only after a critical stretch has been applied to the soft tissue. By assuming collagen fibrils only tauten once they become straight, models can assume that an individual collagen fibril is linearly elastic, that is, it obeys Hooke's law, while still capturing the non-linearity of a tissue's stress-strain response. One example where the non-linear stress-strain of soft tissues was captured by the gradual recruitment of linearly elastic collagen fibrils is the *Sequential Straightening and Loading* (SSL) model developed by Kastelic *et al.* [29]. It is also common in the literature to model the NCM as a neo-Hookean material. Therefore, according to models with tension-compression switches for collagen fibrils, a soft tissue is linearly elastic at small strains, when no collagen fibrils are taut, and larger strains, when every collagen fibril has tautened.

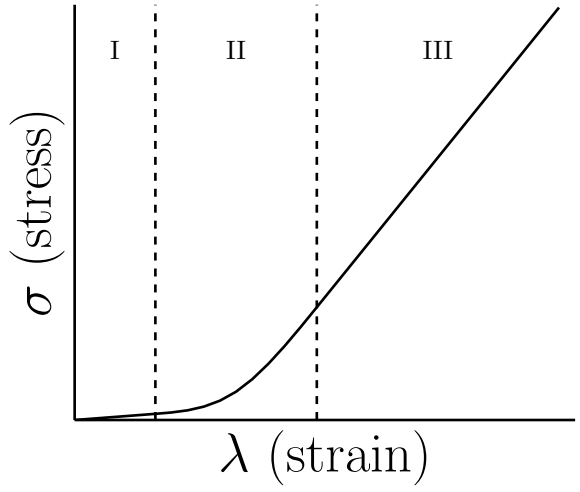

Figure 1.3. A typical stress-strain (σ and λ, respectively) curve. Region I: this is the toe region where only the compliant components are loaded; the collagen fibrils are crimped and slack. Region II: the non-linear, heel region, where gradually the stiff collagen fibrils straighten and become taut. Region III: all the collagen fibrils are taut; the soft tissue is stiff and linearly elastic. If stretched too far, soft tissues will be damaged and eventually fail.

1.3 Soft Tissues

We have introduced the important constituents of soft tissues and the complex macroscopic phenomena that they exhibit when loaded. Now we describe the soft tissues that we study, namely tendons and skin. In particular, we explain how the microstructural materials are oriented and distributed in the soft tissue, and how they affect the material mechanically to enable healthy functioning of the tissue.

1.3.1 Tendons (and ligaments)

Tendons are key to human movement because they connect muscle to bone, transmitting forces and withstanding tension during muscle contraction. (Ligaments, which connect one bone to another, share a similar structure to tendon and are also important to movement.) Tendons are not just important in the transmission of forces, but help with joint stabilisation, shock absorption, and, because of the presence of mechanoreceptors, provide sensory feedback to the muscle [30]. Tendons in the human body are not identical in shape. Instead, they are adapted to their position in the body and the loads that are exerted upon them. Tendons connected to muscles like the quadriceps that create powerful forces tend to be short and thick. Less powerful forces, such as those created by finger muscles, are transmitted by long, thin tendons that allow for more delicate movement [31]. Water comprises approximately 55-70% of the total weight of a tendon, but collagen comprises 60-85% of the dry weight of tendons [21]. Elastic fibres, by contrast, constitute approximately 1-10% of the dry weight of tendon and are localised to the interfascicular matrix, that is, the matrix located in the regions of the tendon that lie between fascicles.

Although cells are not a major constituent of tendons, there are certain types of cells that perform important roles in maintaining normal, healthy function. The majority of cells in

the tendon are fibroblasts, also known as tenoblasts, that synthesise collagen molecules and the building blocks of other components of the NCM [31]. The number of fibroblasts decreases with age, reducing the number of new collagen molecules and, thus, fibrils that are synthesised. Other cells in the tissue include epithelial cells and chondrocytes, which secrete constituents of cartilage. Cells in tendons interact with collagen and the NCM, binding these materials using cell surface receptors such as integrins. The cell composition of a tendon is influenced by the mechanical behaviour of the tissue [30]. For example, physical activity such as exercise, and the subsequent resting periods, has been shown to influence the composition of soft tissues, with increased activity leading to enhanced rates of collagen synthesis in the short- and long-term, and of collagen degradation in the short-term only, with damaged fibrils being replaced.

Collagen Type I is the dominant collagen type in tendons, making up approximately 90% of the collagen content of tendons. The vast majority of the remainder of the collagenous content in tendons is taken up by collagen Type III, which is important for fibrillogenesis as it helps regulate the diameter of Type I fibrils [21]. Traces of collagen type V and the non-fibrillar-forming collagen types XII and XIV are also found in the tendon. These trace collagen types possess important roles: type V collagen is found in the centre of Type I fibrils, and it helps to provide a template for fibrillogenesis, while collagen Types XII and XIV provide a molecular bridge between collagen Type I and the other constituents of the extracellular matrix [21].

Collagen has a multi-level hierarchical structure in tendons, although the exact suprafibrillar hierarchy can be different between papers. For example, some studies have posited an intermediate structure, the sub-fascicle, between collagen fibrils and the fascicle, [32], [33]. However, a basic structure of the hierarchy of collagenous structures in tendons starts with molecules aggregating to form fibrils, which possess diameters ranging from 10 to 500 nm and themselves aggregate to form fascicles that are typically between 150 and 500 μm in diameter [34], Figure 1.4. Fascicles aggregate to form tendon fibres that run almost parallel to the long axis of the tendon [34]. Tendons, themselves, differ in diameter. For example, one study found the mean hamstring tendon diameter to be 7.8 ± 0.7 mm for women and 7.9 ± 0.6 mm for men [35]. On the other hand, patellar tendon diameters in active volleyball players ranged from 3.4 ± 0.4 mm to 6.5 ± 1.8 mm in men and from 3.2 ± 0.4 to 4.6 ± 0.7 mm in women [36]. Tendon thickening was found to be a potential indicator of tendon pathology as well [36].

Fibrils within a fascicle are also largely aligned parallel to one another. This ensures that the tendons are stiff and possess a large ultimate tensile strength when stretched in the direction of the fibrils. This structure best enables tendons to withstand the deformations that they are subjected to physiologically and to retain their structural integrity.

Another mechanism that protects the integrity of tendons, by reducing the chance of fibrils becoming damaged, is that the strain acting on collagen fibrils is less than the strain experienced by the tendons as a whole [37]. Fibril crimp, and the subsequent straightening of the fibrils in deformed tendons, is one mechanism that contributes to this. An additional mechanism

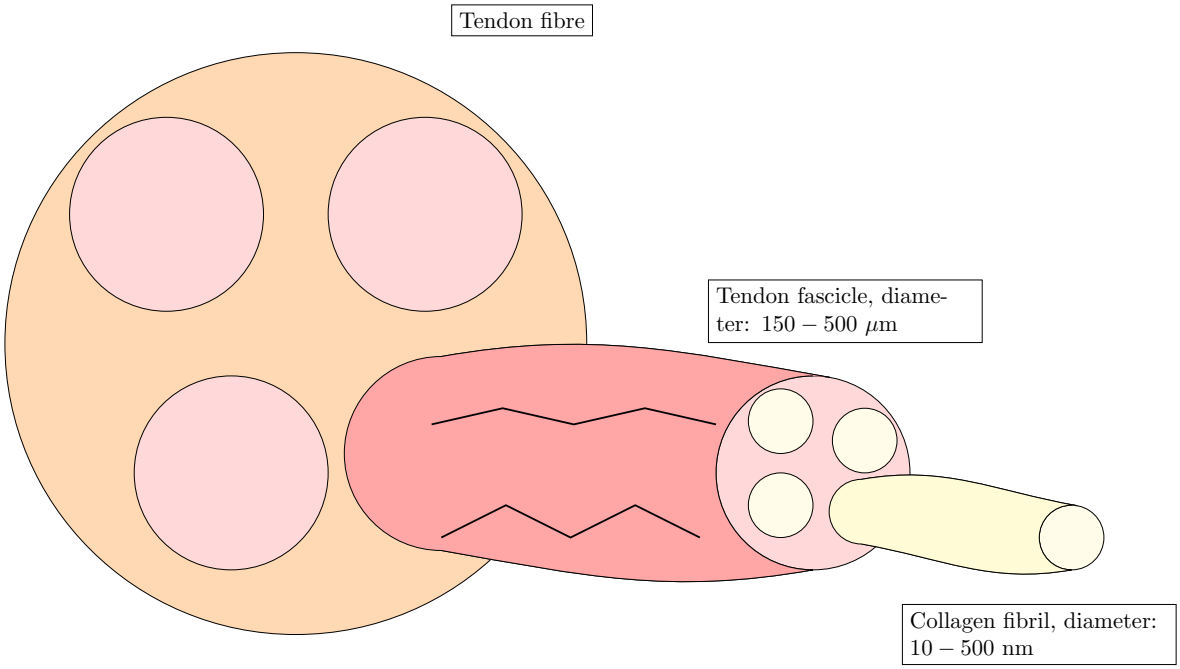

Figure 1.4. An example of the substructure of tendons, on the cross-section of a tendon fibre, with collagen fibrils aggregated into highly regulated fascicles, which themselves aggregate to form tendon fibres. A typical range of diameters for the fibrils and fascicles are listed on the diagram. The crimped black lines on the fascicle signify collagen fibrils. This diagram is concerned with how collagen fibrils and tendon fascicles are situated in tendons, and so that is why we only consider the cross-section of a tendon fibre. In reality, tendon fibres are three-dimensional materials that themselves aggregate to form a tendon.

accounting for fibrils extending less than tendons is fibril sliding [37]. Sliding proteoglycan links between adjacent collagen fibrils are broken when a load is applied to the tissue.

Similar to the effects of physical activity, damage and healing affect the composition, and thus the mechanics, of tendons, with the number of fibroblasts and growth factors in an affected tendon increasing during the recovery phase. Consequently, more collagen is synthesised in the recovery phase while the tendon attempts to heal as fully as possible [38]. As the recovery continues, the collagen present in the tendon changes further, with new cross-links formed between fibrils but the overall collagen content decreasing. Imperfect recovery from injury can have a profound impact on the tissue, as excessive load applied to an injured tendon can cause further damage to tissue constituents [30]. On the other hand, immobilisation of the tendon also has negative consequences, mechanically, as collagen fibrils become thinner and the tendon becomes less stiff without mechanical stimuli. Ageing is another natural process that has a significant impact on the collagen content of tendons. Ageing is associated with a slower fibril turnover rate, changes in the pattern of collagen fibril crimp, a thickening of collagen fibres, a more disorganised structure of collagen compared to the closely aligned collagen fibrils of younger tendons, and an increased number of cross-links between collagen molecules [30]. These age-related changes contribute to older tendons becoming stiffer and less flexible than younger tendons, reducing tendon performance.

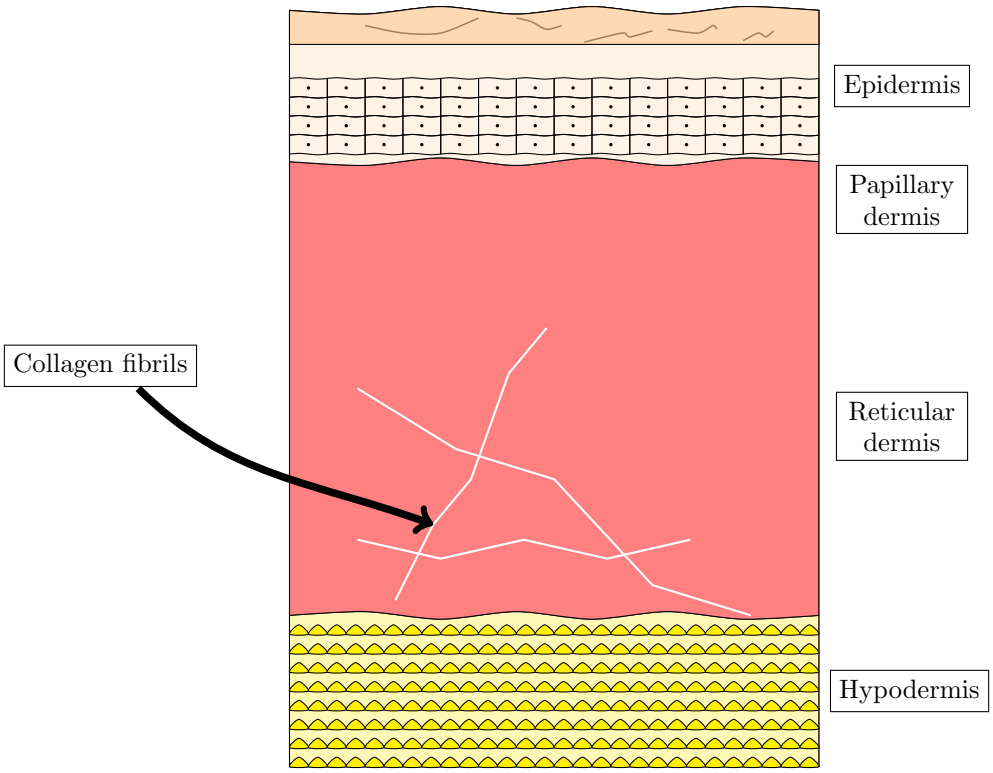

Figure 1.5. The structure of skin, comprising the epidermis, the dermis, and the hypodermis. The collagen content of the skin largely resides in the dermis, which is commonly split into two layers: the papillary dermis lies on the boundary of the epidermis and the reticular dermis constitutes the rest of the dermis.

1.3.2 Skin

Skin is the largest organ of the human body and, as such, plays a pivotal role in the integumentary system, protecting the majority of the body from damage or infection when we come into contact with external objects like bacteria or items that we can touch. This protective barrier for the body extends to providing mechanical resistance when a load is placed upon the skin. This prevents damage to internal blood vessels, tendons, ligaments, muscles, and organs. The structure of skin at a particular point is dependent on the area where it is examined [39]. The epidermis, dermis, and hypodermis, the three layers of skin, Figure 1.5, all differ in size throughout the body. The epidermis is generally thin, between 70—150 μm thick, but thickens considerably to around 600 μm in the palms of hands and the soles of feet [40]. The dermis is thicker than the epidermis. The size of the dermis also varies throughout the body, ranging in thickness from around 2 mm to 4 mm, in the back, for example [40]. Further variation arises as each person's skin is different. Even ignoring the microstructural variations of, for example, the number of cross-links in one person's skin compared to another's, macroscopic variations have been observed. For example, studies by Lee and Hwang [41], and Girardeau *et al*. [42] observed changes between different ethnic groups in the thickness of the epidermis compared to the dermis, and the overall thickness of the epidermis and the upper part of the dermis.

The first layer of skin that we discuss is the epidermis, which is the uppermost layer of the skin and, as mentioned previously, is generally significantly thinner than the dermis. In terms

of its microstructure, the epidermis largely consists of cells, the vast majority of which are keratinocytes, which produce keratin. The keratins are a family of 30 proteins that constitute the majority of the protein mass of the epidermis [43]. The epidermis itself consists of multiple layers: the basal layer is the *stratum germinatum*, and the other layers, going outwards, are the *stratum malpighian*, the *stratum granulosum*, and the *stratum corneum* [44]. For the parts of the body that contain a much thicker epidermis, the epidermis contains an extra layer called the *stratum lucidum*. Cells progress from the *stratum germinatum* upwards through the other layers, creating filaments of keratin to provide strength in the *stratum corneum* while moving through the layers [44]. Blood vessels located at the bottom of the epidermis provide nutrients to the epidermis. Keratinocytes can divide in the *stratum germinatum*, but they lose this function and others as they move upwards through the various layers of the epidermis. By the time keratinocytes reach the *stratum corneum*, they have become anucleated, dead cells. Other cells in the epidermis include melanocytes, which produce melanin that provides skin with both its colour and protection from UV radiation, Langerhans cells, which are immunological cells that form a body's first protective barrier against infection from antigens [45], and Merkel cells, which play a role in the reception of touch [46]. The collagen content of the epidermis is small.

Beneath the epidermis is the dermis. The dermis contains the elastic fibres that provide skin with elasticity, hair follicles, sweat glands, sebaceous glands, which coat hair follicles with sebum, blood vessels, and collagen fibres, which inhabit a large volume fraction of the dermis [44]. Due to the significant, stiff collagen content of the dermis and the size of the dermis, it is the most mechanically important layer of the skin. The dermis consists of two layers: the superficial papillary dermis is located beneath the dermal-epidermal junction, and the reticular dermis is located beneath the papillary dermis.

Collagen fibrils in the dermis, approximately 20-40 nm in diameter in the papillary dermis and approximately 60-100 nm in the reticular dermis, aggregate into collagen fibres that are roughly 0.3-3 μm in diameter in the papillary dermis and 10-40 μm in the reticular dermis [47]. Collagen type III accounts for approximately 15% of the collagen content in the dermis and much of it is found in the papillary dermis, whereas the thicker collagen fibres of the dermis largely consist of Type I collagen [47], [48]. Due to the comparative largeness of the reticular dermis and the thicker fibres located within it, collagen Type I is the most abundant collagen type in skin, accounting for approximately 75% of the total collagen content [49]. Nevertheless, the small amounts of other collagen types are important to the proper functioning of the skin: for example, collagen type IV helps regulate fibre diameter for collagen types I and III [50].

In contrast to the aligned collagenous structures of tendons, bundles of collagen fibres in skin are distributed in a mesh with a significant number of out-of-plane fibres that resist a variety of deformations, including shear deformations. This mesh of collagen fibres occurs in the reticular dermis [51], and this mesh is needed because skin is subjected to deformations that need to be resisted from a wide range of directions. Within this mesh, however, there is still a preferential orientation of the collagen fibrils, which lies parallel to the skin's surface [50].

Beneath the epidermis and dermis is a layer of subcutaneous tissue that is sometimes treated as the third layer of skin, when it is called the hypodermis. Uses of the hypodermis include connecting the skin to the underlying fascia, providing support in wound healing, regulating hair follicle development [52], cushioning the internal parts of the body after it has been subjected to an impact, and providing insulation to the body in colder temperatures [53]. To perform these duties, the hypodermis largely consists of fat tissue, with approximately 80% of body fat in healthy adults stored in it [53]. The collagen content in the dermis decreases close to the dermal-hypodermal border, making this region more compliant than the other regions of the dermis [54]. Due to the lack of collagen situated in the hypodermis, it is not considered to significantly contribute to the stress-strain response of skin.

Collagen degeneration in skin tissue has significant consequences for the skin macroscopically. Likewise, damage to the skin impacts both the microstructure and mechanics of the tissue. Deficiencies in collagen synthesis, degradation, and formation contributes to conditions such as scleroderma [55] and Ehlers-Danlos syndrome [56], which are associated with thick, hardened skin and stretchy, fragile skin, respectively. Smoking damages skin and leads to significant changes within it. For example, smoking affects the balance between the biosynthesis and degradation of dermal fibrous proteins such as elastin and collagen. Additionally, cigarette smoke impacts skin wrinkling and accelerates ageing of the skin [57]. Damage caused by photo-ageing from ultraviolet radiation also impacts the microstructure of the skin and, thus, impacts its macroscopic behaviour. Scarred sections of skin possess a different structure to normal skin: collagen fibres in scarred skin are more aligned in a particular direction than in healthy skin [58]. Furthermore, wound healing is affected by the tension acting on an area of damaged skin and the direction, and shape, of any cuts to skin. Worse healing results have been observed for cuts that lie perpendicular to Langer lines compared to cuts parallel to those lines [58], [59]. Langer lines are natural skin tension lines that are named after the nineteenth-century scientist Karl Langer, and the lines are considered to correspond to the lines of greatest tension in the skin [28]. Langer determined these lines of greatest tension in skin by making circular incisions in the skin of cadavers that eventually deformed as the skin local to each incision possessed greater tension in some directions than others [60], [61]. Langer lines constitute just one way of describing the lines of greatest tension in skin. Other sets of tension lines, such as relaxed skin tension lines, provide alternative ways to describe the lines of greatest tension in skin [62]. Experiments on skin indicate that skin tension lines coincide with directions in which collagen is preferentially oriented in, [28], [62].

Intrinsic factors that occur because of ageing also impact the degradation of skin function, particularly once a person is over the age of 50. Collagen volume fraction is significantly decreased in aged skin, falling from 69% to 46% in the papillary dermis and 81% to 58% in the reticular dermis [63]. The effects of ageing are not consistent: the reticular dermis increases in size until the age of 50 and decreases after that, and the thickness of collagen bundles increases until the age of 45 and decreases after that. Cross-linking of collagen fibrils plays an important role in the age-induced changes in the mechanical behaviour of skin. Cross-links can be harder to break down than the collagen fibrils themselves, so cross-linked collagen

fragments accumulate over time and have been observed more commonly in older individuals than younger ones [63]. These collagen cross-linked fragments also contribute to the collagen fibril network becoming more disorganised over time.

1.4 Remainder of the thesis

The outline for the remainder of the thesis is as follows. In Chapter 2, we introduce the mathematical preliminaries needed to work in the field of soft tissue modelling. We start by introducing a tensor, a linear transformation of a particular mathematical object, a vector, for example, into another of the same type. Tensors are necessary to describe the deformation of soft tissues. Next, we introduce the fields of continuum mechanics and hyperelasticity that are used to construct an SEF that quantifies the deformation of a soft tissue. Before discussing SEFs, however, we derive the equations governing the conservation and balance laws that all deformed materials must obey. We use this set of governing equations to explain why we must derive a constitutive equation in order to fully describe the mathematics of a deformed biological material. We then derive the constitutive equation in terms of the SEF for materials with varying degrees of symmetry. Next, we introduce Bayesian statistics and explain how Bayesian statistical techniques can enhance our understanding of soft tissue behaviour and identify credible values of structural model parameters. Finally, we introduce sampling techniques including Markov chain Monte Carlo (MCMC) that we can use to sample from, and estimate the properties of, probability distributions that cannot be sampled directly.

In Chapter 3, we conduct a literature review. We start by discussing key concepts that researchers must take into account when modelling a soft tissue. We then examine existing phenomenological models of soft tissue deformation, analysing their strengths and weaknesses and determining how these models can be improved upon. Then we examine microstructural models of tendons, arteries, and skin, identifying both the microstructural properties that these models explicitly account for and gaps in these existing models that future models can build upon. Next, we review how the dispersion of collagen fibril orientations has been accounted for, both phenomenologically and microstructurally, in the literature. Finally, we describe how Bayesian statistical techniques such as MCMC have successfully been implemented in a variety of scientific fields to quantify the uncertainty in model parameters.

In Chapter 4, we construct a new microstructural SEF, valid for finite elasticity, that is tractable because of a set of physically reasonable assumptions that we make about the properties of the microstructural components. In order to test the validity of the new model, we first use non-linear optimisation to fit the model to high- and low-resolution data taken from tendons in order to find values for the model's parameters that produce a local best fit to data. We compare the fits obtained using this model of soft tissue deformation to those of a model that is widely used in the literature. Then, we create a random walk Metropolis (RWM) MCMC algorithm to enable us to sample hundreds of thousands of parameter vectors and calculate uncertainty in the values of the model parameters by approximating the marginal posterior distribution for each of the parameters. We fit the newly constructed model of soft tissue

behaviour first to a noisy, synthetic data set to examine whether the algorithm is working and then to the high-resolution experimental tendon data.

In Chapter 5, we fit the microstructural model of soft tissue behaviour to skin. We again fit the model to experimental stress-strain data using, first, non-linear optimisation to find parameter values that produce a local best fit to data before quantifying uncertainty in the model's parameters and approximating marginal posterior distributions using the RWM algorithm.

Finally, in Chapter 6, we summarise the work done in this thesis. We first analyse whether the aims detailed in this introductory chapter have been met by the work done in this thesis. We then identify and briefly describe some logical extensions to the work completed in this thesis that could enable our work to be applied to study more-general deformations than are considered in this thesis.

Chapter 2

Mathematical Preliminaries

2.1 Introduction to continuum mechanics

To study the stress-strain behaviour of complex, anisotropic soft tissues, we need to use a mathematical framework to construct and analyse constitutive models. The framework we use is continuum mechanics. In continuum mechanics, we do not model individual particles within a body, but study the bulk properties associated with the body [64]. We shall start by introducing tensors, linear operators that transform a particular mathematical object, a scalar or vector, for example, into another mathematical object of the same type. Tensors are key to the study of finite soft tissue deformation and the bulk properties that we want to study. We shall, then, define the important bulk properties such as mass, body force, torque, stress, and strain that all deformed materials possess. After defining the bulk properties needed to describe soft tissues, we will then examine important measures of deformation, such as the deformation-gradient, and the left and right Cauchy-Green deformation tensors.

As well as defining bulk properties, we must derive a system of equations that fully relates these properties to one another. These equations belong to two families: conservation and balance laws, and constitutive laws. Conservation and balance laws arise from the preservation of certain parameters, including the net flux of the quantity into or out of the continuum. They apply to any continuum. However, conservation laws do not provide us with enough information to fully describe the physics of a deformed body. In order to obtain this additional, necessary information, we need to derive material-specific, constitutive laws that relate the stress and strain to each other. The constitutive equations are not universal: their form depends upon both the structure and symmetry properties of the material being studied. In this chapter, we will derive the constitutive equation first for isotropic materials and, then, with the structure of biological soft tissues in mind, transversely isotropic and orthotropic materials.

Every physical problem that we encounter contains some degree of uncertainty. For example, whenever experimental measurements are taken, there will be errors associated with the measurements collected. This is inevitable: experimental equipment cannot calculate quantities exactly. It is key, therefore, that we attempt to account for uncertainty when fitting a constitutive model to experimental stress-strain data. One way to account for uncertainty in a problem is with Bayesian statistics, which seeks to incorporate both our prior knowledge of the values of model parameters and the likelihood of a given parameter vector producing the

observed experimental data to calculate a posterior probability distribution. We start, therefore, by introducing Bayesian statistical methods, and the core concepts of prior and posterior probability distributions and the likelihood function. We then introduce Markov chain Monte Carlo (MCMC) methods, which are a widely used set of methods for sampling and accurately estimating posterior distributions that are not known exactly. Finally, we discuss some alternative methods to MCMC for sampling from and estimating complex posteriors and analyse their strengths and weaknesses compared to MCMC.

2.2 Tensors

Physical laws are the same in any coordinate system. This is important, otherwise the laws of physics would change based on where in the universe an object is being observed. The way that we describe these invariant physical laws, however, is dependent on the coordinate system we choose to describe them in. A tensor is a linear operator that transforms one mathematical object into another of the same form. The object that is transformed is dependent on the order of the tensor. For example, a second-order tensor, that is, a matrix, transforms one vector, $\mathbf{u}$, into a different vector [64], $\mathbf{v}$. Representing the tensor as $\mathbf{A}$, in equation form we have

$$\mathbf{v} = \mathbf{A}\mathbf{u}. \tag{2.1}$$

As with physical laws, $\mathbf{A}$ itself is independent of the coordinate system that we use, but the components of $\mathbf{A}$ *are* dependent on the coordinate system. For example, in terms of two three-dimensional coordinate systems, which possess the orthonormal basis vectors $\{\mathbf{e}_i, \mathbf{e}_j, \mathbf{e}_k\}$ and $\{\mathbf{e}_p, \mathbf{e}_q, \mathbf{e}_r\}$, respectively, we can write $\mathbf{A}$ as

$$\mathbf{A} = A_{ij}\mathbf{e}_i \otimes \mathbf{e}_j = A_{pq}\mathbf{e}_p \otimes \mathbf{e}_q, \tag{2.2}$$

where A_{ij} represents the value of the component on the ith row and jth column of the tensor, and $A_{ij} \neq A_{pq}$ in general. In order to transform one set of orthonormal basis vectors into another, we rotate the original basis vectors around the origin as follows:

$$\mathbf{A}' = \mathbf{Q}\mathbf{A}\mathbf{Q}^{\mathrm{T}}, \tag{2.3}$$

where $\mathbf{Q}$ is an orthogonal matrix. A key property of orthogonal matrices is that $\mathbf{Q}\mathbf{Q}^{\mathrm{T}} = \mathbf{I}$. Let us consider the example of Cartesian coordinates and cylindrical polar coordinates. The Cartesian coordinate system is an orthonormal, three-dimensional coordinate system in which points are described by their position relative to the x-, y-, and z-axes. The cylindrical polar coordinate system consists of the r-, θ-, and z-axes, where

$$r = \sqrt{x^2 + y^2} \qquad \theta = \tan^{-1}\left(\frac{y}{x}\right) \qquad z = z. \tag{2.4}$$

The individual components of a tensor in cylindrical polar coordinates and Cartesian coordinates obey the following relation [65]:

$$\begin{bmatrix} A_{rr} & A_{r\theta} & A_{rz} \\ A_{\theta r} & A_{\theta\theta} & A_{\theta z} \\ A_{zr} & A_{z\theta} & A_{zz} \end{bmatrix} = \begin{bmatrix} \cos\theta & \sin\theta & 0 \\ -\sin\theta & \cos\theta & 0 \\ 0 & 0 & 1 \end{bmatrix} \begin{bmatrix} A_{xx} & A_{xy} & A_{xz} \\ A_{yx} & A_{yy} & A_{yz} \\ A_{zx} & A_{zy} & A_{zz} \end{bmatrix} \times \begin{bmatrix} \cos\theta & -\sin\theta & 0 \\ \sin\theta & \cos\theta & 0 \\ 0 & 0 & 1 \end{bmatrix}. \tag{2.5}$$

2.3 Invariants of second-rank tensors

Ignoring relativistic effects, a material's mechanical behaviour must be the same in all inertial frames of reference. A strain-energy function (SEF), a measure of the energy stored in a deformed material due to the deformation [66] that we will discuss in more detail later in this chapter, must, therefore, be invariant under a coordinate transformation. Consequently, the SEF is an invariant of the deformation and can be written as a function of other invariants of the strain. The eigenvalues of a matrix, that is, a second-order tensor, are invariants [65]. To prove this, let us assume that λ_i is the ith eigenvalue associated with the matrix $\mathbf{A}^{'} = \mathbf{QAQ}^{\mathrm{T}}$. The corresponding eigenvector is $\mathbf{n}_i^{'}$. By transformation rules for vectors $\mathbf{n}_i^{'} = \mathbf{Qn}$, where we remove the subscript i to indicate that the vector $\mathbf{n}$ may not necessarily be an eigenvector. By the definition of eigenvalues,

$$\mathbf{A}^{'}\mathbf{n}_{(i)}^{'} = \lambda_{(i)}\mathbf{n}_{(i)}^{'}, \tag{2.6}$$

where we introduce parentheses around the index i to indicate that a summation does not occur. We can write (2.6) as

$$\mathbf{QAQ}^{\mathrm{T}}\mathbf{Qn} = \lambda_{(i)}\mathbf{Qn}, \tag{2.7}$$

$$\mathbf{QAn} = \lambda_{(i)}\mathbf{Qn}, \tag{2.8}$$

which implies,

$$\mathbf{Q}^{\mathrm{T}}\mathbf{QAn} = \lambda_{(i)}\mathbf{Q}^{\mathrm{T}}\mathbf{Q}, \tag{2.9}$$

$$\mathbf{An} = \lambda_{(i)}\mathbf{n}. \tag{2.10}$$

By comparison of (2.10) with (2.6), $\lambda_{(i)}$ remains an eigenvalue after a coordinate transformation.

The eigenvalues of a matrix can be used to define other invariants of $\mathbf{A}$. A common set of three invariants [67] are the three coefficients of the characteristic equation of $\mathbf{A}$. To derive these invariants, we start with the equation

$$\det(\mathbf{A} - \lambda_i \mathbf{I}) = 0. \tag{2.11}$$

Writing $\mathbf{A}$ in the form

$$\begin{pmatrix} A_{11} & A_{12} & A_{13} \\ A_{21} & A_{22} & A_{23} \\ A_{31} & A_{32} & A_{33} \end{pmatrix}, \tag{2.12}$$

$\det(\mathbf{A} - \lambda_i \mathbf{I})$ becomes,

$$\begin{aligned} \det(\mathbf{A} - \lambda_i \mathbf{I}) = (A_{11} - \lambda_i)[(A_{22} - \lambda_i)(A_{33} - \lambda_i) - A_{32}A_{23}] - \\ A_{12}[A_{21}(A_{33} - \lambda_i) - A_{31}A_{23}] + \\ A_{13}[A_{21}A_{32} - A_{31}(A_{22} - \lambda_i)]. \end{aligned} \tag{2.13}$$

By (2.11) and (2.13)

$$-\lambda_i^3 + I_1(\mathbf{A})\lambda_i^2 - I_2(\mathbf{A})\lambda_i + I_3(\mathbf{A}) = 0, \tag{2.14}$$

where $I_1(\mathbf{A})$, $I_2(\mathbf{A})$, and $I_3(\mathbf{A})$ are the coefficients of the polynomial in λ_i. The quantities $I_1(\mathbf{A})$, $I_2(\mathbf{A})$, and $I_3(\mathbf{A})$ are all invariants of $\mathbf{A}$ too. In terms of $\mathbf{A}$,

$$I_1(\mathbf{A}) = \text{tr}\mathbf{A}, \tag{2.15}$$

$$I_2(\mathbf{A}) = \frac{1}{2}\left[(\text{tr}\mathbf{A})^2 - \text{tr}(\mathbf{A}^2)\right], \tag{2.16}$$

$$I_3(\mathbf{A}) = \det\mathbf{A}. \tag{2.17}$$

For an isotropic material, the value of the strain energy acting on the material is only dependent on the deformation applied to the material. However, for a transversely isotropic material, the SEF is, additionally, a function of a preferred direction in the reference configuration, $\mathbf{M}$. However, the mechanical behaviour is not dependent on rotations around this preferred direction $\mathbf{M}$. Therefore, denoting the SEF by Ψ,

$$\Psi(\mathbf{C}, \mathbf{M} \otimes \mathbf{a}_0) = \Psi(\mathbf{Q}\mathbf{C}\mathbf{Q}^{\mathrm{T}}, \mathbf{Q}\mathbf{M} \otimes \mathbf{M}\mathbf{Q}^{\mathrm{T}}), \tag{2.18}$$

where $\mathbf{C}$ is a measure of a deformation known as the right Cauchy-Green deformation tensor and will be introduced in more detail later in this chapter. The aforementioned three isotropic invariants still satisfy the constraint on $\mathbf{C}$ shown in (2.18), but we need a further two invariants to satisfy the constraint on $\mathbf{M}\otimes\mathbf{M}$. We adopt the literature standard [68] and use the following two pseudoinvariants:

$$I_4(\mathbf{M}, \mathbf{C}) = \mathbf{M} \cdot \mathbf{C}\mathbf{a}_0, \tag{2.19}$$

$$I_5(\mathbf{M}, \mathbf{C}) = \mathbf{M} \cdot \mathbf{C}^2\mathbf{M}. \tag{2.20}$$

The quantities I_4 and I_5 are pseudoinvariants because they do not just depend on $\mathbf{C}$, but on the direction $\mathbf{M}$ instead. The pseudoinvariants are unchanged by rotations around $\mathbf{M}$, but are changed by other rotations.

2.4 Deformation terminology

2.4.1 Mass, volume and density

The first bulk properties that we define are the mass, m, and volume, v, of a body Ω. Individual objects can increase or decrease in mass, but we do not consider these phenomena in this thesis. Instead, we will assume that mass is conserved, that is, we have a *closed* system. Similarly, there are regimes within continuum mechanics where volume is conserved, incompressibility, or not conserved, compressibility. We define the density, $\rho(\mathbf{x}, t)$, where $\mathbf{x}$ and t denote position and time, respectively, to be the amount of mass per unit volume within the body. For a mass element δm situated within a volume element δv, the mass-density field is defined as

$$\rho(\mathbf{x}, t) = \lim_{\delta V \to 0} \frac{\delta m}{\delta v}. \tag{2.21}$$

Therefore, an expression for the mass is

$$m = \iiint_{\Omega} \rho(\mathbf{x}, t) \mathrm{d}v. \tag{2.22}$$

2.4.2 Position, velocity and acceleration

The rate of change of position, $\mathbf{x}$, is given by

$$\frac{\mathrm{d}\mathbf{x}}{\mathrm{d}t} = \mathbf{v}(\mathbf{x}, t), \tag{2.23}$$

where $\mathbf{v}(\mathbf{x}, t)$ is the velocity. Similarly, acceleration, $\mathbf{a}$, is the material derivative of $\mathbf{v}(\mathbf{x}, t)$.

2.4.3 Force, traction and stress

We need to define the forces that act upon a continuum before we can study its kinematics. There are two types of forces we must consider: body forces, examples of which include gravity and the Coriolis force, which act on the whole of the continuum; and internal forces, which account for interactions between neighbouring elements of a deformed body [69].

For body forces, we introduce the body force per unit volume $\rho\mathbf{b}$, where $\mathbf{b}$ is the body force per unit mass. For interior forces, we consider a plane cutting through the deformed body Ω and passing through the point $\mathbf{x}$ within Ω [69]. The force, $\delta\mathbf{f}$, acting on the area element δs at time t at $\mathbf{x}$ with unit outward-facing normal of $\mathbf{n}$ is,

$$\delta\mathbf{f} = \mathbf{t}(\mathbf{x}, t, \mathbf{n})\delta s, \tag{2.24}$$

where $\mathbf{t}(\mathbf{x}, t, \mathbf{n})$ is the Cauchy traction vector transmitted through the area element δs at the point $\mathbf{x}$ [65]. Importantly, the traction vector's only dependence on the surface δs is on the normal of δs. This is known as Cauchy's fundamental postulate [66]. Furthermore, Cauchy's stress theorem states that the Cauchy traction vector depends linearly on the normal to the surface δS. That is, there exists a tensor field, $\boldsymbol{\sigma}$ and known as the Cauchy stress tensor, at a point $\mathbf{x}$ at time t such that

$$\mathbf{t}(\mathbf{x}, t, \mathbf{n}) = \boldsymbol{\sigma}(\mathbf{x}, t)\mathbf{n}. \tag{2.25}$$

To prove Cauchy's stress theorem we can analyse the tractions that act on a tetrahedron that contains three faces which possess normals that coincide with the coordinate axes [65], in the negative direction, Figure 2.1. Using Cauchy's law of motion, we also assume that there exists a body force and resultant force acting on the tetrahedron, also. Therefore,

$$-\mathbf{t}_1\delta s_1 - \mathbf{t}_2\delta s_2 - \mathbf{t}_3\delta s_3 + \mathbf{t}^{(n)}\delta s + \rho\mathbf{b}\delta v = \rho\mathbf{f}\delta v, \tag{2.26}$$

where $\mathbf{t}_i$ represents the traction acting on a face with a normal in the ith coordinate direction (the minus sign indicates that the normal to the face is in the direction of decreasing values of i), $\mathbf{t}^{(n)}$ represents the traction on the fourth face of the tetrahedron, which has a unit outward-facing normal in the direction $\mathbf{n}$, and v represents the volume of the body. We can rewrite (2.26) as

$$\mathbf{t}^{(n)}\delta s = \mathbf{t}_1 n_1 \delta s + \mathbf{t}_2 n_2 \delta s + \mathbf{t}_3 n_3 \delta s + \rho(\mathbf{f} - \mathbf{b})\frac{\delta v}{\delta s}. \tag{2.27}$$

Imagine that the tetrahedron is infinitesimally small. For a tetrahedron with an edge length of a, the volume is proportional to the cube of a and the surface area is proportional to the square of a. Therefore, when $a \to 0$, that is, when the tetrahedron becomes infinitesimally

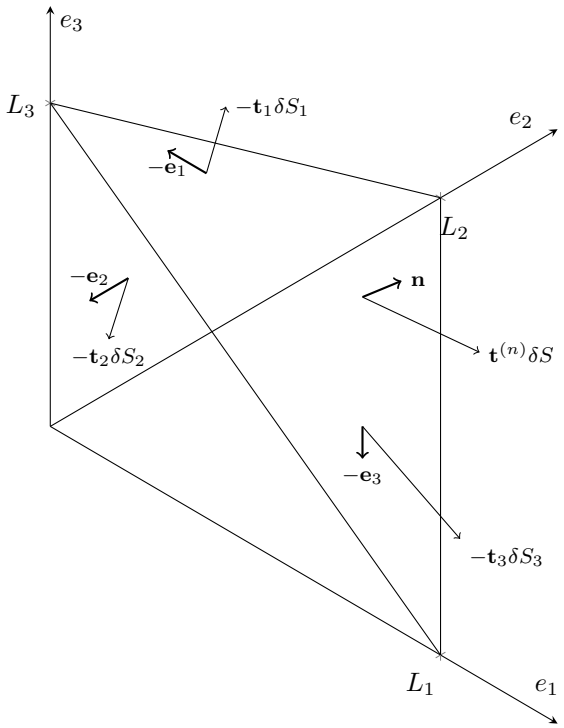

Figure 2.1. A tetrahedron that can be used to prove Cauchy's stress theorem. Adapted from Spencer [65].

small, $(\delta v/\delta s) \to 0$. Therefore, (2.27) becomes

$$\mathbf{t}(\mathbf{x}, t, \mathbf{n}) = \mathbf{t}_1 n_1 + \mathbf{t}_2 n_2 + \mathbf{t}_3 n_3. \tag{2.28}$$

In component form

$$t_i(\mathbf{x}, t, \mathbf{n}) = n_i \sigma_{ij} \mathbf{e}_j. \tag{2.29}$$

From (2.25) and (2.28), we can see that $\mathbf{t}(\mathbf{x}, t, \mathbf{n}) = -\mathbf{t}(\mathbf{x}, t, -\mathbf{n})$.

When a force is applied to a material and the material is deformed, there are two important configurations to consider. The reference configuration describes the material before it is deformed, and the deformed configuration describes the material during the deformation. Because we consider multiple configurations, there are also multiple traction vectors and stress tensors to consider. The first Piola-Kirchhoff or nominal traction vector is a measure of the force per unit *reference* surface area that acts in the same direction as the Cauchy traction vector [69]. Similarly, the first Piola-Kirchhoff traction vector, $\mathbf{T}(\mathbf{X}, t, \mathbf{N})$ can be written linearly in terms of the reference normal vector of the surface, $\mathbf{N}_{\text{ref}}$, in terms of the first Piola-Kirchhoff stress tensor, $\mathbf{P}(\mathbf{X}, t)$. That is,

$$\mathbf{T}(\mathbf{X}, t, \mathbf{N}) = \mathbf{P}(\mathbf{X}, t)\mathbf{N}_{\text{ref}}. \tag{2.30}$$

The transpose of $\mathbf{P}(\mathbf{X}, t)$ is often called the nominal stress tensor, $\mathbf{N}(\mathbf{X}, t)$. For the remainder of the thesis, it is simply denoted as $\mathbf{N}$.

2.4.4 Torque

In addition to linear forces, we need to consider their rotational analogues, torques. When a force, $\tilde{\mathbf{F}}$, acts on a particle with position vector $\mathbf{r}$, the torque, $\boldsymbol{\tau}$, about the origin is given by [70]

$$\boldsymbol{\tau} = \mathbf{r} \times \tilde{\mathbf{F}}. \tag{2.31}$$

2.4.5 Linear and angular momentum

The linear momentum, $\mathbf{p}$, of an object is the product of its mass and velocity

$$\mathbf{p} = m\mathbf{v}(\mathbf{x}, t). \tag{2.32}$$

The rotational analogue of linear momentum is angular momentum, which we denote as $\mathbf{L}$. The angular momentum around a point $\mathbf{z}$ at the point $\mathbf{x}$ is given by the cross product of $\mathbf{x} - \mathbf{z}$ and $m\mathbf{v}(\mathbf{x}, t)$. That is,

$$\mathbf{L} = (\mathbf{x} - \mathbf{z}) \times m\mathbf{v}(\mathbf{x}, t). \tag{2.33}$$

2.4.6 Kinematics

When a force acts on an object it can cause an object to move, deform or both. By move, we mean that the force induces a rigid-body motion on the body, a motion where the shape of the object remains unchanged. Pushing a table or lifting a chair are examples of rigid-body motions. On the other hand, we define deformations as occurring when the displacement between any two volume elements within, or on the surface of, a body changes. As mentioned previously, the reference and deformed configurations describe an object before a deformation is applied and during the deformation, respectively.

Imagine that we have a body Ω_0, Figure 2.2 with surface ∂B in the reference configuration, then we can describe the position of each point in the body by a position vector $\mathbf{X}$. In the deformed configuration, Ω, however, we describe each point by the vector $\mathbf{x}(\mathbf{X}, t)$. Unless otherwise specified, we adopt the convention to denote parameters associated with the reference configuration in upper-case, and parameters associated with the deformed configuration in lower-case.

Let us assume that in the reference configuration there are two points with position vectors $\mathbf{X}$ and $\mathbf{X} + \mathrm{d}\mathbf{X}$, respectively, where $|\mathrm{d}\mathbf{X}| \ll 1$. We can approximate an infinitesimal change of the position vector when the body is deformed by taking a Taylor series expansion of $\mathrm{d}\mathbf{x}$ around $\mathbf{X}$. With this Taylor expansion, we can determine the displacement between the two points in the deformed configuration as

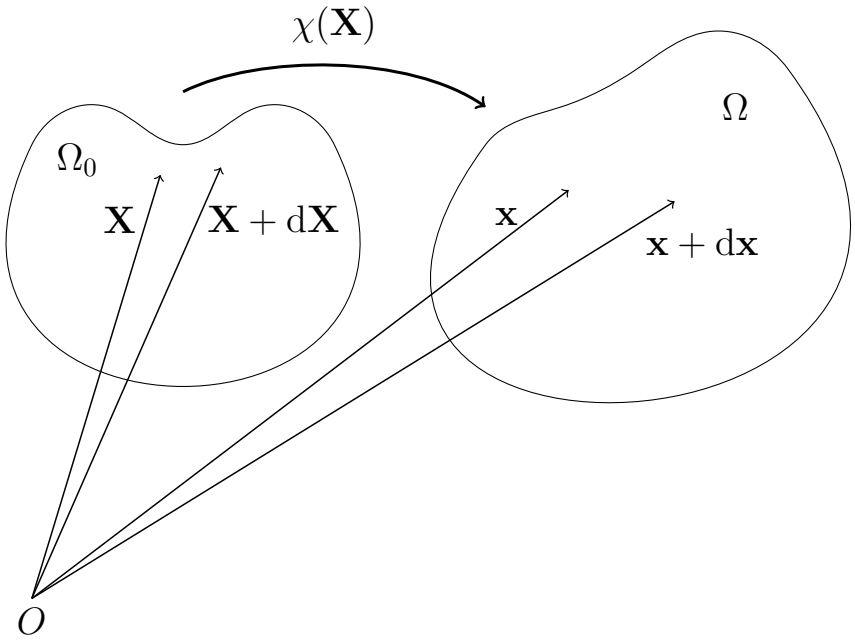

Figure 2.2. The reference and deformed bodies. The deformation mapping $\chi(\mathbf{X})$ provides a one-to-one relation between the reference and deformed coordinates.

$$\mathrm{d}\mathbf{x} = \mathbf{x}(\mathbf{X} + \mathrm{d}\mathbf{X}) - \mathbf{x}(\mathbf{X}), \tag{2.34}$$

$$\simeq \mathbf{x}(\mathbf{X}) + \nabla_{\mathbf{X}}[\mathbf{x}(\mathbf{X})] \cdot (\mathbf{X} + \mathrm{d}\mathbf{X} - \mathbf{X}) - \mathbf{x}(\mathbf{X}), \tag{2.35}$$

$$\simeq \nabla_{\mathbf{X}}[\mathbf{x}(\mathbf{X})] \cdot \mathrm{d}\mathbf{X}. \tag{2.36}$$

Because of this Taylor expansion, we introduce the deformation-gradient, $\mathbf{F}$, which is given by

$$\mathbf{F} = \nabla_{\mathbf{X}}\mathbf{x}(\mathbf{X}). \tag{2.37}$$

In Cartesian coordinates, the gradient operator is $\nabla_{\mathbf{X}} = \left(\frac{\partial}{\partial X_1}, \frac{\partial}{\partial X_2}, \frac{\partial}{\partial X_3}\right)$, where $\mathbf{X}$ is the vector of reference coordinates, that is, $\mathbf{X} = (X_1, X_2, X_3)$. Writing $\mathbf{x} = (x_1, x_2, x_3)$, then $\mathbf{F}$ as defined in (2.37) reduces to, in index notation,

$$F_{\mathrm{iJ}} = \frac{\partial x_i}{\partial X_J}. \tag{2.38}$$

We can obtain further deformation tensors by taking the square of the magnitude of a line element in the deformed configuration, $\mathrm{d}\mathbf{x} \cdot \mathrm{d}\mathbf{x}$, and reference configurations, $\mathrm{d}\mathbf{X} \cdot \mathrm{d}\mathbf{X}$. That is,

$$\mathrm{d}\mathbf{x} \cdot \mathrm{d}\mathbf{x} \quad = (\mathbf{F}\mathrm{d}\mathbf{X}) \cdot (\mathbf{F}\mathrm{d}\mathbf{X}) \quad = \mathbf{F}^{\mathrm{T}}\mathbf{F}\mathrm{d}\mathbf{X} \cdot \mathrm{d}\mathbf{X}, \quad = \mathbf{C}\mathrm{d}\mathbf{X}\mathrm{d}\mathbf{X}, \tag{2.39}$$

$$\mathrm{d}\mathbf{X} \cdot \mathrm{d}\mathbf{X} \quad = (\mathbf{F}^{-1}\mathrm{d}\mathbf{x}) \cdot (\mathbf{F}^{-1}\mathrm{d}\mathbf{x}) \quad = (\mathbf{F}^{-\mathrm{T}}\mathbf{F}^{-1})\mathrm{d}\mathbf{x} \cdot \mathrm{d}\mathbf{x} \quad = \mathbf{B}^{-1}\mathrm{d}\mathbf{x} \cdot \mathrm{d}\mathbf{x}. \tag{2.40}$$

We define the right and left Cauchy-Green deformation tensor, denoted by $\mathbf{C}$ and $\mathbf{B}$, respectively, by

$$\mathbf{C} = \mathbf{F}^{\mathrm{T}}\mathbf{F}, \tag{2.41}$$

$$\mathbf{B} = \mathbf{F}\mathbf{F}^{\mathrm{T}}. \tag{2.42}$$

In contrast to the deformation-gradient, both the right and left Cauchy-Green deformation tensors are symmetric measures of the deformation. Therefore, $\mathbf{B}$ and $\mathbf{C}$ consist of only six independent components, compared to nine independent components for $\mathbf{F}$.

2.5 Conservation Laws

Now that the relevant terminology has been defined, we derive the conservation and balance laws that apply to continua, including when they are deformed.

2.5.1 Conservation of mass

As we do not consider growth or decay in this report, we impose the restriction that the total mass, m, of the deformed body Ω, where we use an upper-case Greek letter as Ω is conventionally used to denote a continuum, does not change. Through this restriction on the mass of Ω, we require that

$$\frac{\mathrm{D}}{\mathrm{D}t}(m) = \frac{\mathrm{D}}{\mathrm{D}t}\iiint_{\Omega} \rho(\mathbf{x}, t)\mathrm{d}v = 0, \tag{2.43}$$

where v represents the volume of the deformed body and D/Dt represents the material time derivative. By the Reynolds Transport Theorem, see Appendix 6.3.3, we can bring the time derivative inside the integral. So (2.43) becomes

$$\frac{\mathrm{D}}{\mathrm{D}t}(m) = \iiint_{\Omega} \left(\frac{\mathrm{D}\rho}{\mathrm{D}t} + \rho \boldsymbol{\nabla}_{\mathbf{x}} \cdot \mathbf{v}(\mathbf{x}, t) \right) \mathrm{d}v = 0. \tag{2.44}$$

Because (2.44) is true for an arbitrary volume v, the integrand must be equal to zero. That is [66],

$$\frac{\mathrm{D}\rho}{\mathrm{D}t} + \rho \boldsymbol{\nabla}_{\mathbf{x}} \cdot \mathbf{v}(\mathbf{x}, t) = 0, \tag{2.45}$$

which is known as the continuity equation. With the assumption of incompressibility, $\mathrm{D}\rho/\mathrm{D}t = 0$, and (2.45) reduces to

$$\boldsymbol{\nabla}_{\mathbf{x}} \cdot \mathbf{v}(\mathbf{x}, t) = 0. \tag{2.46}$$

2.5.2 Balance of linear momentum

Newton's second law states that the resultant force acting on a material is equal to the rate of change of its linear momentum. As discussed earlier, the linear momentum of an object is the product of its mass and its velocity. By (2.43), we can write the total linear momentum acting on an object in the current, or deformed configuration, as

$$\frac{\mathrm{D}}{\mathrm{D}t}\iiint_{\Omega}\rho\mathbf{v}(\mathbf{x},t)\mathrm{d}v=\mathbf{F}, \tag{2.47}$$

where ρ represents the spatial density of the object and $\mathbf{v}(\mathbf{x},t)$ represents the spatial velocity field. As we discussed earlier, the resultant force is the sum of body forces that act on the body of the deformed material and internal forces. Therefore, we can write (2.47) as [65]

$$\frac{\mathrm{D}}{\mathrm{D}t}\iiint_{\Omega}\rho\mathbf{v}(\mathbf{x},t)\mathrm{d}v=\iiint_{\Omega}\rho\mathbf{b}(\mathbf{x},t)\mathrm{d}v+\iint_{\partial\Omega}\mathbf{t}^{(\mathbf{n})}\mathrm{d}s. \tag{2.48}$$

We can write $\mathbf{t}^{(\mathbf{n})}$ as $\boldsymbol{\sigma}\cdot\mathbf{n}$, so that

$$\frac{\mathrm{D}}{\mathrm{D}t}\iiint_{\Omega}\rho\mathbf{v}(\mathbf{x},t)\mathrm{d}v=\iiint_{\Omega}\rho\mathbf{b}(\mathbf{x},t)\mathrm{d}v+\iint_{\partial\Omega}\boldsymbol{\sigma}\cdot\mathbf{n}\mathrm{d}s. \tag{2.49}$$

By the divergence theorem we can transform the surface integral on the right-hand side of (2.49) into a volume integral [65]. Thus, we get

$$\frac{\mathrm{D}}{\mathrm{D}t}\iiint_{\Omega}\rho\mathbf{v}(\mathbf{x},t)\mathrm{d}v=\iiint_{\Omega}\rho\mathbf{b}(\mathbf{x},t)\mathrm{d}v+\iiint_{\Omega}\mathrm{div}\boldsymbol{\sigma}\mathrm{d}v, \tag{2.50}$$

where div represents the divergence. On the left-hand side of (2.50), we can use the Reynolds Transport Theorem to insert the material time derivative into the integrand. Doing that, we obtain

$$\frac{\mathrm{D}}{\mathrm{D}t}\iiint_{\Omega}\rho\mathbf{v}(\mathbf{x},t)\mathrm{d}v=\iiint_{\Omega}\left(\frac{\mathrm{D}}{\mathrm{D}t}(\rho\mathbf{v}(\mathbf{x},t))+(\rho\mathbf{v}(\mathbf{x},t))\boldsymbol{\nabla}_{\mathbf{x}}\cdot\mathbf{v}(\mathbf{x},t)\right)\mathrm{d}v. \tag{2.51}$$

By the conservation of mass, (2.45), we can simplify (2.51)

$$\iiint_{\Omega}\left(\frac{\mathrm{D}}{\mathrm{D}t}(\rho\mathbf{v}(\mathbf{x},t))+(\rho\mathbf{v}(\mathbf{x},t))\boldsymbol{\nabla}_{\mathbf{x}}\cdot\mathbf{v}(\mathbf{x},t)\right)\mathrm{d}v=\iiint_{\Omega}\rho\frac{\mathrm{D}\mathbf{v}(\mathbf{x},t)}{\mathrm{D}t}\mathrm{d}v. \tag{2.52}$$

By (2.52), we have

$$\iiint_{\Omega}\rho\frac{\mathrm{D}\mathbf{v}(\mathbf{x},t)}{\mathrm{D}t}\mathrm{d}v=\iiint_{\Omega}\rho\mathbf{b}(\mathbf{x},t)\mathrm{d}v+\iiint_{\Omega}\mathrm{div}\boldsymbol{\sigma}\mathrm{d}v. \tag{2.53}$$

This is true for an arbitrary volume of a deformed material, so we have the relation

$$\rho\mathbf{a}=\rho\mathbf{b}(\mathbf{x},t)+\mathrm{div}\boldsymbol{\sigma}. \tag{2.54}$$

This is known as *Cauchy's first law of motion* [66].

2.5.3 Balance of angular momentum

The rotational analogue of Newton's second law states that the resultant torque acting on a body, at any point within the body, is equal to the rate of change of angular momentum around a point $\mathbf{z}$ at a point $\mathbf{x}$. That is,

$$\frac{\mathrm{D}((\mathbf{x}-\mathbf{z})\times m\mathbf{v}(\mathbf{x},t))}{\mathrm{D}t}=\boldsymbol{\tau}, \tag{2.55}$$

where, for brevity, we refer to $\mathbf{x}-\mathbf{z}$ as $\mathbf{r}$. By (2.22), (2.31), and the definitions of body forces and tractions stated previously, the balance of angular momentum is

$$\frac{\mathrm{D}}{\mathrm{D}t}\iiint_{\Omega}\mathbf{r}\times\rho\mathbf{v}(\mathbf{x},t)\mathrm{d}v=\iiint_{\Omega}\mathbf{r}\times\rho\mathbf{b}\mathrm{d}v+\iint_{\partial\Omega}\mathbf{r}\times\mathbf{t}^{(\mathbf{n})}\mathrm{d}s. \tag{2.56}$$

We can apply the Reynolds Transport Theorem to the left-hand side of (2.56) and rewrite the traction, to get

$$\iiint_{\Omega}\mathbf{r}\times\rho\mathbf{a}\mathrm{d}v=\iiint_{\Omega}\mathbf{r}\times\rho\mathbf{b}\mathrm{d}v+\iint_{\partial\Omega}\mathbf{r}\times(\boldsymbol{\sigma}\cdot\mathbf{n})\mathrm{d}s. \tag{2.57}$$

Using the divergence theorem on the second term on the right-hand side of (2.57), we get [69]

$$\iiint_{\Omega}\mathbf{r}\times\rho\mathbf{a}\mathrm{d}v=\iiint_{\Omega}\mathbf{r}\times\rho\mathbf{b}\mathrm{d}v+\iint_{\partial\Omega}[\mathbf{r}\times\mathrm{div}\boldsymbol{\sigma}+\boldsymbol{\epsilon}:\boldsymbol{\sigma}^{T}]\mathrm{d}v. \tag{2.58}$$

By Cauchy's first law of motion, most terms cancel out, and we are left with

$$0=\iiint_{\Omega}\boldsymbol{\epsilon}:\boldsymbol{\sigma}^{T}\mathrm{d}v. \tag{2.59}$$

In component form, (2.59) is

$$\epsilon_{ijk}\sigma_{kj}=0. \tag{2.60}$$

Therefore, we have,

$$\sigma_{21}-\sigma_{12}=0 \qquad \sigma_{13}-\sigma_{31}=0 \qquad \sigma_{32}-\sigma_{23}=0. \tag{2.61}$$

Therefore, the Cauchy stress tensor is symmetric by the balance of angular momentum in this scenario.

2.5.4 Conservation of energy

We impose conservation of energy. For a continuum, the kinetic energy, T, is given by, in index notation,

$$T = \frac{1}{2}\iiint_{\Omega} \rho v_i v_i \mathrm{d}v, \tag{2.62}$$

where $v_i v_i$ is index notation for the dot product. In addition to kinetic energy, a continuum also possesses internal energy, E, given by

$$E = \iiint_{\Omega} \rho e \mathrm{d}v, \tag{2.63}$$

where e is the internal energy density. Mechanical energy, U, is the sum of the kinetic and internal energies. The rate of change of mechanical energy must be equal to the sum of the work done by the body and the energy flux in and out of the body. Sources of energy flux include radiation and energy lost as sound, but we only consider heat flux, $\mathbf{q}$, as most energy is dissipated through heat flux [65]. Consequently, the rate of change of mechanical energy is given by

$$\frac{\mathrm{D}}{\mathrm{D}t}\iiint_{\Omega} \rho\left(\frac{1}{2}v_i v_i + e\right)\mathrm{d}v = \iiint_{\Omega} \rho b_i v_i \mathrm{d}v + \iint_{\partial\Omega} (\sigma_{ji} v_i - q_j) n_j \mathrm{d}s. \tag{2.64}$$

The negative sign in front of the heat flux is to signify that we use the outward normal, n_j, for the surface element s, and q is a measure of the influx of energy [65]. As previously, we apply the Reynolds Transport theorem and the divergence theorem to (2.64). Therefore, (2.64) becomes

$$\iiint_{\Omega} \rho\frac{\mathrm{D}}{\mathrm{D}t}\left(\frac{1}{2}v_i v_i + e\right)\mathrm{d}v = \iiint_{\Omega} \left(\rho b_i v_i + \frac{\partial}{\partial x_j}(\sigma_{ji} v_i - q_j)\right)\mathrm{d}v. \tag{2.65}$$

This relation must hold for an arbitrary volume, and so

$$\rho\frac{\mathrm{D}}{\mathrm{D}t}\left(\frac{1}{2}v_i v_i + e\right) = \rho b_i v_i + \frac{\partial}{\partial x_j}(\sigma_{ji} v_i - q_j). \tag{2.66}$$

After expanding the material derivative and rearranging (2.66), we get

$$-v_i\left(\frac{\partial \sigma_{ji}}{\partial x_j} + \rho b_i - \rho a_i\right) + \rho\frac{\mathrm{D}e}{\mathrm{D}t} - \sigma_{ji}\frac{\partial v_i}{\partial x_j} + \frac{\partial q_j}{\partial x_j} = 0. \tag{2.67}$$

The expression in parentheses equals zero by the conservation of linear momentum. We can now rewrite (2.67) as

$$\rho\frac{\mathrm{D}e}{\mathrm{D}t} = \sigma_{ji}\frac{\partial v_i}{\partial x_j} - \frac{\partial q_j}{\partial x_j}. \tag{2.68}$$

Angular-momentum balance means that the Cauchy stress tensor is symmetric, so we can rewrite $\sigma_{ji}\frac{\partial v_i}{\partial x_j}$ as $\sigma_{ij}\frac{\partial v_i}{\partial x_j}$. We can also swap the dummy indices, so $\sigma_{ji}\frac{\partial v_i}{\partial x_j} = \sigma_{ij}\frac{\partial v_j}{\partial x_i}$. Therefore, (2.68) can be rewritten as

$$\rho\frac{\mathrm{D}e}{\mathrm{D}t} = \frac{1}{2}\sigma_{ij}\left(\frac{\partial v_j}{\partial x_i} + \frac{\partial v_i}{\partial x_j}\right) - \frac{\partial q_j}{\partial x_j}. \tag{2.69}$$

We can write (2.69) in terms of the components of $\mathbf{D}$, which is known as the rate-of-deformation or rate-of-strain tensor. That is,

$$D_{ij} = \frac{1}{2}\left(\frac{\partial v_j}{\partial x_i} + \frac{\partial v_i}{\partial x_j}\right), \tag{2.70}$$

$$\rho\frac{\mathrm{D}e}{\mathrm{D}t} = \sigma_{ij}D_{ij} - \frac{\partial q_j}{\partial x_j}. \tag{2.71}$$

In dyadic notation, we have

$$\rho\frac{\mathrm{D}e}{\mathrm{D}t} = \boldsymbol{\sigma} : \mathbf{D} - \boldsymbol{\nabla}\cdot\mathbf{q}. \tag{2.72}$$

In the next section, we neglect thermal effects. Therefore, the only source of internal energy that we consider is the internal mechanical energy. We then introduce a strain energy function that is a measure of the internal potential energy in a deformed object [69]. This enables us to derive a constitutive equation for the material.

2.6 Non-linear elasticity

In total, the conservation and balance laws we derived in the previous subsections provide us with a set of equations that relate a continuum's bulk properties to one another. However, the conservation and balance laws do not provide us with enough information to allow us to describe the system fully. Consequently, to fully describe the system, we must construct a constitutive law, specific to the material, that relates the stress acting on the material to the strain experienced by it.

In the small-strain limit, where the theory of linear elasticity is a good approximation to make, physical stress-strain behaviour can be modelled well using the following constitutive relation [71]:

$$\sigma_{ij} = C_{ijks}E_{ks}, \tag{2.73}$$

where C_{ijks} is the elasticity tensor. Due to strain energy considerations and its symmetry properties, the elasticity tensor can possess up to twenty-one elastic constants [72]. That number decreases, however, for a material if it possesses an axis, or axes, of mechanical

symmetry [73]. The constraints that the elasticity tensor must satisfy are:

$$C_{ijks} = C_{jiks} \qquad C_{ijks} = C_{ijsk} \qquad C_{ijks} = C_{jisk}. \tag{2.74}$$

However, under physiological conditions, soft tissues are subjected to strains significantly greater than the small-strain limit. In this case, finite elasticity theory better approximates the physiological mechanical behaviour of soft tissues. In order to model soft tissue behaviour, we need to derive a constitutive relation that is appropriate for finite elasticity. To do this, we employ a strain-energy function (SEF), W, which is a measure of the energy stored in the material due to the deformation [66]. We assume that the SEF depends arbitrarily on the change in configuration and is, thus, a function of the nine components of the deformation gradient tensor [65], $W = W(\mathbf{F})$.

In order to ensure that W is objective, we impose the condition that it cannot change value under a rigid-body motion. A rigid-body motion can be represented by the orthogonal matrix, $\mathbf{Q}$, so $W(\mathbf{F}) = W(\mathbf{QF})$. By the polar decomposition theorem [66], $\mathbf{F}$ can be decomposed into the product of an orthogonal tensor, $\mathbf{R}$, a tensor whose inverse is equal to its transpose, and a symmetric tensor, $\mathbf{U}$. Thus, $\mathbf{F} = \mathbf{RU}$. As $W(\mathbf{F}) = W(\mathbf{QF})$ for any orthogonal matrix, objectivity is satisfied when $\mathbf{Q} = \mathbf{R}^{\mathrm{T}}$. That is, $W(\mathbf{F}) = W(\mathbf{R}^{\mathrm{T}}\mathbf{RU}) = W(\mathbf{U})$. Furthermore, $\mathbf{C}$ can be rewritten as $\mathbf{C} = \mathbf{U}^{\mathrm{T}}\mathbf{R}^{\mathrm{T}}\mathbf{RU} = \mathbf{U}^{\mathrm{T}}\mathbf{U} = \mathbf{U}^2$. Thus, we can write W as a function of $\mathbf{C}$ instead, i.e. $W = W(\mathbf{C})$.

To begin constructing our constitutive equation, we recall the conservation-of-energy constraint, (2.72), replace e with $W = \rho_0 e$, and neglect heat flux, giving us the relation

$$\frac{\rho}{\rho_0}\frac{\mathrm{D}W}{\mathrm{D}t} = \sigma_{ij}D_{ij}. \tag{2.75}$$

Rewriting $\mathrm{D}W/\mathrm{D}t$, we have

$$\begin{aligned}\frac{\mathrm{D}W}{\mathrm{D}t} &= \frac{\partial W}{\partial C_{RS}}\frac{\mathrm{D}C_{RS}}{\mathrm{D}t},\\ &= \frac{\partial W}{\partial C_{RS}}\frac{\mathrm{D}}{\mathrm{D}t}\left(\frac{\partial x_i}{\partial X_R}\frac{\partial x_i}{\partial X_S}\right),\\ &= \frac{\partial W}{\partial C_{RS}}\left(\frac{\partial v_i}{\partial X_R}\frac{\partial x_i}{\partial X_S} + \frac{\partial x_i}{\partial X_R}\frac{\partial v_i}{\partial X_S}\right),\end{aligned} \tag{2.76}$$

as the coordinates $\mathbf{X}$ do not depend on time. After interchanging the dummy indices R and S on the second term of the right-hand side of (2.76), we obtain

$$\frac{\mathrm{D}W}{\mathrm{D}t} = \left(\frac{\partial W}{\partial C_{RS}} + \frac{\partial W}{\partial C_{SR}}\right)\frac{\partial v_i}{\partial X_R}\frac{\partial x_i}{\partial X_S}. \tag{2.77}$$

We showed when considering the conservation of energy that, assuming there is no heat flux,

$$\sigma_{ij}D_{ij} = \sigma_{ij}\frac{\partial v_i}{\partial x_j}, \tag{2.78}$$

so according to our constitutive law and the symmetry of $\mathbf{C}$

$$\sigma_{ij}\frac{\partial v_i}{\partial x_j} = \frac{\rho}{\rho_0}\left(\frac{\partial W}{\partial C_{RS}} + \frac{\partial W}{\partial C_{SR}}\right)\frac{\partial v_i}{\partial X_R}\frac{\partial x_i}{\partial X_S}, \tag{2.79}$$

$$= 2\frac{\rho}{\rho_0}\frac{\partial W}{\partial C_{RS}}\frac{\partial v_i}{\partial x_j}\frac{\partial x_j}{\partial X_R}\frac{\partial x_i}{\partial X_S}. \tag{2.80}$$

This holds for arbitrary $\partial v_i/\partial x_j$, so [65]

$$\sigma_{ij} = 2\frac{\rho}{\rho_0}\frac{\partial W}{\partial C_{RS}}\frac{\partial x_j}{\partial X_R}\frac{\partial x_i}{\partial X_S}. \tag{2.81}$$

As the SEF is invariant under coordinate transformation, we can write it in terms of other invariants of $\mathbf{C}$. The SEF for isotropic materials can be written in terms of three strain invariants. Recalling (2.15)—(2.17), they are

$$I_1 = C_{MM} = \text{tr}\mathbf{C} = \lambda_1^2 + \lambda_2^2 + \lambda_3^2, \tag{2.82}$$

$$I_2 = \frac{1}{2}(C_{MM}C_{NN} - C_{RS}C_{RS}), \tag{2.83}$$

$$= \frac{1}{2}((\text{tr}\mathbf{C})^2 - \text{tr}\mathbf{C}^2) = \lambda_1^2\lambda_2^2 + \lambda_1^2\lambda_3^2 + \lambda_2^2\lambda_3^2, \tag{2.84}$$

$$I_3 = \det\mathbf{C} = \prod_{i=1}^{3}\lambda_i^2, \tag{2.85}$$

where λ_i represents the ith eigenvalue of $\mathbf{C}$. For transversely isotropic materials, the SEF is not just a function of the deformation itself, but also of the preferred direction in the reference configuration, represented by the unit vector $\mathbf{M}$. To account for this extra dependence, a transversely isotropic SEF is a function of two pseudoinvariants, which account for the material's behaviour in the direction $\mathbf{M}$, in addition to the three isotropic strain invariants. Concentrating on an isotropic material, first, we previously derived the three strain invariants needed to describe the SEF. Physically, the third strain invariant corresponds to the square of the ratio of the volume of the deformed body to the volume of the undeformed body, so $\rho/\rho_0 = \sqrt{I_3}$. As W is a function of these three strain invariants,

$$\frac{\partial W}{\partial C_{RS}} = \frac{\partial W}{\partial I_i}\frac{\partial I_i}{\partial C_{RS}}. \tag{2.86}$$

The derivatives of I_1 and I_2 with respect to C_{RS} are

$$\frac{\partial I_1}{\partial C_{RS}} = \frac{\partial C_{MM}}{\partial C_{RS}} = \delta_{MR}\delta_{MS} = \delta_{RS}, \tag{2.87}$$

$$\frac{\partial I_2}{\partial C_{RS}} = \frac{1}{2}\frac{\partial I_2}{\partial C_{RS}}(C_{MM}C_{NN} - C_{KJ}C_{KJ}), \tag{2.88}$$

$$= \frac{1}{2}(\delta_{MR}\delta_{MS}C_{NN} + \delta_{NR}\delta_{NS}C_{MM} - 2\delta_{KR}\delta_{JS}C_{KJ}), \tag{2.89}$$

$$= \frac{1}{2}(2\delta_{RS}I_1 - 2C_{RS}), \tag{2.90}$$

where we have used the symmetry of $\mathbf{C}$ to write $C_{KJ}C_{JK}$, which is the trace of $\mathbf{C}^2$ in index notation, as $C_{KJ}C_{KJ}$. For I_3, we take the trace of the Cayley-Hamilton theorem, which states that a second-order tensor satisfies its own characteristic equation. Therefore,

$$I_3 = \frac{1}{3}(\text{tr}\mathbf{C}^3 - I_1\text{tr}\mathbf{C}^2 + I_2\text{tr}\mathbf{C}). \tag{2.91}$$

The trace of $\mathbf{C}^3$ can be written in component form as $C_{LM}C_{MN}C_{NL}$. Differentiating, we obtain

$$\begin{aligned}\frac{\partial}{\partial C_{RS}}(C_{LM}C_{MN}C_{NL}) &= \delta_{LR}\delta_{MS}C_{MN}C_{NL} + \delta_{MR}\delta_{NS}C_{LM}C_{NL} &(2.92)\\ &\quad +\delta_{NR}\delta_{LS}C_{LM}C_{MN}. &(2.93)\\ &= 3C_{SN}C_{NR}, &(2.94)\end{aligned}$$

where we swap the dummy indices due to the symmetry of $\mathbf{C}$. Utilising (2.87)—(2.94) and simplifying gives us

$$\frac{\partial I_3}{\partial C_{RS}} = I_2\delta_{RS} - I_1C_{RS} + C_{RP}C_{SP}. \tag{2.95}$$

The Cauchy stress is, therefore, for an isotropic, non-linear elastic material given by

$$\begin{aligned}\sigma_{ij} = 2\frac{\rho}{\rho_0}\frac{\partial x_i}{\partial X_R}\frac{\partial x_j}{\partial X_S}\Bigg[&\left(\frac{\partial W}{\partial I_1} + I_1\frac{\partial W}{\partial I_2} + I_2\frac{\partial W}{\partial I_3}\right)\delta_{RS} &(2.96)\\ &-\left(\frac{\partial W}{\partial I_2} + I_1\frac{\partial W}{\partial I_3}\right)C_{RS} + \frac{\partial W}{\partial I_3}C_{RP}C_{SP}\Bigg]. &(2.97)\end{aligned}$$

In dyadic notation, and introducing the notation $\partial W/\partial I_i = W_i$, we have

$$\boldsymbol{\sigma} = 2(I_3)^{\frac{1}{2}}\mathbf{F}\Big[(W_1 + I_1W_2 + I_2W_3)\mathbf{I} - (W_2 + I_1W_3)\mathbf{C} + W_3\mathbf{C}^2\Big]\mathbf{F}^{\text{T}}. \tag{2.98}$$

If we write the Cauchy stress in terms of $\mathbf{B}$, we have

$$\boldsymbol{\sigma} = 2(I_3)^{\frac{1}{2}}\Big[(W_1 + I_1W_2 + I_2W_3)\mathbf{B} - (W_2 + I_1W_3)\mathbf{B}^2 + W_3\mathbf{B}^3\Big]. \tag{2.99}$$

Using the Cayley-Hamilton theorem, we can eliminate $\mathbf{B}^3$, and by multiplying the Cayley-Hamilton theorem by $\mathbf{B}^{-1}$ we can eliminate $\mathbf{B}^2$ also. Therefore, we have

$$\boldsymbol{\sigma} = 2(I_3)^{\frac{1}{2}}\Big[(I_2W_2 + I_3W_3)\mathbf{I} + W_1\mathbf{B} - I_3W_2\mathbf{B}^{-1}\Big], \tag{2.100}$$

If we assume that the material is incompressible, then $I_3 = 1$. To account for the loss of a degree of freedom, we introduce a Lagrange multiplier, p, to the incompressible SEF, giving

us

$$W = W(I_1, I_2) - \frac{p}{2}(I_3 - 1), \tag{2.101}$$

$$W_3 = -\frac{p}{2}. \tag{2.102}$$

Therefore

$$\boldsymbol{\sigma} = 2\left[\left(I_2 W_2 - \frac{p}{2}\right)\mathbf{I} + 2W_1\mathbf{B} - 2W_2\mathbf{B}^{-1}\right]. \tag{2.103}$$

The Lagrange multiplier is undetermined, and so we can incorporate the other term in parentheses in (2.103) into the Lagrange multiplier. The constitutive equation for an incompressible, isotropic materials is, therefore,

$$\boldsymbol{\sigma} = -p\mathbf{I} + 2W_1\mathbf{B} - 2W_2\mathbf{B}^{-1}. \tag{2.104}$$

As mentioned previously, for transversely isotropic materials, we must account for the dependence of the material's mechanical behaviour on the preferred direction $\mathbf{M}$ through the inclusion of two pseudoinvariants. Following the convention of the literature, the pseudoinvariants we choose are

$$I_4 = \mathbf{M} \cdot (\mathbf{CM}), \tag{2.105}$$

$$I_5 = \mathbf{M} \cdot (\mathbf{C}^2\mathbf{M}). \tag{2.106}$$

To include these pseudoinvariants in our constitutive relation, we need to differentiate them with respect to $\mathbf{C}$ also. The vector $\mathbf{M}$ is only dependent on the initial position $\mathbf{X}$ of the continuum, and so its derivative with respect to $\mathbf{C}$ is zero. The derivatives of the pseudoinvariants with respect to $\mathbf{C}$ in component form are, thus,

$$\frac{\partial I_4}{\partial C_{RS}} = M_I \cdot \delta_{IR}\delta_{JS}M_J = M_R M_S = (\mathbf{M} \otimes \mathbf{M})_{RS}, \tag{2.107}$$

$$\begin{aligned}\frac{\partial I_5}{\partial C_{RS}} &= M_I \cdot (\delta_{IR}\delta_{SJ}M_J + C_{IR}\delta_{JS}M_J), \\ &= M_R C_{SJ} M_J + M_I C_{IR} M_S, \\ &= (\mathbf{M} \otimes \mathbf{CM} + \mathbf{CM} \otimes \mathbf{M})_{RS}.\end{aligned} \tag{2.108}$$

With (2.107) and (2.108), the constitutive law for transverse isotropy is

$$\begin{aligned}\boldsymbol{\sigma} = &-p\mathbf{I} + 2W_1\mathbf{B} - 2W_2\mathbf{B}^{-1} + 2W_4\mathbf{m} \otimes \mathbf{m} \\ &+2W_5(\mathbf{m} \otimes \mathbf{Cm} + \mathbf{Cm} \otimes \mathbf{m}),\end{aligned} \tag{2.109}$$

where $\mathbf{m} = \mathbf{FM}$ is the orientation of the preferred direction in the deformed configuration.

2.7 Bayesian statistics

In this chapter, we have so far derived deterministic constitutive equations that, for a particular parameter vector, produce the same relation between the independent variable, the stretch, and the dependent variable, the stress. In reality, however, there is noise present in the system due to unavoidable errors in the values recorded by experimental equipment and other uncontrollable factors that can have an impact on measurements. We would ideally like to account for this noise. We can try to quantify the noise in the system, while still determining the most probable values for the model's parameters, with the use of statistical methods. Therefore, we now introduce the concept of Bayesian statistics, a field which provides intuitive methods to quantify uncertainty in the values of parameters. In Bayesian statistics, we treat parameters as random variables and seek to determine probability distributions from which we can compute credible intervals of the parameter values. To quantify uncertainty in Bayesian statistics, we must derive two important terms: the *prior* probability distribution contains the information we wish to include about our parameter values before any data is considered; and the *likelihood* function is a measure of how likely a given parameter vector is to produce the experimental data [74]. With these terms, we obtain a *posterior* probability distribution that conditions our prior understanding of the parameter values with the collected data.

The key principle of Bayesian statistics was first defined by Reverend Thomas Bayes, who gives his name to the field, in a posthumously published 1763 essay on chance [75]. This key principle is that posterior probability can be obtained by multiplying our prior probability of parameter values with the likelihood of parameter values producing the experimental data. By updating our prior knowledge with experimental data, we can hopefully ascertain credible intervals for the unknown values of our parameters. In equation form, Bayes' Rule is

$$\pi(\boldsymbol{\theta}|\mathbf{y}) = \frac{L(\mathbf{y}|\boldsymbol{\theta})\pi_0(\boldsymbol{\theta})}{\pi_d(\mathbf{y})}, \tag{2.110}$$

where $\pi_0(\boldsymbol{\theta})$ is the prior distribution of the parameter vector $\boldsymbol{\theta}$, $L(\mathbf{y}|\boldsymbol{\theta})$ is the likelihood function of observing the experimental data $\mathbf{y}$ given $\boldsymbol{\theta}$, $\pi_d(\mathbf{y})$ is the probability of observing the experimental data that acts as a normalisation constant in (2.110), and $\pi(\boldsymbol{\theta}|\mathbf{y})$ is the posterior probability of $\boldsymbol{\theta}$.

The prior is not objective. We choose an appropriate prior based on our understanding of the parameter values before we look at the data. For instance, if a parameter can be negative, we would not assign a prior distribution that only has support along the positive real axis. Even assigning a uniform prior to a parameter is subjective, as we must define the range that the uniform prior extends over and it is a conscious choice to assign equal prior probability to each possible value within a specific set. Rules for selecting priors have been developed. For example, Harold Jeffreys posited his general rule (1946) for defining a prior [76]. In Jeffreys's general rule, we define a prior for a parameter vector $\boldsymbol{\theta}$ in terms of the Fisher Information matrix $\mathbf{I}(\boldsymbol{\theta})$, which summarises the amount of information in the data that is pertinent to the

model parameters [77], and the log-likelihood l as follows:

$$\pi_0(\boldsymbol{\theta}) \propto \det(\mathbf{I}(\boldsymbol{\theta})_{ij})^{-\frac{1}{2}}, \tag{2.111}$$

where

$$\mathbf{I}(\boldsymbol{\theta})_{ij} = E\left(-\frac{\partial^2 l}{\partial\theta_i \partial\theta_j}\right), \tag{2.112}$$

where l is the log-likelihood, $E(\cdot)$ represents the expected value of $\cdot$, and $\det(\cdot)$ represents the determinant of $\cdot$. Priors developed according to Jeffreys's general rule possess the property [78] that, for a transformation of parameters from $\boldsymbol{\theta}$ to $\boldsymbol{\gamma}(\boldsymbol{\theta})$,

$$\pi_0(\boldsymbol{\theta}) = \pi_0(\boldsymbol{\gamma}(\boldsymbol{\theta})) \cdot \left|\frac{\partial\boldsymbol{\gamma}}{\partial\boldsymbol{\theta}}\right|. \tag{2.113}$$

However, these priors, and other priors derived from a particular rule in an attempt to be objective, do possess problems under certain situations and can lead to posteriors with undesirable qualities [78], [79]. With priors, we should be inclusive regarding what parameter values we assign some probability weight to, as we do not want to preclude parameter values that are likely to produce the observed data, according to our likelihood function.

The exact form of the posterior distribution in (2.110) often cannot be determined. This is caused by the impracticality of calculating the normalisation term, $\pi_d(\mathbf{y})$, exactly. An alternate form of $\pi_d(\mathbf{y})$ is

$$\pi_d(\mathbf{y}) = \int L(\mathbf{y}|\boldsymbol{\theta})\pi_0(\boldsymbol{\theta})\mathrm{d}\boldsymbol{\theta}. \tag{2.114}$$

From (2.114), we see that in order to calculate $\pi_d(\mathbf{y})$, we must integrate, potentially over many dimensions, to calculate the posterior weight of each potential parameter vector. That is hard to do, particularly when there are multiple parameters that we wish to identify credible intervals for. By (2.114) and (2.110), however, we know that if we multiply either the prior or likelihood function by a multiplicative constant, then the posterior will remain unchanged. Therefore, we can consider the following alternative form of Bayes's Rule, where we do not need to calculate $\pi_d(\mathbf{y})$,

$$\pi(\boldsymbol{\theta}|\mathbf{y}) \propto L(\mathbf{y}|\boldsymbol{\theta})\pi_0(\boldsymbol{\theta}). \tag{2.115}$$

If $L(\mathbf{y}|\boldsymbol{\theta})\pi_0(\boldsymbol{\theta})$ corresponds to a known distribution, then we can calculate $\pi_d(\mathbf{y})$ and use (2.110) to fully characterise the posterior distribution. However, $L(\mathbf{y}|\boldsymbol{\theta})\pi_0(\boldsymbol{\theta})$ often does not correspond to a known distribution, meaning we only know the posterior up to a multiplicative constant. Therefore, we seek methods that allow us to characterise, or accurately approximate, $\pi(\boldsymbol{\theta}|\mathbf{y})$, when we only know $L(\mathbf{y}|\boldsymbol{\theta})$ and $\pi_d(\mathbf{y})$. Fortunately, there are methods that allow us

to obtain accurate estimates of the full posterior by sampling a subset of potential parameter values that is large enough to represent the entire set. Then, we can use this representative sampled subset to make inferences about the population as a whole by using the subset to approximate the posterior distribution.

2.8 Markov chain Monte Carlo and the Metropolis-Hastings algorithm

In this section, we introduce one widely used technique to sample from an unknown posterior distribution, Markov chain Monte Carlo (MCMC). Furthermore, in the next section we will introduce some alternative Bayesian statistical techniques that can be used to attempt to accurately estimate an unknown posterior distribution, or properties associated with the distribution. In Chapters 4 and 5, we will use MCMC to attempt to predict parameter posteriors. By introducing MCMC in this section, therefore, we seek to explain why it is a reasonable method to quickly and efficiently sample from posterior distributions. Furthermore, in the next section, we will attempt to explain why MCMC is an appropriate choice to measure uncertainty in soft-tissue modelling problems compared to the other methods detailed in the next section.

MCMC combines the two namesake statistical methods into one technique. Firstly, Monte Carlo methods enable us to estimate the expectation values of functions which contain random variables that possess a posterior distribution [80]. For example, if we want to calculate the expectation value of $f(x)$, where $x \sim \pi(x|\mathbf{y})$, exactly, then we must compute

$$E[f(x)] = \int f(x)\pi(x|\mathbf{y})\mathrm{d}x. \tag{2.116}$$

If the integral in (2.116) is impractical to compute, we can obtain a Monte Carlo estimate by randomly sampling from the distribution $\pi(x|\mathbf{y})$ and computing $f(x)$ at each of the points we sample. In other words, if we take N samples, we have the points $\hat{\mathbf{x}} = (\hat{x}_1, \dots, \hat{x}_N)$ in the support of x, according to $\pi(x|\mathbf{y})$, and we compute $f(\hat{x}_1), \dots, f(\hat{x}_N)$. Therefore,

$$E[f(x)] = \int f(x)\pi(x|\mathbf{y})\mathrm{d}x \approx \frac{1}{N}\sum_{i=1}^{N} f(\hat{x}_i). \tag{2.117}$$

By the law of large numbers, the more points we include in the Monte Carlo estimate, the better approximation to the true expected value we obtain.

The problem with obtaining Monte Carlo estimates as in (2.117) arises when the distribution of x is not known and normalised. In that case, we cannot randomly sample from the distribution to obtain a representative sample of points from which to create our Monte Carlo estimate. In that case, we must also employ methods that allow us to obtain a representative sample from our unknown full posterior. In MCMC, Markov chains allow us to take representative samples from the posterior. Markov chains consist of a sequence of 'memory-less' states. By 'memory-less' we mean that the probability of where the Markov chain moves to

at any particular time interval, which we define as the $i+1$th interval, is only dependent on the current position of the Markov chain, that is, the position of the Markov chain at the ith interval. In other words, the history of the chain is not a factor in the future of the chain [80]. In terms of the transition matrix, P, this can be written as

$$P(X_{i+1} = \boldsymbol{\theta}_{i+1} | X_0 = \boldsymbol{\theta}_0, \dots, X_i = \boldsymbol{\theta}_i) = P(X_{i+1} = \boldsymbol{\theta}_{i+1} | X_i = \boldsymbol{\theta}_i), \tag{2.118}$$

where X_i represents the ith position of the chain and $\boldsymbol{\theta}_i$ represents the state in which the Markov chain resides at the position i. Markov chains can possess a stationary distribution, also known as an equilibrium or invariant distribution, that corresponds to the probability distribution of each possible state in the system as $i \to \infty$.

The goal of combining Monte Carlo methods and Markov chains in MCMC is, therefore, to create a sequence of states, with the probability of choosing each state dependent only on the current state of the system, whose invariant density corresponds to the posterior distribution $\pi(\boldsymbol{\theta}|\mathbf{y})$. Therefore, we sample from the posterior in our chosen MCMC algorithm. For our sampling to work, a few conditions must be met. Firstly, the states, that is, parameter vectors, chosen must be ergodic, which means that, collectively, the samples must be representative of the complete distribution, not just a subset of it. By representative, we mean that both the entire range of the distribution must be sampled from and the statistics associated with the true posterior, the mean and variance, for example, must be accurately approximated. For a particular problem, proving ergodicity is hard. Instead, we analyse the estimated posteriors that we obtain at the end of the MCMC algorithm. Quantities such as the acceptance rate in the algorithm are indicators of how efficiently the algorithm has sampled from a posterior distribution [81]. Visual indicators of smooth sampling include cosmetic qualities like the smoothness, the narrowness (or, conversely, the width), and shape of the posterior. Whereas if the posterior is very bumpy, with many peaks and troughs, then it suggests that bad sampling and more samples need to be taken, or a better algorithm used, in order to accurately represent the posterior. There are, however, less subjective diagnostic techniques that can be used to determine when it is safe to stop an MCMC algorithm [82].

A commonly used MCMC technique is the general Metropolis-Hastings (MH) algorithm [82], Algorithm 1. In the Metropolis-Hastings algorithm, a proposal distribution, $q(*|\#)$ is used to propose a parameter vector $*$ based off the current position of the Markov chains, the parameter vector $\#$. Through this choice of proposal distribution, the key concept of 'memory-less' chains is satisfied. It has been shown in the literature that the Metropolis-Hastings algorithm converges to the target posterior, as long as the algorithm obeys the principle of detailed balance, otherwise known as the reversibility condition [83]. However, samples obtained from an MH algorithm are only guaranteed to converge on the target distribution for an infinite number of iterations [84]. There are situations when convergence is slow [85]. Naturally, this is not practical, so convergence diagnostics or inspection of the predicted posteriors we obtain from running the algorithm are needed to determine whether efficient sampling has taken place. If not, more powerful, yet computationally expensive, techniques can be used

to sample from the desired posterior instead. Hamiltonian Monte Carlo (HMC) is one such method, which we discuss in the next section.

We will now prove that detailed balance is satisfied by the Metropolis-Hastings algorithm. Furthermore, it is because of the principle of the detailed balance that the acceptance probability, κ, is introduced into Algorithm 1. The reversibility condition states that the probability of being in a state $\boldsymbol{\theta}$ and moving to the state $\boldsymbol{\theta}^*$ must be the same as being in the state $\boldsymbol{\theta}^*$ and moving to $\boldsymbol{\theta}$. In the MH algorithm, we have a posterior distribution represented by $\pi(*)$ and a proposal distribution, $q(\dagger|*)$. Therefore, the probability of being at $\boldsymbol{\theta}$ and moving to $\boldsymbol{\theta}^*$ is [83]

$$p(\boldsymbol{\theta}^*|\boldsymbol{\theta}) = \pi_0(\boldsymbol{\theta})q(\boldsymbol{\theta}^*|\boldsymbol{\theta}). \tag{2.119}$$

Similarly, the probability of being at $\boldsymbol{\theta}^*$ and moving to $\boldsymbol{\theta}$ is

$$p(\boldsymbol{\theta}|\boldsymbol{\theta}^*) = \pi(\boldsymbol{\theta}^*)q(\boldsymbol{\theta}|\boldsymbol{\theta}^*). \tag{2.120}$$

In general, $p(\boldsymbol{\theta}^*|\boldsymbol{\theta})$ and $p(\boldsymbol{\theta}|\boldsymbol{\theta}^*)$ may not be equal. For the moment, we assume that $p(\boldsymbol{\theta}^*|\boldsymbol{\theta})$ is larger, which means too many moves from $\boldsymbol{\theta}$ to $\boldsymbol{\theta}^*$ are being accepted compared to moves from $\boldsymbol{\theta}^*$ to $\boldsymbol{\theta}$. To satisfy detailed balance and equalise the two probabilities, we introduce an acceptance probability for moves from $\boldsymbol{\theta}$ to $\boldsymbol{\theta}^*$, $\kappa_1(\boldsymbol{\theta}^*, \boldsymbol{\theta})$, and an acceptance probability for moves from $\boldsymbol{\theta}^*$ to $\boldsymbol{\theta}$, $\kappa_2(\boldsymbol{\theta}, \boldsymbol{\theta}^*)$. Therefore,

$$\pi_0(\boldsymbol{\theta})q(\boldsymbol{\theta}^*|\boldsymbol{\theta})\kappa_1(\boldsymbol{\theta}^*, \boldsymbol{\theta}) = \pi(\boldsymbol{\theta}^*)q(\boldsymbol{\theta}|\boldsymbol{\theta}^*)\kappa_2(\boldsymbol{\theta}, \boldsymbol{\theta}^*). \tag{2.121}$$

As we assume that $\pi_0(\boldsymbol{\theta})q(\boldsymbol{\theta}^*|\boldsymbol{\theta}) > \pi(\boldsymbol{\theta}^*)q(\boldsymbol{\theta}|\boldsymbol{\theta}^*)$, then $\kappa_2(\boldsymbol{\theta}, \boldsymbol{\theta}^*) > \kappa_1(\boldsymbol{\theta}^*, \boldsymbol{\theta})$. We want more moves from $\boldsymbol{\theta}^*$ to $\boldsymbol{\theta}$, in relation to the opposite move, than happened previously, so we make $\kappa_2(\boldsymbol{\theta}, \boldsymbol{\theta}^*)$ as large as possible for a probability by setting $\kappa_2(\boldsymbol{\theta}, \boldsymbol{\theta}^*) = 1$. Following this, (2.121) becomes

$$\pi_0(\boldsymbol{\theta})q(\boldsymbol{\theta}^*|\boldsymbol{\theta})\kappa_1(\boldsymbol{\theta}^*, \boldsymbol{\theta}) = \pi(\boldsymbol{\theta}^*)q(\boldsymbol{\theta}|\boldsymbol{\theta}^*). \tag{2.122}$$

Rearranging (2.122), we find that

$$\kappa_1(\boldsymbol{\theta}^*, \boldsymbol{\theta}) = \frac{\pi(\boldsymbol{\theta}^*)q(\boldsymbol{\theta}|\boldsymbol{\theta}^*)}{\pi_0(\boldsymbol{\theta})q(\boldsymbol{\theta}^*|\boldsymbol{\theta})}. \tag{2.123}$$

If we reverse our initial assumption and state that $\pi(\boldsymbol{\theta}^*)q(\boldsymbol{\theta}|\boldsymbol{\theta}^*) > \pi_0(\boldsymbol{\theta})q(\boldsymbol{\theta}^*|\boldsymbol{\theta})$, then our argument also holds in reverse and $\kappa_1(\boldsymbol{\theta}^*, \boldsymbol{\theta}) = 1$. Consequently, we obtain the acceptance probability [83], simply denoted as κ, that is used in the MH algorithm, see Algorithm 1. This derivation of the acceptance probability still holds if the proposal distribution is symmetric.

that is, when $q(\boldsymbol{\theta}|\boldsymbol{\theta}^*) = q(\boldsymbol{\theta}^*|\boldsymbol{\theta})$.

Algorithm 1: Metropolis-Hastings

Result: Estimate of the posterior distribution, $\pi_0(\boldsymbol{\theta})$

Input: $\pi_0(\theta_1)$, ..., $\pi_0(\theta_h)$;

Starting parameter vector, $\boldsymbol{\theta}_0$;

for $i = 1$, ..., n **do**

  Propose $\boldsymbol{\theta}^* \sim q(\boldsymbol{\theta}_{i-1}, ...)$;

  Calculate $\kappa = \min\left(1, \frac{L(\mathbf{y}|\boldsymbol{\theta}^*)\pi_0(\boldsymbol{\theta}^*)q(\boldsymbol{\theta}_{i-1}|\boldsymbol{\theta}^*)}{L(\mathbf{y}|\boldsymbol{\theta}_{i-1})\pi_0(\boldsymbol{\theta}_{i-1})q(\boldsymbol{\theta}^*|\boldsymbol{\theta}_{i-1})}\right)$;

  Generate $u \sim \mathcal{U}(0, 1)$;

  if $u \leqslant \kappa$ **then**

    $\boldsymbol{\theta}_i = \boldsymbol{\theta}^*$;

  else

    $\boldsymbol{\theta}_i = \boldsymbol{\theta}_{i-1}$;

  end

  Set $i = i + 1$;

end

In order to improve the results we obtain from the MH algorithm, we can make a couple of tweaks to it. Firstly, we can define a burn-in phase that we ignore the results of. The burn-in phase constitutes the first k simulations of the algorithm, where k is subjectively chosen by the person running the algorithm. A burn-in phase is introduced into the algorithm because it takes a number of simulations before the Markov chain samples from the target, stationary distribution [86]. In this initial period, the values proposed in the algorithm are dependent on the starting values and are not representative of the target distribution [86]. It is preferable to be cautious and overestimate the number of simulations needed for the burn-in phase, as it ensures that our end results only contain samples from the stationary distribution. Additionally, the required length of the burn-in phase is dependent on the closeness of the starting position of the chain to the support of the target distribution. A poor initial guess for the parameter values ensures that it takes longer for the Markov chains to sample from the target distribution than it would for a good initial choice of the parameter values [80].

Secondly, we can perform adaptive MH [84] in order to make the algorithm more efficient by using previous results to tune algorithmic parameters so that they better match the properties of the stationary distribution [87]. There are numerous ways to perform adaptive Bayesian sampling [88]. For example, if the proposal distribution was a multivariate normal, we might tune the covariance matrix of the distribution in order to more accurately capture the true covariances of the parameters with one another. Especially in the initial stages of the algorithm, when we do not sample from the target distribution, covariances may not be reflective of the true covariances between the parameters. Denoting the covariance matrix of the proposal distribution with $\boldsymbol{\Sigma}^*$, we would tune it at the end of every block of L simulations. In particular, $\boldsymbol{\Sigma}^*$ is amended based on the acceptance rate, α_{block}, of proposed parameter vectors across that particular block. It has been shown in the literature that a random walk Metropolis algorithm, which proposes new parameter vectors through a multivariate normal distribution

centred around the current position of the chains, best samples the entire target distribution, when the acceptance rate is approximately equal to 0.234 [81]. To adapt $\boldsymbol{\Sigma}^*$, we introduce the following relation $\boldsymbol{\Sigma}^* = \beta^2\boldsymbol{\zeta}$, where β^2 is a scaling factor and $\boldsymbol{\zeta}$ represents the covariances of the parameters. We construct $\boldsymbol{\zeta}$ using the parameter vectors accepted in the algorithm for each of the last M simulations. We can treat $M > L$, taking the parameter vectors from multiple blocks, in order to estimate parameter covariances over a wider range of parameters. Similarly, we do not have to include every position in the chain found so far in the algorithm. We adapt β^2 based on the value of α_{block} as follows:

- $\alpha_{\text{lower}} < \alpha_{\text{block}}$: multiply β^2 by $(1-\epsilon)^2$,
- $\alpha_{\text{lower}} \leqslant \alpha_{\text{block}} \leqslant \alpha_{\text{higher}}$: leave β^2 unchanged,
- $\alpha_{\text{higher}} < \alpha_{\text{block}}$: multiply β^2 by $(1+\epsilon)^2$.

These values of β are chosen in order to improve the efficiency of the algorithm. When the acceptance rate is too high, the target distribution is not being sampled from quickly enough, as the proposed moves are too small. Conversely, when the acceptance rate is too low, too few parameter vectors are being accepted to accurately estimate the target posterior. This is true for sampling around both the tails of the distribution and the region, or regions, of high posterior probability. Through adaptation, smaller jumps are proposed when α_{block} is too low and larger jumps are proposed when α_{block} is too high.

We must stop adapting the MH algorithm at some point, however, in order for our MCMC estimates to come from samples of the same distribution. Because we discard the values found in the burn-in phase and, by definition, sample from the target distribution after the end of the burn-in phase, it is a natural choice to stop adapting the MH algorithm at the end of the burn-in phase.

2.9 Alternative statistical methods

As well as MCMC, there are other Bayesian statistical techniques that can be used to characterise unknown, potentially complicated posteriors. We shall now discuss a few of these methods and examine some of them in relation to MCMC. In particular, we will identify reasons why we will use MCMC in later chapters over some of the other methods detailed below.

Firstly, Sequential Monte Carlo (SMC), also known as particle filtering, is another common method used to characterise posterior distributions [89]. This method works by treating the following modified version of Bayes' Rule

$$\pi(\boldsymbol{\theta}|\mathbf{y})_\nu \propto L(\mathbf{y}|\boldsymbol{\theta})^\nu \pi_0(\boldsymbol{\theta}), \tag{2.124}$$

where ν is an exponent that is initially zero, but rises to one by the end of the SMC algorithm. By (2.124) and the definition of ν, the SMC randomly samples from the prior at the beginning of the algorithm. A weight for each point is calculated based on the prior probability and the likelihood of each of the randomly sampled parameter vectors [90]. Next, a resampling is conducted that takes into account the weights of the previously selected points. This ensures that more samples are taken from the values that produce a higher weight, where the posterior probability is greater, and the sampled values are randomly perturbed so that new points are analysed. After a number of these iterations have been performed, we obtain the posterior probability distribution [91].

A more complex and advanced method of sampling from the posterior distribution is Hamiltonian Monte Carlo (HMC), which uses the theory of Hamiltonian mechanics to inform the choices of proposed parameter vectors through the gradient of the log-posterior of the model parameters [92]. An example HMC algorithm is given in Algorithm 2. When the algorithm is tuned correctly, HMC is an efficient and powerful way to sample to take a representative sample from even complex, high-dimensional probability distributions. This is because, through the log-posterior, the choice of proposal vectors are informed by the regions of the parameter space that have a relatively large probability mass. With HMC, we spend more iterations of the algorithm within these regions of high probability. However, as can be seen with the leapfrog algorithm in Algorithm 2, we introduce algorithmic parameters like the step size and the number of steps used in the leapfrog algorithm [89]. It is hard to tune these parameters correctly to sample optimally in the algorithm. As well as being easier to adapt for efficient sampling of the posterior, MCMC is also less computationally intensive than HMC, as multiple calculations of the gradient of a parameter vector are not required to propose new states

in the system.

Algorithm 2: Hamiltonian Monte Carlo

Result: Estimate of the posterior distribution, $\pi_0(\boldsymbol{\theta})$

Input: $\pi_0(\theta_1)$, ..., $\pi_0(\theta_h)$;

Starting parameter vector, $\boldsymbol{\theta}_0$;

Unnormalised log-posterior, $\pi^*(\boldsymbol{\theta}|\mathbf{y})$;

for $i = 1$, ..., n **do**

  Sample $\mathbf{r}^0 \sim \mathcal{N}(0, \mathbf{I}_d)$;

  Set $\tilde{\boldsymbol{\theta}} = \boldsymbol{\theta}^{i-1}$, $\tilde{\mathbf{r}} = \mathbf{r}^0$;

  for $j = 1$, ..., L **do**

    $\tilde{\boldsymbol{\theta}}, \tilde{\mathbf{r}} = \text{Leapfrog}(\tilde{\boldsymbol{\theta}}, \tilde{\mathbf{r}}, \epsilon)$;

  end

  Calculate $\alpha = \min\left(1, \frac{\exp(\pi^*(\tilde{\boldsymbol{\theta}}) - \frac{1}{2}\tilde{\mathbf{r}}\cdot\tilde{\mathbf{r}})}{\exp(\pi^*(\boldsymbol{\theta}_{i-1}) - \frac{1}{2}\mathbf{r}^0\cdot\mathbf{r}^0)}\right)$;

  Generate $u \sim \mathcal{U}(0, 1)$;

  if $u \leqslant \alpha$ **then**

    $\boldsymbol{\theta}_i = \tilde{\boldsymbol{\theta}}$;

    $\mathbf{r}^m = -\tilde{\mathbf{r}}$;

  else

    $\boldsymbol{\theta}_i = \boldsymbol{\theta}_{i-1}$;

    $\mathbf{r}^m = -\mathbf{r}^{m-1}$;

  end

  Set $i = i + 1$;

end

Function Leapfrog($\boldsymbol{\theta}$, $\mathbf{r}$, ϵ)

  Set $\tilde{\mathbf{r}} = \mathbf{r} + (\epsilon/2)\nabla_{\boldsymbol{\theta}}\pi^*(\boldsymbol{\theta})$;

  Set $\tilde{\boldsymbol{\theta}} = \boldsymbol{\theta} + \epsilon\tilde{\mathbf{r}}$;

  Set $\tilde{\mathbf{r}} = \tilde{\mathbf{r}} + (\epsilon/2)\nabla_{\boldsymbol{\theta}}\pi^*(\tilde{\boldsymbol{\theta}})$;

  Return: $\tilde{\boldsymbol{\theta}}$, $\tilde{\mathbf{r}}$;

A different approach to estimating posterior distributions is Approximate Bayesian Computation (ABC). This technique does not use the likelihood [93], but instead samples parameter vectors and instantly discards any proposed parameter vectors that do not provide a close enough fit to the experimental data [94]. Parameter vectors can be sampled randomly from the prior distribution, known as standard ABC, or can be dependent on the previously accepted vector through a proposal distribution, ABC MCMC, see [95] or Algorithm 3. For ABC, we must assign a tolerance that determines the maximum acceptable error between the proposed and experimental data. Alternatively, Sequential Monte Carlo can be introduced to ABC [94]. In this case, we define a sequence of tolerances, ϵ_i, such that $\epsilon_0 > \epsilon_1 > ... > \epsilon_n$. We accept N parameter vectors that produce an acceptably close fit, according to ϵ_i, assign a weight to each accepted parameter vector based on their closeness of fit and then repeat the process, setting the tolerance to ϵ_{i+1} and using the parameter vectors accepted in the previous

step to propose new parameter values.

Algorithm 3: ABC MCMC

Result: Estimate of the posterior distribution, $\pi_0(\boldsymbol{\theta})$

Input: Experimental data $\mathbf{y}_0$;

Starting parameter vector, $\boldsymbol{\theta}_0$;

Tolerance, ϵ;

for $i = 1, ..., n$ **do**

  Propose $\boldsymbol{\theta}^* \sim q(\boldsymbol{\theta}_{i-1}, ...)$;

  Simulate data $\mathbf{y}^*$ from $f(\mathbf{y}|\boldsymbol{\theta}^*)$;

  if $d(\mathbf{y}_0, \mathbf{y}^*) \leqslant \epsilon$ **then**

    Calculate $\alpha = \min\left(1, \frac{\pi(\boldsymbol{\theta}^*)q(\boldsymbol{\theta}_{i-1}|\boldsymbol{\theta}^*)}{\pi(\boldsymbol{\theta}_{i-1})q(\boldsymbol{\theta}^*|\boldsymbol{\theta}_{i-1})}\right)$;

    Generate $u \sim U(0, 1)$;

    if $u \leqslant \alpha$ **then**

      $\boldsymbol{\theta}_i = \boldsymbol{\theta}^*$;

    else

      $\boldsymbol{\theta}_i = \boldsymbol{\theta}_{i-1}$;

    end

  else

    $\boldsymbol{\theta}_i = \boldsymbol{\theta}_{i-1}$;

  end

  Set $i = i + 1$;

end

The main benefit of ABC is that it allows Bayesian statistical methods to be applied to problems where deriving a likelihood function is difficult [93]. For soft tissue modelling, where we can derive a likelihood function by assuming that an experimental stress-strain curve is a set of stresses and strains produced by inputting a parameter vector into a deterministic SEF with IID noise added to each stress in the set, MCMC is preferable to ABC. MCMC is better able to explore the entirety of the posterior, especially the tails of the distribution, because MCMC does not have a tolerance parameter that enforces a particular closeness of fit for a parameter vector to have a chance of being accepted, and MCMC examines the relative probability of a move being accepted. Therefore, when the Markov chains are away from the modes of the posterior, moves can be proposed with a reasonable chance of being accepted. By contrast, it is more difficult to move away from the modes of the posterior in ABC because a parameter vector needs to be proposed that satisfies the distance criterion to the experimental data. For these reasons, the choice of tolerance would be vitally important when using an ABC algorithm to quantify uncertainty in a non-linear, multidimensional model of soft tissue deformation. Finally, in standard ABC, there is no dependence of our random samples on a parameter vector that satisfied the distance criterion [94]. Proposed parameters are dependent on the prior probability weight of values only. This reduces efficiency more in the standard ABC algorithm.

Chapter 3

Literature Review

Models of soft tissue behaviour can broadly be classified into two families: phenomenological and microstructural models, although many models incorporate aspects of both approaches. Phenomenological models are tractable and easy to fit to experimental data, and these models can achieve close fits to experimental data. However, as the models' parameters are not related to the properties of the soft tissue's microstructure, then we cannot derive information about how the microstructure influences the tissue's macroscopic mechanical behaviour from fitting the model. Consequently, phenomenological models can only be used to fit to existing stress-strain or force-strain data: they could not be used to predict the mechanical behaviour of untested samples, including *in vivo* samples, for instance.

Microstructural models, on the other hand, aim to include parameters in the model that have a connection to the arrangement and properties of the constituents of the soft tissue. Theoretically, these models *can* explain how the constituents of a soft tissue cause the macroscopic behaviour that we observe when we perform experiments on tissues. Furthermore, as microstructural models contain biologically relevant parameters, it is theoretically possible to independently measure values for the model's parameters via non-destructive testing on a soft tissue and then input these values into the model to obtain an estimated stress-strain curve, for example. These stress-strain predictions can then be tested against experimental data taken from mechanical testing performed on the same tissue samples that were used to determine the model's parameters non-invasively. This demonstrates the potential additional usefulness that microstructural models possess in terms of what situations they can be used. However, research needs to be done on testing the accuracy of microstructural models by comparing mechanical data collected from a soft tissue sample to the model's predictions when the model parameters have been determined through non-destructive methods on the same tissue sample. Furthermore, directly incorporating elements of the microstructure into an SEF is likely to increase the complexity of the SEF. It is important that microstructural models remain tractable if they are to be widely used.

In this literature review, therefore, we seek to introduce and analyse some previously developed phenomenological, semi-microstructural and microstructural models that demonstrate the key features of each approach. In particular, we aim to analyse, firstly, what assumptions were made in the construction of the model and what phenomena are accounted for in the model. Secondly, we seek to identify strengths and drawbacks of each model and whether any gaps in the literature remain to expand upon the current understanding in soft tissue

modelling. Next, we examine the different approaches, microstructural and phenomenological, that have been used previously in the literature to account for the dispersion of collagen fibres in soft tissues. Finally, we examine fields that Bayesian statistical techniques have been applied in to produce better estimates for the posterior probability distributions of model parameters.

3.1 Soft Tissue Modelling

3.1.1 Phenomenological models

To model the stress-strain behaviour of soft tissues, early phenomenological models used exponential functions and polynomials. Early examples of exponential functions include the models developed by Fung (1967) [96], Tong & Fung (1976) [97] and Chuong & Fung (1983) [98].

Fung studied the rabbit mesentery and introduced this theoretical finite elasticity approach for a number of reasons. Firstly, the approach was designed to better approximate the physical behaviour of soft tissue. Applying linear theory to the stress-strain behaviour of a soft tissue is unphysical because of the highly non-linear mechanical behaviour that soft tissues exhibit. Similarly, definitions of the Young's modulus of soft tissues are unphysical because these materials stiffen with the deformation and, thus, the Young's modulus of the tissue increases with it. Secondly, Fung sought to introduce this theoretical framework to soft tissue mechanics in order to attempt to create a unified model that could be used to model various different deformations. The experiments that were attempted to be unified by Fung include three-dimensional boundary value problems, which are tough to do experimentally because of the network of soft tissues. Fung stated that a goal of theoretical finite models of soft tissues would to be able to predict mechanical behaviour [96].

To characterise the SEF, Fung defined the slope $\mathrm{d}T/\mathrm{d}\lambda$, where λ represents the stretch applied to the tissue and T represents the 'Lagrangian' stress, that is, the tensile force per unit reference area. For instance, the first definition of $\mathrm{d}T/\mathrm{d}\lambda$ was

$$\frac{\mathrm{d}T}{\mathrm{d}\lambda} = aT, \tag{3.1}$$

$$T = T^* \exp(a(\lambda - \lambda^*)), \tag{3.2}$$

$$W(\lambda) = \frac{T^*}{a}\left[\exp(a(\lambda - \lambda^*)) - \exp(a(\lambda - \lambda^*))\right], \tag{3.3}$$

where a is an arbitrary constant, and T^* and λ^* represent a stretch and a stress value of the curve T. More complicated expressions for $\mathrm{d}T/\mathrm{d}\lambda$ and, ultimately, T and W, were also introduced in the paper.

This research was vital, as he acknowledged that models need to account for the change in behaviour of the tissue as the tissue is stretched [96]. By considering a feature of the stress-

strain behaviour, the slope of the $\mathrm{d}T/\mathrm{d}\lambda$, Fung was able to derive a model that can provide a close fit to experimental mechanical data. However, the Fung SEF can only model the soft tissue behaviour phenomenologically because the parameters in the model cannot be related to the microstructure. For instance, the model does not account for the gradual tautening of fibrils. Fung suggested that models assume that the elastic modulus of the tissue increases with the stretch, which only indirectly accounts for the microstructure and how changes within it result in changes to the macroscopic mechanical behaviour of the tissue.

Similarly, the model by Tong & Fung was developed to study skin, and the authors postulated the exponential form because of the closeness of the shape of the stress-strain curve to an exponential curve [97]. The paper also examined differences between the material behaviour of the tissue when strained in two perpendicular directions. The values of the model's parameters, which were obtained through curve-fitting, differed between experiments. The authors theorised that may be because of the different preconditioning regimes employed for the experiments [97]. However, parameter identification also poses a problem in phenomenological modelling because parameters lack a direct, physical basis for inclusion in the model. Therefore, phenomenological parameters can only account indirectly for multiple microstructural properties, whether in part or in full.

The model developed by Chuong and Fung [98] was designed initially to model arteries under the assumption that they are homogeneous and cylindrically orthotropic soft tissues. The model assumes that the mechanical behaviour can be governed according to an exponential function. The SEF is given by

$$\rho_0 W = \frac{c}{2}\exp[b_1 E_\theta^2 + b_2 E_z^2 + b_3 E_r^2 + 2b_4 E_\theta E_z + 2b_5 E_z E_r + 2b_6 E_r E_\theta], \tag{3.4}$$

where W is the strain energy per unit volume in the undeformed configuration; b_1—b_6 and c are material parameters; and E_z, E_θ and E_r are the longitudinal, circumferential and radial Green's strain components. The exponent in (3.4) contains the stretches in the principal directions of the deformation and shear deformations, and each term in the exponent contains a material parameter, b_i, that needs to be fitted to experimental data. Furthermore, another material parameter is introduced as a coefficient of the exponential term. The effect of the deformation on the artery's constituents is not considered. By reducing the number of terms in the exponent to three, the Chuong-Fung model reduces to the model derived by Fung *et al.* (1979) [99]. This simplified Chuong-Fung SEF is

$$\rho_0 W = \frac{c}{2}\exp[b_1 E_\theta^2 + b_2 E_z^2 + 2b_4 E_\theta E_z]. \tag{3.5}$$

For the SEF (3.5) to be applicable in a three-dimensional problem, the material must be incompressible, so that the strain in one principal direction can be rewritten in terms of the stretches in the other two principal directions by the incompressibility constraint. The SEFs (3.4) and (3.5) demonstrate that tractable phenomenological SEFs can be developed with varying degrees of simplicity from considerations of the overall macroscopic behaviour of

the tissue.

However, by changing the number of material constants in the model, the remaining parameters account, partially or fully, for either more or fewer microstructural phenomena, but we cannot ascertain what exactly the phenomena associated with each parameter are. The problem of parameter identification also exists for phenomenological power-law SEFs. For example, Tong & Fung rejected using a power law of the form developed by Blatz (1969) *et al*. [100] because the SEF contained too many parameters, thereby exacerbating the problem of parameter identification [97].

Vaishnav et al. (1972) [101] developed another power law for the stress-strain behaviour of curvilinearly orthotropic arteries. Similar to the exponential SEF of Chuong & Fung, each term in the polynomial is either dependent on the strains in the principal directions of the deformation or on the shear strains. The SEF is

$$\begin{aligned} W = k_1\gamma_{(11)}^2 + k_2\gamma_{(22)}^2 + k_3\gamma_{(33)}^2 + k_4\gamma_{(12)}^2 + k_5\gamma_{(13)}^2 + k_6\gamma_{(23)}^2 \\ + k_7\gamma_{(11)}\gamma_{(22)} + k_8\gamma_{(22)}\gamma_{(33)} + k_9\gamma_{(11)}\gamma_{(33)} + \dots, \end{aligned} \tag{3.6}$$

where $\gamma_{(ij)}$ is the ij component of the Green-St Venant strain tensor, which is a measure of the total strain acting on the material, for example $\lambda - 1$, where λ is the stretch ratio; k_i are material parameters; and the authors set the first-order terms, with regard to the components of the Green strain tensor, to zero. Due to the large number of parameters in (3.6), and the problems of parameter identification associated with a model that contains numerous phenomenological parameters, the authors used a simplified SEF according to the approximation that arteries do not experience shear stresses at physiological strains and are incompressible. Under these assumptions, the SEF is a function of two components of the Green-St Venant strain tensor. The number of parameters in the model is also dependent on the highest degree of Green-St Venant strains that are assumed to have a negligible impact on the tissue's resistance to the deformation. In the paper, the authors derive three-, seven- and twelve-parameter versions of the model. The three- and seven-component SEFs are

$$W_3 = A_1\gamma_{(11)}^2 + B_1\gamma_{(11)}\gamma_{(22)} + C_1\gamma_{(22)}^2, \tag{3.7}$$

$$\begin{aligned} W_7 = A_2\gamma_{(11)}^2 + B_2\gamma_{(11)}\gamma_{(22)} + C_2\gamma_{(22)}^2 + D_2\gamma_{(11)}^3 + E_2\gamma_{(11)}^2\gamma_{(22)} \\ + F_2\gamma_{(11)}\gamma_{(22)}^2 + G_2\gamma_{(22)}^2. \end{aligned} \tag{3.8}$$

The seven- and twelve-parameter models were found to produce very similar fits to data by the authors [101], suggesting that the addition of the extra parameters does not capture more of the physical behaviour of arteries. Indeed, the extra parameters could be associated with problems of overfitting.

Veronda & Westmann (1970) developed a model of finite elasticity in skin. When developing

the model, the authors took into consideration previous experimental work that characterised soft tissues as non-linearly elastic, viscoelastic, and anisotropic. In order to create a tractable model that could fit to data, the authors decided to focus on the non-linear behaviour of the tissue and construct an isotropic, elastic model. To consider the elastic behaviour of the tissue, the authors looked at one monotonically increasing load on the tissue. Regarding the non-linear behaviour of the tissue, the authors cited the work of Ridge and Wright [102]–[104], who, from *in vitro* tests performed on human skin, had ascertained that skin is initially compliant before stiffening as the tissue is stretched further. Ridge and Wright determined that the compliant phase was caused by the collagen fibres straightening, the stiff phase by the straight collagen fibres extending, and the yield phase by collagen fibres breaking. Veronda & Westmann proposed the SEF for the incompressible version of their model to be of the form

$$W = c_1[\mathrm{e}^{\beta(I_1-3)} - 1] + c_2(I_2 - 3) + g(I_3), \tag{3.9}$$

where

$$\frac{\partial g(I_3)}{\partial I_3} = \left.\frac{\partial W}{\partial I_3}\right|_{I_3=1} = p, \tag{3.10}$$

where p is a Lagrange multiplier. The SEF was able to fit experimental data closely, but the values of the model's parameters changed between the multiple fits they performed, demonstrating an issue of including phenomenological parameters in the model.

Early phenomenological exponential SEFs were the inspiration for the independently derived Limbert and Middleton (2005) [105] and Itskov-Aksel (2006) models [106]. These models use a series of exponential functions to create a class of models that consists of polyconvex terms in the SEF. Polyconvexity is a vital property of an SEF because it ensures that, for any deformation state, there is a one-to-one relation between the reference and deformed configurations. Not all earlier models were designed to satisfy this criterion, and for particular deformations some models are not polyconvex, rendering them unphysical [106]. The symmetry properties of the model are accounted for by using what are called generalised structure tensors (GSTs) by the authors [106]. The transversely isotropic and orthotropic GSTs, $\mathbf{L}_i$, that describe the symmetry group of the material are

- Transverse Isotropy: $\mathbf{L}_1 = \mathbf{l}_1 \otimes \mathbf{l}_1, \mathbf{L}_2 = \mathbf{L}_3 = \frac{1}{2}(\mathbf{I} - \mathbf{l}_1 \otimes \mathbf{l}_1)$.
- Orthotropy: $\mathbf{L}_i = \mathbf{l}_i \otimes \mathbf{l}_i,\ i = 1, 2, 3,$

where $\mathbf{l}_i$ is a base vector in the ith principal material direction. From these GSTs, Itskov *et al.* defined a class of polyconvex SEFs given by

$$W = \frac{1}{4}\sum_{r=1}^{s}\left\{\frac{1}{\alpha_r}(\exp[\alpha_r(\tilde{I}_r - 1)] - 1) + \frac{1}{\beta_r}(\exp[\alpha_r(\tilde{K}_r - 1)] - 1)\right\}, \tag{3.11}$$

where $\tilde{K}_r = \mathrm{tr}(\mathbf{C}^{-1}\tilde{\mathbf{L}}_r)$, $\tilde{I}_r = \mathrm{tr}(\mathbf{C}\tilde{\mathbf{L}}_r)$, $\tilde{\mathbf{L}}_r = \sum_{i=1}^{3} w_i^{(r)}\mathbf{L}_i, i = 1, 2, 3.$

An alternative approach to phenomenologically modelling soft tissue is the Bischoff-Arruda-Grosh formulation (2002) [107]. In this model, the authors developed an orthotropic model in which a unit cell contains eight chains, corresponding to collagen fibres, that radiate from the centre of the cell to the corners. Each chain is freely jointed. The model was incorporated into the finite element software package *ABAQUS* and the model was able to fit experimental uniaxial and biaxial data as well as shearing data, at low levels of shear (at higher levels, the fit to data was not as good). Being able to fit to data for these varied deformations is a strength of this model. However, while the model fits well to data, we cannot learn about the nature of collagen fibres in soft tissues using the results of this model because the model does not attempt to explain directly how the microstructure drives the macroscopic behaviour.

Lapeer *et al*. (2010) [108] fitted various models to uniaxial and biaxial stress-strain data collected on abdominal skin taken from women in *in vitro* tests. The models tested included first- and second-order general polynomials with SEFs given by

$$W^{\text{inc}} = \left(\sum_{i+j=1}^{N} c_{ij}(I_1 - 3)^i (I_2 - 3)^j \right) - \frac{1}{2} p(I_3 - 1); \tag{3.12}$$

reduced polynomials of the form

$$W^{\text{inc}} = \left(\sum_{i=1}^{N} c_i (I_1 - 3)^i \right) - \frac{1}{2} p(I_3 - 1) \tag{3.13}$$

up to the sixth-order, and Ogden models with an SEF given by

$$W^{\text{inc}} = \sum_{p=1}^{N} \frac{\mu_p}{\alpha_p} \left(\lambda_1^{\alpha_p} + \lambda_2^{\alpha_p} + \lambda_3^{\alpha_p} - 3 \right) \tag{3.14}$$

up to the sixth-order. To identify the models that would be appropriate to use in finite element meshes, the authors selected models that had an $R^2 \geqslant 0.9$ and passed a Drucker stability test [108]. Here, R^2 is the squared correlation coefficient, also known as the coefficient of determination, and it is given by

$$R^2 = 1 - \frac{SS_{\text{reg}}}{SS_{\text{tot}}}, \tag{3.15}$$

$$SS_{\text{reg}} = \sum_{i=1}^{n} (\sigma_i^{\text{test}} - \sigma_i^{\text{model}}), \tag{3.16}$$

$$SS_{\text{tot}} = \sum_{i=1}^{n} (\sigma_i^{\text{test}} - \bar{\sigma}_i^{\text{model}}), \tag{3.17}$$

where $\bar{\sigma}_i^{\text{model}}$ is the mean stress of the test data [108]. The Drucker stability is a criterion that analyses if the deformation is stable by determining whether the work done is positive when the deformation is increased incrementally [109]. The given reduced polynomial models, mainly of orders three and six, were the only ones to pass these tests. The order three reduced

polynomial is the Yeoh model (1993) [110] and is given by

$$W^{\text{inc}} = c_1(I_1 - 3) + c_2(I_2 - 3)^2 + c_3(I_1 - 3)^3 - \frac{1}{2}p(I_3 - 1). \tag{3.18}$$

These purely phenomenological models are useful. They use established, well-known functions to create a tractable model that is not computationally intensive and is able to fit to data well, in terms of the closeness of fit. However, the models lack any understanding of the microstructure in their formulation, which means the parameters are purely chosen for mathematical reasons. Thus, the choice of the number of parameters in the model is arbitrary. Hence, in fits to data, the results from these phenomenological models cannot inform us about how the microstructure drives the physical behaviour of a soft tissue.

3.1.2 Phenomenological models with microstructural considerations

In addition to phenomenological models, there are semi-microstructural models that consider the structure of a soft tissue in the SEF while including parameters that do not relate directly to the microstructure. One example is the widely used HGO model (2001) [111]. The strain energy function of the HGO model is

$$W^{\text{a/m}} = \frac{c}{2}(I_1 - 3) + \frac{k_1^{\text{a/m}}}{2k_2^{\text{a/m}}}\Big[(\exp[k_2^{\text{a/m}}(I_4^{\text{a/m}} - 1)^2] - 1) + (\exp[k_2^{\text{a/m}}(I_6^{\text{a/m}} - 1)^2] - 1)\Big], \tag{3.19}$$

where c and k_1 are stress-like parameters, k_2 is a dimensionless parameter and the superscript a/m denotes that the SEF is for the adventitia or the media, the two outermost layers of the artery, which the HGO was originally designed to model.

Multiple structural considerations influenced the development of the SEF given in (3.19). Firstly, the contribution of the intima, the innermost layer of the artery, to the HGO SEF is neglected because of its thinness compared to the media and adventitia in healthy arteries. Furthermore, suggested by images of the arteries, the model assumes that collagen fibres in the soft tissue are modelled in two distinct families of fibres. The artery is, thus, assumed to be orthotropic. The collagen content and orientation of the fibres is assumed to differ in the adventitia and media. To reflect that, the stress-like and dimensionless parameters are different for each layer. Additionally, the contribution from the collagen fibres to the SEF is assumed to be solely anisotropic and is separated from the SEF's contribution, which is considered to be solely isotropic.

However, the model is still semi-microstructural because the parameters c, k_1 and k_2 do not model an exact property of the collagen fibres or ECM, such as the stiffness of collagen fibres: they are chosen to replicate microstructural phenomena and to ensure that the SEF possesses the required dimensions in each team. Hence, the exponential form of the SEF,

as in the models of Tong & Fung and Chuong & Fung, was not derived by the authors from the microstructure of arterial tissue, but was chosen in order to replicate experimental arterial stress-strain data. Consequently, while the HGO model is analytical and can easily be adapted to study the experimental behaviour of multiple fibrous soft tissues, the parameters themselves do not elucidate the properties of collagen fibrils or the NCM in the modelled tissue.

Chen *et al*. (2020) [112] developed a model that assumes collagen fibrils are initially crimped and inactive, causing the skin to be linearly elastic and compliant at small strains, where only the less stiff NCM resists the deformation. However, the authors first fit the model to the data collected for strains less than 2%. This enabled estimation of the parameters associated with the NCM's contribution to the stress only. Then, the remaining data points were fitted to in order to ascertain values for the parameters associated with the collagen's resistance to the deformation [112]. In the model, the NCM is modelled as a neo-Hookean material,

$$W^{\text{NCM}}(\mathbf{F}^{\text{NCM}}) = \frac{c^{\text{NCM}}\left(\text{tr}\mathbf{C}^{\text{NCM}} - 3\right)}{2}. \tag{3.20}$$

Collagen fibres in the model are treated as exponentially stiffening materials with the SEF

$$W^{(k)}(\lambda^{(k)}) = \begin{cases} \frac{c_1^{(k)}}{4c_2^{(k)}}\left[\exp(c_2^{(k)}[(\lambda^{(k)}) - 1]^2 - 1]\right], & \lambda^{(k)} > 1, \\ 0, & \lambda^{(k)} \leqslant 0, \end{cases} \tag{3.21}$$

where the superscript (k) denotes the SEF for collagen fibres in the kth family. Using histological and imaging techniques, the model groups families of collagen fibres into bundles located in the tissue. Each bundle of collagen fibres can possess its own SEF. The stretch experienced by a collagen fibre is given by

$$\lambda^{(k)} = G_q\sqrt{\mathbf{N}^{(k)} \cdot \mathbf{C}\mathbf{N}^{(k)}}, \tag{3.22}$$

where $G_q = l_q/L_q$is a tortuosity parameter, called a straightness parameter by the authors of the paper, that defines the ratio between the two ends of a fibre, l_q, and the fibre's length, L_q, and $\mathbf{N}^{(\mathbf{k})}$ is a unit vector that represents the direction of the kth collagen fibre family.

The model makes use of many structural features of skin. Fibre orientation distribution, mass fraction of the collagen fibre network and NCM, and the initial slackness of collagen fibres are key features of the model. However, while soft tissue structure is key to the SEF, it contains phenomenological parameters such as $c_1^{(k)}$ which do not have a physical relevance and, therefore, we cannot use the values of the parameters that we obtain when fitting to data to infer more about the relationship between the tissue's microstructure and macroscopic behaviour.

3.1.3 Microstructural models

After having examined some phenomenological and semi-microstructural soft tissue models, we now analyse some microstructural models of soft tissue behaviour. One model that accounts for both the compliance of soft tissues at small strains and the rapid stiffening at larger strains is the *sequential straightening and loading* (SSL) model proposed by Kastelic *et al*. (1980) [29]. The model assumes that collagen fibrils are crimped in a reference soft tissue sample and straighten as the sample is deformed. A fibril is only assumed to tauten once it has become straight. To capture the non-linear stress-strain behaviour of the soft tissues, the SSL model assumes that collagen fibrils possess different amounts of crimp, so they straighten sequentially. The gradual tautening of the fibrils accounts for non-linearity, as an individual fibril is assumed to be linearly elastic in the SSL model. The use of an exponential SEF in some phenomenological models indirectly replicates the recruitment of fibres and the strengthening of the tissue as the deformation is increased.

In the SSL model, a distribution function is used to quantify variation in the recruitment stretch, that is, the stretch at which a fibre become straight and tautens, throughout the fibrils in the tissue. Kastelic *et al*. [29] assumes that the fibrils closest to the centre of a tendon fascicle straighten and tauten first. Then going radially outwards, fibrils tauten gradually, until the fibrils nearest to the fascicle's edge tauten. The SSL model contained an error in its interpretation of Hooke's law which was rectified in the microstructural tendon model developed by Shearer (2015). To derive the SEF, the SSL model of collagen crimp, with a different distribution function for collagen crimp, was used to calculate the stress experienced by a single collagen fascicle [113]. Through this assumption of gradually recruited collagen fibrils, the resulting SEF is a piecewise function, with the three sub-regions of the SEF corresponding to none, some, and all of the fibrils in the fascicle being taut. The SEF derived by Shearer contained only microstructural parameters which could be independently measured via experiment.

Other SEFs that account for the sequential straightening of collagen fibres or fibrils have been developed. Zulliger (2004) *et al.* [114] expanded the HGO SEF to also consider the structural composition of the arterial wall in the model. The assumption of uncoupled isotropic-elastin and anisotropic-collagen terms remained, but the model introduced new parameters into the model corresponding to the volume fraction of elastin and collagen in the arterial wall. Zulliger et al. made this alteration because changes in the elastin and collagen content in the arterial wall affect the mechanical behaviour of the artery and have been observed in ageing and diseased arterial tissue [114]. However, in contrast to the HGO model, the authors did not assume that the elastin content of the wall was linearly elastic. Instead, a non-linear term involving I_1, the first strain invariant associated with $\mathbf{C}$, the right Cauchy-Green deformation tensor, and equal to $\mathrm{tr}(\mathbf{C})$, was used to model the elastin fibres' contribution to the SEF.

In contrast to the SSL model, Zulliger *et al.* did not assume that an individual collagen fibre

obeys Hooke's law. Instead, the strain energy due to a single collagen fibre is

$$\Psi_{\text{fibre}}(\epsilon) = \begin{cases} 0 & \text{if } \epsilon \leqslant 0, \\ c_{\text{coll}}(\epsilon - \ln(\epsilon + 1)) & \text{if } \epsilon > 0, \end{cases} \tag{3.23}$$

where $\epsilon = \lambda - 1$ is the fibre engagement strain. Similar to the SSL model, however, Zulliger *et al*. neglected the contribution to the SEF of slack collagen fibres. But in this model the recruitment, or critical, stretches of the collagen fibres are governed by the following log-logistic distribution:

$$\rho_{\text{fibre}}(\epsilon) = \begin{cases} 0 & \text{if } \epsilon \leqslant \epsilon_0, \\ \frac{k}{b} \frac{(\epsilon - \epsilon_0/b)^{k-1}}{[1+(\epsilon-\epsilon_0/b)k]^2} & \text{if } \epsilon > \epsilon_0, \end{cases} \tag{3.24}$$

where $b > 0$ is a scaling parameter and the value of k (> 0) determines the shape of the distribution. The authors set ϵ_0 equal to zero, as they assumed that there exists at least one fibre in a soft tissue sample that is straight but unstressed in the reference configuration and immediately tautens when a deformation is applied. The choice of probability distribution for the recruitment stretch was not motivated by histological evidence, but was chosen arbitrarily [114].

Yang and Sherman (2015) [115] developed a model to examine how collagen in skin, and particularly the dermis, helps skin to resist tearing when it is deformed. Skin resists tears through the straightening and subsequent tautening of the collagen fibrils, and fibril sliding, reorientation, and bonding. To replicate the geometry of collagen fibrils, the model assumes fibril waviness can be modelled as possessing the geometry of a succession of connected circular segments. With this geometry, the model can be solved analytically. To calculate the constitutive equation for the model, the model uses Castigliano's method—which describes the deflection from the natural state to the equilibrium state, attained for a particular deformation, as the derivative of the resultant strain energy on the body in terms of the force [116]. Consequently, the stress, σ_0, and strain increment $\mathrm{d}\epsilon$ is given in the model as:

$$\sigma_0 = \int_{r_c}^{r} E' \left(\frac{\csc\theta_0}{r_c \cdot r} \left[r \sin\left(\frac{r_c}{r}\theta_0\right) - r_c\theta_0 \cos\left(\frac{r_c\theta_0}{r}\right) \right] \right) \mathrm{d}r, \sigma_0 = \int_{r_c}^{r} E' \mathrm{d}\epsilon, \tag{3.25}$$

where r_c is the initial circle radius, θ_0 is the initial central angle of the circular segment, and E' is the pseudo-modulus that is dependent on the geometry of the wire. To test the model's predictions against data, steel wires, which represented the tensile stress-strain response of skin, were stretched. The model was found to achieve a good fit to data.

Freed and Rajagopal (2016) developed a model that uses a theory of fibrous soft tissues that assumes we can model the skin as consisting of a network of crimped collagen fibres, treated as strings, attached to straight elastin fibres, which are also treated as springs [117]. The stress-strain response in the Freed-Rajagopal model, therefore, is governed by the following

pattern. At small strains, the stress-strain response is due to the elastin fibres tautening. This initial phase occurs until the microstructure has been reconfigured to the point where collagen fibres become straight and start to tauten. At this stretch, the collagen fibres dominate the response to the tissue, as they are assumed to be much stiffer than the elastin fibres in the tissue. These modelling assumptions replicate the stress-strain response that we typically observe in soft tissues: the model's predictions possess a toe region, where the collagen fibres start to straighten under the deformation and only the compliant constituents of the ground matrix and the elastin fibres resist the deformation, a heel region, where collagen fibres gradually become straight, and a linear region where the stiff, Hookean fibres resist the deformation.

For the constitutive equation of the Freed-Rajagopal model, we treat the stretch $\lambda = \lambda^{\mathrm{C}}\lambda^{\mathrm{E}}$, where $\lambda^{\mathrm{C}} = \mathrm{d}x/\mathrm{d}\eta$ and $\lambda^{\mathrm{E}} = \mathrm{d}\eta/\mathrm{d}X$, and $\mathrm{d}\eta$ represents an infinitesimal separation between particles caused solely by the straightening of collagen fibres. The fibre strain ϵ possesses the relation $\epsilon = \ln\lambda = \epsilon^{\mathrm{C}} + \epsilon^{\mathrm{E}}$, where ϵ^{C} and ϵ^{E} represent the strains for which the collagen fibres and the elastin fibres control the response to the deformation, respectively. The collagen fibres are modelled as Hookean elastic fibres. Therefore, in terms of the true stress, σ, we have $\epsilon^{\mathrm{C}} = \sigma/\mathrm{E}^{\mathrm{C}}$, where E^{C} is the Young's modulus of the linear region of the stress-strain curve. The elastin fibres, by contrast, are modelled as strain-limiting fibres, that is,

$$\epsilon^{\mathrm{E}} = \frac{1}{\beta}\left(1 - \frac{1}{(1 + (\beta - 1)\frac{\sigma}{\mathrm{E}^{\mathrm{E}}})^{\frac{\beta}{(\beta-1)}}}\right), \tag{3.26}$$

where E^{E} is the Young's modulus of the toe region and $\beta = 1/\epsilon^{\mathrm{E}}_{\mathrm{MAX}} (> 1)$ denotes the stretch at which collagen fascicles have straightened.

The model achieved close fits to experimental data taken from porcine *chordae* tendon. Furthermore, the model contains three parameters: E^{C}, E^{E}, and β that possess a physical basis with regard to the microstructure and have been included in the model through microstructural considerations incorporated into the model. By contrast, Babu *et al.* (2015) [118] derived a model with the same three constitutive parameters, but derived phenomenologically [117]. The HGO model formed the basis of the model for Babu *et al.* to fit to the biomechanics of human ascending thoracic aortic dissections [118]. Additionally, Freed and Rajagopal fit to tendon data collected by Freed and Doehring (2005), who themselves modelled the soft tissue as a helical spring model that accounts for the geometry of springs [119].

Aparício *et al.* (2016) [120] introduced a chemo-mechano-biological mathematical model to describe how interdependent chemical, mechanical, and biological processes interact to influence the behaviour of the arterial wall. From the mechanical perspective, the model examines growth and remodelling by describing the effect of collagen synthesis and degradation in wound healing and in the development of an inflammatory aneurysm in the human aorta, modelled by Aparício *et al.* as a bilayer. The model is analytically tractable through the use of a triangular distribution to describe the crimp of collagen fibres in the soft tissue, even though the model does not assume that the fibres are linearly elastic. A triangular probability distri-

bution contains three distribution parameters: the minimum value, a; the maximum value, b; and the modal value, c. Probability increases linearly from the point a to the point c, and the probability decreases linearly from c to b. The mode does not necessarily need to lie half-way between a and b. The use of a triangular distribution introduces three distribution parameters into the model, but each one has a physical meaning, as they represent the minimal, modal, and maximal recruitment stretch of the collagen fibres.

The model by Martufi and Gasser (2012) [121] also employs a triangular distribution to account for crimp of the collagen fibres to study the impact of collagen fibre turnover on abdominal aortic aneurysms. In the model, fibrils aggregate into fibres, and it is the undulation of the fibrils that is governed according to a triangular probability density function (PDF). Through these assumptions, the model produces a piecewise analytical expression for the Cauchy stress of a collagen fibre. The model also assumes that the collagen fibres are dispersed. However, the model initially assumes that the collagen fibres are isotropically distributed throughout the soft tissue, but the orientation density is adjusted over time according to the local stretch field. With these features, the model shows that collagen fibre turnover has an impact on the macroscopic stress field: through fibre turnover, high stress gradients across the arterial wall are avoided [121]. Through the choice of model for collagen fibre turnover, the model predicts physically reasonable stress fields in the artery.

Most models of skin deformation ignore the interactions between the non-collagenous matrix (NCM) and the collagen fibrils. Limbert accounted for these interactions as well as the volumetric deformation, the deviatoric stretch along the fibrils, and the cross-fibre shear in an orthotropic model. Orthotropy was obtained through the addition of a second family of fibres, and Limbert's formulation was built upon the work of Lu and Zhang [122]. The SEF for this model is

$$\psi = \psi^{\nu}(J) + \sum_{i=1}^{2} \left[\psi_i^{\bar{\lambda}}(\bar{\lambda}_i) + \hat{\psi}_i^{1}(\alpha_1^i) + \tilde{\psi}_i^{2}(\alpha_2^i, \bar{\lambda}_i) \right], \tag{3.27}$$

where $J = \sqrt{I_3}$ represents the ratio of deformed to undeformed volume; $\bar{\lambda}_i = I_3^{-\frac{1}{6}} \sqrt{I_4^i}$ is the stretch of the fibres in fibre family i; $\alpha_1^{\bar{i}} = I_1 I_4^i - I_5^i$ is the cross-fibre shear of fibre family i, and $\alpha_2^i = \frac{I_5^i}{(I_4^i)^2}$ represents the interaction between the fibres and the NCM. For $\Psi_i^{\bar{\lambda}}(\bar{\lambda}_i)$, Limbert assumed that collagen fibres behave like a worm-like chain. This ultimately led to a microstructural model with twenty-three physically relevant parameters. The values of these parameters were obtained either by direct fits to data, or by using a global optimisation program to determine parameter values. The model is also multiscale, as it was developed so that nanoscopically important and measurable quantities that impact macroscopic mechanical behaviour were included in the SEF.

3.1.4 Dispersion of collagen fibres

The Gasser-Holzapfel-Ogden (GOH) model (2006) [123] expands upon the HGO model by accounting for the dispersion of collagen fibres. A von Mises distribution, Appendix A, the projection of the normal distribution onto the unit circle, is used to model the distribution of fibre orientations. Therefore, collagen fibres are assumed in the GOH model to be oriented with rotational symmetry around a mean fibre direction, $\mathbf{a}_0$. The model uses the Generalised Structure Tensor (GST) approach, which incorporates dispersion into the model by the introducing a dispersion parameter κ. With an arbitrary referential fibre orientation $\mathbf{M}$, the GST, $\mathbf{H}$, is

$$\mathbf{H} = \frac{1}{4\pi}\int_{\omega} \rho(\Theta,\Phi)\mathbf{M}(\Theta,\Phi)\otimes\mathbf{M}(\Theta,\Phi)\mathrm{d}\omega, \tag{3.28}$$

where $\rho(\Theta,\Phi)$ represents the orientation distribution function and spherical polar coordinates have been used to calculate the GST. In the development of the SEF, the authors assumed $\mathbf{a}_0$, the mean fibre direction, coincided with the $\mathbf{e}_3$ axis and chose $\mathbf{M} = \sin\Theta\cos\Phi\mathbf{e}_1 + \sin\Theta\sin\Phi\mathbf{e}_2 + \cos\Theta\mathbf{e}_3$. Under these assumptions, $\mathbf{H}$ simplifies to

$$\mathbf{H} = \kappa\mathbf{I} + (1-3\kappa)\mathbf{a}_0\otimes\mathbf{a}_0, \tag{3.29}$$

where

$$\kappa = \frac{1}{4}\int_0^{\pi}\rho(\Theta)\sin^3\Theta\mathrm{d}\Theta \tag{3.30}$$

and $\rho(\Theta)$ has lost its dependence on Φ through the authors' choice of $\mathbf{a}_0$ and $\mathbf{M}$ [123]. By accounting for dispersion, the invariant I_4 is replaced in the SEF by the pseudoinvariant I_4^*, where

$$I_4^* = \kappa I_1 + (1-3\kappa)I_4. \tag{3.31}$$

The SEF for an orthotropic artery according to the GOH model is

$$W^{\mathrm{a/m}} = \frac{c}{2}(I_1-3) + \frac{k_1^{\mathrm{a/m}}}{2k_2^{\mathrm{a/m}}}\Big[(\exp[k_2^{\mathrm{a/m}}((I_4^*)^{\mathrm{a/m}}-1)^2]-1) + (\exp[k_2^{\mathrm{a/m}}((I_6^*)^{\mathrm{a/m}}-1)^2]-1)\Big]. \tag{3.32}$$

That is, we have replaced I_4 and I_6 in the SEF for the HGO model, (3.19), with their dispersed-fibre analogues.

The appeal of the GOH model is, therefore, that with an appropriate choice of $\mathbf{M}$, $\rho(\Theta,\Phi)$ and $\mathbf{a}_0$, we can account for fibre dispersion while preserving the tractability of the SEF through the introduction of a single additional parameter. However, there is a problem with the tension-compression switch of the GOH model. The model assumes both that fibres oriented at all

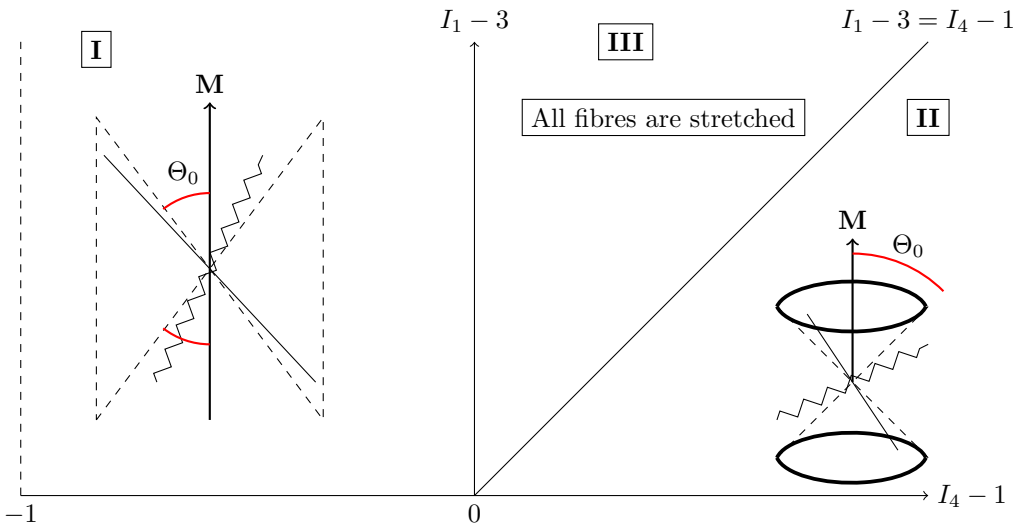

Figure 3.1. The boundaries of the regions of the Latorre-Montans model of dispersion. The fibres that are assumed to be stretched, by the model, and the fibres that are assumed crimped in each region are also shown.

angles become mechanically active and that the soft tissue is incompressible. These two properties of the model contradict each other, as for an incompressible material with dispersed collagen fibres oriented at all angles, there must exist some collagen fibres that contract. Consequently, later models were developed that attempt to retain the tractability of the GOH model, but use a different tension-compression switch that correctly identifies, for a given deformation, which fibres contract and which extend.

One such model was developed by Latorre & Montans (2016) [124]. Like the GOH model, Latorre & Montans assumed that the distribution of collagen fibre orientations in the soft tissue sample adheres to the von Mises distribution. To account for crimped, and thus slack, fibres, they introduced a piecewise SEF with regions that are defined by the direction of the stretched collagen fibres in relation to the mean orientation of the fibres in the reference body. To do this, they examined the average stretch along the mean direction of the fibres, $\lambda_{\mathbf{a}}$, and the average stretch in a plane perpendicular to the mean direction of the fibres, λ_{π}. The boundaries of the piecewise SEF are defined by the values of $\lambda_{\mathbf{a}}$ and λ_{π}, and thus $I_4 - 1$ and $I_1 - 3$, as follows:

- $I_4 - 1 < 0$ ($\lambda_{\mathbf{a}} < 1$): using the symmetry of the fibre distribution, fibres at a polar angle $\theta \in [\Theta_0, \pi - \Theta_0]$ are recruited.
- $I_4 - 1 \geqslant 0$ and $I_4 - 1 \geqslant I_1 - 3$ ($\lambda_{\mathbf{a}} \geqslant 1$ and $\lambda_{\pi} \leqslant 1$): using the symmetry of the fibre orientations, fibres at a polar angle $\theta \in [0, \Theta_0]$ and $\theta \in [\pi - \Theta_0, \pi]$ are recruited.
- $I_4 - 1 \geqslant 0$ and $I_4 - 1 < I_1 - 3$ ($\lambda_{\mathbf{a}} \geqslant 1$ and $\lambda_{\pi} > 1$): every fibre is considered to be recruited.

The regions are represented pictorially in Figure 3.1.

As only a subset of collagen fibres in the soft tissue sample are assumed to be mechanically active for certain deformations, we must modify the generalised structure tensor defined by (3.29) and (3.31). Therefore, we define

$$\kappa_1(\Theta_0) = \frac{1}{2}\int_{\Theta_0}^{\frac{\pi}{2}} \rho(\Theta)\sin^3\Theta \mathrm{d}\Theta, \tag{3.33}$$

$$\tau_1(\Theta_0) = \frac{1}{2}\int_{\Theta_0}^{\frac{\pi}{2}} \rho(\Theta)\sin\Theta \mathrm{d}\Theta, \tag{3.34}$$

$$\kappa_2(\Theta_0) = \frac{1}{2}\int_{0}^{\Theta_0} \rho(\Theta)\sin^3\Theta \mathrm{d}\Theta, \tag{3.35}$$

$$\tau_2(\Theta_0) = \frac{1}{2}\int_{0}^{\Theta_0} \rho(\Theta)\sin\Theta \mathrm{d}\Theta, \tag{3.36}$$

where Θ_0 is a function of the deformation and, hence, the invariants I_1 and I_4, and we replace I_4^* with the pseudoinvariant $\epsilon(\Theta_0)$. The value of the pseudoinvariant $\epsilon(\Theta_0)$ is dependent on the aforementioned conditions on $I_4 - 1$ and $I_1 - 3$. When $I_4 - 1 < 0$,

$$\epsilon(\Theta_0) = \kappa_1(\Theta_0)(I_1 - 3) + [\tau_1(\Theta_0) - 3\kappa_1(\Theta_0)](I_4 - 1). \tag{3.37}$$

When $I_4 - 1 \geqslant 0$ and $I_4 - 1 \geqslant I_1 - 3$,

$$\epsilon(\Theta_0) = \kappa_2(\Theta_0)(I_1 - 3) + [\tau_2(\Theta_0) - 3\kappa_2(\Theta_0)](I_4 - 1). \tag{3.38}$$

And when $I_4 - 1 \geqslant 0$ and $I_4 - 1 < I_1 - 3$

$$\epsilon(\Theta_0) = \kappa(I_1 - 3) + [1 - 3\kappa](I_4 - 1). \tag{3.39}$$

However, there are problems associated with this model too. The authors derived a much simpler form of the GST than we do. To calculate the stress, we must compute the GST by differentiating $\epsilon(\Theta_0)$ with respect to $\mathbf{C}$. In terms of I_1 and I_4

$$\mathbf{H}_{\text{LM}} = \frac{\partial\epsilon(\Theta_0)}{\partial\mathbf{C}} = \frac{\partial\epsilon(\Theta_0)}{\partial I_1}\frac{\partial I_1}{\partial\mathbf{C}} + \frac{\partial\epsilon(\Theta_0)}{\partial I_4}\frac{\partial I_4}{\partial\mathbf{C}}. \tag{3.40}$$

If we differentiate the first case of $\epsilon(\Theta_0)$, (3.37), with respect to I_1, denoted by $\frac{\partial\epsilon_1(\Theta_0)}{\partial I_1}$, then we find that

$$\frac{\partial\epsilon_1(\Theta_0)}{\partial I_1} = \frac{\partial\kappa_1(\Theta_0)}{\partial I_1}(I_1 - 3) + \kappa_1(\Theta_0) + \left[\frac{\partial\tau_1(\Theta_0)}{\partial I_1} - 3\frac{\partial\kappa_1(\Theta_0)}{\partial I_1}\right](I_4 - 1). \tag{3.41}$$

We find similar for the other partial derivatives with respect to I_1 and I_4 for (3.38) and (3.39). However, Latorre & Montans found the following much simpler form of the derivative:

$$\frac{\partial\epsilon(\Theta_0)}{\partial\mathbf{C}} = \kappa^*\mathbf{I} + (\tau^* - 3\kappa^*)\mathbf{a}_0 \otimes \mathbf{a}_0, \tag{3.42}$$

where κ^* and τ^* represent expressions of the two quantities given in (3.37)—(3.39). Latorre

& Montans stated in their original derivation of the model that the additional terms in (3.41) and the other partial derivatives of the quantity $\epsilon(\Theta_0)$ with respect to I_1 and I_4 cancel out to produce (3.42) [124]. Cancelling out the additional terms in the partial derivatives is, therefore, key to obtaining the analytical form of the SEF given in the paper. However, we have not been able to simplify derivatives such as (3.41) to obtain (3.42). Instead, we have found discontinuities in the values of the stress at the boundaries of the various regions.

Additionally, the model assumes that there exist deformations for which every fibre in the soft tissue sample is stretched. However, the assumptions that the material is incompressible and that the distribution of fibre orientations is governed by a von Mises distribution ensure that not all fibres can be stretched in the material. The probability distribution function used in the paper by Latorre and Montans is

$$\rho(\Theta) = 2\sqrt{\frac{2r}{\pi}}\frac{1}{\operatorname{erfi}(\sqrt{2r})}\exp(2r\cos^2\Theta), \tag{3.43}$$

where r is a concentration parameter. Consequently, $\rho(\Theta) > 0$ for all possible values of Θ, and for a given Θ fibres are equally distributed in all directions. By the incompressibility constraint, $\lambda_1\lambda_2\lambda_3 = 1$, so when one principal direction is stretched, at least one other principal direction must be contracted. Hence, any fibres oriented in that principal direction must be contracted and slack. This discrepancy arises because the model focuses on the average stretch along both the mean fibre direction and in a plane perpendicular to the mean fibre direction, and when the deformation is such that $I_4 - 1 \geqslant 0$ and $I_4 - 1 < I_1 - 3$, both average stretches are greater than one.

Another model that attempted to rectify the tension-compression switch of the GOH model was built by Holzapfel & Ogden (2017) [125]. According to this model, the geometry of stretched fibres is governed by the equation $(\mathbf{CN})\cdot\mathbf{N} = 1$, where $\mathbf{C}$ is the right Cauchy-Green deformation tensor and $\mathbf{N}$ is a vector denoting the reference orientation of an arbitrary fibre. The authors' choice of $\mathbf{N}$ and, thus, $(\mathbf{CN})\cdot\mathbf{N}$ were

$$\mathbf{N} = \sin\Theta\cos\Phi\mathbf{E}_1 + \sin\Theta\sin\Phi\mathbf{E}_2 + \cos\Theta\mathbf{E}_3, \tag{3.44}$$

$$\begin{aligned}(\mathbf{CN})\cdot\mathbf{N} = {} & \sin^2\Theta(C_{11}\cos^2\Phi + 2C_{12}\sin\Phi\cos\Phi + C_{22}\sin^2\Phi) \\ & +2\sin\Theta\cos\Theta(C_{13}\cos\Phi + C_{23}\sin\Phi) + C_{33}\cos^2\Theta,\end{aligned} \tag{3.45}$$

where $\mathbf{E}_i$, $i \in \{1,2,3\}$, represent unit vectors along the three coordinate axes in the reference configuration, and Θ and Φ still denote the polar and azimuthal angles of the spherical coordinate system, respectively.

As with the Latorre-Montans model, the dispersion parameter κ is modified to account for the stretched fibres only. If the fibres are stretched in the mean fibre direction, denoted as $\mathbf{M}$ in the Holzapfel-Ogden model, then

$$\kappa_1(\Theta_0) = \frac{1}{4}\int_0^{\Theta_0} \rho(\eta)\sin^3\eta \mathrm{d}\eta + \frac{1}{4}\int_{\Theta_0}^{\pi} \rho(\eta)\sin^3\eta \mathrm{d}\eta, \tag{3.46}$$

$$= \frac{1}{2}\int_0^{\Theta_0} \rho(\eta)\sin^3\eta \mathrm{d}\eta, \tag{3.47}$$

by the symmetry of the fibre distribution, assuming we use a von Mises distribution, and Θ_0 is the angle between $\mathbf{M}$ and the boundary of, in this case, the cone defined by $(\mathbf{CN})\cdot\mathbf{N} = 1$. The expression (3.47) is of the same form as $\kappa_2(\Theta_0)$ in the Latorre-Montans model, (3.35), and is crucially different to the quantity, κ, in the structural tensor for the GOH model, (3.30), which assumes all collagen fibrils become taut when a tissue is stretched along the mean fibril orientation. Conversely, if the fibres are contracted along the mean fibre direction, then the dispersion parameter is

$$\kappa_2(\Theta_0) = \frac{1}{2}\int_{\Theta_0}^{\frac{\pi}{2}} \rho(\eta)\sin^3\eta \mathrm{d}\eta, \tag{3.48}$$

where the symmetry of the fibre orientations has again been used. Importantly, Θ_0 in (3.47) and (3.48) is a function of the deformation. To avoid the problems of discontinuous stresses present in the Latorre-Montans model, Holzapfel and Ogden examined the derivative of $\kappa_1(\Theta_0)$, which is [125]

$$\kappa_1'(\Theta) = \frac{1}{2}\rho(\Theta)\sin^3(\Theta). \tag{3.49}$$

In the GOH model, when all fibres are assumed to be active at the same time, κ is given by

$$\kappa = \frac{1}{2}\int_0^{\frac{\pi}{2}} \rho(\Theta)\sin^3\Theta \mathrm{d}\Theta. \tag{3.50}$$

Holzapfel & Ogden argue that we can assume $\rho(\Theta) = 0$ for $\Theta \in [\Theta_0^+, \frac{\pi}{2}]$, but $\rho(\Theta) = 0$ for this set of angles is not technically correct, as there are fibres oriented in those directions. However, they are crimped, so mechanically, the crimped fibres can be treated as not being present. Thus, $\kappa_1'(\Theta_0^+) = 0$ and we can treat $\kappa_1(\Theta_0)$ similarly to κ in the GOH model. That is, $\kappa_1(\Theta_0)$ is treated as being stationary when differentiated with respect to $\mathbf{C}$ [125]. A similar argument can be made for $\rho(\Theta)$ for $\Theta \in [0, \frac{\pi}{2} - \Theta_0^-]$ for $\kappa_2'(\Theta_0)$.

Therefore, the problem of derivatives of the dispersion parameter that result in discontinuous stresses is resolved in the Holzapfel-Ogden model. However, there is still one significant problem with the model: for a general deformation, it is not possible to calculate the geometry of the stretched fibres that is needed to compute the dispersion parameter, $\kappa_{1,2}(\Theta, \Psi)$ analytically. For a general stretch, we cannot rewrite (3.45) to get a solution for Θ and, thus, identify which fibres are stretched and which are not. The GST method's benefit of tractability only applies to the Holzapfel-Ogden model for a limited set of deformations, a stretch along the mean fibre direction, for example, which produces a cone of stretched fibres centred around

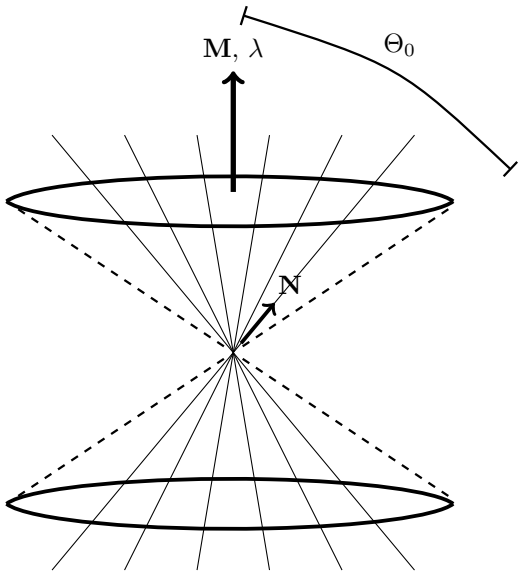

Figure 3.2. The cone of collagen fibres that are stretched, according to the Holzapfel-Ogden model, when a tissue with dispersed fibres that possess rotational symmetry around the mean direction **M** are stretched, uniaxially, along **M**. The vector **N** represents the orientation of an arbitrary collagen fibre within the tissue and Θ_0 represents the angle made between **M** and the fibres located at the boundary of the cone.

the mean fibre direction, Figure 3.2

The *Angular Integration* (AI) approach to dispersion of collagen fibre orientations was proposed by Lanir (1983) [126]. In the AI approach, the contributions to the SEF of collagen fibres oriented at all possible polar and azimuthal angles in a reference sphere are computed to calculate the total contribution to the tissue's strain energy from the collagen fibres. Lanir assumed that elastic and collagen fibres in soft tissues must have their contributions to the SEF calculated separately. Consequently, the strain energy in the collagen and elastic fibres per unit volume, as calculated by Lanir, is

$$W = \sum_{k} \sum_{u} S_k \cdot R_k(\mathbf{u}) \cdot w_k(\lambda) \cdot \delta\Omega, \tag{3.51}$$

where S_k is the volume fraction of fibre type k, $w_k(\lambda)$ is the strain energy in a single fibre at stretch ratio λ, $R_k(\mathbf{u})$ represents the volumetric fraction of fibres oriented in the direction $\mathbf{u}$ and $\delta\Omega$ denotes the proportion of the surface of the sphere for which the term is being calculated. The load per unit reference cross-sectional area of fibre type k is

$$f_k(\lambda) = \frac{\partial w_k(\lambda)}{\partial \lambda}. \tag{3.52}$$

In this formulation, the deformation and the strain energy due to a single fibre are incorporated into the model. However, we still need to account for collagen crimp. Therefore, Lanir adapted the expression in (3.52) by assuming that fibrous proteins in soft tissues possess a non-uniform distribution of crimp and that fibre orientations do not change as the fibres straighten [126]. By these assumptions, the load per unit reference cross-sectional area of

fibre type k becomes

$$f^*_{k,\mathbf{u}}(\lambda) = \sum_{X=1.0}^{\lambda} D_{k,\mathbf{u}}(X) \cdot f_k\left(\frac{\lambda}{X}\right)\delta X, \tag{3.53}$$

where $D_{k,\mathbf{u}}(X)$ is an undulation density function that defines the distribution of the critical stretch, X, the stretch at which a fibre becomes straight and taut, for fibres of type k in the direction $\mathbf{u}$.

In contrast to the GST method for modelling dispersion, the Angular Integration approach can successfully differentiate between taut and slack fibres throughout the reference sphere for a general deformation. However, the analytical form of the SEF is lost in the AI approach and we must use numerical integration to calculate the stress, which is a computationally intensive process. In the literature, this effect has partially been mitigated by making some simplifying assumptions to the model proposed by Lanir. For example, elastin fibres are often considered to have a negligible contribution to the tissue's ability to resist the deformation. Thus, as one constituent of a non-collagenous matrix, they are assumed to be linearly elastic. Furthermore, rather than including an additional factor corresponding to the undulation density of the fibres, collagen crimp can be incorporated into the SEF of a single collagen fibre.

The Flynn-Rubin-Nielsen model (2011) [127] attempts to model dispersion of collagen fibres, co-aligned within a particular bundle, phenomenologically while eradicating the use of the costly and time-intensive numerical integrals associated with the *Angular Integration* approach. The model assumes that there are six fibrous bundles that consist of an elastin fibre in parallel with a collection of undulated collagen fibres that are oriented along two opposing vertices in a regular icosahedron. In this model a single collagen fibre is assumed to be linearly elastic, so analytical forms of the stress and SEF can be derived when collagen fibre crimp is governed using a step distribution or a triangular distribution [127].

3.2 Markov chain Monte Carlo

Previously in this chapter, we have examined a representative subset of phenomenological, semi-microstructural, and microstructural models of soft tissue behaviour. This analysis has enabled us to identify key features that we would like a new model of soft tissue behaviour to possess in order to advance the existing field of soft tissue behaviour and, potentially, be used in the future to predict tissue behaviour and inform important medical procedures that can be performed on tissues. In this section, we briefly detail a history of MCMC and discuss some scientific fields that Bayesian statistics has successfully been implemented within in the past. These examples come from a wide variety of fields to demonstrate the utility, in general science, of accounting for uncertainty in a problem. These examples will include instances where MCMC has successfully been applied to sample posterior distributions, or properties of the distributions. These examples will also provide motivation for attempting to examine soft tissue modelling with a Bayesian approach. We will also include examples of

other Bayesian statistical techniques being applied to a problem. This is done in order to show the robustness of the Bayesian approach and to demonstrate that, if MCMC does not prove to efficiently sample the posteriors of our model parameters in later chapters, that further work could be done to apply other statistical techniques to the problem.

The origin of Markov chain Monte Carlo methods can be traced back to Metropolis and Ulam (1949) [128]. In the paper, the authors were mainly concerned with applying statistical techniques to study the problem of interacting molecules moving through a medium and being involved in collisions that create new molecules. Studying this problem was important for the work in the nuclear sciences that was then being done at Los Alamos. At the time, studying this problem without Monte Carlo methods required time-intensive calculations to obtain approximate solutions to even the most simple of problems. Using a Monte Carlo approach, the authors proposed applying random processes on a set of numbers corresponding to independent variables that describe the motion and position of each nuclear particle in order to estimate the probability distribution for the independent variables at a later time.

A few years later, Metropolis co-authored a 1953 paper that outlined an alternative method to standard Monte Carlo sampling [129] that was used to study the properties of substances that consist of interacting molecules. The authors proposed new states by moving one of the N particles, situated at (X, Y), to the position (X^*, Y^*) in a repeating square as follows:

$$X^* \to X + \alpha\xi_1, \tag{3.54}$$

$$Y^* \to Y + \alpha\xi_2, \tag{3.55}$$

where α is the maximum distance that can be moved by a particle in any given direction and $\xi_{1,2} \in [-1, 1]$. The symmetric proposal distribution for this problems proposes moves in a square of length 2α. Standard Monte Carlo methods would accept the moves. The authors, however, posited that, in their new method, the new position is accepted based on the potential energy of the proposed state compared to the potential energy of the current state. If the potential energy, E, of the proposed system is less than that of the current system, then $\exp(-E/kT)$—where k is Boltzmann's constant and T is the temperature in degrees Kelvin—is increased and the move is accepted. Conversely, if the potential energy of the proposed system is higher than that of the current system, then $\exp(-E/kT)$ is reduced and we accept the move with probability $\exp(-\Delta E/kT)$, where ΔE represents the increase in energy from the current state to the proposed state. Compared to standard Monte Carlo, this algorithm enables sampling to be performed more commonly on states with lower potential energy while also allowing transitions to less probable states with high potential energies. This algorithm is ergodic and for a particular state r, the posterior probability of the system being in state r is proportional to $\exp(-E_r/kT)$. This problem is similar to the MCMC technique simulated annealing.

In 1970, Hastings generalised the Metropolis algorithm for MCMC problems where the proposal distribution is asymmetric [130]. Due to increased computational power, MCMC has

become a well-established and frequently used Bayesian statistical method in a wide variety of mathematical fields. For example, MCMC has been applied to flood frequency analysis [131] and classification of malignant breast cancer tumours [132]. Additionally, van Ravenzwaaij (2018) *et al*. [80] demonstrated how MCMC can be used, according to a Metropolis algorithm, to calculate the mean of normally distributed in-class test scores for a known variance. Through this simplified example, for which there exists an analytical expression for the distribution of test scores, $N(100, 15)$, the necessity of a burn-in phase when the initial guesses for the distribution's parameters are poor can be highlighted. Huang *et al*. (2006) [133] studied the dynamics of HIV in patients undergoing retroviral therapy using Markov chain Monte Carlo in hierarchical Bayesian methods for mixed-effect models. This demonstrates the applicability of Bayesian methods for complex systems with difficult posteriors to sample from.

Acquaviva *et al*. (2011) [134] created an MCMC algorithm to use a galaxy's spectral energy distribution to estimate physical properties of the galaxy like its age, stellar mass, and redshift. The construction of the MCMC algorithm was motivated because parameters used in the modelling of galaxies are correlated due to the interactions between galactic phenomena [134]. The correlation between parameters ensure that the posterior distributions are highly non-Gaussian and, thus, χ^2 minimisation is not an effective method of parameter estimation [134].

Bray (2002) [135] used MCMC methods to study incidence and mortality rates of various cancers. With the lack of immediate access to private medical data, Bayesian estimates of current incidence and mortality rates aids long-term health planning. Mathew *et al*. [136] used adaptive MCMC methods to estimate the value of genetic parameters. In the model, the set of phenotypic observations—the observable characteristics of a person that are dependent on both the individual's genotype and environmental factors—was considered to be a function of environmental, random additive and dominant genetic effects, as well as error terms. An adaptive algorithm which used parameter covariances in the algorithm to estimate an appropriate multivariate proposal distribution was employed by the authors. This adaptive algorithm provided a more efficient process for sampling from the posterior distributions.

Mehta *et al*. used MCMC techniques to study problems in machining. These problems are extremely complex to study without probabilistic sampling due to the multi-physical nature of machine cutting or assembling. Additional complexity arises because of the uncertainty present in the problem from variation in the geometry of machine parts and in the environment, temperature, and humidity. The authors avoided having to perform multiple physical tests to capture enough data to construct a reliable model by applying Bayesian inference to a smaller range of data [137]. This provided a more feasible, less costly, and less time-intensive test of the model in assessing the ability of the model to approximate physical behaviour. Comparisons to experimental data demonstrated that the MCMC approach inferred values for the model's parameters that produced good approximations to experimental data. Furthermore, the estimates obtained through Bayesian inference were found to better those obtained through least square estimations [137].

Bayesian statistics has also been applied to phylogenetics, which analyses how groups of organisms or species have developed and diversified genetically. Phylogenetic models must contain many parameters that quantify the evolution of large data sets that correspond to the molecular data stored in multiple genes of an organism. Bayesian statistical method simplify the study of these complex problems significantly. Baele *et al*. demonstrated the versatility of the MCMC approach by writing an algorithm with a multivariate proposal distribution that used multicore processing to update the likelihood function of each block of the large molecular data set simultaneously [138]. With this algorithm, the authors achieved significantly faster results than an alternative MCMC approach that used a univariate proposal distribution to propose new values of the model's parameters and update the likelihood function of a block one at a time. Again, adaptive methods were used to make the algorithm more efficient by tuning the proposal distribution so that it better replicated the covariances of the model's parameters with one another [138].

Chapter 4

A Bayesian Approach to the Hyperelastic Modelling of Tendons

4.1 Tendon paper introduction

To start this thesis, we demonstrated both the complex behaviour of fibrous soft tissues and how that complexity is a result of tissue microstructure. We then described a continuum mechanical framework that describes the behaviour of deformed fibrous soft tissues. Next, we introduced Bayesian statistical methods and showed how this field provides a robust group of methods to accurately quantify uncertainty in the values of parameters, including in complicated non-linear models. And finally, we have analysed the literature to identify reasons why seeking to create tractable, hyperelastic microstructural models of skin deformation is desirable, and to elucidate the range of fields that Bayesian statistical methods have been applied to.

Now we present a new microstructural model of soft tissue deformation that is tractable and only contains parameters that have a physical basis for inclusion. We then fit the model to experimental uniaxial tendon tensile data using both non-linear optimisation and a random walk Metropolis Markov chain Monte Carlo (RWM MCMC) algorithm. We produce two versions of the new microstructural model. One version assumes that the distribution of recruitment stretch in the tendon is governed by a symmetric triangular distribution. The second version of the model, on the other hand, assumes that a general triangular distribution governs the variation of recruitment stretch in the tendon. Furthermore, we derive a RWM MCMC algorithm where we fit to experimental data in order to determine credible intervals for the values of the parameters in the symmetric-triangular-distribution version of the model. We fit to tendon data first because tendons possess a highly regulated structure where collagen fibrils are largely aligned with one another. Additionally, tendons are important fibrous tissues that are ubiquitous in, and vital to normal physiological function of, humans and animals. Advances in our understanding of how tendon microstructure and macroscopic behaviour are related have the potential to benefit society greatly.

In its entirety, this work constitutes a significant undertaking that could have been split into two papers: one on the model derivation and model fitting using non-linear optimisation; and another that focused on deriving a RWM MCMC algorithm that quantifies uncertainty

in the parameter values of a model of soft tissue behaviour. However, we decided to submit this work as one paper, as the justification for the statistical approach is so closely linked to the rest of the paper. This paper has been submitted to the *Journal of the Royal Society Interface*. Also provided in this chapter, after the main paper, is the supplementary material. The supplementary material contains a substantial piece of work, in particular, providing full derivations of our microstructural model and the RWM MCMC algorithm. This is because, the content in the supplementary material did not fit into the main paper submission due to the word limit for article submissions in the *Journal of the Royal Society Interface*. The main paper and supplementary material are currently under review. For this paper, I performed the following tasks:

- Helped to calculate the exact algebraic form of both versions of the new strain energy function (SEF) described in this paper submission, and checked the algebra in both versions of the SEF to ensure the continuity of the two versions of the SEF and the stress measures associated with them.
- Coded both the non-linear optimisation problem and the RWM MCMC algorithm used to compute the credible intervals of the model's parameters. This included helping to derive the expressions for the posterior probability distribution and the transition probability that are detailed in the paper submission.
- Created the figures and plots.
- Wrote the initial draft of the paper, and edited all subsequent drafts.

Bayesian inference on a microstructural, hyperelastic model of tendon deformation

Bayesian inference on a microstructural, hyperelastic model of tendon deformation

James Haughton[1], Simon Cotter[1], William J. Parnell[1], and Tom Shearer[1, 2]

[1] *Department of Mathematics, University of Manchester, Manchester M13 9PL, United Kingdom*
[2] *Department of Materials, University of Manchester, Manchester M13 9PL, United Kingdom*

Abstract

Microstructural models of soft tissue deformation are important in applications including artificial tissue design and surgical planning. The basis of these models, and their advantage over their phenomenological counterparts, is that they incorporate parameters that are directly linked to the tissue's microscale structure and constitutive behaviour and can therefore be used to predict the effects of structural changes to the tissue. Although studies have attempted to determine such parameters using diverse, state-of-the-art, experimental techniques, values ranging over several orders of magnitude have been reported, leading to uncertainty in the true parameter values and creating a need for models that can handle such uncertainty. We derive a microstructural, hyperelastic model for transversely isotropic soft tissues and use it to model the mechanical behaviour of tendons. To account for parameter uncertainty, we employ a Bayesian approach and apply an adaptive Markov chain Monte Carlo algorithm to determine posterior probability distributions for the model parameters. The obtained posterior distributions are consistent with parameter measurements previously reported and enable us to quantify the uncertainty in their values for each tendon sample that was modelled. This approach could serve as a prototype for quantifying parameter uncertainty in other soft tissues.

Keywords: tendon, modelling, microstructural, hyperelastic, Bayesian, uncertainty

1 Introduction

Fibrous soft tissues such as tendons, skin, and arteries are vital to life. Tendons and ligaments, for example, enable movement by transmitting forces around the body [1]. It is critical, therefore, that we understand soft tissue mechanical behaviour to advance fields such as tissue engineering [2] and surgery [3]. Soft tissues exhibit complex macroscopic phenomena, including anisotropy and non-linearity, that are induced predominantly by the microstructure of the tissue. Anisotropy arises from the presence of collagen fibrils, which locally reinforce the tissue in a preferred direction. Initially, the fibrils are crimped and stress-free, but they straighten as the tissue deforms, contributing to its resistance to further deformation once taut [4]. This gradual recruitment of collagen fibrils leads to the non-linear stress-strain profile typical of soft tissues [5], as illustrated in Figure 1a with a plot of the Cauchy stress, σ, against stretch, λ.

Additionally, soft tissues are *viscoelastic*, so assuming that their behaviour can be described by an elastic model is a simplification. Practically speaking, before tests to measure mechanical properties are performed, a tissue is subjected to cyclic loading until the stress-strain behaviour of the tissue is consistent between consecutive cycles (see Figure 1b). Then, the tissue can be treated as pseudoelastic and modelled as a particular elastic material upon loading and a different elastic material upon unloading [6]. In reality, energy is dissipated in the tissue during the loading-unloading cycle, but we can apply elasticity theory to the tissue as long as we only examine one loading path. Furthermore, for sufficiently slow (quasi-static) or extremely rapid deformations, the loading and unloading curves are almost identical.

To model soft tissue deformation, we will use the theory of hyperelasticity, relating the stress to the strain via a strain-energy function (SEF). There are two approaches to developing a hyperelastic model: the phenomenological and structural approaches (although any one SEF can incorporate features of both). Phenomenological models seek to achieve the best quantitative fit to experimental data. They do not attempt to determine how the microstructure influences the macroscopic behaviour observed in mechanical testing because the model's parameters do not

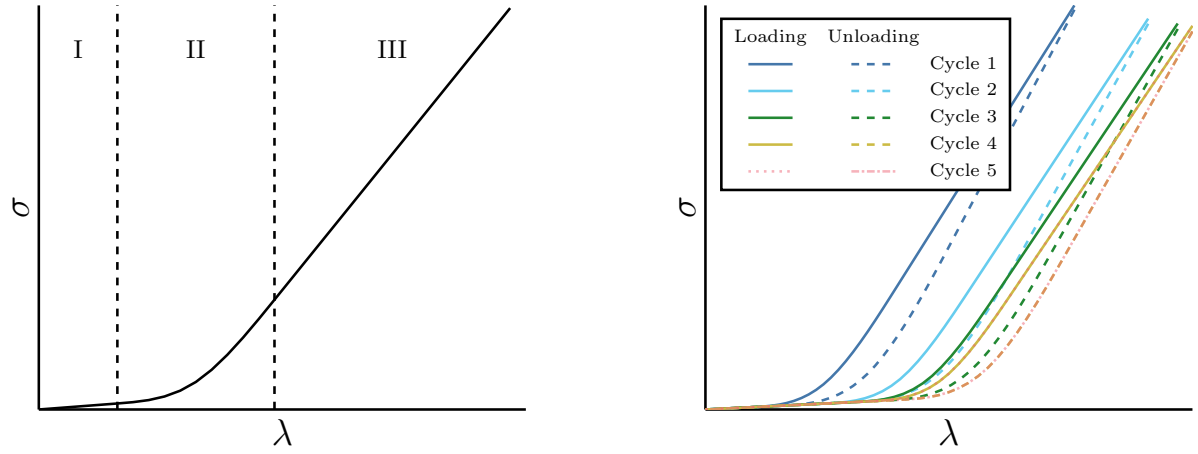

(a) (b)

Figure 1: (a) The stress-strain behaviour of soft tissues. Region I: only the compliant components are loaded; the collagen fibrils are crimped and slack. Region II: gradually, the stiff collagen fibrils straighten and become taut. Region III: all the collagen fibrils are taut; the soft tissue is stiff and linearly elastic. (b) Successive loading-unloading cycles of a viscoelastic soft tissue until the tissue can be treated as pseudoelastic.

necessarily have a clear physical interpretation. By contrast, structural models incorporate physically relevant parameters to elucidate the relationship between the arrangement and properties of the tissue's constituents and its mechanical behaviour. Incorporating microstructural information into an SEF often increases its complexity, and it is important that a structural SEF remains tractable if it is to be viable for studying soft tissue deformation. This is important when employing a Bayesian framework with Monte Carlo sampling, where we require many solutions of the forward model. Therefore, simplifying assumptions about the microstructure are often required.

Values for unknown structural parameters can be obtained via imaging methods such as serial block face-scanning electron microscopy [7], [8] and X-ray computed tomography [9]–[12], and for constitutive parameters using micromechanical techniques like force spectroscopy [13] and atomic force microscopy [14]. These techniques are challenging, however, and a wide range of values has been reported for certain quantities. The collagen fibril Young's modulus, for example, has been reported to have a value ranging from 32 MPa [13] to 2.8 GPa [14]. This uncertainty makes it difficult to predict soft tissue mechanical behaviour using optimisation techniques alone. Therefore, in this paper, we take a Bayesian approach to the modelling process to characterise the likely ranges of values that microstructural and micromechanical parameters can take.

Due to their importance and the fact that they have been studied extensively, we focus on tendons in this paper. The mechanical properties of different tendons are distinct from one another, with energy-storing tendons being more extensible than positional tendons due to differences in their microstructures [15], [16]. One feature that is common to all tendons is that their collagen is structured in a regulated, hierarchical fashion and aligned closely with the tendon's axis [1]. Collagen molecules form cross-links and aggregate into fibrils with diameters ranging from 12 to 500 nm [7]. Collections of fibrils collect into larger structures called fibres, with diameters of 150 to 1000 μm, which themselves form fascicles, with diameters of 1000 to 3000 μm, [17]. In other soft tissues, collagen fibrils are less strongly aligned and form a network, but by aligning many fibrils in one direction, the tendon is stronger in that direction [18].

Models such as the Holzapfel-Gasser-Ogden (HGO) model [19], which was initially created to study arteries, have been adapted to study tendons [20]. This model is structural in the sense that it incorporates a strain invariant that is directly related to the stretch in the collagen fibres, but phenomenological in the sense that an exponential function is used to describe collagen recruitment, and the stretches in individual fibrils are not tracked. Other models have explicitly incorporated the crimp morphology of the fibrils [21]–[25] and produced a good fit to experimental data. Several probability density functions (PDFs) have been used to describe the distribution of fibril length, including the Weibull [26] and triangular distributions [27], [28], as summarised in a review article by Thompson *et al.* [29].

In this paper, we derive a structural SEF for modelling soft tissues that assumes collagen fibrils are linearly elastic and have a triangular length distribution. We test the efficacy of the model using non-linear optimisation to find a parameter vector that produces a local best fit to data. Secondly, we repeat the fitting process using a

Bayesian framework. This enables us to incorporate prior beliefs about the unknown model parameters, a statistical model for noisy observations of the stress-strain curves and our non-linear model to obtain posterior distributions for the model parameters. Through these distributions, we identify and quantify the uncertainty in the parameters, and the directions in parameter space in which the model is more or less sensitive.

The structure of the paper is as follows. In Section 2, we describe the underpinning continuum mechanical theory that is required to model the deformation of an anisotropic soft tissue and, using physical considerations, derive a new constitutive equation to model tendons. In Section 3, we use non-linear optimisation to fit the model to experimental stress-strain data and compare its quality of fit to that of the widely-used HGO model and a microstructural tendon model. In Section 4, we account for noise in the experimental data using a likelihood function that allows us to study the problem under a Bayesian framework. In Section 5, we derive the posterior distribution for the model's microstructural and micromechanical parameters. In Section 6, we summarise our findings and discuss potential ways to expand upon our work.

2 Model derivation

2.1 Preliminaries

Prior to considering the constitutive response of soft tissues, we need to consider kinematics, i.e. how to formulate the mechanism of deformation. First, we distinguish between two configurations, the reference (initial) configuration and the deformed configuration. Points on the reference and deformed bodies are described by the vectors $\mathbf{X}$ and $\mathbf{x}$, respectively. The two sets of coordinates are related via the deformation mapping, χ, i.e. $\mathbf{x} = \chi(\mathbf{X})$. We define the deformation gradient, $\mathbf{F}$, as

$$\mathbf{F} = \nabla_{\mathbf{X}}\mathbf{x}, \tag{1}$$

where $\nabla_{\mathbf{X}}$ represents the gradient operator with respect to the reference coordinates. From the deformation gradient, we define two symmetric measures of the deformation, known as the left and right Cauchy-Green deformation tensors, $\mathbf{B} = \mathbf{F}\mathbf{F}^{\mathrm{T}}$ and $\mathbf{C} = \mathbf{F}^{\mathrm{T}}\mathbf{F}$, respectively [30].

The SEF W allows one to define the constitutive equation of a hyperelastic material, relating stress to strain via derivatives of W. In order to determine the exact form of this constitutive response, we must first identify the symmetry properties of the material. The mechanical behaviour of transversely isotropic materials, such as tendons, is only invariant for rotations around a preferred direction, $\mathbf{M}$. Furthermore, the SEF must be objective, as the laws of physics are the same in any inertial frame of reference. As the SEF is invariant under a coordinate transformation, we can write it as a function of invariants of the deformation. For an isotropic material, there are only three invariants, $I_1 = \mathrm{tr}(\mathbf{C})$, $I_2 = \frac{1}{2}((\mathrm{tr}(\mathbf{C}))^2 - \mathrm{tr}(\mathbf{C}^2))$ and $I_3 = \det(\mathbf{C})$. For a transversely isotropic material, we must introduce an additional two pseudoinvariants that depend on $\mathbf{M}$: $I_4 = \mathbf{M}\cdot\mathbf{C}\mathbf{M}$ and $I_5 = \mathbf{M}\cdot\mathbf{C}^2\mathbf{M}$ [30].

2.2 The model

Collagen fibrils in tendons are crimped when the tendon is relaxed, but straighten out as it is stretched [4]. We model the distribution of fibril lengths using a triangular distribution, which enables us to obtain an explicit, analytical form for the SEF, as we shall show shortly. When the triangular distribution is symmetric, it approximates the normal distribution (see Figure 2a). An individual collagen fibril is assumed to be stress-free until becoming taut at a recruitment stretch λ_r. Once taut, it is assumed to be linearly elastic. The non-linearity of the SEF arises through the gradual recruitment of collagen fibrils [31]. Fibrils in the tendon are assumed to be locally coaligned. We follow the widely-used assumption that we can accurately describe soft tissue mechanics using only the isotropic invariant I_1 to model the tendon's non-collagenous matrix (NCM) and the anisotropic invariant I_4 [19], [22] to model the fibrils. We decouple the contributions of the collagen fibrils and NCM in the SEF and assume that each component's contribution is proportional to its volume fraction. Finally, we assume that tendons are incompressible. Thus, the SEF, $W(I_1, I_4)$, is

$$W(I_1, I_4) = (1-\phi)W_{\mathrm{NCM}}(I_1) + \phi W_{\mathrm{coll}}(I_4), \tag{2}$$

where ϕ is the collagen volume fraction.

To determine the form of $W_{\mathrm{coll}}(I_4)$, we start by defining the stress exerted upon a single collagen fibril. We assume the fibrils are slack while crimped and obey Hooke's law once taut, so that the stress can be expressed as

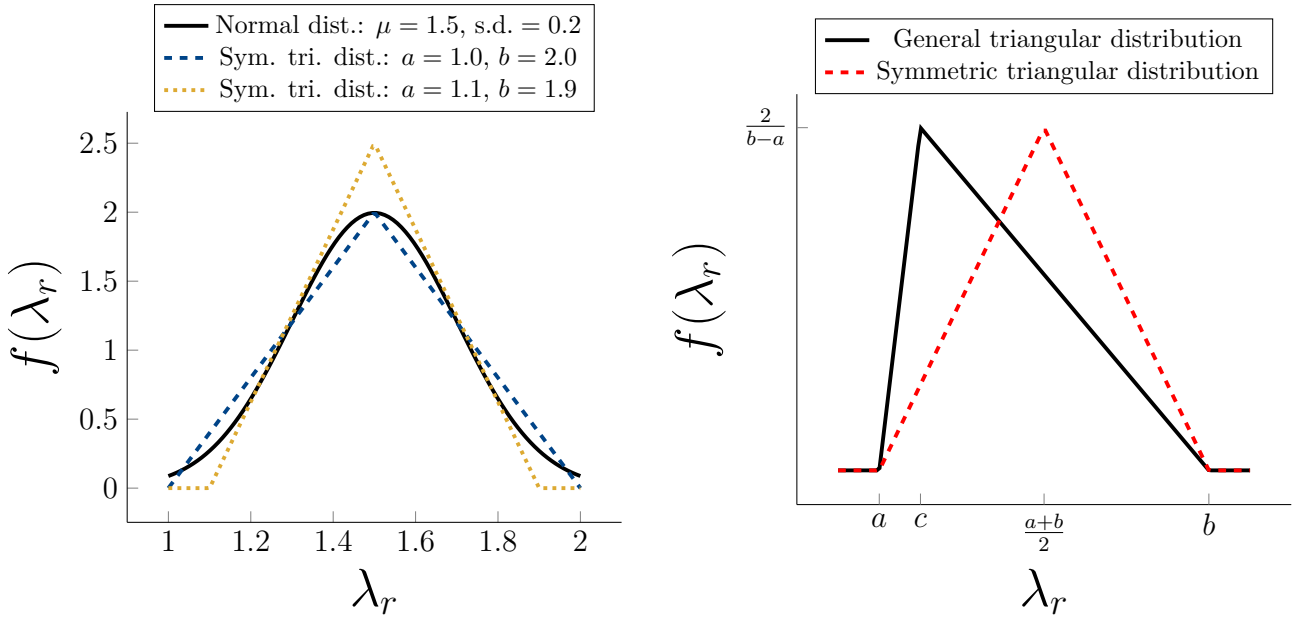

(a) (b)

Figure 2: (a) The PDFs, $f(\lambda_r)$, for a normal distribution and two symmetric triangular distributions, with minimal value a and maximal value b, that approximate the normal distribution. s.d. = standard deviation. (b) The PDFs, $f(\lambda_r)$, for the symmetric and general triangular distributions.

$$\sigma_{\text{fib}}(\lambda, \lambda_r) = \begin{cases} 0, & \lambda \leqslant \lambda_r, \\ E\left(\frac{\lambda - \lambda_r}{\lambda_r}\right), & \lambda > \lambda_r, \end{cases} \tag{3}$$

where E is the Young's modulus of the collagen fibrils. We can determine the total (Cauchy) stress acting upon the collagen fibrils that are aligned in a given direction within a representative volume element by calculating the following integral:

$$\sigma_F(\lambda) = \int_0^{\lambda} f(\lambda_r)\sigma_{\text{fib}}(\lambda, \lambda_r)\mathrm{d}\lambda_r, \tag{4}$$

where $f(\lambda_r)$ represents the PDF of the recruitment stretch. We derive SEFs for two different triangular distributions: a symmetric distribution and a general distribution. We refer to them as the symmetric triangular (ST) and general triangular (GT) models, respectively. For both distributions, the first fibril becomes mechanically active at $\lambda = a$, and the last fibril becomes mechanically active at $\lambda = b$. For the ST distribution, the mode is half-way between a and b, whereas, for the GT distribution, the mode is designated by a third parameter c, with $a < c < b$. The PDF for the GT distribution, $f_{\text{gen}}(\lambda_r)$, is

$$f_{\text{gen}}(\lambda_r) = \begin{cases} 0, & \lambda_r < a, \\ \frac{2(\lambda_r - a)}{(b-a)(c-a)}, & a \leqslant \lambda_r \leqslant c, \\ \frac{2(b - \lambda_r)}{(b-a)(b-c)}, & c \leqslant \lambda_r \leqslant b, \\ 0, & \text{if } \lambda_r > b. \end{cases} \tag{5}$$

The PDF for the ST distribution, $f_{\text{sym}}(\lambda_r)$, is obtained by setting $c = \frac{a+b}{2}$ in (5) (see Figure 2b).

Using (3) and the PDF of the fibril recruitment stretch distribution, we can evaluate the integral in (4) analytically. Exploiting the fact that $I_4 = \lambda^2$, i.e. I_4 is equal to the square of the stretch of the fibrils, we obtain

$$\sigma_F(I_4) = E\left(A(I_4) + B(I_4)\sqrt{I_4} + C(I_4)I_4 + \frac{D(I_4)}{2}\sqrt{I_4}\log I_4\right), \tag{6}$$

where $A(I_4), \ldots, D(I_4)$ are piecewise constants whose values depend on I_4 (see Appendix A). The *form* of the stress, σ_F, acting on the fibrils is the same for both the ST and GT distributions; however, the piecewise constants are different in each case. In order to convert (6) into an expression for the fibrils' contribution to the SEF, we use a technique presented by Shearer [22] to write the left side of (6) in terms of $W_{\text{coll}}(I_4)$. Eventually, we obtain

$$W_{\text{coll}}(I_4) = E\left(\frac{A(I_4)}{2}\log I_4 + (B(I_4) - D(I_4))\sqrt{I_4} + \frac{C(I_4)}{2}I_4 + \frac{D(I_4)}{2}\sqrt{I_4}\log I_4 + G(I_4)\right), \tag{7}$$

where $G(I_4)$ is a piecewise constant that ensures the continuity of $W_{\text{coll}}(I_4)$. We further assume that the mechanical response of the NCM can be modelled by a neo-Hookean SEF [23], giving

$$\begin{aligned} W(I_1, I_4) =& (1-\phi)\frac{\mu}{2}(I_1 - 3) \\ &+ E\phi\left(\frac{A(I_4)}{2}\log I_4 + (B(I_4) - D(I_4))\sqrt{I_4} + \frac{C(I_4)}{2}I_4 + \frac{D(I_4)}{2}\sqrt{I_4}\log I_4 + G(I_4)\right), \end{aligned} \tag{8}$$

where μ is the NCM shear modulus. A full derivation of this SEF is provided in the supplementary material.

For an incompressible, transversely isotropic SEF that is a function of I_1 and I_4 only, the constitutive equation, in terms of the Cauchy stress, is

$$\boldsymbol{\sigma} = -p\mathbf{I} + 2\frac{\partial W}{\partial I_1}\mathbf{B} + 2\frac{\partial W}{\partial I_4}\mathbf{m}\otimes\mathbf{m}, \tag{9}$$

where p is a Lagrange multiplier associated with the incompressibility constraint, and $\mathbf{m} = \mathbf{FM}$ is the direction of the collagen fibrils in the deformed configuration.

3 Non-Linear Optimisation

We now examine the ability of the derived constitutive model to fit experimental data. We fitted to data using standard, non-linear optimisation, using the software package *Mathematica 12* [Mathematica Version 12.3.1.0, Wolfram Research Inc., https://www.wolfram.com/mathematica, Champaign, IL, 2021] and the function *NonlinearModelFit*. We used the Nelder-Mead algorithm within the *NMinimize* method of *NonlinearModelFit*. The Nelder-Mead algorithm for an n-dimensional problem constructs a polytope of $n+1$ points, $x_1, x_2, \ldots, x_{n+1}$, and uses the centroid of the polytope to propose a new vertex x_p that is accepted if it provides a closer fit to data than the second-worst-fitting vertex on the polytope [32]. We set the maximum number of iterations in *NonlinearModelFit* to be one thousand.

The first two sets of stress-strain data that we fitted were experiments on mouse tail tendons collected by Goh *et al.* [33], [34]. We used two data sets designated as mtt01_1_t5c and mtt01_1_t6b_trunc. We shall refer to them as t5c and t6b for brevity. The second two sets of data were collected by Thorpe *et al.* [15] and were previously modelled using a different SEF by Shearer *et al.* [16]. We used the data sets designated as equine common digital extensor tendon (CDET) from horse number 39 and equine superficial digital flexor tendon (SDFT) from horse number 16. These data sets were selected as they have a particularly large elastic region, with the onset of failure not occurring until around 10% strain. For brevity, we refer to them as CDET and SDFT, respectively.

In this work, we only consider elastic behaviour. Both damage and failure of tendon constituents are beyond the scope of the models that we study. The data that we model, however, were calculated to study damage and failure of the tendons. Therefore, we must only consider a limited range of data points, corresponding to the stress-strain values that are assumed to lie within the region of elasticity. For the data collected by Thorpe *et al.* we used all data points up to 10% strain in accordance with [16]. The 10% strain limit was chosen in that work because it represented a medium between the reported maximum *in vivo* stretches for equine CDET and SDFT (3% strain and 16.6% strain, respectively). Furthermore, although 10% strain is over triple the maximum *in vivo* stretch for CDETs, the authors of the study declared that they did not observe the effects of damage on the stress-strain curves of CDET at 10% strain. For the data collected by Goh *et al.*, the authors provided a *MATLAB* script, [34], that enabled the experimental data to be analysed. As part of this analysis, the *MATLAB* script detailed multiple properties associated with the experimental stress-strain data. One property was the strain at which the maximum stress-strain gradient was estimated to be at. Therefore, we chose this strain to be the upper limit at which the studied material did not suffer from damage.

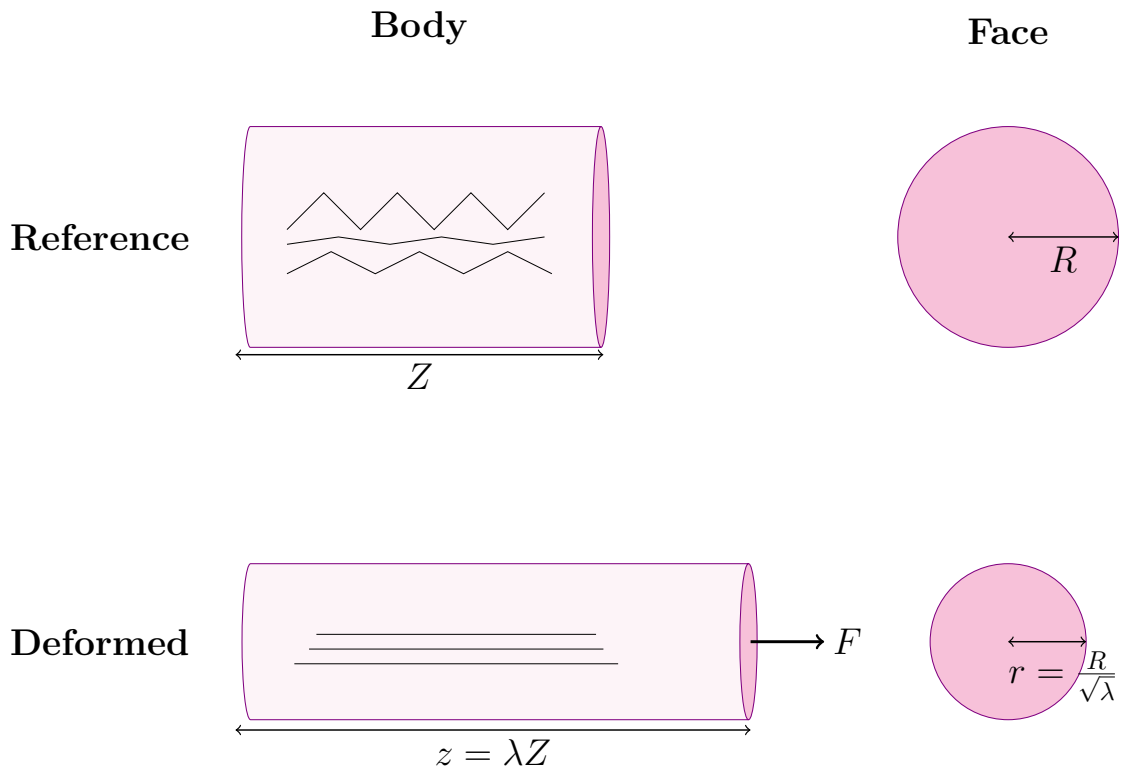

Figure 3: The tendon sample in the reference configuration (upper left) and face with normal in the Z-direction (upper right), and the deformed body (lower left) and face (lower right) after a force of $F\mathbf{e}_z$ is applied to the tissue.

To derive the constitutive equation, we assumed that a cylindrical tendon sample, described using cylindrical polar coordinates, is stretched along the axis of the aligned fibrils, which are oriented along the Z-axis (see Figure 3). For this deformation, given the assumed incompressibility and symmetry of the material, the reference and deformed coordinates, $\mathbf{X} = (R, \Theta, Z)$ and $\mathbf{x} = (r, \theta, z)$, are related by

$$(r, \theta, z) = \left(\frac{R}{\sqrt{\lambda}}, \Theta, \lambda Z \right). \tag{10}$$

The Cauchy stress, (9), gives the force acting on the deformed material per unit *deformed* area; however, the quantity recorded in the experiments being modelled is the engineering stress, the force per unit *reference* area, which is denoted as N in Figure 4. Therefore, after substituting our SEF into (9), we divide the resulting expression through by λ to obtain

$$N = (1-\phi)\mu \left(\lambda - \frac{1}{\lambda^2} \right) + \frac{\phi E}{\lambda} \left(A(\lambda^2) + B(\lambda^2)\lambda + C(\lambda^2)\lambda^2 + D(\lambda^2)\lambda \log \lambda \right), \tag{11}$$

where $I_4 = \lambda^2$ by (10) and the assumed alignment of the fibrils. While the form of N in (11) is unchanged by whether the symmetric or general triangular distribution is used to model the fibril recruitment stretch distribution, the values of $A(I_4)$—$D(I_4)$ differ depending on which fibril recruitment stretch distribution is used. See Appendix A.

To provide a benchmark for the fit of our model to data, we also fitted the tendon data using the commonly-used HGO model [19]. The HGO model was originally developed for modelling arteries and incorporates two families of collagen fibres; however, it has been adapted to study an extensive range of biological soft tissues, including tendons, and has been implemented in several finite element software packages. To model collagen in tendons, which contain one family of collagen fibres, we use the following transversely isotropic version of the HGO SEF:

$$W(I_1, I_4) = \frac{c_{\mathrm{HGO}}}{2}(I_1 - 3) + \frac{k_1}{2k_2}(\exp(k_2(I_4 - 1)^2) - 1), \tag{12}$$

where c_{HGO} and k_1 are parameters with dimensions of stress and k_2 is a dimensionless model parameter. The engineering stress produced by this SEF (12) is

$$N_{\mathrm{HGO}} = \frac{c_{\mathrm{HGO}}}{2}\left(\lambda - \frac{1}{\lambda^2}\right) + 2k_1\lambda(\lambda^2-1)\exp(k_2(\lambda^2-1)). \tag{13}$$

To test our model against an existing microstructural tendon model, we used the following SEF [22]:

$$W(I_1,I_4) = (1-\phi)\mu\,(I_1-3) + \begin{cases} 0, & I_4 < 1, \\ \frac{\phi E}{6\sin^2\theta_o}\left(4\sqrt{I_4} - 3\log I_4 - \frac{1}{I_4} - 3\right), & 1 \leqslant I_4 \leqslant \frac{1}{\cos^2\theta_o}, \\ \phi E\left(\frac{2(1-\cos^3\theta_o)}{3\sin^2\theta_o}\sqrt{I_4} - \frac{1}{2}\log I_4 - \frac{1}{2} - \frac{\cos^2\theta_o}{\sin^2\theta_o}\log\left(\frac{1}{\cos\theta_o}\right)\right), & I_4 > \frac{1}{\cos^2\theta_o}, \end{cases} \tag{14}$$

where θ_o is the initial crimp angle of the outermost, most-crimped fibrils in the tendon's fascicles. We adapted the SEF by including a shifting parameter, γ, that corresponds to the engineering strain at which the first collagen fibril becomes mechanically active. In (14), this corresponds to replacing λ with $\lambda - \gamma$, that is, replacing $I_4 = \lambda^2$ with $I_4 = (\lambda-\gamma)^2$. The engineering stress for this modified tendon model is

$$N_{\mathrm{tendon}} = (1-\phi)\mu\left(\lambda - \frac{1}{\lambda^2}\right) + \begin{cases} 0, & \lambda < (1+\gamma), \\ \frac{\phi E}{3\sin^2\theta_o}\left(2 - \frac{3}{\lambda-\gamma} - \frac{1}{(\lambda-\gamma)^3}\right), & (1+\gamma) \leqslant \lambda \leqslant (\frac{1}{\cos\theta_o} + \gamma), \\ \phi E\left(\frac{2(1-\cos^3\theta_o)}{3\sin^2\theta_o} - \frac{1}{\lambda-\gamma}\right), & \lambda > (\frac{1}{\cos\theta_o} + \gamma). \end{cases} \tag{15}$$

As ϕ, μ, and E only appear in the SEF (8) in the distinct terms $(1-\phi)\mu$ and ϕE, we treated $(1-\phi)\mu$ and ϕE as two independent fitting parameters. Thus, the ST SEF contains four fitting parameters, $(1-\phi)\mu$, ϕE, a, and b. The GT SEF has an additional fitting parameter, c. In order to obtain physically realistic values for the parameters, we constrained them as follows: for the ST model, $0 < (1-\phi)\mu$, $0 < \phi E$, $1 < a < b$, $a < \lambda_{\max}$, where $\lambda_{\max}$ represents the maximum stretch in the data; for the GT model, we replaced $1 < a < b$ with $1 < a < c < b$; for the HGO model, (12), $0 < c_{\mathrm{HGO}}$, $0 < k_1$, and $0 < k_2$; and for the modified tendon model, $0 \leqslant \gamma < (\lambda_{\max} - 1)$, $0 < \theta_o < \frac{\pi}{2}$, $(1-\phi)\mu > 0$, $\phi E > 0$.

The mean absolute error, Δ, between the experimental data, $\mathbf{y}$, and simulated data, $\hat{\mathbf{y}}$, is

$$\Delta = \frac{1}{d}\sum_{i=1}^{d} |y_i - \hat{y}_i|, \tag{16}$$

where d is the length of the data set. Similarly, the mean relative error, δ, is

$$\delta = \frac{1}{d}\sum_{i=1}^{d} \frac{|y_i - \hat{y}_i|}{|y_i|}. \tag{17}$$

The values of Δ and δ when fitting each model to the four data sets are given in Table 1. Furthermore, the values of the model parameters for the fits are given in Table 2. Both versions of our SEF achieve a closer fit to the data than the microstructural tendon model for each data set. Additionally, they only perform worse than the HGO model for the relative fit to the t6b data set. Additionally, the values of the microstructural parameters in Table 2 are physically reasonable. This highlights that it is possible to find close fits to data with values that lie in the broad region of parameter values given in the literature. Between the ST and GT models, the mean absolute and relative errors for the four data sets are similar, with the former surprisingly outperforming and matching the latter for the t5c and t6b data sets, respectively. This is particularly interesting because the GT model contains an additional degree of freedom. This is likely because non-linear optimisation only provides a local best fit to data and only 1000 iterations of the Nelder-Mead algorithm were performed. Two examples of the fit of our model to the experimental data are presented in Figure 4. The supplementary material shows all sixteen fits.

Finally, the *NonlinearModelFit* algorithm was rerun for the fit of each of the four models to the four data sets. The parameter values, and average relative and absolute errors for each model, obtained from runs with two sets of randomly selected starting values, are given in Table 3. Again, the Nelder-Mead algorithm, with a maximum number of one thousand iterations, was used to fit the models to the data sets. For the ST and GT models, the values given in Table 3 contain some significantly different parameter values to those listed in Table 2. Furthermore, some parameter values found are physically unrealistic, such as 13000 MPa for ϕE or a value of 11.7 for b, and some fits to data are poor. This suggests that in *NonlinearModelFit* our new models are dependent on the initial guesses

Model		t5c	t6b	CDET	SDFT
HGO	δ	0.242	0.169	5.50	1.48
	Δ (MPa)	0.396	0.223	4.59	2.54
Tendon	δ	0.200	0.276	0.0967	0.173
	Δ (MPa)	0.159	0.280	0.290	0.184
ST	δ	0.103	0.178	0.0811	0.149
	Δ (MPa)	0.100	0.173	0.290	0.182
GT	δ	0.110	0.178	0.0725	0.0695
	Δ (MPa)	0.101	0.173	0.290	0.113

Table 1: Mean relative and absolute errors for the four models studied against experimental tendon data. All values are given to three significant figures.

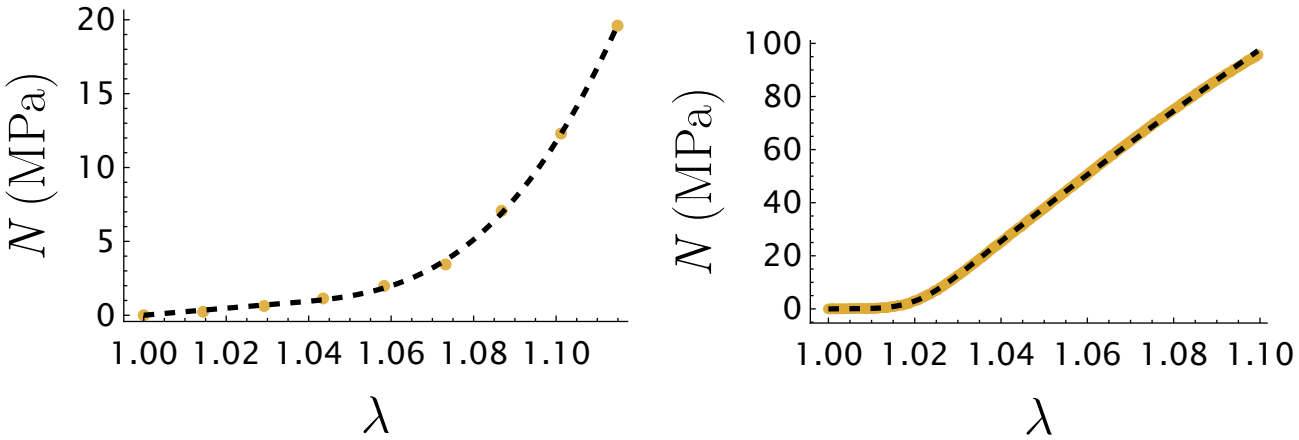

(a) (b)

Figure 4: Fits of (a) the ST model to the t5c data, and (b) the GT model to the CDET data. Yellow dots represent the experimental data and black, dashed lines represent model fits.

to find good fits to data, and it is hard to find a global best fit to data. This could partially explain why the ST model, even with one fewer fit parameter than the GT model, is able to closely match or beat the fit achieved by the GT model in some cases. By contrast, the HGO model seems best equipped to find a global best fit to data in *NonlinearModelFit* even if the model cannot match the best fit of the ST and GT models to some tendon data sets. These results provide some important avenues of research to analyse in the future: is this behaviour of the ST and GT models limited to the Nelder-Mead method of fitting to data in *NonlinearModelFit*? Is it inherently easier to find a global best fit to data via standard optimisation techniques using the HGO model? These results do, however, provide further motivation to use a RWM algorithm to estimate probability distributions for the parameters. By sampling hundreds of thousands of simulations in that algorithm, we are more likely to sample in the area of parameter space that produces a global best fit to data when fitting the ST model, in the case of this paper, to experimental data.

4 Markov chain Monte Carlo (MCMC)

Through non-linear optimisation, we have found the best fit to experimental data local to the algorithm's initial guesses for the parameter values; however, this approach does not quantify the uncertainty in the parameter values. Uncertainties arise for a number of reasons, including observational noise in the experimental stress-strain data. To address this, we apply a Bayesian framework to the same problem studied with the optimisation approach and estimate the likely ranges of the true values of the ST model's parameters. Using the posterior distributions we obtain from the algorithm, we can estimate likely parameter values and quantify the uncertainty in those estimates.

Model		t5c	t6b	CDET	SDFT
HGO	c_{HGO} (MPa)	0	0	0	0
	k_1 (MPa)	6.41	9.67	157	43.9
	k_2	29.6	45.6	8.37	21.7
Tendon	$(1-\phi)\mu$ (MPa)	10.4	17.6	7.69	17.1
	ϕE (MPa)	600	1200	1330	778
	θ	0.330	0.382	0.192	0.254
	γ	0.058	0.0461	0.0115	0.0248
ST	$(1-\phi)\mu$ (MPa)	8.36	14.9	5.31	16.2
	ϕE (MPa)	950	1760	1360	820
	a	1.04	1.03	1.01	1.02
	b	1.16	1.15	1.03	1.07
GT	$(1-\phi)\mu$ (MPa)	8.36	15.1	4.78	12.3
	ϕE (MPa)	931	782	1360	828
	a	1.04	1.03	1.01	1.01
	c	1.10	1.09	1.02	1.06
	b	1.16	1.09	1.03	1.06

Table 2: Parameter values (to three significant figures) for each model's fit to the four data sets. To avoid confusion with c in the GT model, the stress-like parameter for the HGO model is written as c_{HGO}.

4.1 Markov chain Monte Carlo

The goal of Bayesian statistics is, given new data, to update any prior knowledge about the values of a model's parameters via the likelihood of a particular parameter vector $\boldsymbol{\theta}$ (the vector of constitutive and structural parameters in our SEF) producing the observed (experimental) data $\mathbf{y}$. Through this, we obtain what is known as the posterior probability distribution of $\boldsymbol{\theta}$, $\pi(\boldsymbol{\theta}|\mathbf{y})$, which is related to $\pi_0(\boldsymbol{\theta})$, the prior probability of $\boldsymbol{\theta}$, and the likelihood via Bayes' rule:

$$\pi(\boldsymbol{\theta}|\mathbf{y}) \propto L(\mathbf{y}|\boldsymbol{\theta})\pi_0(\boldsymbol{\theta}), \tag{18}$$

where $L(\mathbf{y}|\boldsymbol{\theta})$ denotes a function proportional to the likelihood density. The posterior is only known up to a constant of proportionality, which often cannot be explicitly computed. Under those circumstances, a common method to characterise the posterior distribution is to sample from it using numerical methods such as Markov chain Monte Carlo (MCMC).

Monte Carlo methods can be used to estimate expectations with respect to a particular measure, for example $\pi(\boldsymbol{\theta}|\mathbf{y})$; however, for Bayesian inverse problems, we cannot usually directly sample from the posterior distribution. Instead, we can indirectly sample from the posterior using MCMC methods, which construct an ergodic Markov chain whose unique stationary density is equal to the posterior. Monte Carlo estimates taken with respect to this Markov chain can be shown to converge to expectations taken with respect to the posterior distribution. Initially, Markov chains do not sample from the stationary distribution and values proposed in the MCMC algorithm are dependent on the chains' starting position. This initial period is called the burn-in phase, the size of which depends on the quality of the initial guess, and the rate of mixing of the Markov chain. We do not include samples from the burn-in phase when calculating MCMC estimates, or when visualising the posterior distribution.

4.2 Hierarchical Bayesian approach and conjugate priors

In Section 2.2, we derived a deterministic SEF. Now, in order to derive the likelihood function for this modelling problem, we assume that the observed data is given by the model output perturbed by some noise. We choose the standard modelling assumption that the noise is additive, mean-zero, Gaussian and independently and identically distributed (IID), giving us a diagonal covariance matrix for which the diagonal entries are equal to the observational noise variance σ^2. This gives us the following statistical model for our observations:

$$\mathbf{y} = \mathbf{M}(\boldsymbol{\theta}) + \boldsymbol{\eta}, \qquad \boldsymbol{\eta} \sim \mathcal{N}(\mathbf{0}, \sigma^2\mathbf{I}_d), \tag{19}$$

where d is the length of $\mathbf{y}$, $\mathbf{I}_d$ is a $d \times d$ identity matrix, $\mathcal{N}(\mathbf{0}, \sigma^2\mathbf{I}_d)$ represents a normal distribution with mean $\mathbf{0}$ and covariance matrix $\sigma^2\mathbf{I}_d$, $\mathbf{y} \in \mathbb{R}^d$, and $\mathbf{M}(\boldsymbol{\theta})$ denotes the output of the model given input values $\boldsymbol{\theta}$. From (19),

Model		t5c		t6b		CDET		SDFT	
		1	2	1	2	1	2	1	2
HGO	c_{HGO} (MPa)	0	0	0	0	0	0	0	0
	k_1 (MPa)	6.41	6.41	9.67	9.67	157	157	43.9	43.9
	k_2	29.6	29.6	45.6	45.6	8.37	8.37	21.7	21.7
	δ	0.242	0.242	0.169	0.169	5.50	5.50	1.48	1.48
	Δ (MPa)	0.396	0.396	0.223	0.223	4.59	4.59	2.54	2.54
Tendon	$(1-\phi)\mu$ (MPa)	10.4	13.2	17.6	17.6	97.2	0	0	17.1
	ϕE (MPa)	2060	227	723	5040	9660	1350	7350	778
	θ	0.664	0.145	0.293	0.868	1.57	0.199	1.41	0.254
	γ	0.0580	0.0610	0.0461	0.0461	6.51×10^{-5}	0.0105	0.0108	0.0248
	δ	0.199	0.422	0.276	0.276	3.04	0.140	0.251	0.172
	Δ (MPa)	0.156	1.01	0.280	0.280	3.16	0.301	0.836	0.184
ST	$(1-\phi)\mu$ (MPa)	8.05	8.36	14.8	14.8	9.90	5.32	1.64×10^{-4}	16.2
	ϕE (MPa)	2470	950	2690	4270	1350	1360	879	820
	a	1.03	1.04	1.03	1.03	1.01	1.01	1.01	1.02
	b	1.24	1.08	1.18	1.22	1.03	1.03	1.07	1.07
	δ	0.101	0.110	0.178	0.178	0.138	0.0755	0.237	0.149
	Δ (MPa)	0.103	0.101	0.103	0.103	0.296	0.289	0.308	0.182
GT	$(1-\phi)\mu$ (MPa)	38.2	8.05	49.4	14.8	4.78	312	1.56	12.3
	ϕE (MPa)	13000	4110	6860	5740	1360	83300	864	828
	a	1.11	1.03	1.09	1.03	1.01	1.10	1.00	1.01
	c	6.55	1.14	8.05	1.09	1.02	84.6	1.06	1.06
	b	11.7	1.38	13.4	1.41	1.03	208	1.06	1.06
	δ	2.20	0.101	1.76	0.178	0.0725	8.18	0.157	0.0695
	Δ (MPa)	3.11	0.103	2.91	0.173	0.290	8.06	0.182	0.113

Table 3: Parameter values, and average relative and absolute errors (to three significant figures) for the four models obtained from two additional fits to data. To avoid confusion with c in the GT model, the stress-like parameter for the HGO model is written as c_{HGO}.

we derive the likelihood, which is the probability of the noise $\boldsymbol{\eta}$ accounting for the difference in value between the observed data, $\mathbf{y}$, and the model's prediction:

$$L(\mathbf{y}|\boldsymbol{\theta},\sigma^2) = \frac{1}{(\sigma\sqrt{2\pi})^d}\exp\left(-\frac{1}{2\sigma^2}\|\mathbf{y}-\mathbf{M}(\boldsymbol{\theta})\|_2^2\right). \tag{20}$$

This is sufficient if we have a clear idea of the value of the observational noise variance σ^2, but in practice this is rarely the case. The value of σ^2 can be very important, potentially causing under- or over-fitting. Therefore, we take a hierarchical Bayesian approach and assign a prior distribution to σ^2. *A priori*, we assume that the parameters are independent of one another, so the joint prior distribution is the product of the parameters' individual prior distributions. That is,

$$\pi_0(\boldsymbol{\theta},\sigma^2) = \pi_0(\boldsymbol{\theta})\pi_0(\sigma^2) = \pi_0(\theta_1)\cdots\pi_0(\theta_h)\pi_0(\sigma^2), \tag{21}$$

where h denotes the length of $\boldsymbol{\theta}$. By (18) and (21),

$$\pi(\boldsymbol{\theta},\sigma^2|\mathbf{y}) \propto L(\mathbf{y}|\boldsymbol{\theta},\sigma^2)\pi_0(\theta_1)\cdots\pi_0(\theta_h)\pi_0(\sigma^2). \tag{22}$$

Using a conjugate prior for σ^2, we avoid having to infer σ^2 explicitly by integrating out the dependence of the posterior distribution with respect to σ^2, since this integral can be computed analytically. In this instance, our likelihood function is a Gaussian PDF, so an appropriate conjugate prior for the observational noise variance is an inverse-gamma distribution. After multiplying the likelihood function by the product of prior densities (21), we arrive at the posterior distribution. The posterior predictive can then be derived by integrating out σ^2, giving a Student's t-distribution multiplied by the prior density on the remaining unknowns, giving us the target distribution,

$$\pi(\boldsymbol{\theta}|\mathbf{y}) \propto \mathrm{t}_{2\alpha_\sigma}\left(\mathbf{y};\mathbf{M}(\boldsymbol{\theta}),\frac{\beta_\sigma}{\alpha_\sigma}\mathbf{I}_d\right)\pi_0(\boldsymbol{\theta}), \tag{23}$$

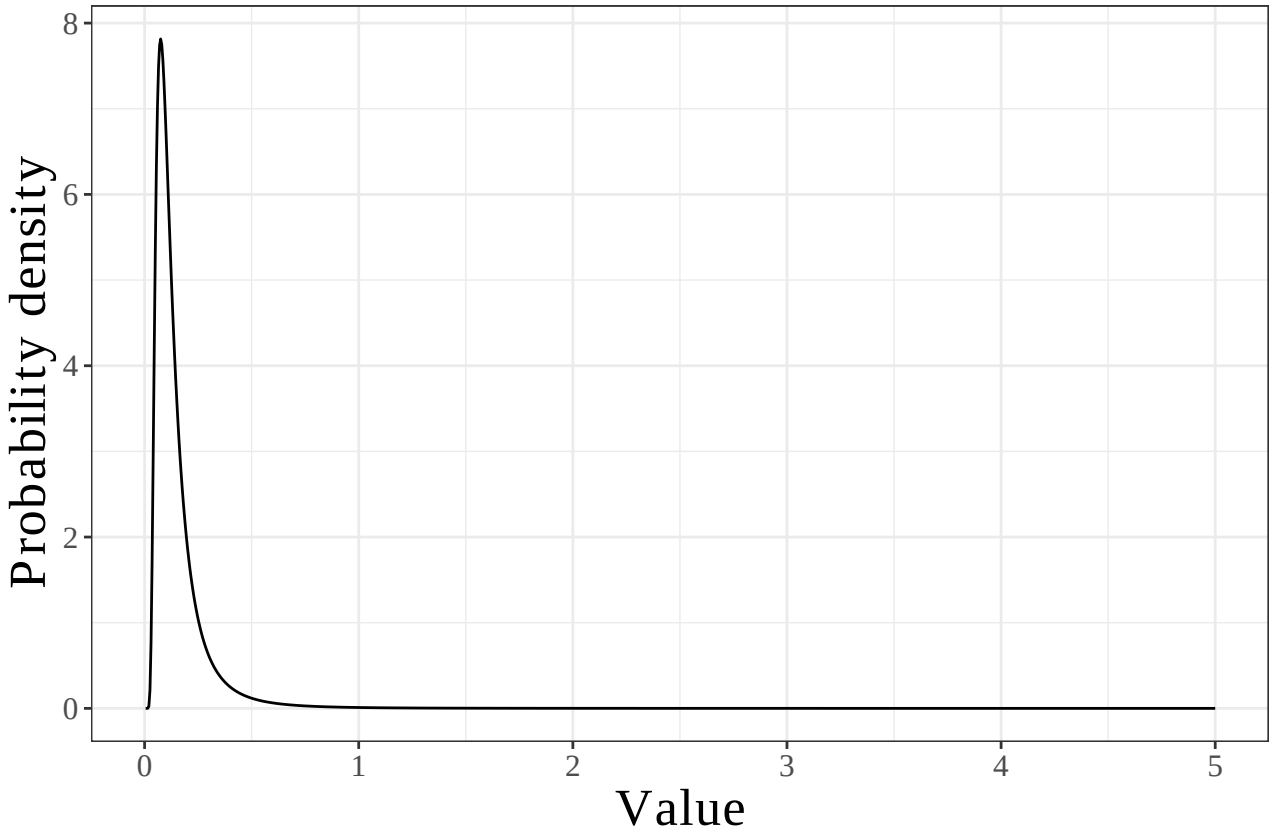

Figure 5: The inverse-gamma prior for σ^2. For this particular distribution, $\alpha_\sigma = 3$ and $\beta_\sigma = 0.3$. The majority of this probability lies between zero and 0.5, that is, at small positive values, which is reasonable for experimental noise.

where we define $t_{2\alpha_\sigma}(*; \boldsymbol{\gamma}, \boldsymbol{\psi})$ as the posterior predictive density of $*$ according to a Student's t-distribution of $2\alpha_\sigma$ degrees of freedom with mean $\boldsymbol{\gamma}$ and covariance matrix $\boldsymbol{\psi}$, and where $\alpha_\sigma, \beta_\sigma > 0$ are parameters of the hyperprior on σ^2. In the sampling discussed in later sections, we set $\alpha_\sigma = 3$ and $\beta_\sigma = 0.3$. These values for the hyperparameters on σ^2 were chosen because the corresponding inverse-gamma prior for σ^2 contained the majority of its probability mass in the area of reasonable values of σ^2, rather than values that are too large for experimental noise. A plot of the inverse-gamma distribution with $\alpha_\sigma = 3$ and $\beta_\sigma = 0.3$ is found in Figure 5. Other values of the hyperparameters could have been chosen. In order to ascertain the effect that changing the hyperparameters would have had on the estimated posteriors of the model parameters, a sensitivity analysis, as has been performed in machine learning and convolutional neural networks, [35], would need to be performed. Furthermore, keeping the values of the hyperparameters constant enabled a given distribution to be sampled from in the RWM algorithm that we derive in this paper. A full derivation of the posterior predictive is provided in the supplementary material.

4.3 Random walk Metropolis algorithm

We cannot integrate (23) analytically and determine the normalisation constant; therefore, we choose to characterise the posterior predictive by sampling from the target distribution using the random walk Metropolis (RWM) algorithm. This method enables us to construct an ergodic Markov chain with invariant density equal to $\pi(\boldsymbol{\theta}|\mathbf{y})$. We can then use the computed Markov chain for Monte Carlo estimates and to visualise the target distribution. Lasting for n simulations and using $\mathcal{U}(0, 1)$ to denote a uniform distribution between zero and one, the RWM algorithm is given in Algorithm 1.

Algorithm 1: RWM

Result: Estimate of the posterior distribution, $\pi(\boldsymbol{\theta})$
Input: $\pi_0(\theta_1)$, ..., $\pi_0(\theta_h)$;
Starting parameter vector, $\boldsymbol{\theta}_0$;
for $i = 1, \ldots, n$ **do**
  Propose $\boldsymbol{\theta}^* \sim \mathcal{N}(\boldsymbol{\theta}_{i-1}, \boldsymbol{\Sigma})$;
  Calculate $\kappa = \min\left(1, \frac{\mathrm{t}_{2\alpha_\sigma}\left(\mathbf{y}; \mathbf{M}(\boldsymbol{\theta}^*), \frac{\beta_\sigma}{\alpha_\sigma}\mathbf{I}_d\right)\pi_0(\boldsymbol{\theta}^*)}{\mathrm{t}_{2\alpha_\sigma}\left(\mathbf{y}; \mathbf{M}(\boldsymbol{\theta}_{i-1}), \frac{\beta_\sigma}{\alpha_\sigma}\mathbf{I}_d\right)\pi_0(\boldsymbol{\theta}_{i-1})}\right)$;
  Generate $u \sim \mathcal{U}(0, 1)$;
  if $u \leqslant \kappa$ **then**
    $\boldsymbol{\theta}_i = \boldsymbol{\theta}^*$;
  else
    $\boldsymbol{\theta}_i = \boldsymbol{\theta}_{i-1}$;
  end
  Set $i = i + 1$;
end

The covariance matrix of the proposal distribution, $\boldsymbol{\Sigma}$, is a parameter that affects the efficiency of RWM algorithms. It controls both the scale of the proposal variance, and also the correlations between coordinates in the sampled vector. Adaptive random walk algorithms allow us to adapt $\boldsymbol{\Sigma}$ in order to optimise the efficiency of the algorithm. In order to address both the scale and correlation of the sample vector, we adapt the covariance matrix to $\boldsymbol{\Sigma} = \beta^2\boldsymbol{\zeta}$, where β^2 is a scaling parameter, with $\beta > 0$, and $\boldsymbol{\zeta} \in \mathbb{R}^{h\times h}$ is the covariance matrix of the model parameters constructed from a chosen set of parameter vectors.

Regarding scale, it has been shown that the optimal acceptance rate for multivariate RWM is 0.234 [36]. For a given value of $\boldsymbol{\zeta}$, the value of β can be tuned in order to achieve an acceptance rate close to this value. Small values of β lead to a proposal density closely concentrated around the current state, which leads to a high acceptance rate but slow exploration. Conversely, large values of β lead to a diffuse proposal density where sampled vectors are likely to be in the tails of the posterior distribution, leading to low acceptance rates and therefore also slow exploration.

Efficient proposal distributions reflect the correlation structures in the target density. For instance, if the probability density is concentrated close to a lower dimensional manifold, then proposal distributions which favour bigger moves in the directions parallel to the manifold will lead to faster exploration than isotropic proposal distributions. We do not know the correlation structure of the target *a priori*, but this can be learned through initial exploration with an isotropic proposal distribution.

In our simulations, we recalculated $\boldsymbol{\Sigma}$ after every block of 500 simulations. To construct $\boldsymbol{\zeta}$, we used the position of the Markov chains over the last 10,000 simulations. To ensure $\boldsymbol{\Sigma}$ was positive definite during the algorithm, we regularised by adding the identity matrix multiplied by a small number, 1×10^{-5}, to $\boldsymbol{\zeta}$ whenever it was recalculated. We let the value of β^2 depend on the acceptance rate within a block, α_{block}. The conditions for updating β^2 at the end of each block were

- $\alpha_{\text{block}} < \alpha_{\text{LowerTol}}$: multiply β^2 by 0.95^2;
- $\alpha_{\text{LowerTol}} \leqslant \alpha_{\text{block}} \leqslant \alpha_{\text{UpperTol}}$: keep β^2 at the same value;
- $\alpha_{\text{UpperTol}} < \alpha_{\text{block}}$: multiply β^2 by 1.05^2,

where α_{LowerTol} and α_{UpperTol} denote the lower and upper bounds of the allowed acceptance rates for the algorithm, which we set equal to 0.184 and 0.284, respectively (0.234 ± 0.05). The tolerances account for the range of acceptance rates for which an RWM algorithm is assumed to run efficiently enough. We must stop iterating the values of β^2 and $\boldsymbol{\zeta}$ at some point in the algorithm, since adaptive MCMC algorithms must satisfy the property of diminishing adaptation in order to maintain ergodicity [37]. We stopped adaptation of $\boldsymbol{\Sigma}$ at the end of the burn-in phase, which consisted of the first 500,000 simulations out of a total of 1.5 million.

5 Application of Bayesian methods to tendon deformation

Before running the RWM algorithm, we transformed the parameters of the ST model so that their support extended over the whole of $\mathbb{R}$. We did this because sampling parameters whose support matches the support of the proposal

distributions improves the efficiency of the algorithm. Each element of the untransformed parameter vector, $\boldsymbol{\psi} = [(1-\phi)\mu, \phi E, a, b]$, is non-negative, and the uncertain parameters a, b must satisfy $a > 1$ and $a < b$. These last two conditions give rise to the natural choice of parameters for inference given by $a - 1 > 0$ and $b - a > 0$. Along with the other non-negative, uncertain parameters, we assigned log-normal priors to ensure well-posedness. Taking the logarithm of these parameters, we obtained the parameter vector $\boldsymbol{\theta} \in \mathbb{R}^4$, where

$$\boldsymbol{\theta} = \begin{pmatrix} \nu \\ \eta \\ \tau \\ \rho \end{pmatrix} = \begin{pmatrix} \log((1-\phi)\mu) \\ \log(\phi E) \\ \log(a-1) \\ \log(b-a) \end{pmatrix} = \mathrm{T}(\boldsymbol{\psi}), \tag{24}$$

where $\mathrm{T}(\boldsymbol{\psi})$ represents an invertible, non-linear transformation of the target parameters $\boldsymbol{\psi}$. This transformation, in turn, leads to a transformation of the likelihood and posterior distributions. When performing RWM on the transformed parameters, $\boldsymbol{\psi}$, the target density is given by the pullback $\tilde{\pi}$ of the posterior $\pi(\boldsymbol{\theta}|Y)$ through the map T, which has density

$$\tilde{\pi}(\boldsymbol{\theta}) = \pi(T^{-1}(\boldsymbol{\theta})|Y).|\det D_{T^{-1}}(\boldsymbol{\theta})|, \tag{25}$$

where $D_{T^{-1}}(\boldsymbol{\theta})$ is the Jacobian of T^{-1}. The value of this additional factor is detailed in the supplementary material. As we assigned a log-normal prior to their exponents, each parameter in $\boldsymbol{\theta}$ has a normal prior distribution. The supplementary material details how the two parameters of the log-normal prior, and, thus, the mean and variance of the corresponding normal prior, were chosen for $(1-\phi)\mu$, ϕE, $a-1$, and $b-a$.

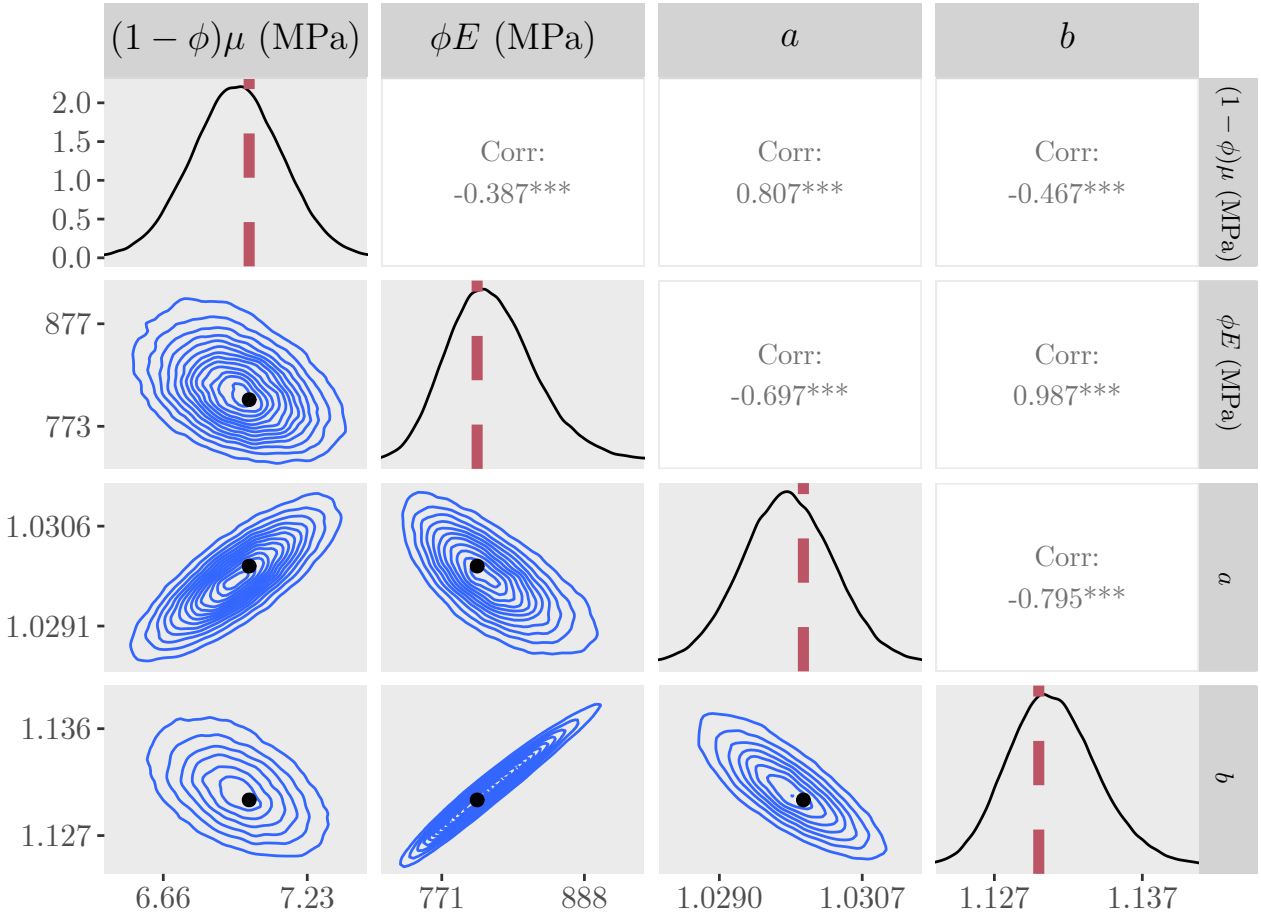

Figure 6: Plots of the posterior distributions calculated using the RWM algorithm on synthetic data. Main diagonal: marginal posteriors. Lower half: two-dimensional contour plots of the joint distributions. Upper half: posterior correlations between parameters. The parameter values used to create the synthetic data are represented by a red line on the posteriors and a black dot on the contour plots. For the correlation values, three asterisks represent $p < 0.001$. In order to create this figure, the 1 million samples were thinned by a factor of ten.

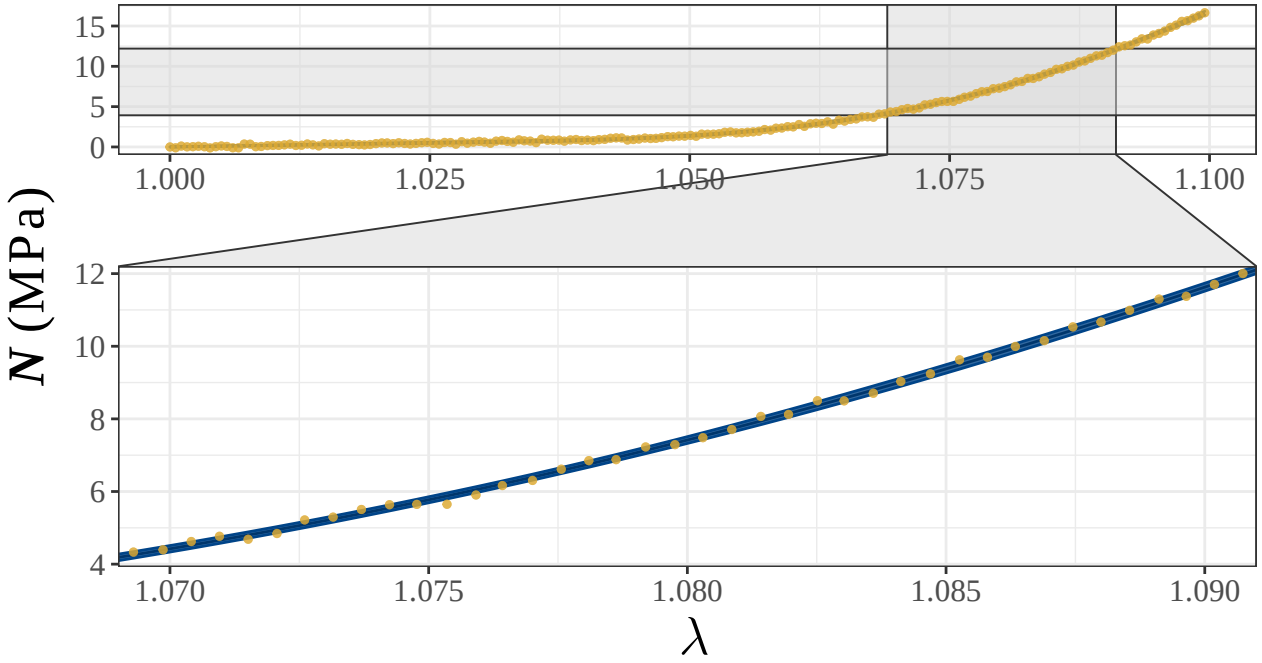

Figure 7: The 5σ confidence band (blue) around the mean of the predicted stresses from 50,000 parameter vectors from the Markov chains against the synthetic data (yellow dots).

5.1 Synthetic data

We ran the algorithm firstly with a synthetic data set created with a chosen parameter vector, and then with the CDET and SDFT data sets. We also ran the algorithm for the data collected by Goh *et al.* The results of fitting to those data sets with the RWM algorithm are discussed in the supplementary material. Fitting to synthetic data acts as a proof-of-concept for our approach, and the implementation of the MCMC methods, that enables us to study the posterior distributions when we know the 'true' parameter values associated with the data. To create the synthetic stress values, we inputted the same set of strains as the SDFT data set and parameters corresponding to $[(1-\phi)\mu, \phi E, a, b] = [7 \text{ MPa}, 800 \text{ MPa}, 1.03, 1.13]$ into the deterministic SEF. In order to replicate experimentally collected data, we added IID noise to the stresses obtained in the model. In order to test the algorithm rigorously, we chose to make the synthetic data noisier than the real data sets by choosing a variance of 0.01 for the IID noise.

The marginal posterior distributions and the two-dimensional joint distributions of the parameters that we obtain when fitting to the synthetic data are shown in Figure 6. Although they do not align exactly with the modes of their respective posteriors, the parameter values used to create the synthetic data are not located in the tails of the posterior, but lie in regions of relatively high posterior probability. The smoothness of the empirical distribution also implies that the algorithm is sampling efficiently.

Figure 7 shows the fit between the synthetic data and a 5σ confidence band around the mean predicted stresses for a sample of 50,000 parameter vectors from the chains. A close fit is achieved in each region of the J-shaped stress-strain curve. This synthetic experiment demonstrates that accurate estimates of the constitutive parameters, and representations of the uncertainty inherent in those estimates, can be derived through a Bayesian framework, and characterised using our tuned adaptive RWM algorithm.

5.2 SDFT and CDET data

We now analyse the algorithm's predictions when we fit the ST model to the high-resolution tendon data collected by Screen *et al.* For the SDFT data, Figure 8 contains the estimated posteriors and contour plots obtained from the adaptive RWM algorithm and Figure 9 shows a confidence band of 5σ around the mean stress-strain curve of 50,000 parameter vectors from the chains plotted against the data. As in the synthetic example, the empirical posterior distribution is smooth, implying a good level of convergence of the tuned adaptive RWM algorithm. For the structural parameter ϕE, we have a physically realistic posterior: the 95% credible interval for ϕE is 814-827 MPa, rounded to the nearest whole number, which is feasible compared to literature values for ϕ and E in tendon, [14]. The stretches at which the first and last collagen fibrils straighten and tauten are also realistic. There

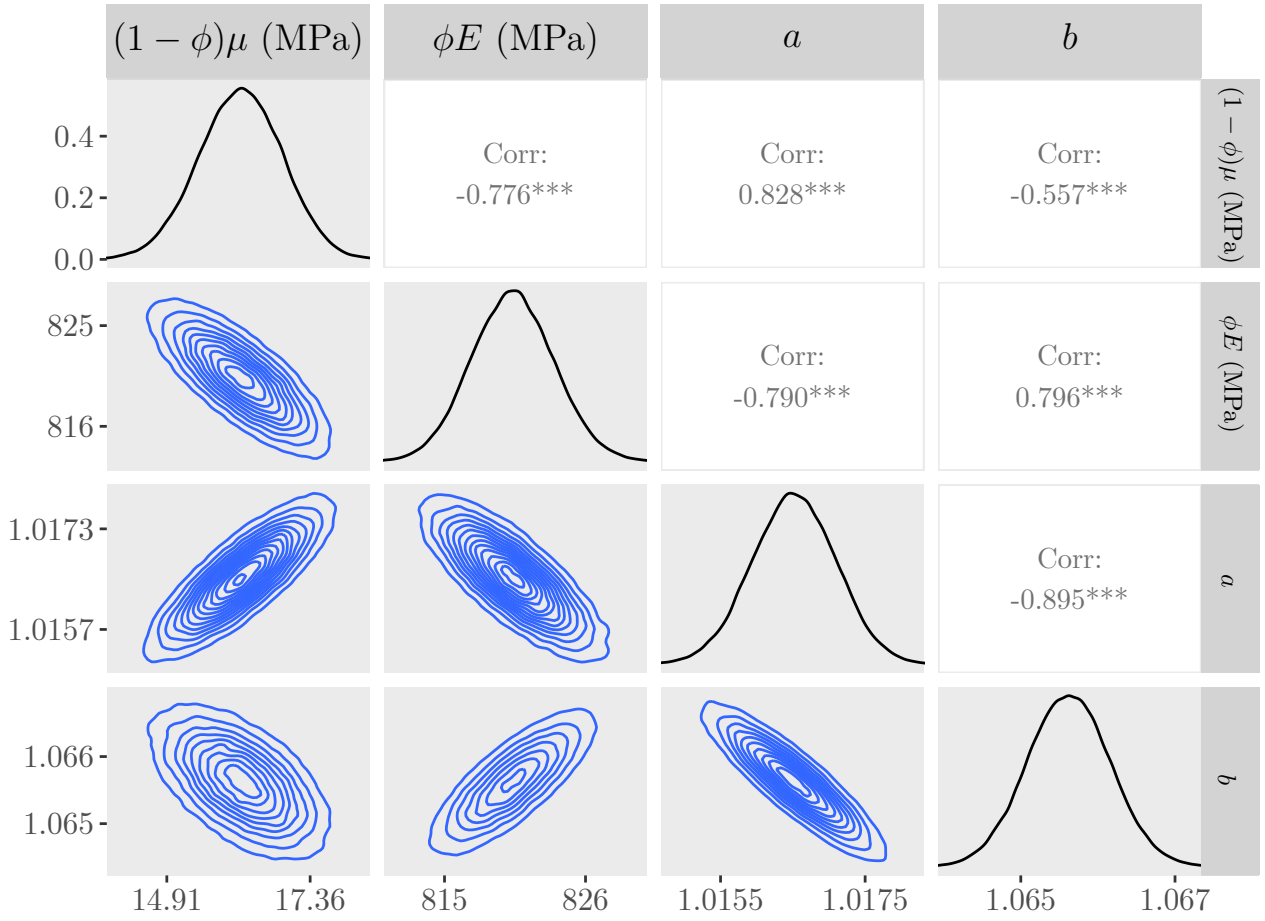

Figure 8: Approximate posteriors and contour plots of the parameters for the SDFT data. Samples were thinned by a factor of ten.

are parameters with large positive correlations: $(1-\phi)\mu$ and a, and ϕE and b. These indicate that to replicate the experimental data closely, the NCM must be stiffer if collagen fibrils are slack for longer, and fibrils must be stiffer if fewer are mechanically active. Likewise, large negative correlations between a and b and $(1-\phi)\mu$ and ϕE indicate that all fibrils must be taut sooner if they are all slack for longer, and the fibrils must be stiffer if the NCM is more compliant. These are all physically reasonable conclusions, demonstrating the benefit of full posterior characterisation as opposed to the more traditional optimisation approach.

Figure 9 demonstrates that the model can fit the SDFT data closely and that the algorithm, through the posterior distributions, identifies parameter vectors that produce these close fits. For all stretches, the experimental data lies close to the posterior mean stress, and either within or close to the 5σ confidence band that is narrower than for the noisier synthetic data. Again, the confidence band is consistently sized, demonstrating the model's ability to quantify how different microstructural components and phenomena (the NCM and the gradual tautening of collagen fibrils) influence the macroscopic mechanical response of the tendon. As the strain nears 10%, however, the model's predicted stresses are slightly higher than the experimental data, indicating a degree of discrepancy between the model and data. This could be due to damage to some fibrils as the stretch nears 10% strain, contradicting an assumption of the model. To achieve the best fit to the data overall, while retaining the linearity of the model, some underestimates of the experimental stress occur at smaller stretches to compensate for the overestimates of the experimentally observed stress as the strain approaches 10%.

For the CDET data, the parameter $(1-\phi)\mu$ possesses a high predicted posterior probability mass very close to zero (see Figure 10), with a long tail as the value of $(1-\phi)\mu$ increases. Due to the extremely large negative correlation between $(1-\phi)\mu$ and ϕE, the shape of the marginal distribution for ϕE is also affected. The shape of the posterior for $(1-\phi)\mu$ likely occurs because few data points lie in the toe region, with the proposed values of a lying close to one, meaning that the stiff collagen fibrils dominate the response to the deformation even at small stretches. As the density lies close to zero for one of the parameters, taking the logarithm of the posterior

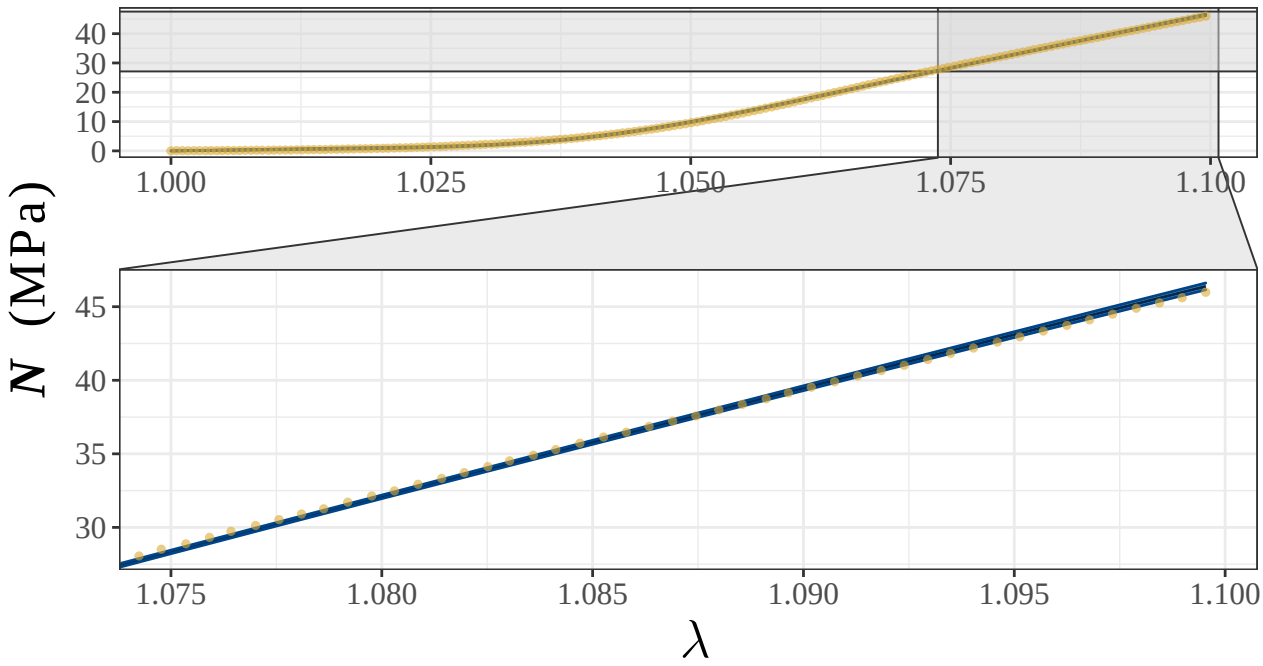

Figure 9: The 5σ confidence band (blue) around the mean of the predicted stresses from 50,000 parameter vectors from the Markov chains against the SDFT data (yellow dots).

results in a curved posterior, whose global covariance structure is less informative for making effective proposals. Therefore, in order to obtain smoother estimated posteriors, 10 million samples were taken, again after a burn-in phase of 500,000 simulations. An alternative approach would be to use more sophisticated methods, such as the Metropolis-Adjusted Langevin algorithm or Hamiltonian Monte Carlo [38]. The posteriors for a and b are smooth, implying a good level of convergence to the posterior distributions. Furthermore, close fits to the data from the sampled parameters are still achieved (see Figure 11). With a 95% credible interval of 1342-1380 MPa, we obtain physically reasonable estimates of ϕE from the algorithm [14].

6 Discussion

In this paper, we developed a tractable model of soft tissue mechanical behaviour that only contains microstructurally relevant parameters. When fitted to experimental murine and equine tendon data using non-linear optimisation, our SEF provides a closer fit than a microstructural tendon model to all four data sets studied and a closer fit than the HGO model to three out of the four data sets, only narrowly providing a worse relative fit to the t6b data set. However, more work needs to be done to ascertain what parameter vectors we obtain from fitting the ST and GT models to experimental data in standard non-linear optimisation. In particular, work needs to be done to determine whether an optimisation algorithm is able to converge on a particular set of parameter vectors for when the GT and ST models are fit to. We also implemented an adaptive RWM algorithm to characterise posterior probability distributions to quantify the uncertainty in the values of the fitting parameters. This algorithm samples effectively when fitting to both synthetic data and high-resolution experimental data. Furthermore, it samples parameter vectors that provide a close fit to the data, with the 95% credible intervals for the important physical parameter ϕE containing realistic values when compared with existing estimates of the parameters ϕ and E.

As the model is pseudoelastic, the Young's and shear moduli predicted by our model are specific to the strain-rates used in the experiments we fitted. The effective moduli would increase with increasing strain-rate. Our findings suggest that ϕE differs from sample to sample. Consequently, either the collagen volume fraction varies between the samples we fitted, or there may not be a universal collagen fibril Young's modulus. In particular, it may be wrong to assign a Young's modulus to collagen on the fibrillar level, as molecular differences may cause some fibrils to be stiffer than others. If so, our model would need to be modified to allow for variation in the constitutive, as well as the structural, parameters. The Bayesian approach assumes that our model is 'correct' in the sense that it incorporates all of the physics necessary to predict the microstructural and constitutive parameters accurately.

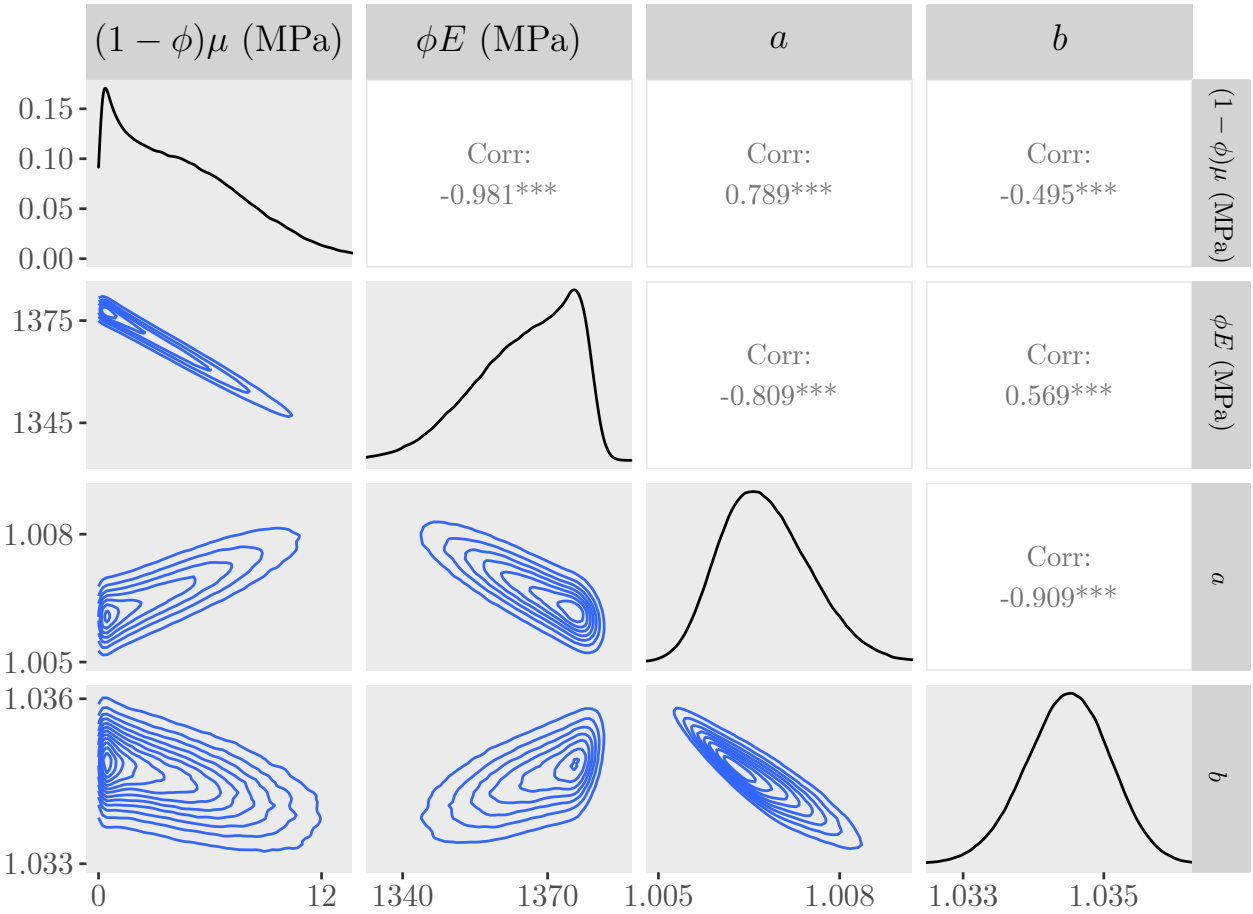

Figure 10: Approximate posteriors and contour plots of the parameters for the CDET data. Samples were thinned by a factor of ten.

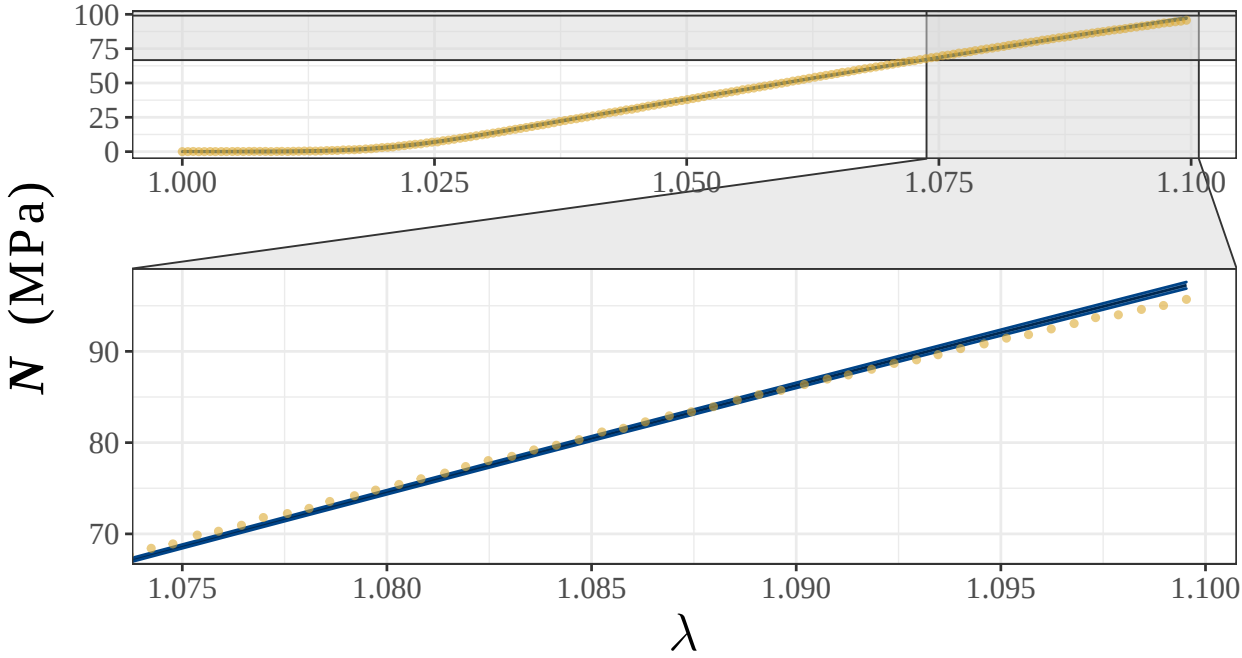

Figure 11: The 5σ confidence band (blue) around the mean of the predicted stresses from 50,000 parameter vectors from the Markov chains against the CDET data (yellow dots).

If a significant feature is absent in the model, this would lead to inaccuracies in the predicted parameter values; however, the quality of fit our model demonstrates and the agreement of the predicated parameter values with experimental values reported in the literature provide confidence that it does indeed include all of the necessary physical features.

So far, we have used the triangular distribution to model the distribution of collagen fibril lengths in tendon. Other tractable SEFs could be derived by modelling fibril lengths with alternative distributions, such as the step distribution, for example, which would also lead to a convenient analytic representation. Additionally, more-efficient sampling methods, such as Hamiltonian Monte Carlo, which uses derivatives of the log-posterior with respect to model parameters to propose parameter vectors in areas of high posterior probability, could be used instead. We have studied tendons, which possess a more regulated collagen structure than in tissues such as skin, where fibrils are generally splayed. By applying our model, and the Bayesian approach used here, to deformations of other soft tissues, we could quantify uncertainty in a broader range of scenarios. A plausible test of the aforementioned 'correctness' of the model and its assumptions would be to fit multiple data sets simultaneously, enforcing the constitutive parameters to be the same between the data sets and varying the structural parameters only. The estimated posterior probability distributions could quantify the inter-sample variation in the constitutive parameters within a particular tissue in any given species.

7 Acknowledgements

JH is grateful to the Department of Mathematics, University of Manchester for PhD funding. SLC is grateful to the Alan Turing Institute for a Turing fellowship. Parnell is grateful to the Engineering and Physical Sciences Research Council (EPSRC) for funding via grant EP/S019804/1.

A The piecewise constants $A(I_4)$, $B(I_4)$, $C(I_4)$, $D(I_4)$ and $G(I_4)$

The values of the piecewise constants for the general triangular distribution are

$$A(I_4) = \begin{cases} 0, & I_4 < a^2, \\ -\frac{a^2}{(b-a)(c-a)}, & a^2 \leqslant I_4 \leqslant c^2, \\ \frac{c^2}{(c-a)(b-c)} - \frac{a^2}{(b-a)(c-a)}, & c^2 < I_4 \leqslant b^2, \\ -1, & I_4 > b^2, \end{cases} \tag{26}$$

$$B(I_4) = \begin{cases} 0, & I_4 < a^2, \\ \frac{2a\log a}{(b-a)(c-a)}, & a^2 \leqslant I_4 \leqslant c^2, \\ \frac{2a\log a}{(b-a)(c-a)} - \frac{2c\log c}{(c-a)(b-c)}, & c^2 < I_4 \leqslant b^2, \\ \frac{2a\log a}{(b-a)(c-a)} + \frac{2b\log b}{(b-a)(b-c)} - \frac{2c\log c}{(c-a)(b-c)}, & I_4 > b^2, \end{cases} \tag{27}$$

$$C(I_4) = \begin{cases} 0, & I_4 < a^2, \\ \frac{1}{(b-a)(c-a)}, & a^2 \leqslant I_4 \leqslant c^2, \\ -\frac{1}{(b-a)(b-c)}, & c^2 < I_4 \leqslant b^2, \\ 0, & I_4 > b^2, \end{cases} \tag{28}$$

$$D(I_4) = \begin{cases} 0, & I_4 < a^2, \\ -\frac{2a}{(b-a)(c-a)}, & a^2 \leqslant I_4 \leqslant c^2, \\ \frac{2b}{(b-a)(b-c)}, & c^2 < I_4 \leqslant b^2, \\ 0, & I_4 > b^2, \end{cases} \tag{29}$$

$$G(I_4) = \begin{cases} 0, & I_4 < a^2, \\ \frac{a^2\log a}{(b-a)(c-a)} - \frac{5a^2}{2(b-a)(c-a)}, & a^2 \leqslant I_4 \leqslant c^2, \\ \frac{2a^2\log a}{(b-a)(c-a)} - \frac{c^2\log c}{(c-a)(b-c)} - \frac{5a^2}{2(b-a)(c-a)} + \frac{5c^2}{2(b-c)(c-a)}, & c^2 \leqslant I_4 \leqslant b^2, \\ \frac{a^2\log a}{(b-a)(c-a)} - \frac{c^2\log c}{(c-a)(b-c)} + \frac{b^2\log b}{(b-c)(b-a)} - \frac{5a^2}{2(b-a)(c-a)} + \frac{5c^2}{2(b-c)(c-a)} - \frac{5b^2}{2(b-a)(c-a)}, & I_4 > b^2. \end{cases} \tag{30}$$

The corresponding quantities for the symmetric triangular distribution are obtained by setting $c = (a+b)/2$.

References

[1] R. James, G. Kesturu, G. Balian, and A. B. Chhabra, "Tendon: Biology, biomechanics, repair, growth factors, and evolving treatment options," *The Journal of hand surgery*, vol. 33, no. 1, pp. 102–112, 2008.

[2] L. Geris, T. Lambrechts, A. Carlier, and I. Papantoniou, "The future is digital: In silico tissue engineering," *Current Opinion in Biomedical Engineering*, vol. 6, pp. 92–98, 2018.

[3] N. Famaey and J. V. Sloten, "Soft tissue modelling for applications in virtual surgery and surgical robotics," *Computer methods in biomechanics and biomedical engineering*, vol. 11, no. 4, pp. 351–366, 2008.

[4] M. Franchi, M. Fini, M. Quaranta, *et al.*, "Crimp morphology in relaxed and stretched rat achilles tendon," *Journal of anatomy*, vol. 210, no. 1, pp. 1–7, 2007.

[5] K. M. Hamdia, M. Marino, X. Zhuang, P. Wriggers, and T. Rabczuk, "Sensitivity analysis for the mechanics of tendons and ligaments: Investigation on the effects of collagen structural properties via a multiscale modeling approach," *International journal for numerical methods in biomedical engineering*, vol. 35, no. 8, e3209, 2019.

[6] Y. Fung, "On pseudo-elasticity of living tissues," in *Mechanics today*, Elsevier, 1980, pp. 49–66.

[7] T. Starborg, N. S. Kalson, Y. Lu, *et al.*, "Using transmission electron microscopy and 3view to determine collagen fibril size and three-dimensional organization," *Nature protocols*, vol. 8, no. 7, pp. 1433–1448, 2013.

[8] J. Chang, R. Garva, A. Pickard, *et al.*, "Circadian control of the secretory pathway maintains collagen homeostasis," *Nature cell biology*, vol. 22, no. 1, pp. 74–86, 2020.

[9] T. Shearer, S. Rawson, S. J. Castro, *et al.*, "X-ray computed tomography of the anterior cruciate ligament and patellar tendon," *Muscles, ligaments and tendons journal*, vol. 4, no. 2, p. 238, 2014.

[10] T. Shearer, R. S. Bradley, L. A. Hidalgo-Bastida, M. J. Sherratt, and S. H. Cartmell, "Three-dimensional visualisation of soft biological structures by x-ray computed micro-tomography," *Journal of cell science*, vol. 129, no. 13, pp. 2483–2492, 2016.

[11] R. Balint, T. Lowe, and T. Shearer, "Optimal contrast agent staining of ligaments and tendons for x-ray computed tomography," *PloS one*, vol. 11, no. 4, e0153552, 2016.

[12] S. D. Rawson, T. Shearer, T. Lowe, *et al.*, "Four-dimensional imaging of soft tissue and implanted biomaterial mechanics: A barbed suture case study for tendon repair," *ACS applied materials & interfaces*, vol. 10, no. 45, pp. 38 681–38 691, 2018.

[13] J. S. Graham, A. N. Vomund, C. L. Phillips, and M. Grandbois, "Structural changes in human type i collagen fibrils investigated by force spectroscopy," *Experimental cell research*, vol. 299, no. 2, pp. 335–342, 2004.

[14] R. B. Svensson, P. Hansen, T. Hassenkam, *et al.*, "Mechanical properties of human patellar tendon at the hierarchical levels of tendon and fibril," *Journal of Applied Physiology*, vol. 112, no. 3, pp. 419–426, 2012.

[15] C. T. Thorpe, C. P. Udeze, H. L. Birch, P. D. Clegg, and H. R. Screen, "Specialization of tendon mechanical properties results from interfascicular differences," *Journal of the Royal Society Interface*, vol. 9, no. 76, pp. 3108–3117, 2012.

[16] T. Shearer, C. T. Thorpe, and H. R. Screen, "The relative compliance of energy-storing tendons may be due to the helical fibril arrangement of their fascicles," *Journal of the Royal Society Interface*, vol. 14, no. 133, p. 20 170 261, 2017.

[17] P. Kannus, "Structure of the tendon connective tissue," *Scandinavian journal of medicine & science in sports*, vol. 10, no. 6, pp. 312–320, 2000.

[18] C. K. Revell, O. E. Jensen, T. Shearer, Y. Lu, D. F. Holmes, and K. E. Kadler, "Collagen fibril assembly: New approaches to unanswered questions," *Matrix Biology Plus*, vol. 12, p. 100 079, 2021.

[19] G. A. Holzapfel, T. C. Gasser, and R. W. Ogden, "A new constitutive framework for arterial wall mechanics and a comparative study of material models," in *Cardiovascular soft tissue mechanics*, Springer, 2001, pp. 1–48.

[20] A. R. Akintunde and K. S. Miller, "Evaluation of microstructurally motivated constitutive models to describe age-dependent tendon healing," *Biomechanics and modeling in mechanobiology*, vol. 17, no. 3, pp. 793–814, 2018.

[21] A. D. Freed and K. Rajagopal, "A promising approach for modeling biological fibers," *Acta Mechanica*, vol. 227, no. 6, pp. 1609–1619, 2016.

[22] T. Shearer, "A new strain energy function for the hyperelastic modelling of ligaments and tendons based on fascicle microstructure," *Journal of biomechanics*, vol. 48, no. 2, pp. 290–297, 2015.

[23] ——, "A new strain energy function for modelling ligaments and tendons whose fascicles have a helical arrangement of fibrils," *Journal of biomechanics*, vol. 48, no. 12, pp. 3017–3025, 2015.

[24] T. Shearer, W. J. Parnell, B. Lynch, H. R. Screen, and I. David Abrahams, "A recruitment model of tendon viscoelasticity that incorporates fibril creep and explains strain-dependent relaxation," *Journal of Biomechanical Engineering*, vol. 142, no. 7, p. 071 003, 2020.

[25] J. Gregory, A. L. Hazel, and T. Shearer, "A microstructural model of tendon failure," *Journal of the mechanical behavior of biomedical materials*, vol. 122, p. 104 665, 2021.

[26] C. Hurschler, B. Loitz-Ramage, and R. Vanderby Jr, "A structurally based stress-stretch relationship for tendon and ligament," *Journal of Biomechanical Engineering*, vol. 119, no. 4, pp. 392–399, 1997, ISSN: 0148-0731. DOI: 10.1115/1.2798284. eprint: https://asmedigitalcollection.asme.org/biomechanical/article-pdf/119/4/392/5766812/392_1.pdf. [Online]. Available: https://doi.org/10.1115/1.2798284.

[27] P. Watton, N. Hill, and M. Heil, "A mathematical model for the growth of the abdominal aortic aneurysm," *Biomechanics and modeling in mechanobiology*, vol. 3, no. 2, pp. 98–113, 2004.

[28] P. Aparıcio, M. S. Thompson, and P. N. Watton, "A novel chemo-mechano-biological model of arterial tissue growth and remodelling," *Journal of biomechanics*, vol. 49, no. 12, pp. 2321–2330, 2016.

[29] M. S. Thompson, M. N. Bajuri, H. Khayyeri, and H. Isaksson, "Mechanobiological modelling of tendons: Review and future opportunities," *Proceedings of the Institution of Mechanical Engineers, Part H: Journal of Engineering in Medicine*, vol. 231, no. 5, pp. 369–377, 2017.

[30] G. A. Holzapfel, *Nonlinear solid mechanics : a continuum approach for engineering*, eng. Chichester: Wiley, 2000, ISBN: 047182304X.

[31] J. Kastelic, I. Palley, and E. Baer, "A structural mechanical model for tendon crimping," *Journal of biomechanics*, vol. 13, no. 10, pp. 887–893, 1980.

[32] F. Gao and L. Han, "Implementing the nelder-mead simplex algorithm with adaptive parameters," *Computational Optimization and Applications*, vol. 51, no. 1, pp. 259–277, 2012.

[33] K. L. Goh, D. F. Holmes, H.-Y. Lu, *et al.*, "Ageing Changes in the Tensile Properties of Tendons: Influence of Collagen Fibril Volume Fraction," *Journal of Biomechanical Engineering*, vol. 130, no. 2, Mar. 2008, 021011, ISSN: 0148-0731. DOI: 10.1115/1.2898732. eprint: https://asmedigitalcollection.asme.org/biomechanical/article-pdf/130/2/021011/5489672/021011_1.pdf. [Online]. Available: https://doi.org/10.1115/1.2898732.

[34] K. L. Goh, D. Holmes, Y. Lu, *et al.*, "Bimodal collagen fibril diameter distributions direct age-related variations in tendon resilience and resistance to rupture," *Journal of applied physiology*, vol. 113, no. 6, pp. 878–888, 2012.

[35] R. Taylor, V. Ojha, I. Martino, and G. Nicosia, "Sensitivity analysis for deep learning: Ranking hyper-parameter influence," in *2021 IEEE 33rd International Conference on Tools with Artificial Intelligence (ICTAI)*, 2021, pp. 512–516. DOI: 10.1109/ICTAI52525.2021.00083.

[36] G. O. Roberts and J. S. Rosenthal, "Optimal scaling for various metropolis-hastings algorithms," *Statistical science*, vol. 16, no. 4, pp. 351–367, 2001.

[37] ——, "Coupling and ergodicity of adaptive markov chain monte carlo algorithms," *Journal of applied probability*, vol. 44, no. 2, pp. 458–475, 2007.

[38] M. Girolami and B. Calderhead, "Riemann manifold langevin and hamiltonian monte carlo methods," *Journal of the Royal Statistical Society: Series B (Statistical Methodology)*, vol. 73, no. 2, pp. 123–214, 2011. DOI: https://doi.org/10.1111/j.1467-9868.2010.00765.x. eprint: https://rss.onlinelibrary.wiley.com/doi/pdf/10.1111/j.1467-9868.2010.00765.x. [Online]. Available: https://rss.onlinelibrary.wiley.com/doi/abs/10.1111/j.1467-9868.2010.00765.x.

Bayesian inference on a microstructural, hyperelastic model of tendon deformation: Supplementary material

1 SEF derivation

For the reasons stated in the main paper, we assume that the SEF, $W(I_1, I_4)$, is given by

$$W(I_1, I_4) = (1-\phi)W_{\text{NCM}}(I_1) + \phi W_{\text{coll}}(I_4), \tag{1}$$

where ϕ is the collagen volume fraction, $W_{\text{NCM}}(I_1)$ and $W_{\text{coll}}(I_4)$ denote the contributions to the SEF from the non-collagenous matrix (NCM) and collagen fibrils, respectively, I_1 is a strain invariant, and I_4 is the square of the stretch in the direction of the collagen fibrils. As an individual fibril is slack when crimped and obeys Hooke's law when it is taut, the non-dimensional stretch experienced by a fibril, λ_{fib}, in terms of the recruitment stretch, λ_r, at a macroscale stretch λ is

$$\lambda_{\text{fib}}(\lambda, \lambda_r) = \begin{cases} 1, & \lambda < \lambda_r, \\ \frac{\lambda}{\lambda_r}, & \lambda \geqslant \lambda_r. \end{cases} \tag{2}$$

By (2) and the assumptions of the model, the stress in a fibril, $\sigma_{\text{fib}}(\lambda, \lambda_r)$, is

$$\sigma_{\text{fib}}(\lambda, \lambda_r) = Ee_{\text{fib}} = \begin{cases} 0, & \lambda < \lambda_r, \\ E\frac{(\lambda-\lambda_r)}{\lambda_r}, & \lambda \geqslant \lambda_r, \end{cases} \tag{3}$$

where E is the Young's modulus of the fibril and $e_{\text{fib}} = \lambda_{\text{fib}} - 1$ is the engineering strain experienced by the fibril. In order to calculate the total stress acting on the collagen fibrils, we must assign a distribution function to model the different recruitment stretches amongst the collagen fibrils. Consequently, $\sigma_F(\lambda)$, the total stress acting on the fibrils, is

$$\sigma_F(\lambda) = \int_0^{\lambda} \sigma_{\text{fib}}(\lambda, \lambda_r) f(\lambda_r) \mathrm{d}\lambda_r, \tag{4}$$

where $f(\lambda_r)$ denotes the recruitment-stretch distribution function.

1.1 General triangular distribution

The probability density function (PDF) for the general triangular distribution is given by

$$f(\lambda_r) = \begin{cases} 0, & \lambda_r < a, \\ \frac{2(\lambda_r - a)}{(b-a)(c-a)}, & a \leqslant \lambda_r \leqslant c, \\ \frac{2(b-\lambda_r)}{(b-a)(b-c)}, & c < \lambda_r \leqslant b, \\ 0, & \lambda_r > b, \end{cases} \tag{5}$$

where a, b, and c are the minimal, maximal, and modal recruitment stretches, respectively. Substituting (3) and (5) into (4), gives

$$\sigma_F(\lambda) = E(A(\lambda) + B(\lambda)\lambda + C(\lambda)\lambda^2 + D(\lambda)\lambda \log \lambda), \tag{6}$$

where $A(\lambda)$, $B(\lambda)$, $C(\lambda)$, and $D(\lambda)$ are piecewise constants that possess the same boundaries as $f(\lambda_r)$ in (5). As the stretch in the direction of the fibrils is λ, then $I_4 = \lambda^2$. Rewriting (6) in terms of I_4, we obtain

$$\sigma_F(I_4) = E\left(A(I_4) + B(I_4)\sqrt{I_4} + C(I_4)I_4 + \frac{D(I_4)}{2}\sqrt{I_4}\log I_4\right), \tag{7}$$

where

$$A(I_4) = \begin{cases} 0, & I_4 < a^2, \\ -\frac{a^2}{(b-a)(c-a)}, & a^2 \leqslant I_4 \leqslant c^2, \\ \frac{c^2}{(c-a)(b-c)} - \frac{a^2}{(b-a)(c-a)}, & c^2 < I_4 \leqslant b^2, \\ -1, & I_4 > b^2, \end{cases} \tag{8}$$

$$B(I_4) = \begin{cases} 0, & I_4 < a^2, \\ \frac{2a\log a}{(b-a)(c-a)}, & a^2 \leqslant I_4 \leqslant c^2, \\ \frac{2a\log a}{(b-a)(c-a)} - \frac{2c\log c}{(c-a)(b-c)}, & c^2 < I_4 \leqslant b^2, \\ \frac{2a\log a}{(b-a)(c-a)} + \frac{2b\log b}{(b-a)(b-c)} - \frac{2c\log c}{(c-a)(b-c)}, & I_4 > b^2, \end{cases} \tag{9}$$

$$C(I_4) = \begin{cases} 0, & I_4 < a^2, \\ \frac{1}{(b-a)(c-a)}, & a^2 \leqslant I_4 \leqslant c^2, \\ -\frac{1}{(b-a)(b-c)}, & c^2 < I_4 \leqslant b^2, \\ 0, & I_4 > b^2, \end{cases} \tag{10}$$

$$D(I_4) = \begin{cases} 0, & I_4 < a^2, \\ -\frac{2a}{(b-a)(c-a)}, & a^2 \leqslant I_4 \leqslant c^2, \\ \frac{2b}{(b-a)(b-c)}, & c^2 < I_4 \leqslant b^2, \\ 0, & I_4 > b^2. \end{cases} \tag{11}$$

From the main paper, in terms of $W(I_1, I_4)$, the Cauchy stress, $\boldsymbol{\sigma}$, is

$$\boldsymbol{\sigma} = -p\mathbf{I} + 2\frac{\partial W}{\partial I_1}\mathbf{B} + 2\frac{\partial W}{\partial I_4}\mathbf{m} \otimes \mathbf{m}, \tag{12}$$

where p is a Lagrange multiplier that accounts for the loss of a degree of freedom that is caused by the assumption of incompressibility, $\mathbf{B}$ is the left Cauchy-Green deformation tensor, and $\mathbf{m}$ is the deformed orientation of the collagen fibrils. By (1) and (12), the fibril contribution to the Cauchy stress, $\boldsymbol{\sigma}_{\text{coll}}$, is

$$\boldsymbol{\sigma}_{\text{coll}} = 2\frac{\partial W_{\text{coll}}(I_4)}{\partial I_4}\mathbf{m} \otimes \mathbf{m}. \tag{13}$$

We can rewrite the right side of (13) in terms of I_4 using the method outlined in [1]. First, we calculate the traction, $\mathbf{t}_{\text{coll}}$, associated with the contribution to the stress from the collagen fibrils that acts on a face normal to the fibrils. Then we calculate the component of $\mathbf{t}_{\text{coll}}$ that acts in the direction of the fibrils. We find

$$\left(\boldsymbol{\sigma}_{\text{coll}} \cdot \left(\frac{\mathbf{m}}{|\mathbf{m}|}\right)\right) \cdot \frac{\mathbf{m}}{|\mathbf{m}|} = \frac{\mathbf{t}_{\text{coll}} \cdot \mathbf{m}}{|\mathbf{m}|} = \left(2\frac{\partial W_{\text{coll}}(I_4)}{\partial I_4}|\mathbf{m}|\mathbf{m}\right) \cdot \frac{\mathbf{m}}{|\mathbf{m}|} = 2I_4\frac{\partial W_{\text{coll}}(I_4)}{\partial I_4}. \tag{14}$$

By (7) and (14),

$$2I_4\frac{\partial W_{\text{coll}}(I_4)}{\partial I_4} = E\left(A(I_4) + B(I_4)\sqrt{I_4} + C(I_4)I_4 + \frac{D(I_4)}{2}\sqrt{I_4}\log I_4\right). \tag{15}$$

Consequently,

$$W_{\text{coll}}(I_4) = E\left(\frac{A(I_4)}{2}\log I_4 + (B(I_4) - D(I_4))\sqrt{I_4} + \frac{C(I_4)}{2}I_4 + \frac{D(I_4)}{2}\sqrt{I_4}\log I_4 + G(I_4)\right), \tag{16}$$

where $G(I_4)$ ensures the continuity of $W_{\text{coll}}(I_4)$ across each boundary of $A(I_4)$—$D(I_4)$, and is equal to

$$G(I_4) = \begin{cases} 0, & I_4 < a^2, \\ \frac{a^2\log a}{(b-a)(c-a)} - \frac{5a^2}{2(b-a)(c-a)}, & a^2 \leqslant I_4 \leqslant c^2, \\ \frac{a^2\log a}{(b-a)(c-a)} - \frac{c^2\log c}{(c-a)(b-c)} - \frac{5a^2}{2(b-a)(c-a)} + \frac{5c^2}{2(b-c)(c-a)}, & c^2 \leqslant I_4 \leqslant b^2, \\ \frac{a^2\log a}{(b-a)(c-a)} - \frac{c^2\log c}{(c-a)(b-c)} + \frac{b^2\log b}{(b-c)(b-a)} - \frac{5a^2}{2(b-a)(c-a)} + \frac{5c^2}{2(b-c)(c-a)} - \frac{5b^2}{2(b-a)(b-c)}, & I_4 > b^2. \end{cases} \tag{17}$$

We assume a neo-Hookean contribution to the SEF from the NCM. Therefore, the new SEF is given by

$$W(I_1, I_4) = (1-\phi)\frac{\mu}{2}(I_1 - 3) + \phi E\left(\frac{A(I_4)}{2}\log I_4 + (B(I_4) - D(I_4))\sqrt{I_4} + \frac{C(I_4)}{2}I_4 + \frac{D(I_4)}{2}\sqrt{I_4}\log I_4 + G(I_4)\right). \tag{18}$$

1.2 Symmetric triangular distribution

We can restrict the triangular distribution to be symmetric. That is, we set the mode, c, to be equal to $\frac{a+b}{2}$. Therefore, (5) becomes

$$f(\lambda_r) = \begin{cases} 0, & \lambda_r < a, \\ \frac{4(\lambda_r - a)}{(b-a)^2}, & a \leqslant \lambda_r \leqslant \frac{a+b}{2}, \\ \frac{4(b-\lambda_r)}{(b-a)^2}, & \frac{a+b}{2} < \lambda_r \leqslant b, \\ 0, & \lambda_r > b. \end{cases} \tag{19}$$

We can insert (3) and (19) into (4) to calculate the total contribution to the stress from the fibrils. Similar to (6), we find that

$$\sigma^*(I_4) = E\left(A^*(I_4) + B^*(I_4)\sqrt{I_4} + C^*(I_4)I_4 + \frac{D^*(I_4)}{2}\sqrt{I_4}\log I_4\right), \tag{20}$$

where $I_4 = \lambda^2$ and

$$A^*(I_4) = \begin{cases} 0, & I_4 < a^2, \\ -\frac{2a^2}{(b-a)^2}, & a^2 \leqslant I_4 \leqslant \left(\frac{a+b}{2}\right)^2, \\ \frac{(b^2 - a^2 + 2ab)}{(b-a)^2}, & \left(\frac{a+b}{2}\right)^2 < I_4 \leqslant b^2, \\ -1, & I_4 > b^2, \end{cases} \tag{21}$$

$$B^*(I_4) = \begin{cases} 0, & I_4 < a^2, \\ \frac{4a\log a}{(b-a)^2}, & a^2 \leqslant I_4 \leqslant \left(\frac{a+b}{2}\right)^2, \\ \frac{4a\log a}{(b-a)^2} - \frac{4(b+a)}{(b-a)^2}\log\left(\frac{a+b}{2}\right), & \left(\frac{a+b}{2}\right)^2 < I_4 \leqslant b^2, \\ \frac{4a\log a}{(b-a)^2} + \frac{4b\log b}{(b-a)^2} - \frac{4(b+a)}{(b-a)^2}\log\left(\frac{a+b}{2}\right), & I_4 > b^2, \end{cases} \tag{22}$$

$$C^*(I_4) = \begin{cases} 0, & I_4 < a^2, \\ \frac{2}{(b-a)^2}, & a^2 \leqslant I_4 \leqslant \left(\frac{a+b}{2}\right)^2, \\ -\frac{2}{(b-a)^2}, & \left(\frac{a+b}{2}\right)^2 < I_4 \leqslant b^2, \\ 0, & I_4 > b^2, \end{cases} \tag{23}$$

$$D^*(I_4) = \begin{cases} 0, & I_4 < a^2, \\ -\frac{4a}{(b-a)^2}, & a^2 \leqslant I_4 \leqslant \left(\frac{a+b}{2}\right)^2, \\ \frac{4b}{(b-a)^2}, & \left(\frac{a+b}{2}\right)^2 < I_4 \leqslant b^2, \\ 0, & I_4 > b^2. \end{cases} \tag{24}$$

By (20) and (14),

$$W^*_{\text{coll}}(I_4) = E\left(\frac{A^*(I_4)}{2}\log I_4 + (B^*(I_4) - D^*(I_4))\sqrt{I_4} + \frac{C^*(I_4)}{2}I_4 + \frac{D^*(I_4)}{2}\sqrt{I_4}\log I_4 + G^*(I_4)\right), \tag{25}$$

where G^* is an integration constant that ensures the continuity of $W^*_{\text{coll}}(I_4)$ at each of the boundaries defined in $A^*(I_4)$—$D^*(I_4)$, and is given by

$$G^*(I_4) = \begin{cases} 0, & I_4 < a^2, \\ \frac{2a^2 \log a}{(b-a)^2} - \frac{5a^2}{(b-a)^2}, & a^2 \leqslant I_4 \leqslant \left(\frac{a+b}{2}\right)^2, \\ \frac{2a^2 \log a}{(b-a)^2} - \frac{(a+b)^2 \log\left(\frac{a+b}{2}\right)}{(b-a)^2} - \frac{5a^2}{(b-a)^2} + \frac{5(a+b)^2}{2(b-a)^2}, & \left(\frac{a+b}{2}\right)^2 \leqslant I_4 \leqslant b^2, \\ \frac{2a^2 \log a}{(b-a)^2} - \frac{(a+b)^2 \log\left(\frac{a+b}{2}\right)}{(b-a)^2} + \frac{2b^2 \log b}{(b-a)^2} - \frac{5a^2}{(b-a)^2} + \frac{5(a+b)^2}{2(b-a)^2} - \frac{5b^2}{(b-a)^2}, & I_4 > b^2. \end{cases} \tag{26}$$

Again, we choose to model the contribution to the SEF from the non-collagenous matrix with a neo-Hookean model. Therefore,

$$\begin{aligned} W^*(I_1, I_4) &= (1-\phi)\frac{\mu}{2}(I_1 - 3) \\ &\quad + \phi E \left(\frac{A^*(I_4)}{2} \log I_4 + (B^*(I_4) - D^*(I_4))\sqrt{I_4} + \frac{C^*(I_4)}{2} I_4 + \frac{D^*(I_4)}{2}\sqrt{I_4} \log I_4 + G^*(I_4) \right). \end{aligned} \tag{27}$$

2 Mathematica Plots

In the main paper, we analyse the quality of fit achieved by multiple models of soft tissue deformation to two sets of stress-strain data taken from tendon samples by Goh *et al.*, designated in the paper as t5c and t6b, and two sets of mechanical equine tendon data collected by Screen *et al.*, designated as superficial digital flexor tendon (SDFT) and common digital extensor tendon (CDET). These fits were created using the software program Mathematica 12.3.1.0. A couple of the fits achieved are shown in the main paper. In this supplementary material, however, we provide the fits to each data set from all four of the models that we fit to the data sets. The fits to the four data sets for the HGO model and the microstructural tendon model are provided in Figure 1 and Figure 2, respectively. For the ST and GT models, the fits are in Figure 3 and Figure 4, respectively.

3 Hierarchical Bayes and the posterior predictive

In the main paper, we model the noise inherent in the problem with a Gaussian distribution of mean zero and covariance matrix $\sigma^2 \mathbf{I}_d$, where d is the length of the data. Therefore, we obtain the following expression for the likelihood function, $L(\mathbf{y}|\boldsymbol{\theta}, \sigma^2)$:

$$\begin{aligned} L(\mathbf{y}|\boldsymbol{\theta}, \sigma^2) &= \prod_{i=1}^{d} \frac{1}{\sqrt{2\pi\sigma^2}} \exp\left(-\frac{1}{2\sigma^2}(y_i - M(\boldsymbol{\theta})_i)^2 \right), \\ &= \left(\frac{1}{2\pi\sigma^2} \right)^{\frac{d}{2}} \exp\left(-\frac{1}{2\sigma^2} \sum_{i=1}^{d} (y_i - M(\boldsymbol{\theta})_i)^2 \right), \end{aligned} \tag{28}$$

where $\mathbf{y}$ is the experimental data, $\boldsymbol{\theta}$ is the parameter vector, and $\mathbf{M}(\boldsymbol{\theta})$ is the predicted stress-strain vector. In (28), $L(\mathbf{y}|\boldsymbol{\theta}, \sigma^2)$ possesses the same form for $\mathbf{y}$ as a Gaussian distribution with mean $\mathbf{M}(\boldsymbol{\theta})$ and variance $\sigma^2 \mathbf{I}_d$.

To find the posterior distribution, up to a normalisation constant, we multiply the likelihood function in (28) by the prior distributions of the model's parameters, $\boldsymbol{\theta}$ and σ^2. *A priori*, we assume that the parameters are independent of one another, and so the joint prior is just a product of the parameters' individual priors. That is,

$$\pi_0(\boldsymbol{\theta}, \sigma^2) = \pi_0(\theta_1) \cdots \pi_0(\theta_h) \pi_0(\sigma^2), \tag{29}$$

where $\pi_0(*)$ represents the prior distribution of $*$ and h denotes the length of $\boldsymbol{\theta}$. With (29) and by Bayes' rule, the posterior distribution, $\pi(\boldsymbol{\theta}, \sigma^2|\mathbf{y})$, is

$$\pi(\boldsymbol{\theta}, \sigma^2|\mathbf{y}) \propto L(\mathbf{y}|\boldsymbol{\theta}, \sigma^2) \pi_0(\theta_1) \cdots \pi_0(\theta_h) \pi_0(\sigma^2). \tag{30}$$

To characterise the posterior distribution fully, we must compute the following multidimensional integral

$$Z = \int_{\mathbb{R}^h} \int_{\mathbb{R}} L(\mathbf{y}|\boldsymbol{\theta}, \sigma^2) \pi_0(\theta_1) \cdots \pi_0(\theta_h) \pi_0(\sigma^2) \mathrm{d}\sigma^2 \mathrm{d}\boldsymbol{\theta}. \tag{31}$$

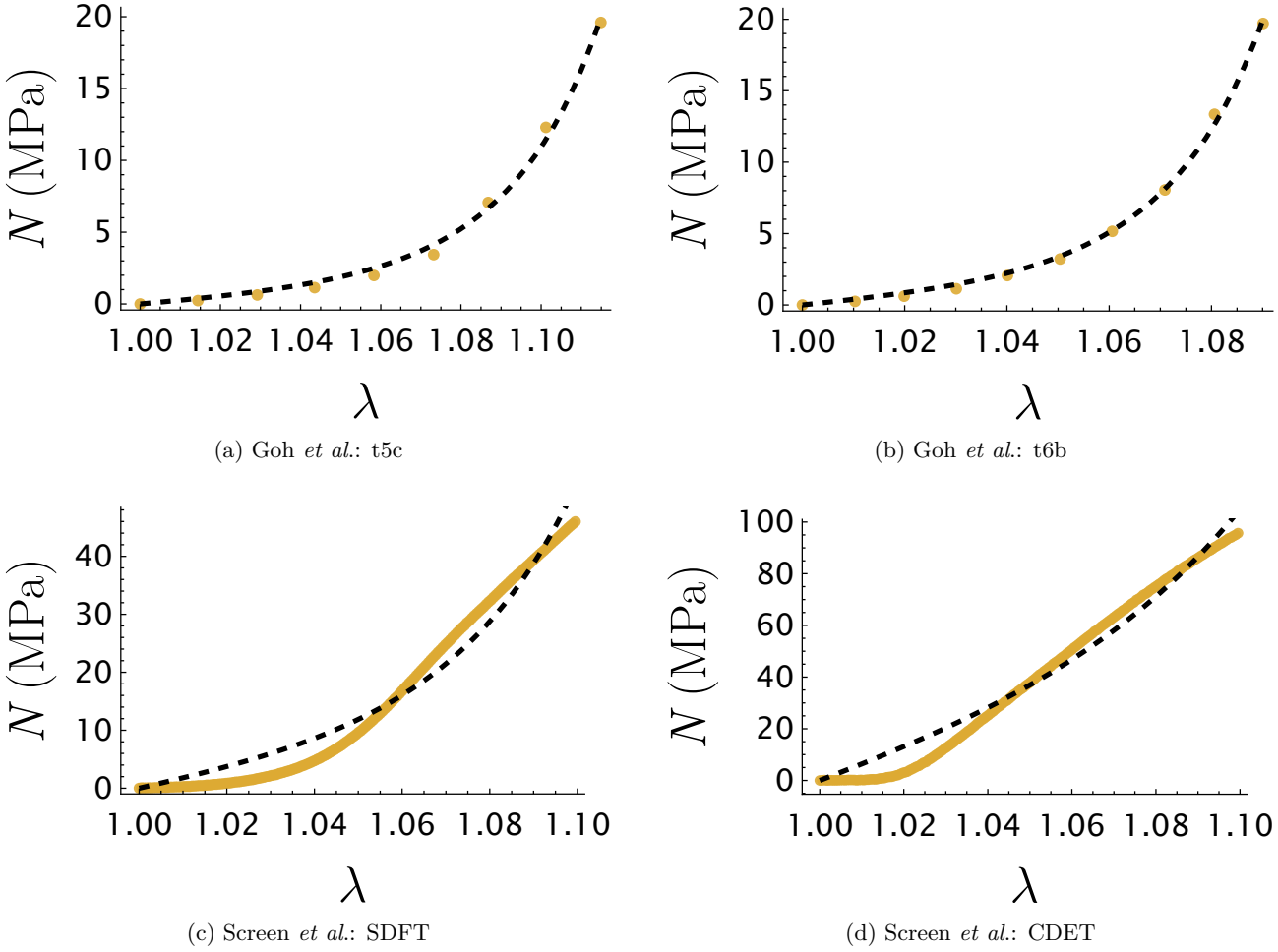

(a) Goh *et al.*: t5c

(b) Goh *et al.*: t6b

(c) Screen *et al.*: SDFT

(d) Screen *et al.*: CDET

Figure 1: Closest fits (black, dashed lines) to the experimental tendon stress-strain data (yellow circles) using the HGO model.

To compute Z as defined in (31) would be impractical due to the non-linear nature of the likelihood; however, because of the form of the likelihood in (28), we can use a technique employed in the literature [2] to simplify the problem by integrating the posterior with respect to σ^2. To enable this integration to be performed, we make an appropriate choice of $\pi_0(\sigma^2)$, known as a conjugate prior, which ensures that $L(\mathbf{y}|\boldsymbol{\theta}, \sigma^2)\pi_0(\sigma^2)$ retains the same functional form as the conjugate prior itself. We choose the conjugate prior, $\pi_0(\sigma^2)$, to be an inverse-gamma distribution, which possesses the following PDF:

$$\pi_0(\sigma^2|\alpha_\sigma, \beta_\sigma) = \frac{\beta_\sigma^{\alpha_\sigma}}{\Gamma(\alpha_\sigma)}(\sigma^2)^{-\alpha_\sigma - 1} \exp\left(-\frac{\beta_\sigma}{\sigma^2}\right), \tag{32}$$

where $\Gamma(*)$ represents the Gamma function of $*$, and α_σ and β_σ are distribution parameters of the inverse-gamma distribution, which correspond to the shape and scale of the PDF, respectively. The parameters α_σ and β_σ are hyperparameters. In Bayesian statistics, hyperparameters are parameters of the prior distributions that we assign to the model parameters that we seek to estimate posteriors for. In this case, the hyperparameters α_σ and β_σ are associated with the prior we have assigned to the parameter σ^2, the variance of the IID noise. We can choose to assign a prior distribution, known as a hyperprior, to the hyperparameters. However, we do not sample the hyperparameters in the random walk Metropolis (RWM) algorithm. Instead, we assign values to them, thereby treating them as constants. We make this choice because we want to integrate the dependence on σ^2 out of the posterior and focus on sampling just the model parameters. Future work could adapt the RWM algorithm we produce in this work to treat the hyperparameters as unknown variables and examine the impact that change has on the posterior distributions we obtain for the model parameters. Consequently, by (28) and (32),

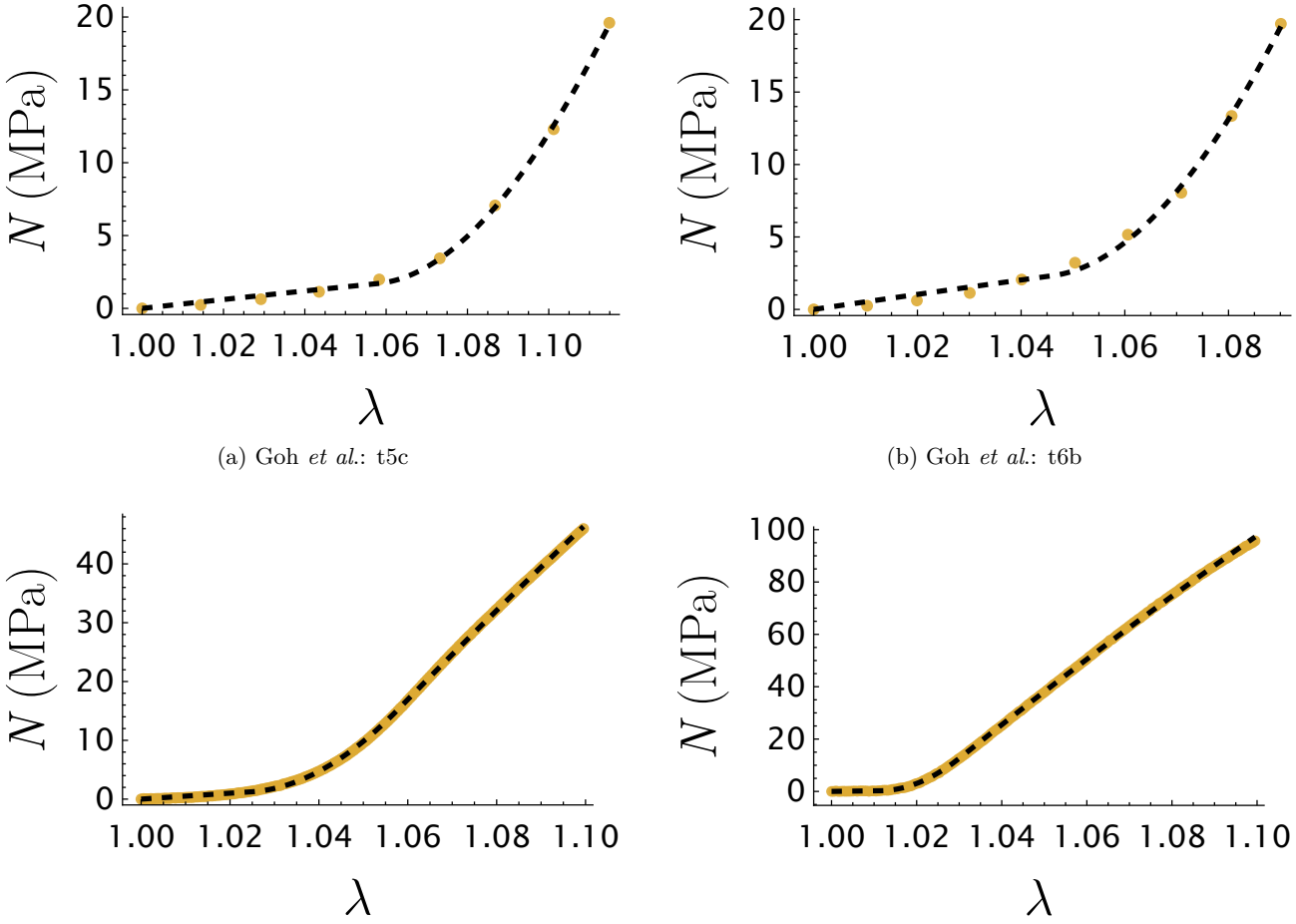

(a) Goh *et al.*: t5c

(b) Goh *et al.*: t6b

(c) Screen *et al.*: SDFT

(d) Screen *et al.*: CDET

Figure 2: Closest fits (black, dashed lines) to the experimental tendon stress-strain data (yellow circles) using the modified microstructural tendon model.

$$\int_0^\infty L(\mathbf{y}|\boldsymbol{\theta},\sigma^2)\pi_0(\sigma^2)\mathrm{d}\sigma^2 = \int_0^\infty \frac{\beta_\sigma^{\alpha_\sigma}\cdot(\sigma^2)^{-\frac{d}{2}}}{(2\pi)^{\frac{d}{2}}\Gamma(\alpha_\sigma)}\exp\left(-\frac{\Delta^2}{2\sigma^2}\right)(\sigma^2)^{-\alpha_\sigma-1}\exp\left(-\frac{\beta_\sigma}{\sigma^2}\right)\mathrm{d}\sigma^2,$$
$$\propto \int_0^\infty (\sigma^2)^{-\left(\frac{d}{2}+\alpha_\sigma\right)-1}\exp\left(-\frac{(\frac{\Delta^2}{2}+\beta_\sigma)}{\sigma^2}\right)\mathrm{d}\sigma^2, \tag{33}$$

where $\Delta^2 = \sum_{i=1}^d (y_i - M(\boldsymbol{\theta})_i)^2$. By choosing an inverse-gamma prior for σ^2, $L(\mathbf{y}|\boldsymbol{\theta},\sigma^2)\pi_0(\sigma^2)$ shares the same functional form as $\pi_0(\sigma^2)$, (32) and (33), with α_σ replaced by $\frac{d}{2}+\alpha_\sigma$, and β_σ replaced by $\frac{\Delta^2}{2}+\beta_\sigma$. Therefore, when we integrate $L(\mathbf{y}|\boldsymbol{\theta},\sigma^2)\pi_0(\sigma^2)$ with respect to σ^2, we obtain

$$\int_0^\infty (\sigma^2)^{-\left(\frac{d}{2}+\alpha_\sigma\right)-1}\exp\left(-\frac{(\frac{\Delta^2}{2}+\beta_\sigma)}{\sigma^2}\right)\mathrm{d}\sigma^2 = \frac{\Gamma(\frac{d}{2}+\alpha_\sigma)}{(\frac{\Delta^2}{2}+\beta_\sigma)^{\frac{d}{2}+\alpha_\sigma}}. \tag{34}$$

By (28), (32) and (34),

$$L^{(\sigma^2)}(\mathbf{y}|\boldsymbol{\theta}) = \frac{\beta_\sigma^{\alpha_\sigma}\Gamma(\frac{d}{2}+\alpha_\sigma)}{(2\pi)^{\frac{d}{2}}\Gamma(\alpha_\sigma)(\frac{\Delta^2}{2}+\beta_\sigma)^{\frac{d}{2}+\alpha_\sigma}}. \tag{35}$$

The quantity $L^{(\sigma^2)}(\mathbf{y}|\boldsymbol{\theta})$ is known as the posterior-predictive.

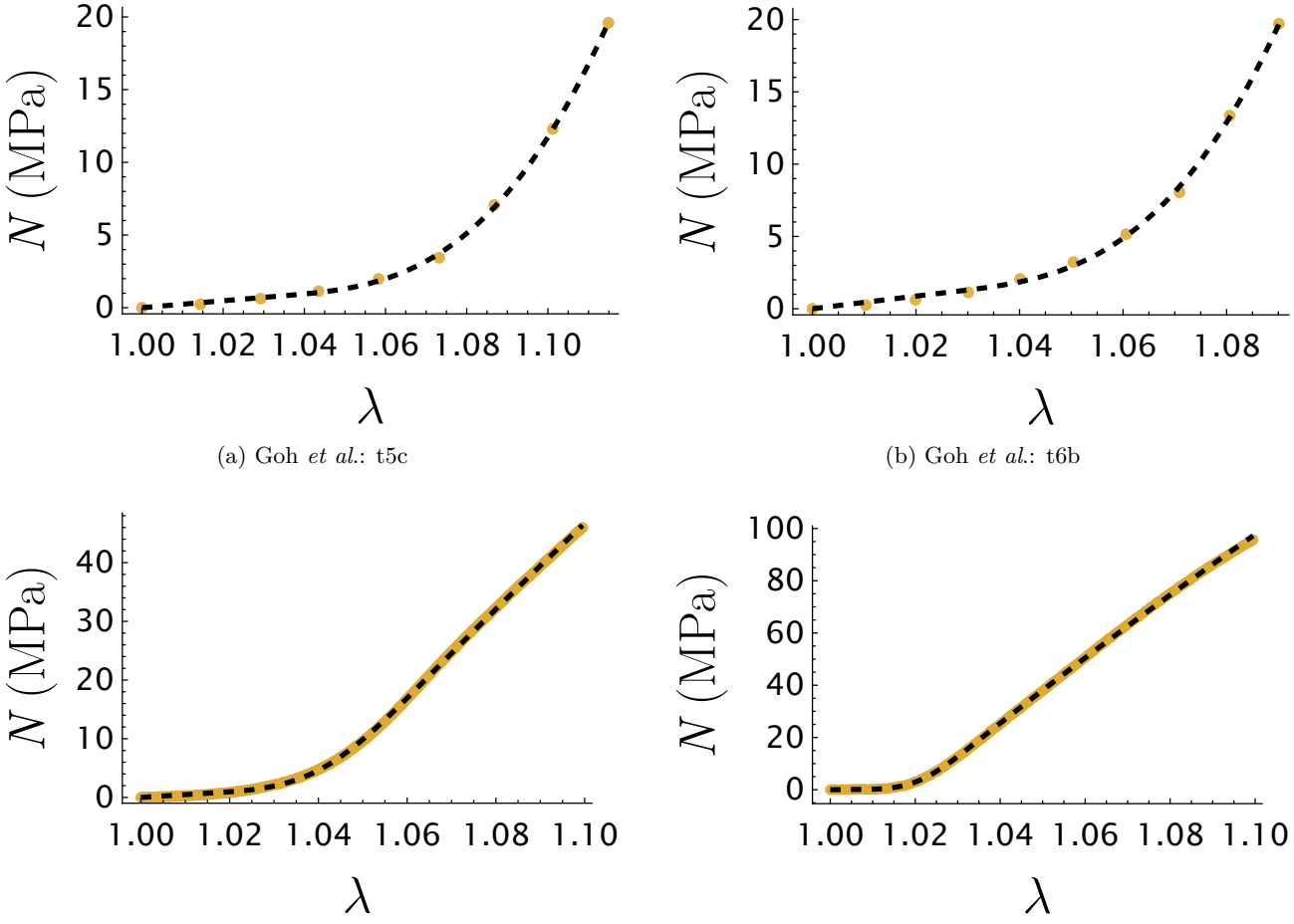

(a) Goh *et al.*: t5c

(b) Goh *et al.*: t6b

(c) Screen *et al.*: SDFT

(d) Screen *et al.*: CDET

Figure 3: Closest fits (black, dashed lines) to the experimental tendon stress-strain data (yellow circles) using the ST model.

For a t-random vector $\mathbf{x}$ of length d, the PDF of the Student's t distribution with mean $\boldsymbol{\mu}$, symmetric matrix parameter $\boldsymbol{\Sigma}$, and ν degrees of freedom is

$$\mathrm{t}_\nu(\mathbf{x};\boldsymbol{\mu},\boldsymbol{\Sigma}) = \frac{\Gamma\left(\frac{\nu+d}{2}\right)}{\Gamma\left(\frac{\nu}{2}\right)} \frac{1}{(\nu\pi)^{\frac{d}{2}}} \frac{1}{\sqrt{\det(\boldsymbol{\Sigma})}} \left(1 + \frac{1}{\nu}(\mathbf{x}-\boldsymbol{\mu})^T\boldsymbol{\Sigma}^{-1}(\mathbf{x}-\boldsymbol{\mu})\right)^{-\frac{d+\nu}{2}}. \tag{36}$$

If we set $\mu = \mathbf{M}(\boldsymbol{\theta})$, $\boldsymbol{\Sigma} = \frac{\beta_\sigma}{\alpha_\sigma}\mathbf{I}_d$, $\mathbf{x} = \mathbf{y}$, and $\nu = 2\alpha_\sigma$, then we eventually recover (35). To show this, we start with (36) and make the aforementioned substitutions,

$$\begin{aligned}
\mathrm{t}\left(\mathbf{y};\mathbf{M}(\boldsymbol{\theta}),\frac{\beta_\sigma}{\alpha_\sigma}\mathbf{I}_d,2\alpha_\sigma\right) &= \frac{\Gamma\left(\alpha_\sigma+\frac{d}{2}\right)}{\Gamma\left(\alpha_\sigma\right)} \frac{1}{(2\alpha_\sigma\pi)^{\frac{d}{2}}} \frac{1}{\sqrt{\frac{\beta_\sigma^d}{\alpha_\sigma^d}}} \left(1 + \frac{1}{2\alpha_\sigma}(\mathbf{y}-\mathbf{M}(\boldsymbol{\theta}))^{\mathrm{T}}\left(\frac{\beta_\sigma}{\alpha_\sigma}\mathbf{I}_d\right)^{-1}(\mathbf{y}-\mathbf{M}(\boldsymbol{\theta}))\right)^{-\omega}, \\
&= \frac{\Gamma(\alpha_\sigma+\frac{d}{2})}{\Gamma(\alpha_\sigma)} \frac{\alpha_\sigma^{\frac{d}{2}}}{(2\alpha_\sigma\pi)^{\frac{d}{2}}} \frac{1}{\beta_\sigma^{\frac{d}{2}}} \left(1 + \frac{1}{2\beta_\sigma}\sum_{i=1}^{d}(y_i - M(\boldsymbol{\theta})_i)^2\right)^{-\omega}, \\
&= \frac{\Gamma(\alpha_\sigma+\frac{d}{2})}{\Gamma(\alpha_\sigma)} \frac{\beta_\sigma^{\alpha_\sigma}}{(2\pi)^{\frac{d}{2}}} \left(\beta_\sigma + \frac{1}{2}\sum_{i=1}^{d}(y_i - M(\boldsymbol{\theta})_i)^2\right)^{-\omega},
\end{aligned} \tag{37}$$

where $\omega = \frac{d}{2} + \alpha_\sigma$. Therefore, the posterior predictive, $L^{(\sigma^2)}(\mathbf{y}|\boldsymbol{\theta})$, is $\mathrm{t}_{2\alpha_\sigma}(\mathbf{y};\mathbf{M}(\boldsymbol{\theta}),\frac{\beta_\sigma}{\alpha_\sigma}\mathbf{I}_d)$, and, by Bayes' rule,

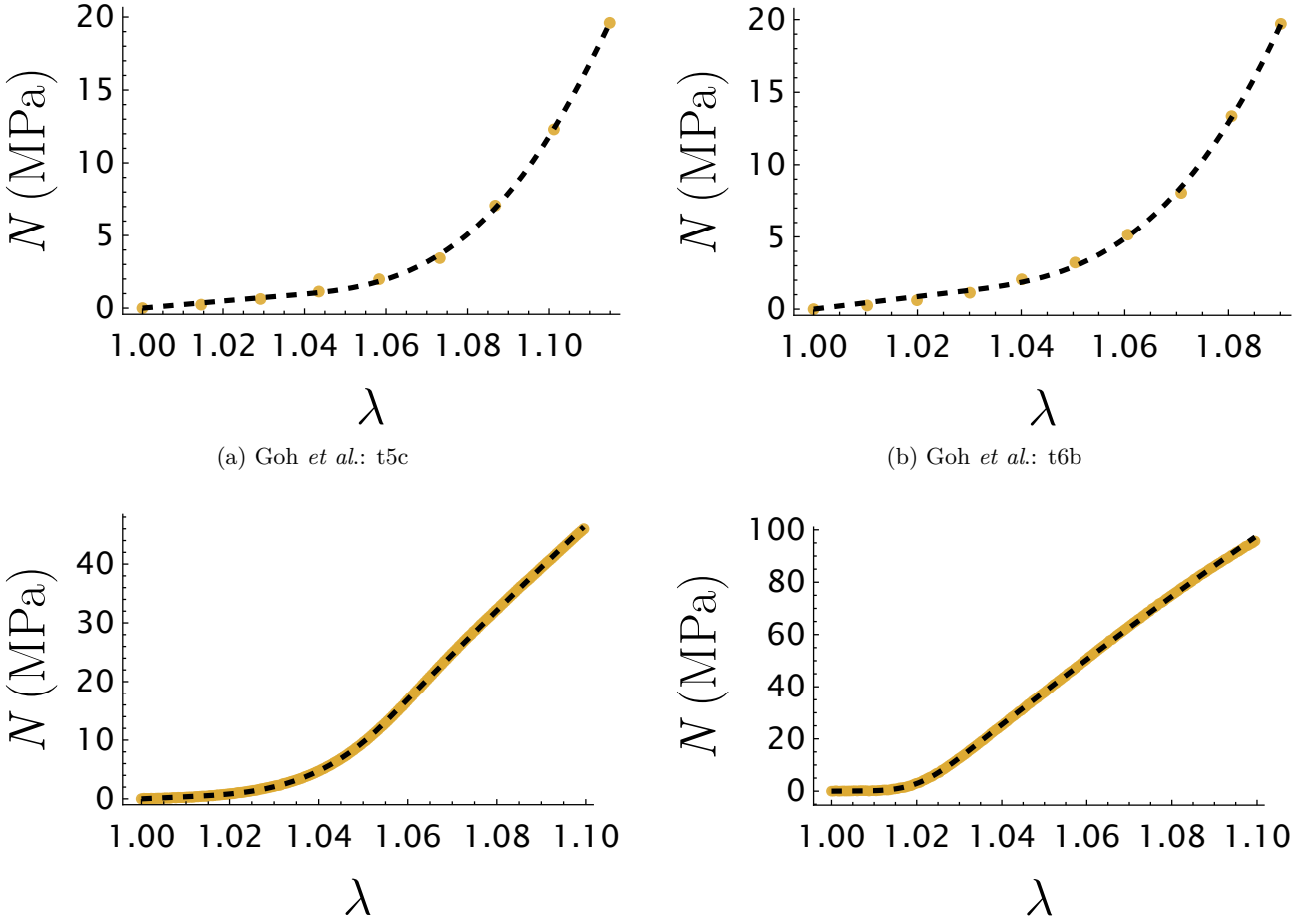

(a) Goh *et al.*: t5c

(b) Goh *et al.*: t6b

(c) Screen *et al.*: SDFT

(d) Screen *et al.*: CDET

Figure 4: Closest fits (black, dashed lines) to the experimental tendon stress-strain data (yellow circles) using the GT model.

$$\begin{aligned}\pi(\boldsymbol{\theta}|\mathbf{y}) &\propto L^{(\sigma^2)}(\mathbf{y}|\boldsymbol{\theta})\pi_0(\boldsymbol{\theta}),\\ &\propto \mathrm{t}_{2\alpha_\sigma}\left(\mathbf{y}; \mathbf{M}(\boldsymbol{\theta}), \frac{\beta_\sigma}{\alpha_\sigma}\mathbf{I}_d\right)\pi_0(\boldsymbol{\theta}).\end{aligned} \tag{38}$$

In order to obtain the exact form of the posterior distribution, we must compute the following integral:

$$Z = \int_{\mathbb{R}^h} L^{(\sigma^2)}(\mathbf{y}|\boldsymbol{\theta})\pi_0(\theta_1)\cdots\pi_0(\theta_h)\mathrm{d}\boldsymbol{\theta}. \tag{39}$$

However, with the form of the posterior predictive and the prior distributions we assign to the model parameters, which are detailed in the main paper, we cannot perform the multidimensional integration needed to characterise the posterior distribution exactly. Therefore, we use Markov chain Monte Carlo methods to sample from the distribution instead.

4 Map-induced density

In the main paper, we discuss transforming the unknown parameters in order to sample a set of parameters whose support stretches over the real numbers, thereby matching the support of the proposal distribution. This improves the efficiency of the algorithm and, thus, the quality of our results. Because the transformation between the *target*

(untransformed) parameters and the *reference* (transformed) parameter vectors is non-linear, we must account for the effect that sampling in the reference parameter space has on both the posterior probability for a particular reference vector (and their corresponding values in the target parameter space) and, ultimately, on which proposed vectors are accepted. We must do this when the transformation is non-linear because, in the RWM algorithm, we use a multivariate Gaussian proposal distribution that ensures the probability of moving from a proposed reference parameter vector, $\boldsymbol{\theta}^*$, to the current position of the Markov chains, $\boldsymbol{\theta}_{\text{curr}}$, is the same as moving from $\boldsymbol{\theta}_{\text{curr}}$ to $\boldsymbol{\theta}^*$. However, the probability of moving from the corresponding proposed vector in the target space, $\boldsymbol{\psi}^*$, to $\boldsymbol{\psi}_{\text{curr}}$ may not be the same as the probability of moving from $\boldsymbol{\psi}_{\text{curr}}$ to $\boldsymbol{\psi}^*$. As mentioned in the main paper, we account for this effect by multiplying the posterior probability associated with $\boldsymbol{\theta}$ by the term $|\det D_{T^{-1}}(\boldsymbol{\theta})|$, where $\mathrm{T}^{-1}(\boldsymbol{\theta})$ represents the transformation of $\boldsymbol{\theta}$ to $\boldsymbol{\psi}$, $D_{T^{-1}}(\boldsymbol{\theta})$ represents the Jacobian of $\mathrm{T}^{-1}(\boldsymbol{\theta})$, and det denotes the determinant of the matrix. Writing the target density with respect to the transformed parameters as $\tilde{\pi}(*)$ and in the original parameter space as $\pi(*)$,

$$\tilde{\pi}(\boldsymbol{\theta}) = \pi(T^{-1}(\boldsymbol{\theta})|Y).|\det D_{T^{-1}}(\boldsymbol{\theta})|, \tag{40}$$

The quantity $\tilde{\pi}(\boldsymbol{\theta})$ is also known as the map-induced density. As defined in the main paper,

$$\boldsymbol{\psi} = \begin{pmatrix} (1-\phi)\mu \\ \phi E \\ a \\ b \end{pmatrix}, \quad T(\boldsymbol{\psi}) = \boldsymbol{\theta} = \begin{pmatrix} \nu \\ \eta \\ \tau \\ \rho \end{pmatrix} = \begin{pmatrix} \log\left((1-\phi)\mu\right) \\ \log\left(\phi E\right) \\ \log\left(a-1\right) \\ \log\left(b-a\right) \end{pmatrix}. \tag{41}$$

Therefore, the transformation T^{-1} is given by

$$T^{-1}(\boldsymbol{\theta}) = \boldsymbol{\psi} = \begin{pmatrix} \exp(\nu) \\ \exp(\eta) \\ \exp(\tau)+1 \\ \exp(\rho)+\exp(\tau)+1 \end{pmatrix}. \tag{42}$$

Therefore, $D_{T^{-1}}(\boldsymbol{\theta})$ is given by

$$D_{T^{-1}}(\boldsymbol{\theta}) = \begin{pmatrix} \exp(\nu) & 0 & 0 & 0 \\ 0 & \exp(\eta) & 0 & 0 \\ 0 & 0 & \exp(\tau) & 0 \\ 0 & 0 & \exp(\tau) & \exp(\rho) \end{pmatrix}. \tag{43}$$

The determinant of the 4×4 matrix $D_{T^{-1}}(\boldsymbol{\theta})$ is thus

$$\det D_{T^{-1}}(\boldsymbol{\theta}) = \exp(\nu+\eta+\tau+\rho). \tag{44}$$

In the RWM algorithm, the acceptance probability involves the evaluation of the target density at the current and proposed states, which, in this instance, is given by the map-induced density

$$\tilde{\pi}(\boldsymbol{\theta}) = \pi(T^{-1}(\boldsymbol{\theta})|Y).\exp(\nu+\eta+\tau+\rho). \tag{45}$$

5 Transformation of the engineering stress using the new parameters

In this section, we rewrite the constitutive equation for the ST model in terms of the transformed parameters, ν, η, τ, and ρ. Respectively, these parameters are the natural logarithms of $(1-\phi)\mu$, ϕE, $a-1$, $b-a$. For a uniaxial stretch along the z-axis, which coincides with the orientation of the collagen fibrils, and assuming traction-free boundary conditions on faces that are not normal to the z-axis, the only non-zero component of the Cauchy stress as defined in (12), σ_{zz}, is

$$\sigma_{zz} = (1-\phi)\mu\left(\lambda^2 - \frac{1}{\lambda}\right) + \phi E(A^*(\lambda) + B^*(\lambda)\lambda + C^*(\lambda)\lambda^2 + D^*(\lambda)\lambda\log\lambda). \tag{46}$$

We can use (21)—(24) and (46) to write σ_{zz} explicitly in terms of λ and the transformed parameters for each region specified in the piecewise constants. As discussed in the main paper, the following equations for σ_{zz} are divided by λ and can then be used in the adaptive RWM algorithm to fit to stress-strain data.

5.1 Region 1

In this region, every collagen fibril is crimped and slack. Only the non-collagenous matrix contributes to the tendon's resistance to the deformation. In terms of the transformed parameters, this region is defined as $\lambda < 1 + \mathrm{e}^{\tau}$ and the Cauchy stress is

$$\sigma_{zz} = \mathrm{e}^{\nu}\left(\lambda^2 - \frac{1}{\lambda}\right). \tag{47}$$

5.2 Region 2

In this region, collagen fibrils begin to tauten, with the number of fibrils tautening increasing with the stretch. This region is defined by $(1 + \mathrm{e}^{\tau}) \leqslant \lambda \leqslant \frac{(2+2\mathrm{e}^{\tau}+\mathrm{e}^{\rho})}{2}$, and the Cauchy stress is

$$\sigma_{zz} = \mathrm{e}^{\nu}\left(\lambda^2 - \frac{1}{\lambda}\right) + 4\mathrm{e}^{(\eta-2\rho)}\left(\frac{\lambda^2}{2} - (1+\mathrm{e}^{\tau})\lambda\log\left(\frac{\lambda}{1+\mathrm{e}^{\tau}}\right) - \frac{(1+\mathrm{e}^{\tau})^2}{2}\right). \tag{48}$$

5.3 Region 3

In this region, collagen fibrils continue to tauten, but the number of fibrils tautening decreases with the stretch. This region is defined as $\frac{(2+2\mathrm{e}^{\tau}+\mathrm{e}^{\rho})}{2} < \lambda \leqslant (1 + \mathrm{e}^{\tau} + \mathrm{e}^{\rho})$, and the Cauchy stress is

$$\begin{aligned}\sigma_{zz} = \mathrm{e}^{\nu}\left(\lambda^2 - \frac{1}{\lambda}\right) + 4\mathrm{e}^{(\eta-2\rho)}\Bigg((1+\mathrm{e}^{\tau})\lambda\log(1+\mathrm{e}^{\tau}) - \frac{(1+\mathrm{e}^{\tau})^2}{2} - \frac{\lambda^2}{2} + (1+\mathrm{e}^{\tau}+\mathrm{e}^{\rho})\lambda\log(\lambda)\\ - (2+2\mathrm{e}^{\tau}+\mathrm{e}^{\rho})\lambda\log\left(\frac{2+2\mathrm{e}^{\tau}+\mathrm{e}^{\rho}}{2}\right) + \frac{(2+2\mathrm{e}^{\tau}+\mathrm{e}^{\rho})^2}{4}\Bigg).\end{aligned} \tag{49}$$

5.4 Region 4

In this region, every collagen fibril is taut. The region is defined as $(1 + \mathrm{e}^{\tau} + \mathrm{e}^{\rho}) < \lambda$, and the Cauchy stress is

$$\begin{aligned}\sigma_{zz} = \mathrm{e}^{\nu}\left(\lambda^2 - \frac{1}{\lambda}\right) + 4\mathrm{e}^{(\eta-2\rho)}\Bigg(-(2+2\mathrm{e}^{\tau}+\mathrm{e}^{\rho})\lambda\log\left(\frac{2+2\mathrm{e}^{\tau}+\mathrm{e}^{\rho}}{2}\right) + (1+\mathrm{e}^{\tau})\lambda\log(1+\mathrm{e}^{\tau})\\ + (1+\mathrm{e}^{\tau}+\mathrm{e}^{\rho})\lambda\log(1+\mathrm{e}^{\tau}+\mathrm{e}^{\rho}) - \frac{\mathrm{e}^{2\rho}}{4}\Bigg).\end{aligned} \tag{50}$$

6 Determining the parameters of the prior distribution

In order to determine the parameters, μ and σ^2, used in the log-normal priors of $(1-\phi)\mu$, ϕE, $a-1$, and $b-a$, and the normal priors of their logarithms, we estimated the values at which the cumulative probability density (CPD) of the prior reached 0.01 and 0.99 for each parameter and then used the quantile function to determine μ and σ^2. For the log-normal distribution, the quantile function is

$$q = \exp(\mu + \sqrt{2\sigma^2}\mathrm{erf}^{-1}(2p-1)), \tag{51}$$

where q is the value of the parameter, erf^{-1} represents the inverse error function, and p is the CPD. The list of values chosen for 0.01 and 0.99 cumulative density and the reasons for choosing them are listed in Table 1.

7 Additional RWM plots

As mentioned in the main paper, we also estimated parameter posteriors by fitting to the t5c and t6b data sets in the RWM algorithm. For the t5c data set, the estimated posteriors and the two-dimensional contour plots of the various joint distributions are given in Figure 5 for the untransformed parameters. The mean and 5σ confidence band of a set of 50,000 positions from the Markov chains, that is, parameter vectors, are also plotted in Figure 6. For the t6b data set, we also plotted the estimated parameter posteriors and two-dimensional contour plots of the joint distributions in Figure 7, and the means and 5σ confidence band of a subset of 50,000 parameter vectors from

Parameter	0.01 CPD	0.99 CPD	Reason
$(1-\phi)\mu$ (MPa)	0.001	10	**Lower**: motivated by the values of μ for tendon fascicles obtained by Purslow [3] **Higher**: inclusive upper bound.
ϕE (MPa)	3.072	13,600	**Lower**: inclusive lower bound using low estimates of $\phi = 0.096$ [4] and $E = 32$ MPa by [5]. **Higher**: inclusive upper bound using an estimate of $\phi = 0.85$ and $E = 16$ GPa given by [6] and [7], respectively.
$a - 1$	0.005	0.1	**Lower**: attempt to provide an inclusive lower bound. **Higher**: assumption that at least one fibril has tautened by the end of the stress-strain data we fit to.
$b - a$	0.005	0.15	**Lower**: attempt to provide an inclusive lower bound. **Higher**: attempt to provide an inclusive upper bound.

Table 1: A table of values used to calculate the mean and variance of the prior distributions of the ST model's parameters. In order to allow the posterior parameter space to be fully sampled in the RWM algorithm, the priors were designed to be inclusive of a wide range of parameter values.

the Markov chains in Figure 8. To create Figures 5 and 7, the samples from the Markov chains were thinned by a factor of ten, as they were for the higher-resolution data sets discussed in the main paper.

Comparing Figures 5—8 with their counterparts for the higher-resolution data shown in the main paper, the estimated parameter posteriors are generally broader and, in some cases, possess a long tail in one direction of the distribution, causing more probability mass to be located in the tail. Furthermore, the confidence bands of the estimated stress values from parameter vectors in the Markov chains are significantly wider, with the 'curves' being more angular than equivalent curves for the synthetic, SDFT, and CDET data sets due to the lack of data points we fit to. In order to ensure we sampled from the target distributions, we extended the burn-in phase to be 1 million simulations. Before we attempt to identify why these differences occur, we note that the data collected by Goh *et al.* were not intended to be used in the fitting of hyperelastic SEFs, but instead to study tendon behaviour for elastic and plastic deformation and, then, failure.

The lack of points to fit to likely causes the aforementioned differences in the posteriors for two main reasons. Firstly, it is harder to distinguish the regions of the SEF from one another when there are fewer points to fit to. The value of $(1-\phi)\mu$ is less important, in terms of the overall fit, when there are few data points in the toe region and collagen fibrils are active for nearly all data points. A wider range of values for $(1-\phi)\mu$ can be proposed and accepted, therefore. This has also been shown in the main paper with the high-resolution CDET data. Secondly, the posterior-predictive is dependent on the difference between the experimental and predicted stresses, and the acceptance probability κ is dependent on the ratio of the value of the posterior-predictive of the proposed parameter vector to that of the current position of the Markov chains. Fitting to fewer points means that differences in the value of the posterior-predictive will be less pronounced between close and relatively poor fits to data. Therefore, the prior ratio and the posterior-modification ratio have a greater effect on the calculation of κ. The latter ratio is dependent on the proposed value of ϕE, for instance. Consequently, large values of ϕE are proposed and accepted, as we see in Figures 5 and 7.

As mentioned previously, the posteriors of parameters such as ϕE and b are broad for these data sets with wide tails in certain directions. Consequently, the confidence bands, calculated from the predicted stresses of 50,000 positions of the Markov chains, are broader than for the high-resolution data. In contrast to the high-resolution h16 SDFT data and the synthetic data, some two-dimensional contour plots possess contour lines that are not elliptical, but instead are more complex in shape. This makes it harder for the RWM algorithm to propose enough parameter vectors that are accepted, which impacts the ability of the algorithm to run efficiently. However, the posteriors are generally smooth, which suggests that some level of convergence in the posteriors has been reached, and justifies the use of a longer burn-in phase. Additionally, all the data points lie within the 5σ confidence band and close to the mean line, demonstrating the ability of the model to replicate experimental data.

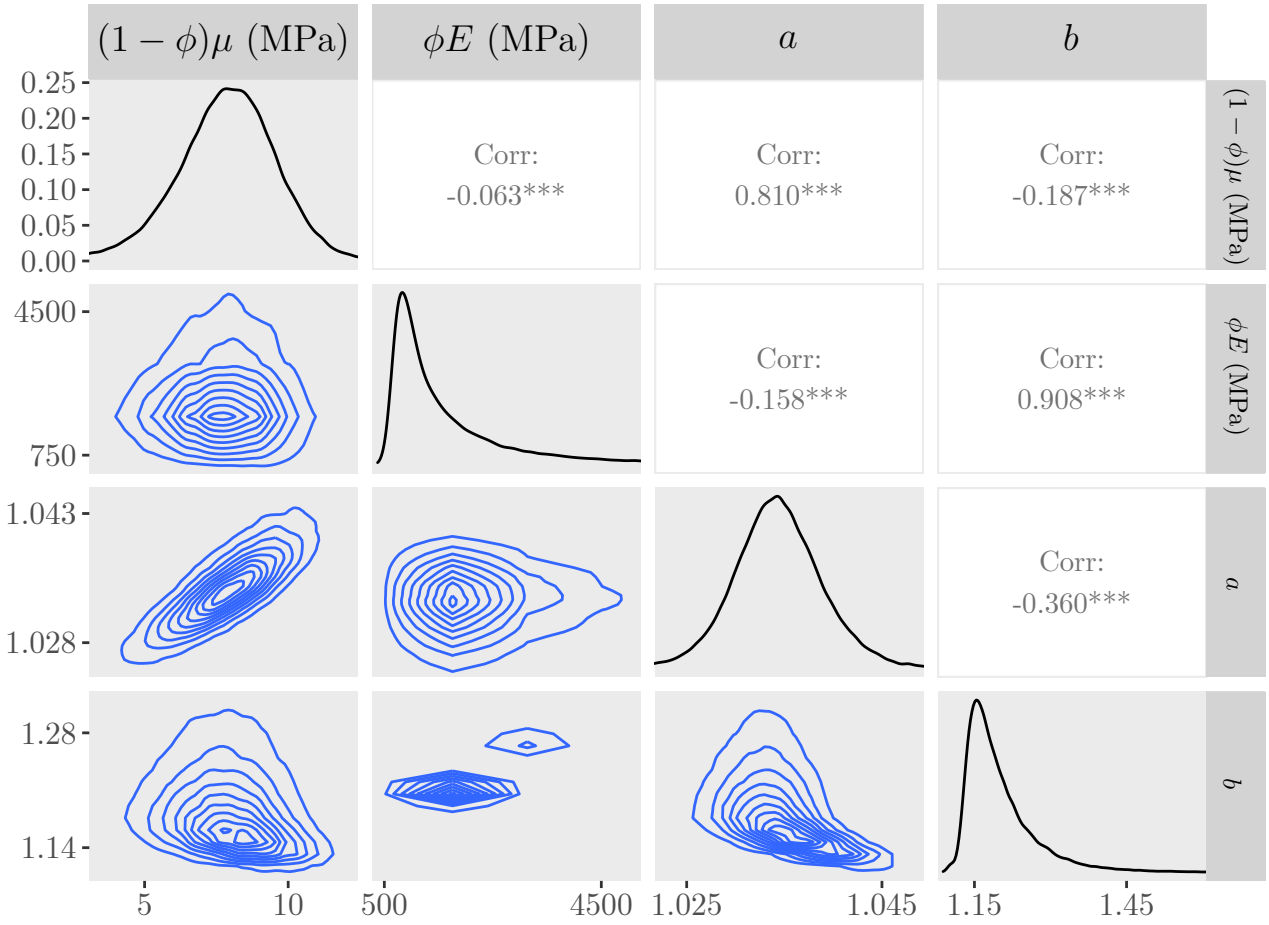

Figure 5: Estimated posteriors and contours of the joint distributions of the untransformed parameters for the fit to the t5c data.

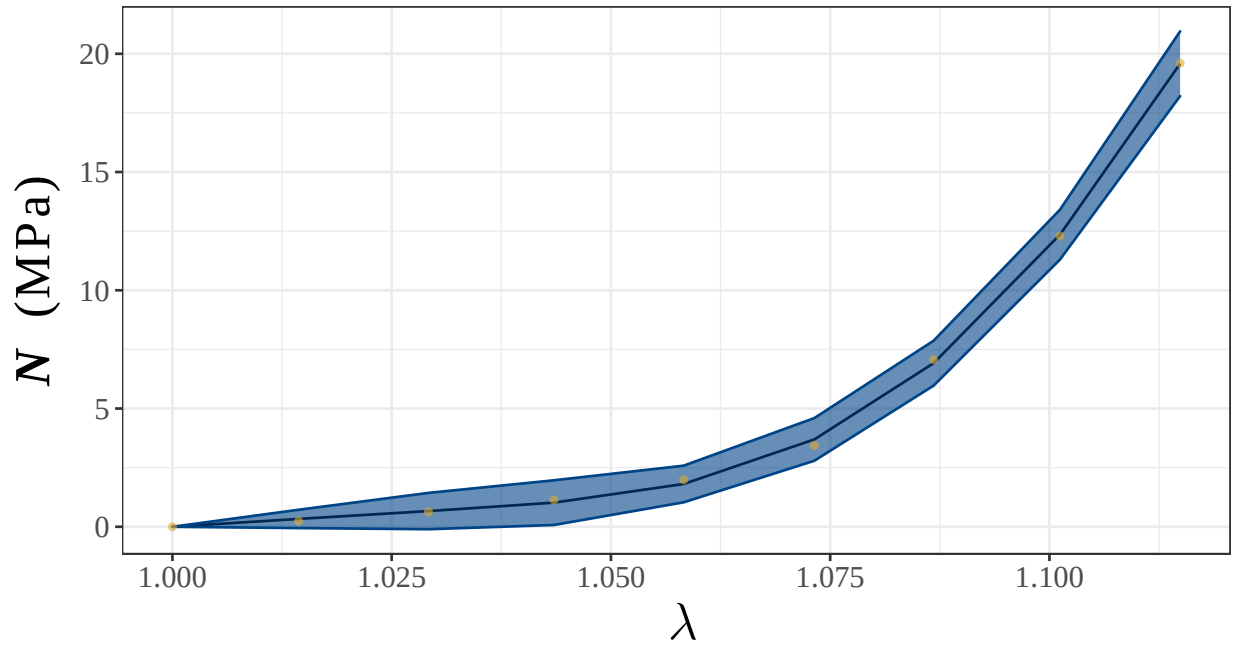

Figure 6: The mean (black) and 5σ confidence band (blue) of the fits to the t5c data (yellow dots).

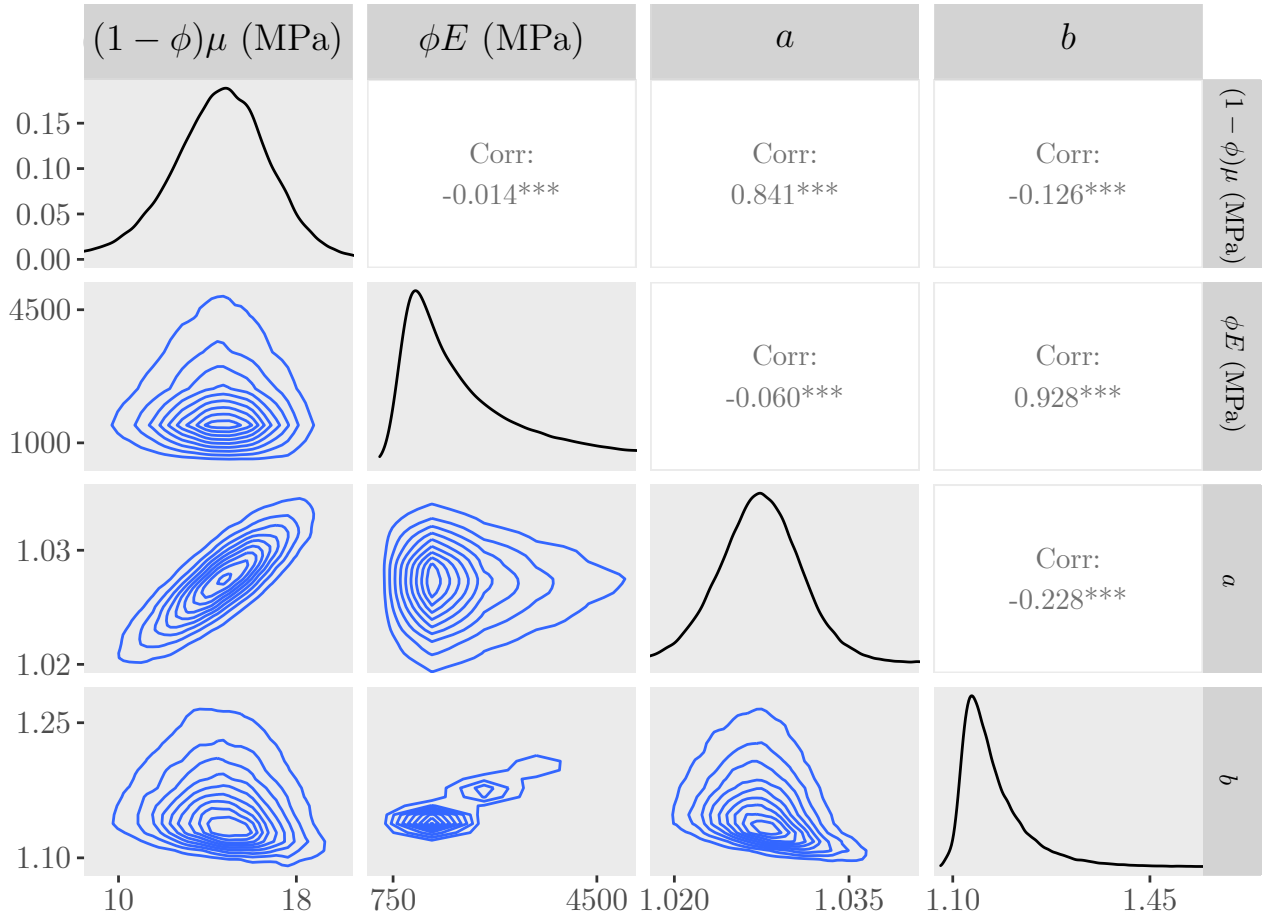

Figure 7: Estimated posteriors and contours of the joint distributions of the untransformed parameters for the fit to the t6b data.

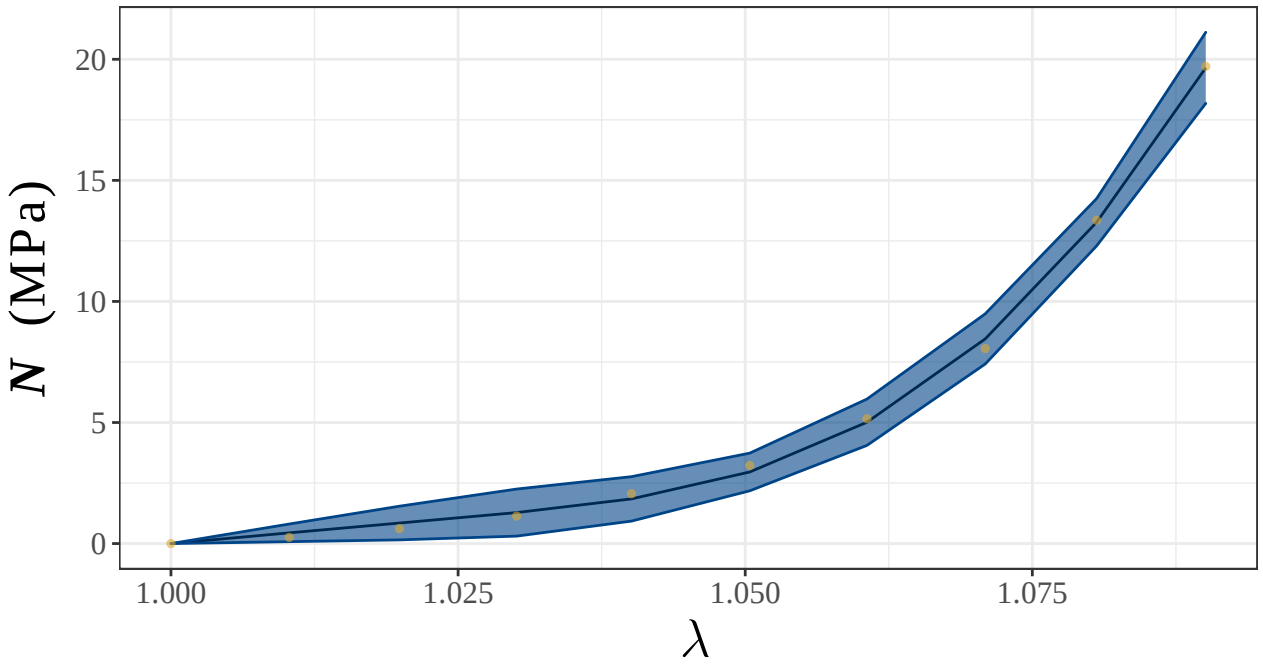

Figure 8: The mean (black) and 5σ confidence band (blue) of the fits to the t6b data (yellow dots).

References

[1] T. Shearer, "A new strain energy function for the hyperelastic modelling of ligaments and tendons based on fascicle microstructure," *Journal of biomechanics*, vol. 48, no. 2, pp. 290–297, 2015.

[2] J. A. Rynn, S. L. Cotter, C. E. Powell, and L. Wright, "Surrogate accelerated bayesian inversion for the determination of the thermal diffusivity of a material," *Metrologia*, vol. 56, no. 1, p. 015 018, 2019.

[3] P. P. Purslow, "The shear modulus of connections between tendon fascicles," in *2009 IEEE Toronto International Conference Science and Technology for Humanity (TIC-STH)*, IEEE, 2009, pp. 134–136.

[4] F. H. Silver, G. P. Seehra, J. W. Freeman, and D. DeVore, "Viscoelastic properties of young and old human dermis: A proposed molecular mechanism for elastic energy storage in collagen and elastin," *Journal of Applied Polymer Science*, vol. 86, no. 8, pp. 1978–1985, 2002.

[5] J. S. Graham, A. N. Vomund, C. L. Phillips, and M. Grandbois, "Structural changes in human type i collagen fibrils investigated by force spectroscopy," *Experimental cell research*, vol. 299, no. 2, pp. 335–342, 2004.

[6] K. L. Goh, D. F. Holmes, H.-Y. Lu, *et al.*, "Ageing Changes in the Tensile Properties of Tendons: Influence of Collagen Fibril Volume Fraction," *Journal of Biomechanical Engineering*, vol. 130, no. 2, Mar. 2008, 021011, ISSN: 0148-0731. DOI: 10.1115/1.2898732. eprint: https://asmedigitalcollection.asme.org/biomechanical/article-pdf/130/2/021011/5489672/021011_1.pdf. [Online]. Available: https://doi.org/10.1115/1.2898732.

[7] A. Gautieri, S. Vesentini, A. Redaelli, and R. Ballarini, "Modeling and measuring visco-elastic properties: From collagen molecules to collagen fibrils," *International Journal of Non-Linear Mechanics*, vol. 56, pp. 25–33, 2013.

Chapter 5

A Bayesian Approach to the Hyperelastic Modelling of Skin

5.1 Skin paper introduction

We have fitted two versions of our new microstructural model to experimental mechanical data taken from tendons and also fitted one version of the model in a random walk Metropolis Markov chain Monte Carlo (RWM MCMC) algorithm. Now we extend the work to studying uniaxial mechanical data on skin samples. Skin is a multi-layered material that is required to withstand deformations in a much wider set of directions than in tendons. To support this task, skin has a distinct microstructure compared to tendons, with collagen fibrils in skin demonstrating more-splayed orientations compared to the largely aligned fibrils found in tendons, although there are still preferred orientations in skin. This more complex structure is a good extension in terms of testing both versions of the new model. Furthermore, like tendons, skin performs many tasks vital to normal bodily function and improvements in our knowledge of the mechanics of skin could benefit a wide variety of real-world industries.

If more time had been available, work would have been done to modify our microstructural model to account for dispersion in the strain energy function. This would have been done for a few important and related reasons. Firstly, assuming fibrils in skin are dispersed better approximates the microstructure of skin that has been observed by numerous research teams. Secondly, it would have been ideal to analyse what effect introducing an additional microstructural phenomenon directly to the model would have had on the parameter values obtained, particularly in the RWM MCMC algorithm. For instance, with splayed fibrils, would the estimated credible interval of the Young's modulus of the collagen fibrils increase in magnitude? Thirdly, introducing dispersion to a model allows it to be used to study more-general deformations, uniaxial stretches performed on the same skin in two distinct directions, for example. Because we have been unable to get dispersion working in the RWM MCMC algorithm, some of the material of this chapter is similar to the chapter on tendon modelling. This is especially true for Sections 2 and 4 of this chapter.

This chapter has been written in the same style as the paper in the previous chapter, which has been submitted to the *Journal of the Royal Society Interface*. For this paper draft, I performed the following tasks:

- Digitally converted stress-strain and force-strain data sets from digital images into numerical values, as described in the following paper draft, taken from the literature.
- Fitted multiple SEFs to the data sets in Mathematica using standard regression and fit one version of our new microstructural SEF to two of the data sets in the RWM MCMC algorithm.
- Wrote and edited this paper draft. This includes creating the figures shown in the thesis.

Bayesian inference on a microstructural, hyperelastic model of skin deformation

Bayesian inference on a microstructural, hyperelastic model of skin deformation

James Haughton[1], Simon Cotter[1], William J. Parnell[1], and Tom Shearer[1, 2]

[1] *Department of Mathematics, University of Manchester, Manchester M13 9PL, United Kingdom*
[2] *Department of Materials, University of Manchester, Manchester M13 9PL, United Kingdom*

Abstract

The macroscopic stress-strain behaviour that fibrous soft tissues such as skin exhibit are caused by the arrangement and properties of the tissue's constituents. It is of great importance, therefore, to account for the microstructure in models of soft tissue behaviour. We fitted a tractable microstructural model to extracted values of experimental skin data. The model fit skin data closely, with it bettering the fits of a much-used semi-structural model and an existing microstructural tendon model for three out of the four extracted data sets fit to. Furthermore, we used a random walk Metropolis Markov chain Monte Carlo algorithm to determine both marginal posterior probability distributions and joint distributions for one version of our microstructural model. Efficient sampling and smooth, well-defined posteriors were obtained for fits to a synthetic data set extracted pigskin stress-strain data. However, we were not able to sample efficiently for extracted stress-strain data from cadaveric human skin.

1 Introduction

Skin is the largest organ in the human body, constituting around 15% of the weight of the body [1]. Skin is a vital part of the integumentary system, protecting the body from outside materials such as bacteria and viruses, and playing an important role in perception and regulation of the body [2]. Through contact with outside objects and interactions with the interior of the body, skin is subjected to many deformations every day. It is vital that skin withstands these deformations in order to ensure that the body it protects remains intact and healthy. Understanding how the skin behaves is important. Advances in skin modelling would possess important applications in such varied fields, amongst others, as cosmetics, surgery and skin regeneration [2], [3]. Our goal, therefore, in this chapter is to investigate whether a microstructural model that we have previously developed to study tendon behaviour can also adequately describe uniaxial tensile data taken from skin.

Analysing the ability of our model to fit to skin behaviour is a good extension to the work we have performed on tendons. Firstly, skin consists of the same constituents as tendons, with the most important mechanical component in the extracellular matrix (ECM) in both tissues being the stiff protein collagen. Skin is a multi-layer material, consisting of, from outermost to innermost, the epidermis, the dermis, and the hypodermis (although sometimes the hypodermis is not considered part of the skin). The dermis contains the vast majority of the skin's collagen content and is much thicker than the epidermis, so it is the most mechanically important layer of skin. The microstructures of tendons and skin differ from each other, as they are adapted so that either tissue can perform the tasks required of it. Collagen fibrils in tendon have a highly regulated structure, largely aligning with one another to resist high loads in a particular direction. Collagen fibrils in the dermis, however, aggregate to form collagen fibres that are arranged in a network [4], which enables the skin to resist deformations from a range of directions. Other constituents of the ECM include the fibrous protein elastin and various proteoglycans [5].

When skin is deformed, it exhibits similar complex macroscopic behaviour to the tendon behaviour discussed in the previous chapter. Skin is anisotropic, viscoelastic [6], and exhibits nonlinear stress-strain behaviour. In particular, when skin is stretched, we observe a J-shaped stress-strain curve that is typical of fibrous human soft tissues [7]. This behaviour enables skin to be compliant at small strains, but stiffen rapidly as the strain increases. As with tendons, these macroscopic behaviours are driven by the microstructure of the tissue. Collagen fibrils, when taut, confer mechanical strength to skin. These fibrils are heterogeneously distributed in skin, causing the tissue to be anisotropic [8]. Multiple microstructural mechanisms for viscoelasticity have been posited, including friction caused by constituents such as collagen fibrils rubbing over one another, or energy dissipated due to molecular relaxations that occur in the ECM [9]–[11].

Variations in the microstructure between skin and tendons exist, resulting in differences in the mechanical behaviour of the two tissues. For example, the aforementioned network of collagen fibrils in skin means that the material can resist large deformations in multiple directions. By contrast, tendons possess largely aligned collagen fibrils, which confer significant strength in the relatively narrow range of directions that a tendon is commonly stretched in. Skin can also undergo larger stretches than tendons, generally, as evidenced by the stress-strain data sets tested in Chapter 4 and later on in this chapter. Skin, therefore, provides a good extension to tendon: their mechanical behaviours are of a similar form and driven by the same constituents, but skin exhibits different mechanical behaviour because of a more complicated microstructure.

As we did in the previous chapter for tendons, we model skin as a fibre-reinforced hyperelastic composite in which the stress acting on a skin sample is related to the strain experienced by the sample via a strain-energy function (SEF), W. Again, skin is a viscous material, but samples can be preconditioned before experiments are performed on them in order to allow us to treat the tested sample as pseudoelastic [12]. This enables us to fit a hyperelastic SEF to experimental stress-strain data taken from skin. Although the arrangement of collagenous structures is more complex in skin than the highly ordered structure present in tendons, we still desire to accurately model tissue behaviour with a microstructural model. The reasons for this are the same as in Chapter 4: microstructural models that consist solely of physically relevant parameters could, in theory, be used in a greater range of applications than phenomenological models, predicting the behaviour of skin samples, or even *in vivo* skin. This potential usage highlights the need to develop accurate microstructural models for future use. We apply the same tests to the microstructural SEF for skin as we did for modelling to tendon data: fitting the model, using non-linear optimisation to four experimental stress-strain data sets before estimating parameter posterior distributions using a Random Walk Metropolis (RWM) Markov chain Monte Carlo algorithm (MCMC).

For the skin problem, we again compare the two versions of our microstructural model, which correspond to the distribution of collagen fibril recruitment stretches being governed by a symmetric and general triangular distribution, to the HGO model [13] and a modified tendon model based off a model created by Shearer [14]. The HGO model still provides a good complement to the new model, as it has been adapted to model skin behaviour before [3], [15], and, in contrast to our model, it contains phenomenological parameters, although structural considerations are key to the overall form of the SEF. The modified tendon model of Shearer is also a good benchmark to study our microstructural model against: both models are microstructural and have been shown to fit tendon data well in the previous chapter.

Additionally, in this chapter, we attempt to accurately estimate posterior distributions for the model parameters for similar reasons to those we discussed for tendons. Differences in skin structure have been observed in the literature [16]. Additionally, skin differs across an individual, with eyelid skin being particularly thin and skin on the soles of the feet being particularly thick [4]. Smoking and damage, whether from trauma or sunlight, also affect skin. In these instances, the composition, arrangement, and properties of the constituents, and thus the mechanics of skin, are also impacted. Models cannot directly measure all of these microstructural variations. If a model attempted to, it would be too complex for practical use in all but a few situations, at best. Furthermore, values given in the literature for microstructural properties of soft tissues differ. Values stated for the Young's modulus of collagen, for example, have ranged from the orders of tens of megapascals to gigapascals [17], [18]. This is to be expected with these values calculated using different methods used to study different skin samples from different subjects. These are all sources of uncertainty in the modelling of skin behaviour and the parameter values we obtain when fitting to data. Consequently, it is important to attempt to quantify the uncertainty present in the values of a model's parameters when it is fitted to experimental data by determining probability distributions for the values of a model's parameters. For the tendon problem, we demonstrated that the symmetric-triangular-distribution version of our model could be used in an RWM MCMC algorithm to estimate posterior distributions for the model's parameters when fit to tendon data. We aim, in this chapter, to show the same occurs when skin data is fitted to.

The outline for the rest of the chapter is as follows. In Section 2, we introduce the continuum mechanical framework that is used to describe the deformations of soft tissues, and define the SEFs we fit to data. In Section 3, we fit the models to extracted experimental stress-strain and force-strain data of uniaxial extensions on skin samples using a standard non-linear optimisation technique in *Mathematica 12* [Mathematica Version 12.3.1.0, Wolfram Research Inc., https://www.wolfram.com/mathematica, Champaign, IL, 2021], and we compare and analyse the fits of the models to one another. In Section 4, we briefly introduce the field of Bayesian statistics and derive an RWM MCMC algorithm that can be used to sample from unknown posterior probability distributions. We also describe adaptive methods that can improve the efficiency of the algorithm. In Section 5, we apply our RWM MCMC algorithm to fit to synthetic and extracted experimental data sets and examine the result. Finally, in Section 6 we summarise the main conclusions of the chapter and explain how we had wished to expand upon the

material covered in this chapter.

2 Continuum mechanics and the microstructural model

2.1 Preliminary notation

As we did for tendons, we consider two configurations in the deformation of skin: the reference configuration, Ω_0, which represents the material before a deformation is applied; and the deformed configuration, Ω, which represents the material after the deformation is applied. The reference and deformed configurations are described by the coordinates $\mathbf{X}$ and $\mathbf{x}$, respectively, where the two sets of coordinates are described by the deformation mapping $\mathbf{x} = \chi(\mathbf{X})$. Again, the key measures of the deformation are the deformation-gradient $\mathbf{F}$, and the left and right Cauchy-Green deformation tensors, $\mathbf{B}$ and $\mathbf{C}$, respectively, which are related by

$$\mathbf{F} = \nabla_{\mathbf{X}}\mathbf{x}, \qquad \mathbf{B} = \mathbf{F}\mathbf{F}^{\mathrm{T}}, \qquad \mathbf{C} = \mathbf{F}^{\mathrm{T}}\mathbf{F}. \tag{1}$$

As we did for tendons in the previous chapter, we assume that skin is a transversely isotropic material. The assumption we make to treat skin as transversely isotropic is a base one, and developing the complexity of the model would be an ideal route for future work, but it is important, as an initial test, to examine how well a transversely isotropic model can fit to experimental data. By treating skin as transversely isotropic, SEFs used to model it are dependent on just two things: the deformation applied to the material; and the direction, which we again represent in the reference configuration by $\mathbf{M}$, around which rotations of a skin sample do not affect material behaviour. Therefore, $W = W(\mathbf{C}, \mathbf{M}\otimes\mathbf{M})$, where $\mathbf{M}\otimes\mathbf{M}$ is used because it is a symmetric function of $\mathbf{M}$. As discussed in the previous chapter, the SEF is objective, and we can, thus, write it in terms of three invariants of $\mathbf{C}$ and two pseudoinvariants of $\mathbf{M}\otimes\mathbf{M}$. These are $I_1 = \mathrm{tr}(\mathbf{C})$, $I_2 = \frac{1}{2}((\mathrm{tr}(\mathbf{C}))^2 - \mathrm{tr}(\mathbf{C}^2))$ and $I_3 = \det(\mathbf{C})$, $I_4 = \mathbf{M}\cdot\mathbf{C}\mathbf{M}$ and $I_5 = \mathbf{M}\cdot\mathbf{C}^2\mathbf{M}$. However, as we did in the previous chapter, we assume that we can accurately model skin with an SEF of the form $W = W(I_1, I_4) - p(I_3 - 1)$. With this form of W the constitutive equation in terms of the Cauchy stress, $\boldsymbol{\sigma}$, is

$$\boldsymbol{\sigma} = -p\mathbf{I} + 2\frac{\partial W}{\partial I_1}\mathbf{B} + 2\frac{\partial W}{\partial I_4}\mathbf{m}\otimes\mathbf{m}, \tag{2}$$

where $\mathbf{m} = \mathbf{F}\mathbf{M}$ is the direction of the collagen fibrils in the deformed configuration.

2.2 SEFs

For the SEFs we use to model skin behaviour, we make the same assumptions that we did when modelling to tendon. That is, we assume that a neo-Hookean non-collagenous matrix (NCM) contains collagen fibrils that are initially slack and crimped, but straighten and become mechanically active as a section of skin is stretched. Furthermore, we assume that the contributions to the SEF from the NCM and collagen fibrils can be decoupled and are proportional to the volume fraction of the material. We again consider the distribution of recruitment stretches in the tissue to adhere to a general triangular distribution, $f(\lambda_r)$, and a symmetric triangular distribution, $f^*(\lambda_r)$, which are given by

$$f(\lambda_r) = \begin{cases} 0, & \lambda_r < a, \\ \frac{2(\lambda_r - a)}{(b-a)(c-a)}, & a \leqslant \lambda_r \leqslant c, \\ \frac{2(b-\lambda_r)}{(b-a)(b-c)}, & c < \lambda_r \leqslant b, \\ 0, & \lambda_r > b, \end{cases}, \qquad f^*(\lambda_r) = \begin{cases} 0, & \lambda_r < a, \\ \frac{4(\lambda_r - a)}{(b-a)^2}, & a \leqslant \lambda_r \leqslant \frac{a+b}{2}, \\ \frac{4(b-\lambda_r)}{(b-a)^2}, & \frac{a+b}{2} < \lambda_r \leqslant b, \\ 0, & \lambda_r > b. \end{cases} \tag{3}$$

By the method introduced in Chapter 4, we eventually find the SEF for the general triangular distribution to be

$$\begin{aligned} W_{\mathrm{gen}}(I_1, I_4) =& (1-\phi)\frac{\mu}{2}(I_1 - 3) \\ &+ E\phi\left(\frac{A(I_4)}{2}\log I_4 + (B(I_4) - D(I_4))\sqrt{I_4} + \frac{C(I_4)}{2}I_4 + \frac{D(I_4)}{2}\sqrt{I_4}\log I_4 + G(I_4)\right), \end{aligned} \tag{4}$$

and for the symmetric triangular distribution to be

$$W_{\text{sym}}(I_1, I_4) = (1-\phi)\frac{\mu}{2}(I_1 - 3) + E\phi\left(\frac{A^*(I_4)}{2}\log I_4 + (B^*(I_4) - D^*(I_4))\sqrt{I_4} + \frac{C^*(I_4)}{2}I_4 + \frac{D^*(I_4)}{2}\sqrt{I_4}\log I_4 + G^*(I_4)\right). \quad (5)$$

2.3 The other SEFs

As in Chapter 4, we test our new models against the widely used HGO model and a modified version of a microstructural model by Shearer. The modification consists of adding a shifting parameter, γ, that shifts the stretch at which the first fibril is recruited, according to the model. A transversely isotropic, one-layer version of the HGO SEF is

$$W(I_1, I_4) = \frac{c_{\text{HGO}}}{2}(I_1 - 3) + \frac{k_1}{2k_2}(\exp(k_2(I_4 - 1)^2) - 1), \quad (6)$$

where c_{HGO} and k_1 are parameters with dimensions of stress and k_2 is a dimensionless model parameter. As with the tendon problem, the microstructural tendon model originally defined in [14] is modified via the introduction of a shifting parameter γ. This parameter corresponds to the engineering strain at which the first collagen fibril becomes mechanically active. Through the inclusion of the shifting parameter γ, the strain on a collagen fibril at an applied stretch λ is $\lambda - \gamma$. Consequently, the pseudoinvariant I_4 is given by $(\lambda - \gamma)^2$. With this new definition of I_4, the SEF for this modified version of the microstructural tendon model is

$$W(I_1, I_4) = \frac{(1-\phi)\mu\,(I_1 - 3)}{2} + \begin{cases} 0, & I_4 < 1, \\ \frac{\phi E}{6\sin^2\theta_o}\left(4\sqrt{I_4} - 3\ln I_4 - \frac{1}{I_4} - 3\right), & 1 \leqslant I_4 \leqslant \frac{1}{\cos^2\theta_o}, \\ \phi E\left(\frac{2(1-\cos^3\theta_o)}{3\sin^2\theta_o}\sqrt{I_4} - \frac{1}{2}\ln I_4 - \frac{1}{2} - \frac{\cos^2\theta_o}{\sin^2\theta_o}\log\left(\frac{1}{\cos\theta_o}\right)\right), & I_4 > \frac{1}{\cos^2\theta_o}, \end{cases} \quad (7)$$

where θ_o is the initial crimp angle of the outermost, most-crimped fibrils in the tendon's fascicles.

3 Fitting to experimental uniaxial stress-strain data

As we did in the previous chapter, we fit the models to experimental stress-strain data under the assumption that a uniaxial stretch is applied in the direction that collagen fibrils are oriented in. We consider this direction to coincide with one of the coordinate axes. Without loss of generality, we pick the z-axis, as we did when fitting to tendons. Together, the assumptions we have made provide a base simplification of the multi-axial deformations that skin is subjected to *in vivo*. This problem serves, however, as a preliminary test of the accuracy of the SEFs models in order to ascertain the potential viability of these SEFs for use in studying more complex skin deformations.

As the skin sample studied is incompressible, the reference and deformed coordinates are related as follows:

$$(x, y, z) = \left(\frac{X}{\sqrt{\lambda}}, \frac{Y}{\sqrt{\lambda}}, \lambda Z\right), \quad (8)$$

where the reference and deformed coordinates are denoted by the vectors (X, Y, Z) and (x, y, z), respectively. The behaviour in the X and Y directions is the same because of the symmetry of the problem we study. With this deformation,

$$\mathbf{C} = \mathbf{B} = \text{diag}\left(\lambda^{-1}, \lambda^{-1}, \lambda^2\right). \quad (9)$$

The Cauchy stress, (2), gives the force acting on the deformed material per unit *deformed* area; however, the quantity recorded in the experiments being modelled is the engineering stress, the force per unit *reference* area, which we denote as N. By the deformation we impose, we can obtain the engineering stress by inputting the SEF we use to model skin behaviour into (2) and then by dividing the resulting expression by λ. For the version of our SEF created using a general triangular distribution to model the variation of recruitment stretches in the tissue (GT model), the engineering stress is

$$N_{\text{gen}} = (1-\phi)\mu\left(\lambda - \frac{1}{\lambda^2}\right) + \frac{\phi E}{\lambda}\left(A(\lambda^2) + B(\lambda^2)\lambda + C(\lambda^2)\lambda^2 + D(\lambda^2)\lambda\ln\lambda\right), \quad (10)$$

where $I_4 = \lambda^2$. Similarly, for the version of our SEF created using a symmetric triangular distribution to model the variation of recruitment stretches in the tissue (the ST model), the engineering stress is

$$N_{\text{sym}} = (1-\phi)\mu\left(\lambda - \frac{1}{\lambda^2}\right) + \frac{\phi E}{\lambda}\left(A^*(\lambda^2) + B^*(\lambda^2)\lambda + C^*(\lambda^2)\lambda^2 + D^*(\lambda^2)\lambda\ln\lambda\right). \tag{11}$$

For the HGO model, the engineering stress is

$$N_{\text{HGO}} = \frac{c_{\text{HGO}}}{2}\left(\lambda - \frac{1}{\lambda^2}\right) + 2k_1\lambda(\lambda^2-1)\exp(k_2(\lambda^2-1)). \tag{12}$$

Finally, for the tendon model, the engineering stress is

$$N_{\text{tendon}} = \frac{(1-\phi)\mu}{2}\left(\lambda - \frac{1}{\lambda^2}\right) + \begin{cases} 0, & \lambda < (1+\gamma), \\ \frac{\phi E}{3\sin^2\theta_o}\left(2 - \frac{3}{\lambda-\gamma} - \frac{1}{(\lambda-\gamma)^3}\right), & (1+\gamma) \leqslant \lambda \leqslant (\frac{1}{\cos\theta_o} + \gamma), \\ \phi E\left(\frac{2(1-\cos^3\theta_o)}{3\sin^2\theta_o} - \frac{1}{\lambda-\gamma}\right), & \lambda > (\frac{1}{\cos\theta_o} + \gamma). \end{cases} \tag{13}$$

3.1 Data Sets

Now that we have derived the constitutive equation for the four SEFs that we use to fit to data, we introduce the data sets that we use. The four data sets are as follows:

- Lanir & Fung [19]: force-strain from an *in vitro* test on rabbit skin,
- Ankersen *et al.* [20]: stress-strain data from an *in vitro* test on pigskin,
- Gunner *et al.* [21]: force-strain data from an *in vivo* test on a living nine-year-old girl.
- Dunn *et al.* [22]: stress-strain data from an *in vitro* test on human chest skin samples taken from cadavers aged between forty-seven and eighty-six.

It should be noted, however, that each of the data sets have been extracted from the relevant stress-strain curves plotted in the papers and are not the true data collected in experiments. This is because none of the data from the four experiments were published. To estimate the data we calculated the pixel number, in *Microsoft Paint*, in the x and y directions for the stress-strain and force-strain curves and converted those pixel counts into stretches, and stresses or forces. Naturally, this adds more uncertainty to the values of the data fit to, further motivating the use of a Bayesian approach to model uncertainty later in this chapter.

Lanir & Fung and Gunner *et al.* plotted force against strain. Because Lanir & Fung did not state the dimension of the samples used and Gunner *et al.* performed an *in vivo* test, we cannot convert the existing data into a stress-strain curve. Because engineering stress is a measure of the force per unit reference area, we fit to these data sets by multiplying the expressions for the engineering stress, (10)—(13), using a reference-area parameter, A. Additionally, the orientation of the collagen fibrils was not determined for these experiments. In papers that uniaxially stretched skin samples in multiple directions, we assumed that the direction in which a skin sample was found to be stiffest was the direction that the collagen fibrils were oriented in, according to our model.

The general experimental set-up for the data collected by Ankersen *et al.* and Dunn *et al.* is shown in Figure 1. Soft tissues consist mainly of water, so clamping to skin samples is tough, as they tend to slip when they are clamped to [23]. Hence, dumbbell-shaped skin samples are excised and secured to the clamps and measurements are considered to be taken over the middle portion of the skin sample [24]. This section for which measurements are taken over is called the *gauge length*. The data collected by Lanir & Fung were taken from skin samples that were not dumbbell-shaped, Figure 2. The *in vivo* test performed by Gunner *et al.* was performed using an extensometer on the test subject's axilla (armpit).

3.2 Results

We fit each of the four models to data using the function *NonlinearModelFit* from the package *Mathematica 12* [Mathematica Version 12.3.1.0, Wolfram Research Inc., https://www.wolfram.com/mathematica, Champaign, IL, 2021]. The Nelder-Mead algorithm is again used because existing literature sources detail the algorithm. We again restrict the model parameters as follows: for the ST model, $0 < (1-\phi)\mu$, $0 < \phi E$, $1 < a < b$, $a < \lambda_{\max}$, where $\lambda_{\max}$ represents the maximum stretch in the data; for the GT model, we replaced $1 < a < b$ with $1 < a < c < b$;

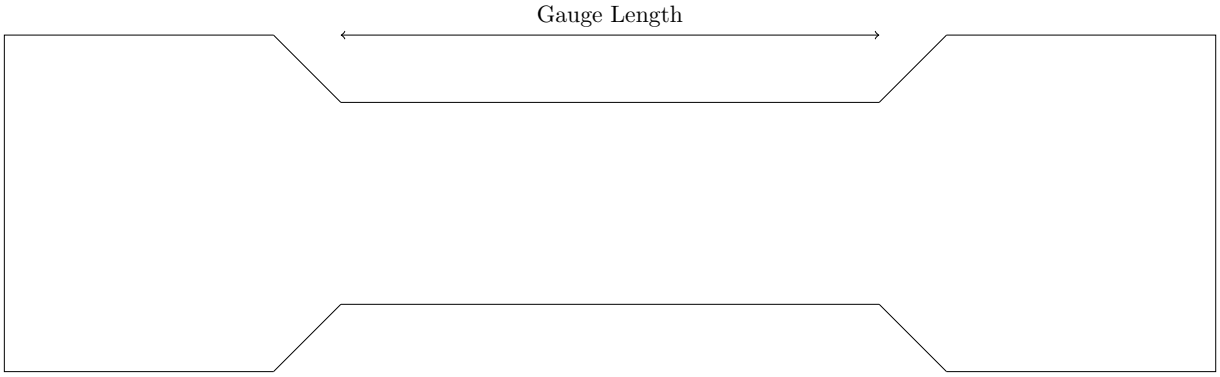

Figure 1: The experimental set-up for the data sets obtained by Ankersen *et al.* and Dunn *et al.* The mechanical behaviour of the skin over the gauge length was measured.

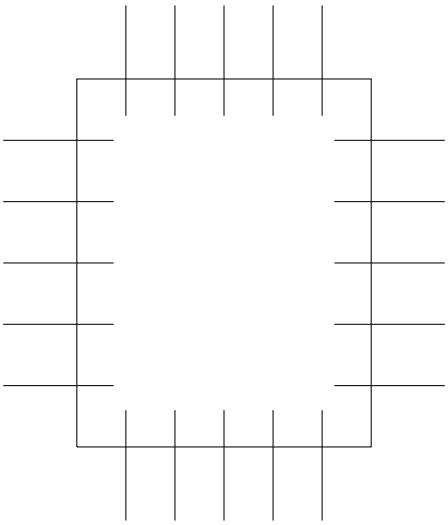

Figure 2: The experimental set-up for the data set obtained by Lanir & Fung [19]. The square face of a cuboidal skin sample had hooks attached to it that could stretch in one or two directions simultaneously.

for the HGO model, (6), $0 < c_{\text{HGO}}$, $0 < k_1$, and $0 < k_2$; and for the modified tendon model, $0 \leqslant \gamma < (\lambda_{\max} - 1)$, $0 < \theta_o < \frac{\pi}{2}$, $(1-\phi)\mu > 0$, $\phi E > 0$.

The mean absolute error, Δ, between the experimental data, $\mathbf{y}$, and simulated data, $\hat{\mathbf{y}}$, is

$$\Delta = \frac{1}{d}\sum_{i=1}^{d} |y_i - \hat{y}_i|, \tag{14}$$

where d is the length of the data set. Similarly, the mean relative error, δ, is

$$\delta = \frac{1}{d}\sum_{i=1}^{d} \frac{|y_i - \hat{y}_i|}{|y_i|}. \tag{15}$$

The relations (14) and (15) hold for the two data sets where we fit to stress-strain values and the two data sets where we fit to the force-strain values.

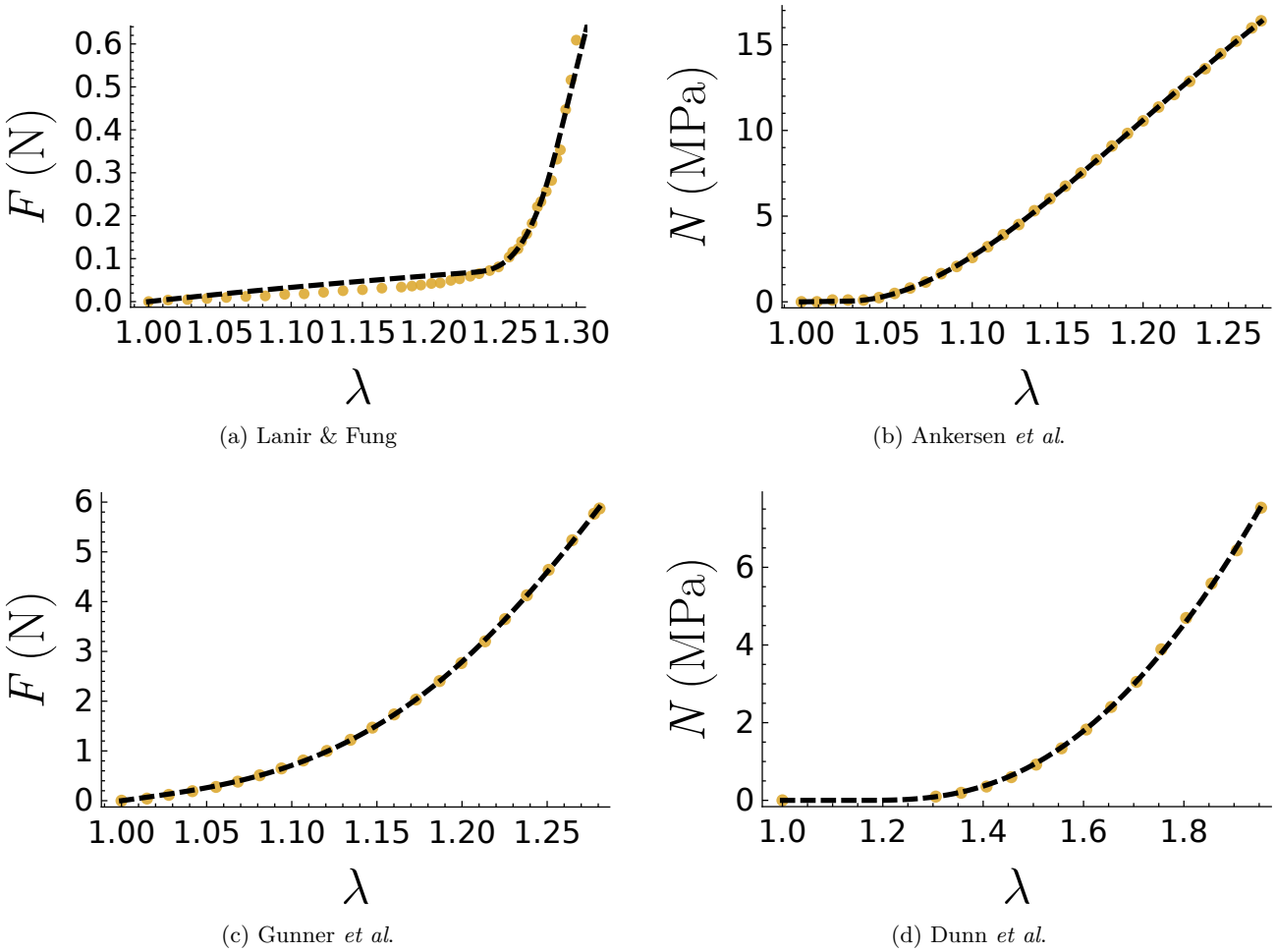

(a) Lanir & Fung

(b) Ankersen *et al.*

(c) Gunner *et al.*

(d) Dunn *et al.*

Figure 3: Closest fits (black, dashed lines) to the experimental tendon data (yellow circles) using the GT model.

The values of Δ and δ found when fitting each model to the four data sets are given in Table 1. The parameter values found in these fits are listed in Table 2. Some proposed parameter values for ϕE are lower than we would expect given the range of values stated in the literature. For the data sets that fit the force rather than stress acting on the skin sample, this could be due to the area parameter A multiplying ϕE. For instance, for the GT model for the Ankersen *et al.* and Dunn *et al.* data sets, the value of ϕE is physically reasonable at 117 MPa and 176 MPa, respectively. The ST model achieves a closer fit to the data than the microstructural tendon model for each data set and to the HGO model for three of the four data sets. Furthermore, the GT model also achieves a closer fit to data than the microstructural tendon and HGO models for three out of the four data sets studied, although it

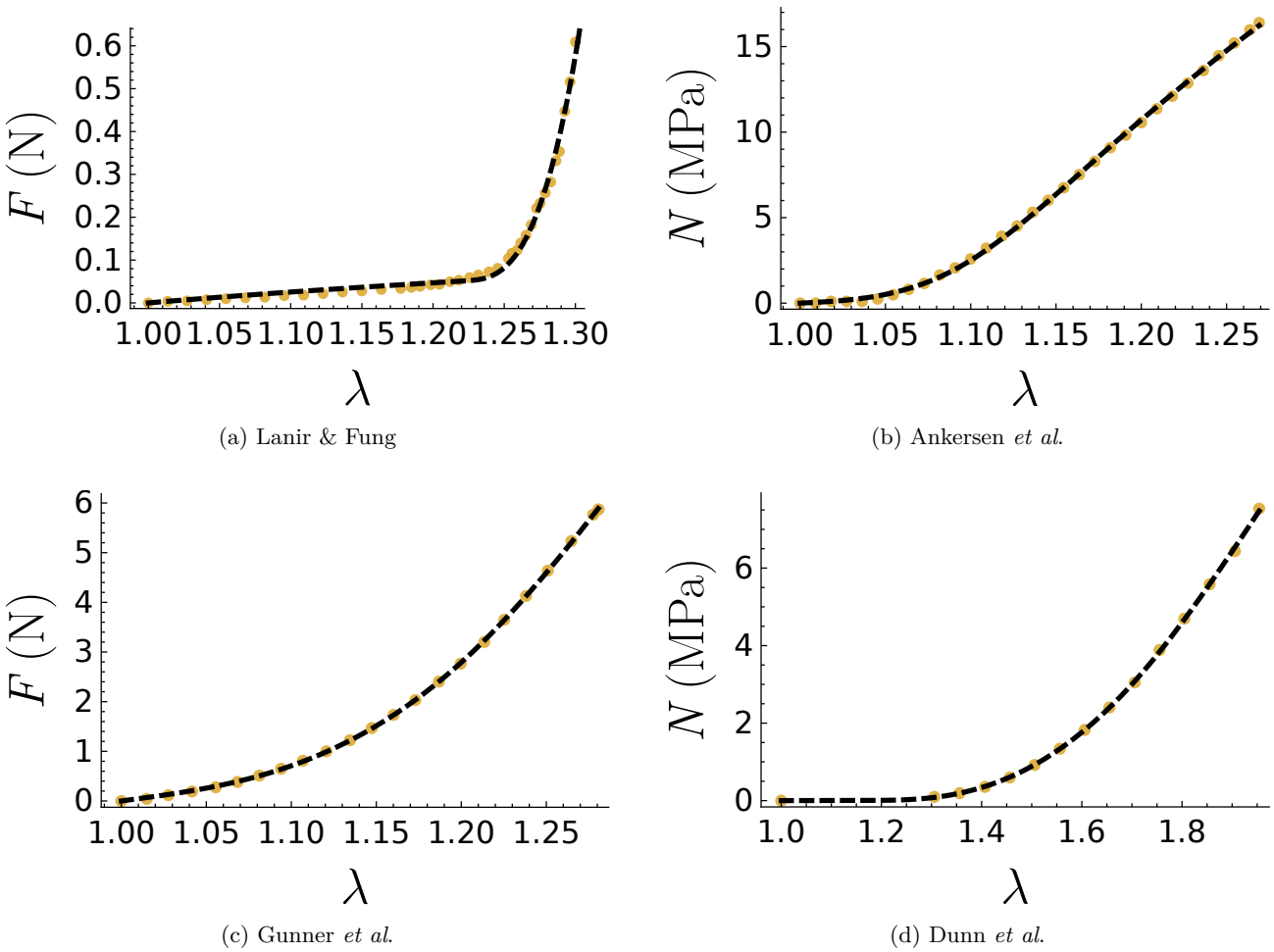

(a) Lanir & Fung

(b) Ankersen *et al.*

(c) Gunner *et al.*

(d) Dunn *et al.*

Figure 4: Closest fits (black, dashed lines) to the experimental tendon data (yellow circles) using the ST model.

provides the worst fit out of the four SEFs to the Lanir & Fung data. Only for the data collected by Lanir & Fung does the HGO model outperform the ST and GT models. Surprisingly, the ST model outperforms the GT model in every data set other than the data from Ankersen *et al.* The GT model contains an additional degree of freedom when it comes to fitting to data, so we would expect that model to outperform the ST model. This surprising result is likely because non-linear optimisation only provides a local best fit to data and only 1000 iterations of the Nelder-Mead algorithm were performed. The fits to data for the GT, ST, HGO, and modified tendon models can be found in Figures 3—6, respectively.

Finally, as we also did in Chapter 4, we produced a table of parameter values achieved from a couple of other fits, using the same four models, to the four data sets. Again, the starting values for these fits were randomly chosen. As we did for tendons, we observe that the HGO model is the model for which parameter vectors obtained at the end of the fits are closest to one another. The parameter vectors for the ST and GT model, for example, often show significant differences. This is expected for the skin problem because, by virtue of the fact that we work with extracted data in this problem, the data is lower-resolution and will contain larger errors than the data used for the tendon problem. Therefore, it is harder for an optimisation method to move into a particularly close-fitting region of the parameter space.

4 Bayesian Statistics

We have fitted to the experimental stress-strain behaviour of skin using non-linear optimisation. Next, we attempt to fit to the data via a Random Walk Metropolis (RWM) Markov chain Monte Carlo (MCMC) algorithm in order to estimate posterior distributions for the model's parameters. As discussed in Chapter 4, we introduce the RWM

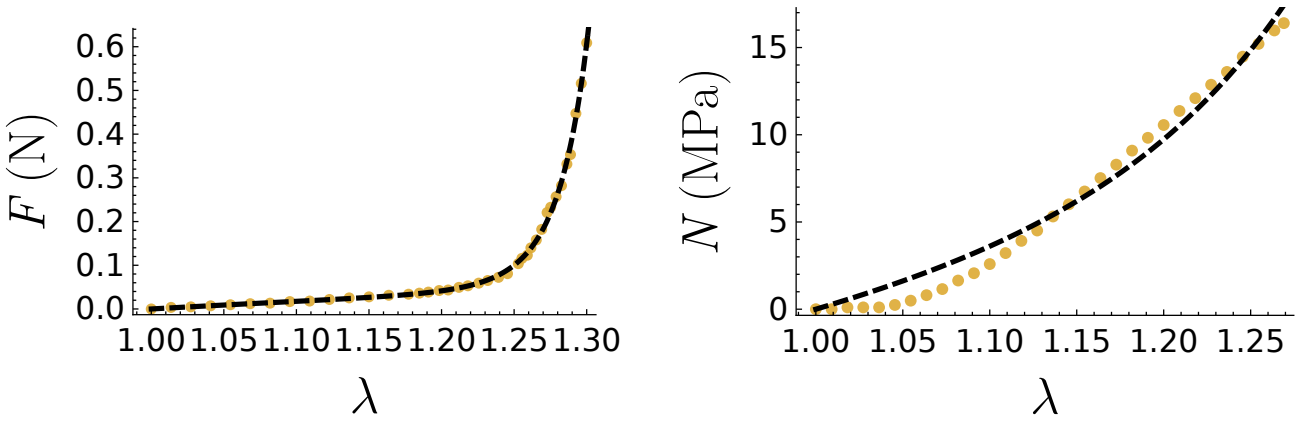

(a) Lanir & Fung

(b) Ankersen *et al.*

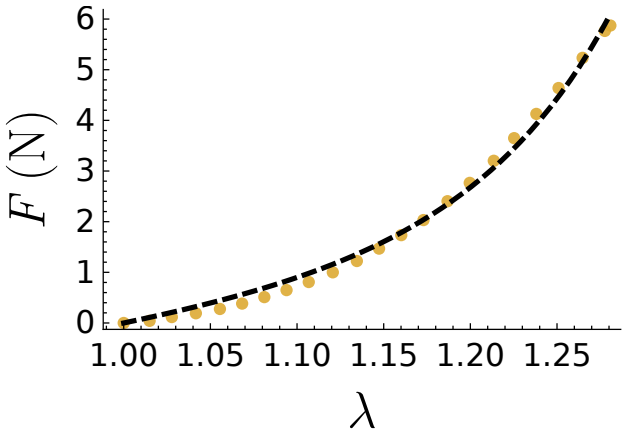

(c) Gunner *et al.*

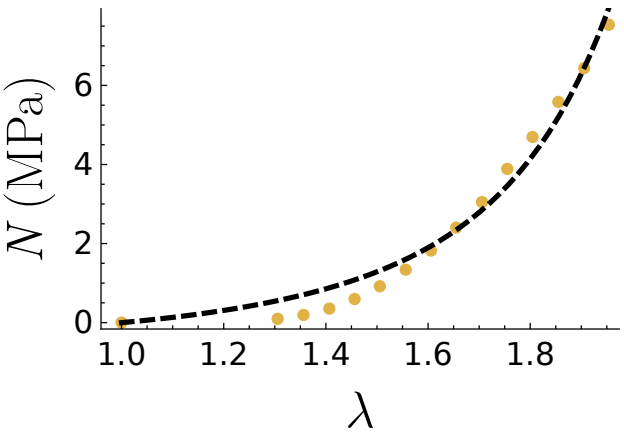

(d) Dunn *et al.*

Figure 5: Closest fits (black, dashed lines) to the experimental tendon data (yellow circles) using the HGO model.

algorithm to sample from the posterior distributions of the parameters because we cannot derive an exact form of the posteriors. We again start under the assumption that we can account for uncertainty by assuming that the experimental data is produced via the sum of the deterministic model's output with independently and identically distributed (IID) noise. In equation form, that is

$$\mathbf{y} = \mathbf{M}(\boldsymbol{\theta}) + \boldsymbol{\eta}, \qquad \boldsymbol{\eta} \sim \mathcal{N}(\mathbf{0}, \sigma^2 \mathbf{I}_d), \tag{16}$$

where d is the length of $\mathbf{y}$, $\mathbf{I}_d$ is a $d \times d$ identity matrix, $\mathcal{N}(\mathbf{0}, \sigma^2 \mathbf{I}_d)$ represents a normal distribution with mean $\mathbf{0}$ and covariance matrix $\sigma^2 \mathbf{I}_d$, and $\mathbf{y} \in \mathbb{R}^d$. As shown in Chapter 4, we find that the likelihood function for our problem is

$$L(\mathbf{y}|\boldsymbol{\theta}, \sigma^2) = \frac{1}{(\sigma\sqrt{2\pi})^d} \exp\left(-\frac{1}{2\sigma^2} \|\mathbf{y} - \mathbf{M}(\boldsymbol{\theta})\|_2^2\right). \tag{17}$$

As we were able to do in Chapter 4, we integrate out the posterior's dependence on σ^2 by assigning an inverse-gamma prior to it that contains the hyperparameters α_σ and β_σ. We use the same value for the hyperparameters that we used for the tendon problem. That is, $\alpha_\sigma = 3$ and $\beta_\sigma = 0.3$. This value for the hyperparameters is most likely less reasonable for the skin problem as for the tendon because, as mentioned previously, the extracted skin data will contain larger errors than the tendon data did. Therefore, it would be useful to study what impact, if any, that changing the hyperparameters to values which assign more probability mass for values of σ^2 greater than 0.5 would have on the estimated posteriors we obtain at the end of the algorithm. From this we obtain the following expression for the posterior

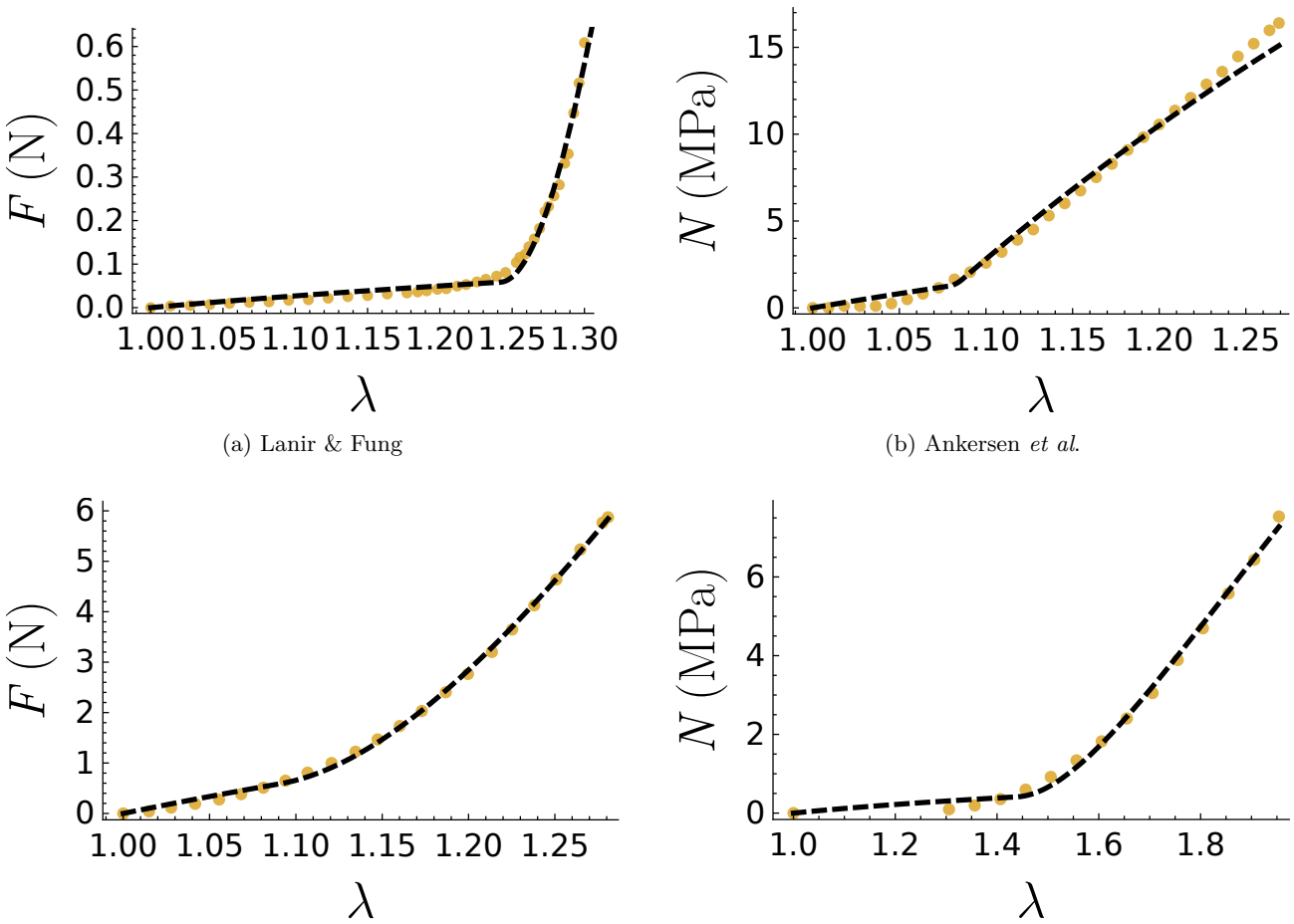

(a) Lanir & Fung

(b) Ankersen *et al.*

(c) Gunner *et al.*

(d) Dunn *et al.*

Figure 6: Closest fits (black, dashed lines) to the experimental tendon data (yellow circles) using the modified tendon model.

$$\pi(\boldsymbol{\theta}|\mathbf{y}) \propto \mathrm{t}_{2\alpha_\sigma}\left(\mathbf{y}; \mathbf{M}(\boldsymbol{\theta}), \frac{\beta_\sigma}{\alpha_\sigma}\mathbf{I}_d\right)\pi_0(\theta_1)\cdots\pi_0(\theta_h), \tag{18}$$

where $\mathrm{t}_{2\alpha_\sigma}$ represents a Student's t-distribution with $2\alpha_\sigma$ degrees of freedom and is known as the posterior-predictive.

4.1 The random walk Metropolis algorithm

The RWM algorithm that we use to sample from the posteriors of the parameters is the same as the one we used for modelling to tendon and is shown in Algorithm 1. Again, we adapt $\boldsymbol{\Sigma}$, the covariance matrix of the proposal distribution, in order to ensure that the algorithm runs as efficiently as possible. As before, we write $\boldsymbol{\Sigma} = \beta^2\boldsymbol{\zeta}$, where β^2 is a scaling parameter and $\boldsymbol{\zeta}$ is the covariance matrix of the model parameters. The expressions for β^2 and $\boldsymbol{\zeta}$ remain unchanged from the previous section. That is, $\boldsymbol{\zeta}$ is calculated from the covariance of the parameters over the last ten thousand simulations with β^2 initially set equal to one and its value changed at the end of each block of five hundred simulations. The conditions for changing β^2 at the end of a block of simulations are

- $\alpha_{\text{block}} < \alpha_{\text{LowerTol}}$: multiply β^2 by 0.95^2;
- $\alpha_{\text{LowerTol}} \leqslant \alpha_{\text{block}} \leqslant \alpha_{\text{UpperTol}}$: keep β^2 at the same value;
- $\alpha_{\text{UpperTol}} < \alpha_{\text{block}}$: multiply β^2 by 1.05^2,

Data		GT	ST	HGO	Tendon
L	δ	0.372	0.193	0.0386	0.243
	Δ (N)	0.0137	0.00930	0.00343	0.0124
A	δ	0.0559	0.131	1.20	0.501
	Δ (MPa)	0.0389	0.0898	0.690	0.401
G	δ	0.0498	0.0468	0.258	0.164
	Δ (N)	0.0123	0.0117	0.127	0.0525
D	δ	0.0321	0.0181	0.771	0.135
	Δ (MPa)	0.0379	0.0211	0.316	0.121

Table 1: Mean relative and absolute errors for the four models studied against experimental skin data. All values are given to three significant figures. For the data column, L = Lanir & Fung, A = Ankersen *et al.*, G = Gunner *et al.*, D = Dunn *et al.*

Model		An	D	G	L
HGO	c_{HGO} (MPa)	0	0	0	17.4
	k_1 (MPa)	7.44	0.286	5.26	0.267
	k_2	1.11	0.117	1.77	12.2
	A (mm^2)	N/A	N/A	0.342	0.00351
Tendon	$(1-\phi)\mu$ (MPa)	5.73	0.432	0.389	0.296
	ϕE (MPa)	72.9	36.1	8.60	53.7
	θ	0.126	0.850	0.573	0.334
	γ	0.0786	0.0440	0.0909	0.242
	A (mm^2)	N/A	N/A	6.04	0.333
ST	$(1-\phi)\mu$ (MPa)	1.63	0.0143	0.0338	0.231
	ϕE (MPa)	117	89.9	18.5	163
	a	1	1.17	1	1.23
	b	1.18	2.28	1.41	1.38
	A (mm^2)	N/A	N/A	4.56	0.403
GT	$(1-\phi)\mu$ (MPa)	0.518	0	0.0936	1.99
	ϕE (MPa)	125	176	5.56	364
	a	1.03	1.16	1.00	1.23
	c	1.03	2.30	1.20	1.28
	b	1.23	2.30	1.47	1.29
	A (mm^2)	N/A	N/A	16.9	0.0609

Table 2: Parameter values (to three significant figures) for each model's fit to the four data sets. To avoid confusion with c in the GT model, the stress-like parameter for the HGO model is written as c_{HGO}. For the data row, An = Ankersen *et al.*, G = Gunner *et al.*, D = Dunn *et al.*, and L = Lanir & Fung.

where $\alpha_{\mathrm{LowerTol}} = 0.184$ and $\alpha_{\mathrm{UpperTol}} = 0.284$ again. As occurred when fitting to tendon data in the algorithm, adaptation of $\mathbf{\Sigma}$ stops at the end of the burn-in phase, which we again consider to consist of the first 500,000 simulations.

Model		An		D		G		L	
		1	2	1	2	1	2	1	2
HGO	c_{HGO} (MPa)	0	0	0	0	5.28×10^{-9}	0	0.00136	0.0676
	k_1 (MPa)	7.44	7.44	0.286	0.286	2.01	0.00111	2.83	0.0103
	k_2	1.11	1.11	0.117	0.117	1.77	1.77	9.69	12.2
	A (mm^2)	N/A	N/A	N/A	N/A	0.897	1630	0.00114	0.906
	δ	1.2	1.2	0.771	0.771	0.258	0.258	0.386	0.386
	Δ (MPa)	0.690	0.690	0.316	0.316	0.127	0.127	0.0121	0.00343
Tendon	$(1-\phi)\mu$ (MPa)	0.273	0	0.432	0.432	8.54	2.51	0.00831	0.164
	ϕE (MPa)	118	427	63.3	36.4	7.3	189	4.74	149
	θ	0.511	1.56	1.47	0.854	0.103	1.56	0.621	0.822
	γ	0.0214	0.00984	0.0440	0.0440	0.159	0.0909	0.242	0.242
	A (mm^2)	N/A	N/A	N/A	N/A	0.706	0.937	11.9	0.600
	δ	0.855	0.194	0.135	0.135	1.10	0.164	0.243	0.243
	Δ (MPa)	0.0636	0.191	0.121	0.121	0.655	0.0525	0.0124	0.0124
ST	$(1-\phi)\mu$ (MPa)	20.1	9.03	0.0143	0.0143	5.38	4.11	0.906	0.417
	ϕE (MPa)	1300	240	89.9	89.9	216	1580	490	405
	a	1	1	1.33	1.33	1.02	1.00	1.13	1.22
	b	5.49	1.43	2.28	2.28	1.37	2.15	2.36	1.41
	A (mm^2)	N/A	N/A	N/A	N/A	0.802	0.402	0.184	0.223
	δ	2.51	0.989	0.0181	0.0181	0.802	0.0641	0.923	0.196
	Δ (MPa) 1.75	0.578	0.0211	0.0211	0.0181	0.0216	0.0618	0.00930	
GT	$(1-\phi)\mu$ (MPa)	20.3	20.3	3.06	0.0416	2.74	0.433	0.140	0.0772
	ϕE (MPa)	4560	583	4615	472	1180	86.9	773	33.2
	a	1.26	1.26	1.18	1.25	1.09	1	1.22	1.22
	c	2.50	9.87	1.64	2.97	2.41	1.54	1.30	1.30
	b	9.96	25.2	66.0	3.38	3.95	1.64	2.48	1.32
	A (mm^2)	N/A	N/A	N/A	N/A	1.95	3.81	0.664	1.20
	δ	2.53	2.53	0.0112	3.16	0.922	0.0641	0.192	0.193
	Δ (MPa)	1.83	1.82	0.0198	1.73	0.581	0.0216	0.00930	0.00930

Table 3: Parameter values, and average relative and absolute errors (to three significant figures) for the four models obtained from two additional fits to data. To avoid confusion with c in the GT model, the stress-like parameter for the HGO model is written as c_{HGO}. For the data row, An = Ankersen *et al.*, G = Gunner *et al.*, D = Dunn *et al.*, and L = Lanir & Fung.

Algorithm 1: RWM

Result: Estimate of the posterior distribution, $\pi(\boldsymbol{\theta})$
Input: $\pi_0(\theta_1)$, ..., $\pi_0(\theta_h)$;
Starting parameter vector, $\boldsymbol{\theta}_0$;
for $i = 1, \ldots, n$ **do**
  Propose $\boldsymbol{\theta}^* \sim \mathcal{N}(\boldsymbol{\theta}_{i-1}, \boldsymbol{\Sigma})$;
  Calculate $\kappa = \min\left(1, \frac{\mathrm{t}_{2\alpha_\sigma}\left(\mathbf{y}; \mathbf{M}(\boldsymbol{\theta}^*), \frac{\beta_\sigma}{\alpha_\sigma}\mathbf{I}_d\right)\pi_0(\boldsymbol{\theta}^*)}{\mathrm{t}_{2\alpha_\sigma}\left(\mathbf{y}; \mathbf{M}(\boldsymbol{\theta}_{i-1}), \frac{\beta_\sigma}{\alpha_\sigma}\mathbf{I}_d\right)\pi_0(\boldsymbol{\theta}_{i-1})}\right)$;
  Generate $u \sim \mathcal{U}(0,1)$;
  if $u \leqslant \kappa$ **then**
    $\boldsymbol{\theta}_i = \boldsymbol{\theta}^*$;
  else
    $\boldsymbol{\theta}_i = \boldsymbol{\theta}_{i-1}$;
  end
  Set $i = i + 1$;
end

5 Bayesian inference on the new model

Before we sample from the parameter posteriors with the algorithm detailed in the previous section, we need to transform the model parameters. As discussed in the previous chapter, we replace our current parameters, $\boldsymbol{\psi}$, with a set of transformed parameters, $\boldsymbol{\theta}$, whose support matches that of the proposal distribution, that is, $\mathbb{R}$. The non-negative and transformed parameter vectors, $\boldsymbol{\psi}$ and $\boldsymbol{\theta}$, respectively, are related to each other as follows

$$\boldsymbol{\theta} = \begin{pmatrix} \nu \\ \eta \\ \tau \\ \rho \end{pmatrix} = \begin{pmatrix} \log((1-\phi)\mu) \\ \log(\phi E) \\ \log(a-1) \\ \log(b-a) \end{pmatrix} = \mathrm{T}(\boldsymbol{\psi}), \tag{19}$$

where $\mathrm{T}(\boldsymbol{\psi})$ represents the invertible, non-linear transformation of the target parameters $\boldsymbol{\psi}$. To account for the non-linear transformation of parameters, we must instead calculate the pullback through the transformation map, $\tilde{\pi}(\boldsymbol{\theta})$, which has density

$$\tilde{\pi}(\boldsymbol{\theta}) = \pi(T^{-1}(\boldsymbol{\theta})|Y).|\det D_{T^{-1}}(\boldsymbol{\theta})|, \tag{20}$$

where, for this problem, $|\det D_{T^{-1}}(\boldsymbol{\theta})| = \exp(\nu+\eta+\tau+\rho)$. Finally, we assign a normal prior to the transformed parameters, that is, a log-normal prior to their exponents. Table 4 contains the values at which we assign a 0.005 and 99.995 cumulative probability distribution to it.

5.1 Synthetic data

The first run we did for the algorithm involved a synthetic data set. Fitting to synthetic data enables us to study the posterior distributions when we know the 'true' parameter values associated with the data and, thus, the ability of our algorithm to estimate parameter distributions. To create the synthetic data, we took the stretches used for the Ankersen data set and input the parameter vector $[(1-\phi)\mu, \phi E, a, b] = [5\text{ MPa}, 500\text{ MPa}, 1.05, 1.20]$ into the model. We then added IID noise to the output of the model. In order to test the algorithm rigorously and to account for the fact that, with these skin data sets, we have not fit directly to the experimentally measured values, we chose to make the synthetic data noisy. We chose a variance of 0.1 for the IID noise. To determine the parameters for the prior distributions of the parameters, we determined the values at which we expected to find 0.5% and 99.5% cumulative probability distribution (CPD) and used the quantile function of the log-normal distribution to determine the values of the prior parameters. The values used for an estimate at 0.5% and 99.5% CPD are listed in Table 4. Finally, for the synthetic data we chose the burn-in length to be 500,000 simulations, with a total of 1.5 million simulations performed.

To visualise the marginal posterior distributions and the two-dimensional joint distributions that we obtain from fitting to the synthetic data in the algorithm, we have included these plots, along with valuations of the correlations between the parameters, in a plot matrix, Figure 7. To analyse the fit to data, we have taken a subset of 50,000 parameter vectors from our samples, that is, positions of the Markov chain, and calculated the mean stress values, at each stretch in the data set, of this set of vectors. Furthermore, we have added a confidence band that shows all stress values within 5σ of the mean stress, Figure 8.

From Figure 7, we see that, despite the noisiness of the values we fit to, the values for ϕE, a, and, especially, b lie in the relatively narrow region of high posterior probability. The parameter $(1-\phi)\mu$ lies more towards the tail of the distribution, while still having a non-negligible posterior probability. This parameter, however, is much smaller than ϕE because the collagen fibrils, when taut, dominate the response to the deformation. The importance of the value of $(1-\phi)\mu$ to the stress response is lessened, therefore. The contour lines of the joint distributions are elliptical, and the marginal posteriors are smooth, demonstrating that the algorithm fits well to this synthetic data. Furthermore, Figure 8 shows that close fits to the synthetic data are achieved in the algorithm. Even though the data is noisy, the mean stresses of the 50,000 chosen vectors lie close to the data and the confidence band contains all the data points. This is the case for all stages of the J-shaped curve, demonstrating the ability of the ST model to describe tissue behaviour when different microstructural phenomena are driving the macroscopic behaviour.

5.2 Ankersen *et al.* data

We now analyse the algorithm's predictions when we fit the ST model to the skin data collected by Ankersen *et al.* For this data set, we chose the burn-in length to be 500,000 simulations, with a total of 2.5 million simulations performed. Figure 9 contains the estimated posteriors and contour plots obtained from the adaptive RWM algorithm, and Figure 10 shows a confidence band of 5σ around the mean stress-strain curve of 50,000 parameter

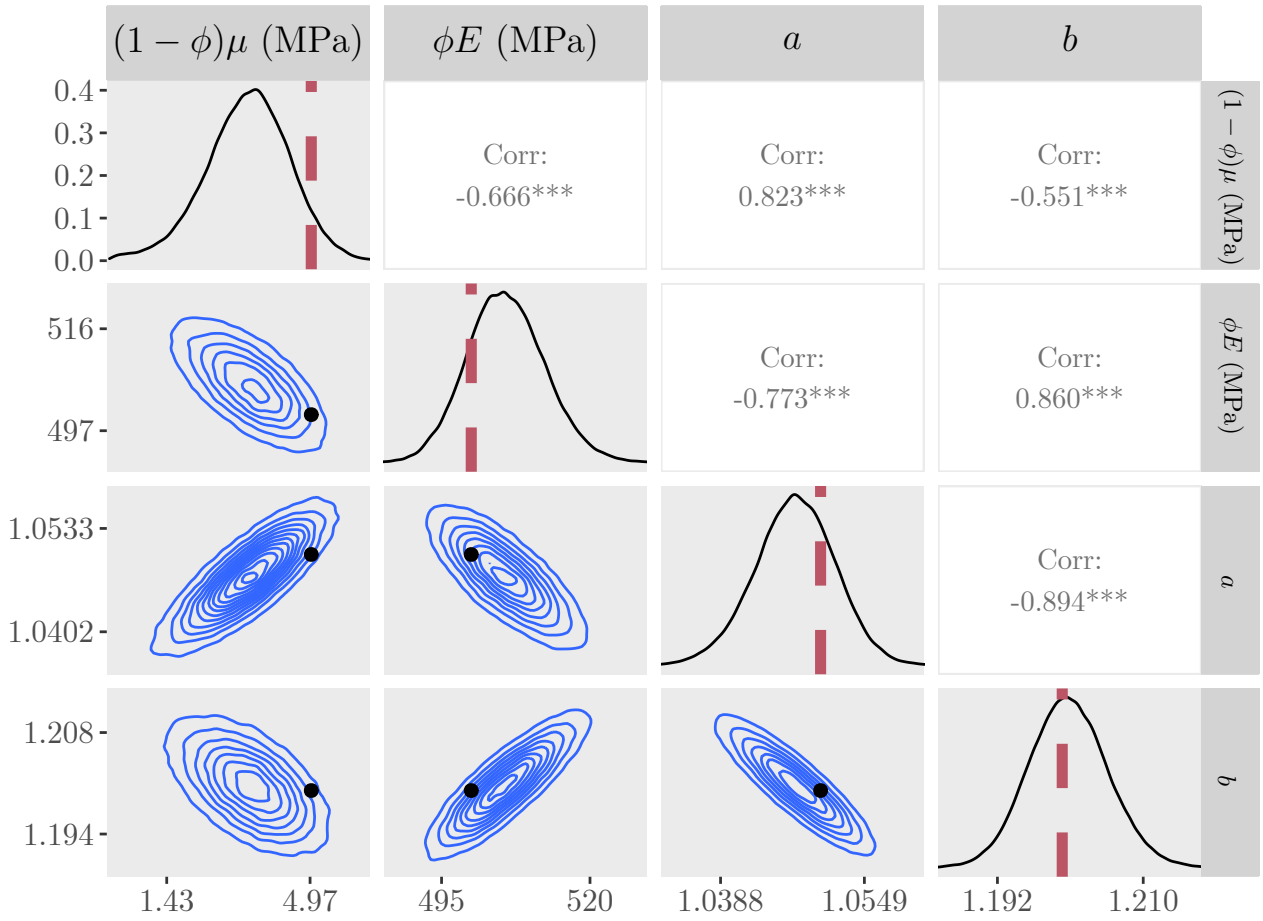

Figure 7: Approximate posteriors and contour plots of the parameters for the synthetic data. Samples were thinned by a factor of ten to create this plot matrix.

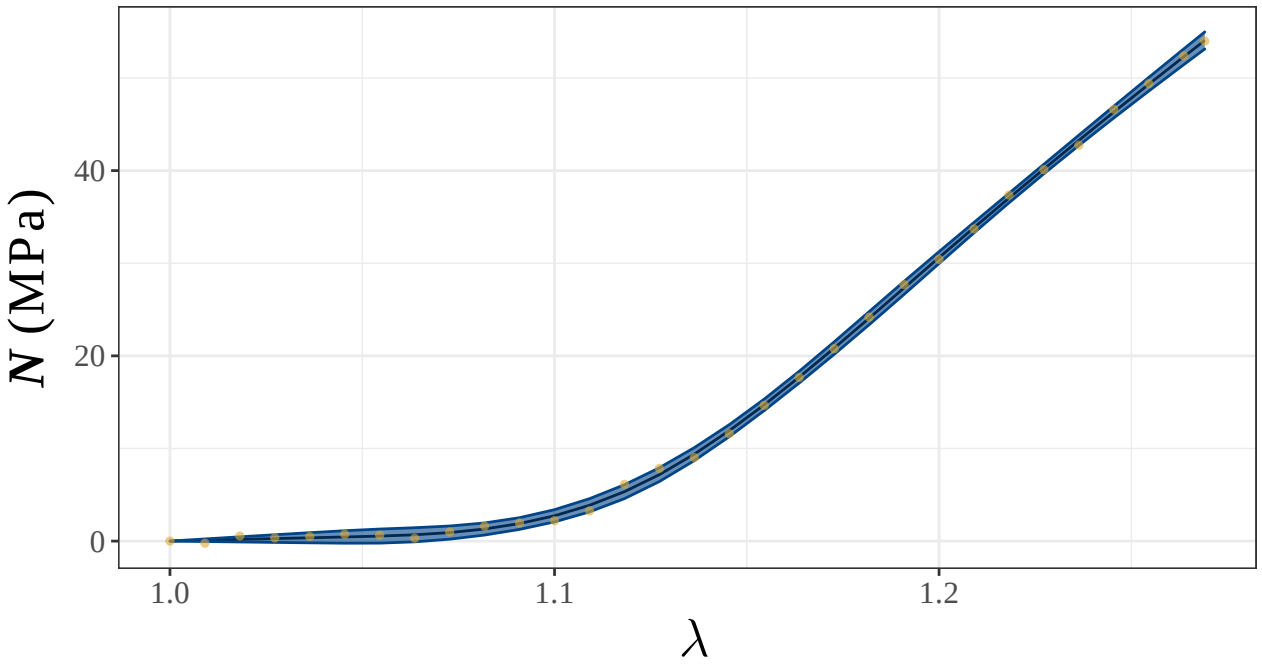

Figure 8: The 5σ confidence band (blue) around the mean (black line) of the predicted stresses from 50,000 parameter vectors from the Markov chains against the synthetic data (yellow dots).

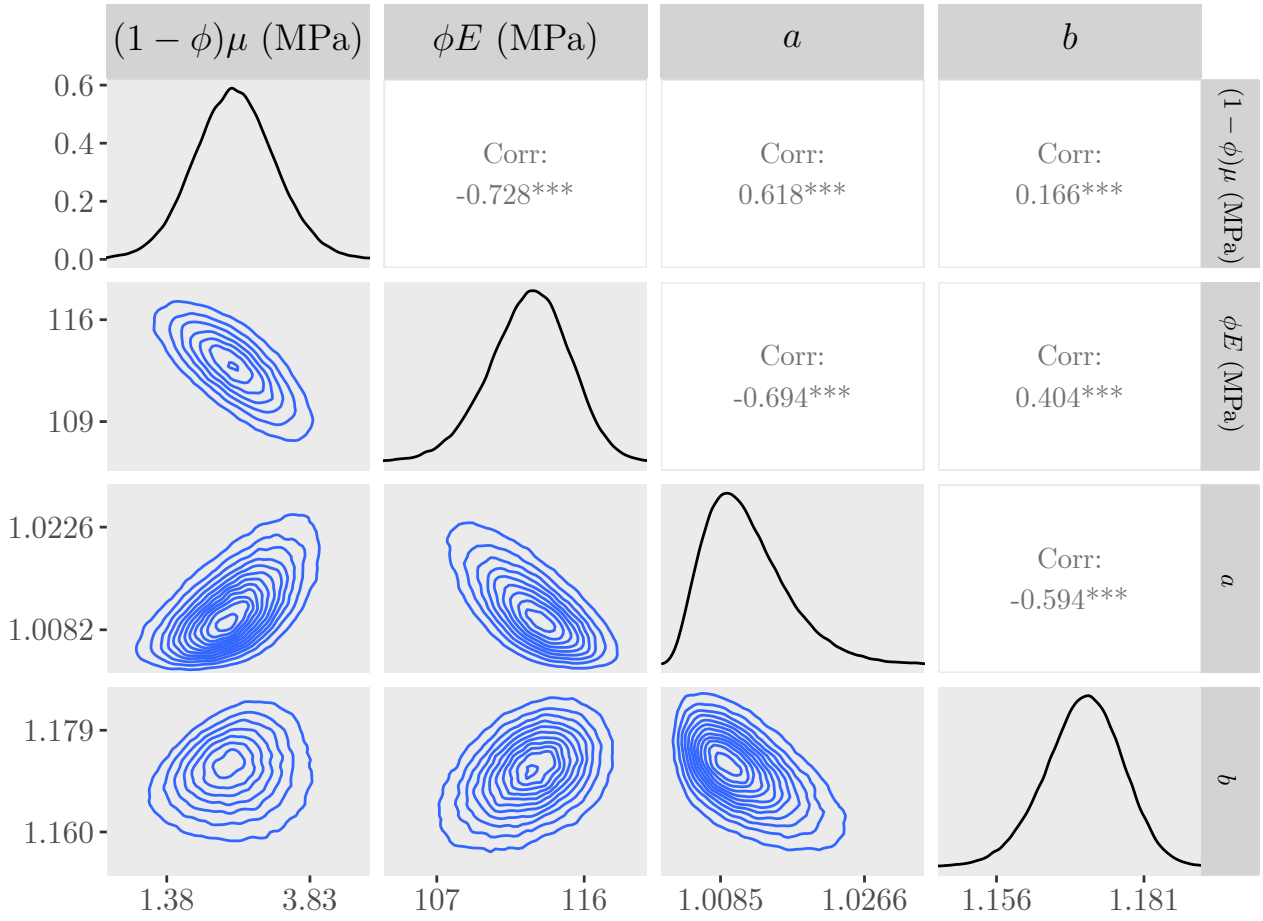

Figure 9: Approximate posteriors and contour plots of the parameters for the Ankersen *et al.* data. Samples were thinned by a factor of ten.

vectors from the Markov chains plotted against the data. As in the synthetic example, the empirical posterior distribution is smooth, implying a good level of convergence of the tuned adaptive RWM algorithm, with narrow marginal posteriors. The contours of the joint distribution are also approximately elliptical. For the structural parameter ϕE, we have a physically realistic posterior: the 95% credible interval for ϕE is 107-117 MPa, rounded to the nearest whole number, which is feasible compared to literature values for ϕ and E in skin, [17], [18], [25], [26]. The stretches at which the first and last collagen fibrils straighten and tauten are also realistic for skin. The large positive and negative correlations also produce physically realistic conclusions. For instance, the largest negative correlation is between $(1-\phi)\mu$ and ϕE, which tells us that if the NCM is more compliant, according to the model, then the collagen fibrils need to be stiffer to compensate. As with the tendon problem, the RWM MCMC has given us insights into the parameters that demonstrate the benefit of full posterior characterisation as opposed to the more traditional optimisation approach. Furthermore, when we plot the stresses of a subset of vectors from the samples obtained in the algorithm, we can see that the model fits well to data throughout the entirety of the stress-strain curve. As with the synthetic data, this demonstrates the ability of the ST model to describe elastic behaviour governed by different microstructural phenomena. The confidence band is narrower for larger stretches, when the tissue is stiffer, than for smaller stretches.

5.3 Dunn *et al.* data

Finally, we study the algorithm's predictions when we fit to the data taken from Dunn *et al.* For this data set, we chose the burn-in length to be one million simulations, with a total of three million simulations performed. Figure 11 contains the estimated posteriors and contour plots obtained from the adaptive RWM algorithm, and Figure 12 shows a confidence band of 5σ around the mean stress-strain curve of 50,000 parameter vectors from the Markov chains plotted against the data. As opposed to when the synthetic and Ankersen *et al.* data sets were fit to, the

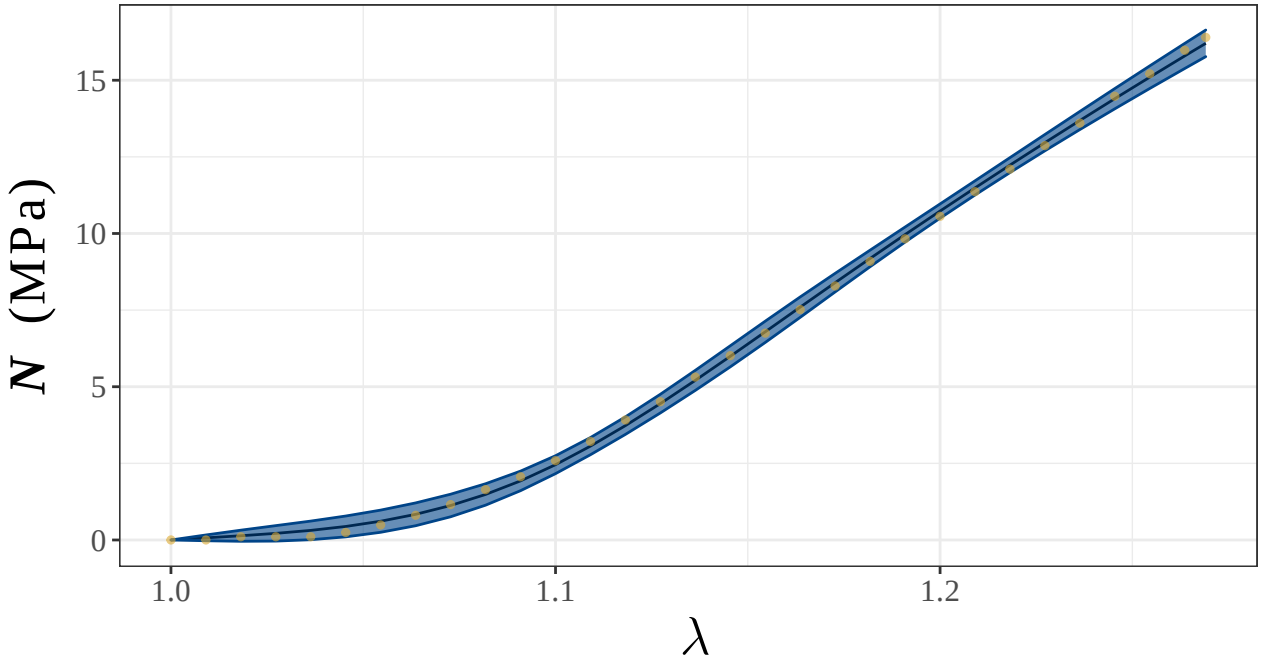

Figure 10: The 5σ confidence band (blue) around the mean (black line) of the predicted stresses from 50,000 parameter vectors from the Markov chains against the Ankersen *et al.* data (yellow dots).

marginal posteriors for this data set are much harder to sample from. In particular, the posterior for ϕE is very broad, with a long tail that stretches over 1 GPa. The marginal for b, which shares a high positive correlation with ϕE, also possesses a long tail. As soft tissues can be subjected to plastic deformation and failure, the values of b that lie on the tails of the distribution are physically unrealistic. Additionally, the contour lines of the joint distributions are not elliptical and are complex in shape. On the other hand, the means of the stress for 50,000 parameter vectors selected from the Markov chain closely match the experimental data. The 5σ confidence band, however, is broader than for either the synthetic data or the data collected by Ankersen *et al.* This is to be expected with the broadness of the posterior for ϕE.

6 Discussion

In this chapter, we have successfully applied a microstructural model that we first tested again mechanical tendon data to study skin data as well. When fitted to experimental data collected from testing on the skin of humans, rabbits, and pigs using non-linear optimisation, our microstructural SEF performed favourably when compared to the fits produced by both a semi-structural model that has been widely used in the literature and another microstructural model of tendon behaviour. As with tendon data, we have managed to implement, for noisy, synthetic data and for experimental pigskin data, an adaptive RWM algorithm that efficiently characterises posterior probability distributions of model parameters. Furthermore, for the pigskin data, the 95% credible intervals for the important physical parameter ϕE contain realistic values when compared to existing literature values of these quantities. The parameter vectors sampled in the algorithm also fit closely to experimental data.

If there had been time available, the work currently discussed in this chapter would have been expanded upon. We would have examined the effect that incorporating dispersion into our microstructural model would have had on the likely values of the model parameters, according to the RWM algorithm. We would have been particularly interested in determining whether accounting for dispersion in the model would have led to an increase in the predicted value of ϕE. This would seem likely as currently all the fibrils are assumed to be oriented in the direction of stretch, so each fibril extends. However, if the fibrils were dispersed, some fibrils, according to the model, may remain slack. If fewer fibrils tauten according to the model, then the model will need to compensate in terms of other microstructural properties in order for the experimental data to be fit to closely. One possible way for the model to compensate would be for it to predict that the fibrils that do tauten are stiffer than when we do not account for dispersion. The 95% credible interval for ϕE when the Ankersen *et al.* data were fit to was found to

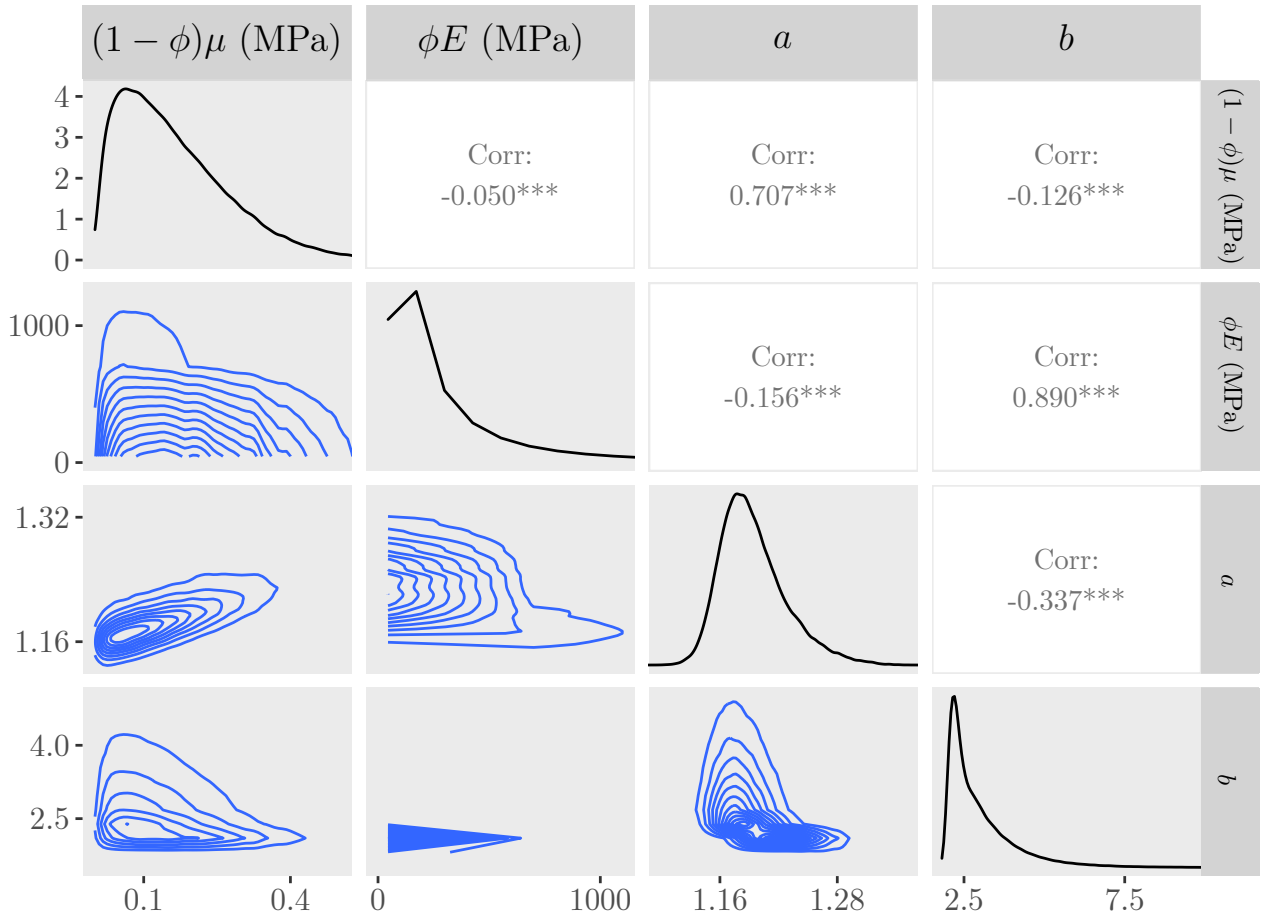

Figure 11: Approximate posteriors and contour plots of the parameters for the Dunn *et al.* data. Samples were thinned by a factor of ten.

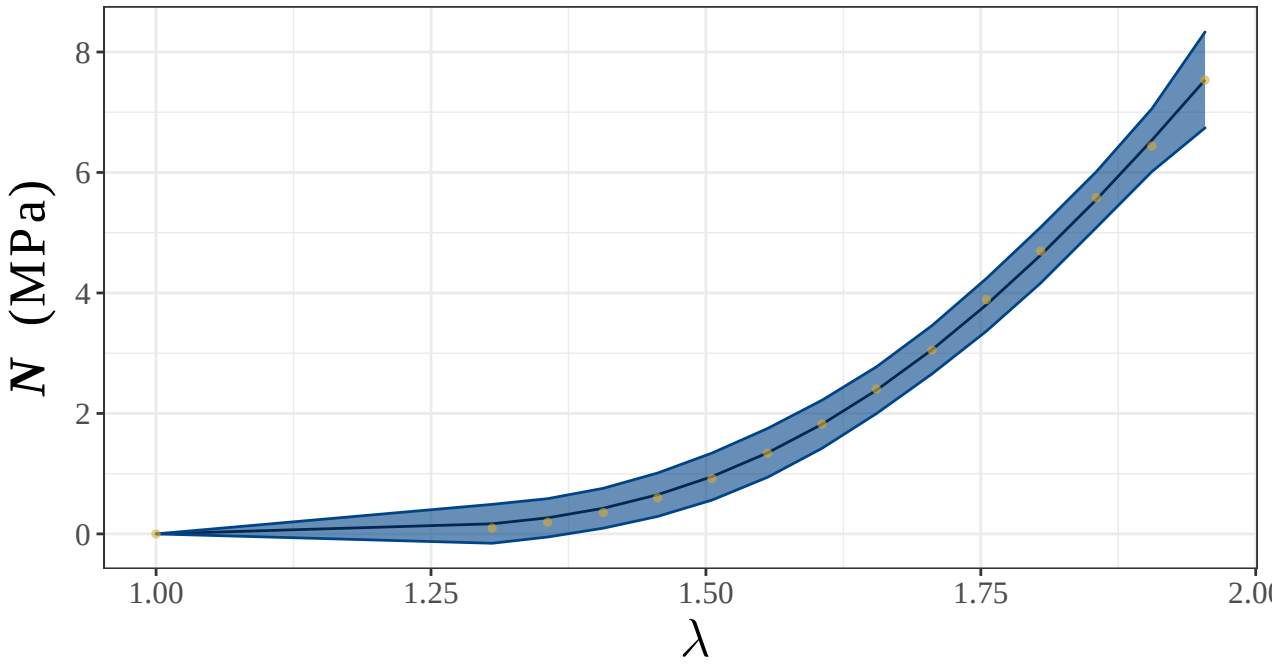

Figure 12: The 5σ confidence band (blue) around the mean (black line) of the predicted stresses from 50,000 parameter vectors from the Markov chains against the Dunn *et al.* data (yellow dots).

Parameter	0.005 CPD	0.995 CPD	Motivation
$(1-\phi)\mu$ (MPa)	0.001	10	**Lower**: motivated by the values of μ for tendon fascicles obtained by Purslow [27] **Higher**: inclusive upper bound.
ϕE (MPa)	3.072	13,600	**Lower**: inclusive lower bound using low estimates of $\phi = 0.096$ [9] and $E = 32$ MPa by [17]. **Higher**: inclusive upper bound using an estimate of $\phi = 0.85$ and $E = 16$ GPa given by [28] and [29], respectively.
$a - 1$	0.005	0.3 (S, A), 0.8 (D)	**Lower**: attempt to provide an inclusive lower bound. **Higher**: assumption that at least one fibril has tautened by the end of the stress-strain data we fit to.
$b - a$	0.005	0.3 (S, A), 0.8 (D)	**Lower**: attempt to provide an inclusive lower bound. **Higher**: attempt to provide an inclusive upper bound.

Table 4: A table of values used to calculate the mean and variance of the prior distributions of the ST model's parameters. In order to allow the posterior parameter space to be fully sampled in the RWM algorithm, the priors were designed to be inclusive of a wide range of parameter values.

be 107-117 MPa. While some reported values of the collagen fibril Young's modulus would support this credible interval for ϕE, other literature values would support a higher value for E. Accounting for dispersion in our model would also allow it to be tested against multi-axial experimental stress-strain data or uniaxial strains performed in multiple directions on the same skin sample. These more-general data demonstrate the ability of skin to resist deformations in multiple directions, which is due to skin consisting of a network of fibrils, and they would provide a more-complicated problem to test our model against.

In addition to dispersion, there may be other microstructural phenomena that our microstructural model does not account for. The marginal posteriors that we have discussed in this chapter assume that the current microstructural model is correct. If the model is adapted in the future to include additional phenomena relevant to macroscopic mechanical behaviour, the current estimates of our model parameters may change, as we discussed in the previous paragraph about the potential effect that incorporating dispersion into the model could have on the predicted value of ϕE. However, the quality-of-fit to data of the new microstructural model and the results of the RWM algorithm when the synthetic and extracted Ankersen *et al.* data were fit to are encouraging signs that the assumptions of our current model are not incorrect.

When we attempted to fit the Dunn *et al.* data set in the RWM algorithm, we encountered problems with sampling from the parameter posteriors, despite using a longer burn-in period for fitting to this data. The extracted stress-strain data of Dunn *et al.* contain fewer points than the extracted data of Ankersen *et al.*, with the first stress value extracted from the data being calculated at a stretch ratio of around 1.3. The results produced by the RWM algorithm for the extracted Dunn *et al.* data were possibly hampered by the low-resolution and poor quality of the values fit to. The extraction method used for the data fit to in this chapter, counting pixels in *Microsoft Paint*, could be replaced with a program that automates more of the pixel-counting process, thereby reducing sources of human error. Preferably, however, future work would source data that has been made available for general use by researchers. Higher-resolution skin data would also be a useful test of our model. For the tendon problem, the high-resolution superficial digital flexor tendon data produced smoother marginal posteriors and more-elliptical contour lines for the joint distribution than when we fitted to lower-resolution stress-strain data taken from larger data sets recorded by Goh *et al.* To better understand the RWM algorithm's ability to estimate parameter values when fitting to skin data, it would be an appropriate extension to the work covered in this chapter to fit our model to high-resolution data recorded in an experiment.

Additionally, in this chapter, we chose to use the Nelder-Mead algorithm to perform nonlinear optimisation. There may be better methods for finding a global best fit to data contained within the *Mathematica* function *NonlinearModelFit*. This is suggested by fits to data using pseudorandom starting values, which return different parameter vectors. This fact, however, further motivates our choice of MCMC, where we construct probability

distributions rather than find a local best fit to data.

Beyond improving the quality of the data fit to, using more-efficient statistical methods, such as Hamiltonian Monte Carlo, may help to better sample from complex posteriors. As well as potentially affecting the predicted values of model parameters, incorporating dispersion into the microstructural model would allow us to apply our model to study the mechanics of multi-axial skin deformations. This would include the potential of fitting to multiple mechanical tests of the same tissue, which would provide a greater test of the model's ability to accurately describe how the microstructure influences the macroscopic behaviour of the tissue.

A The piecewise constants for our microstructural SEF

The values of the piecewise constants for the general triangular distribution are

$$A(I_4) = \begin{cases} 0, & I_4 < a^2, \\ -\frac{a^2}{(b-a)(c-a)}, & a^2 \leqslant I_4 \leqslant c^2, \\ \frac{c^2}{(c-a)(b-c)} - \frac{a^2}{(b-a)(c-a)}, & c^2 < I_4 \leqslant b^2, \\ -1, & I_4 > b^2, \end{cases} \tag{21}$$

$$B(I_4) = \begin{cases} 0, & I_4 < a^2, \\ \frac{2a\log a}{(b-a)(c-a)}, & a^2 \leqslant I_4 \leqslant c^2, \\ \frac{2a\log a}{(b-a)(c-a)} - \frac{2c\log c}{(c-a)(b-c)}, & c^2 < I_4 \leqslant b^2, \\ \frac{2a\log a}{(b-a)(c-a)} + \frac{2b\log b}{(b-a)(b-c)} - \frac{2c\log c}{(c-a)(b-c)}, & I_4 > b^2, \end{cases} \tag{22}$$

$$C(I_4) = \begin{cases} 0, & I_4 < a^2, \\ \frac{1}{(b-a)(c-a)}, & a^2 \leqslant I_4 \leqslant c^2, \\ -\frac{1}{(b-a)(b-c)}, & c^2 < I_4 \leqslant b^2, \\ 0, & I_4 > b^2, \end{cases} \tag{23}$$

$$D(I_4) = \begin{cases} 0, & I_4 < a^2, \\ -\frac{2a}{(b-a)(c-a)}, & a^2 \leqslant I_4 \leqslant c^2, \\ \frac{2b}{(b-a)(b-c)}, & c^2 < I_4 \leqslant b^2, \\ 0, & I_4 > b^2, \end{cases} \tag{24}$$

$$G(I_4) = \begin{cases} 0, & I_4 < a^2, \\ \frac{a^2\log a}{(b-a)(c-a)} - \frac{5a^2}{2(b-a)(c-a)}, & a^2 \leqslant I_4 \leqslant c^2, \\ \frac{2a^2\log a}{(b-a)(c-a)} - \frac{c^2\log c}{(c-a)(b-c)} - \frac{5a^2}{2(b-a)(c-a)} + \frac{5c^2}{2(b-c)(c-a)}, & c^2 \leqslant I_4 \leqslant b^2, \\ \frac{a^2\log a}{(b-a)(c-a)} - \frac{c^2\log c}{(c-a)(b-c)} + \frac{b^2\log b}{(b-c)(b-a)} - \frac{5a^2}{2(b-a)(c-a)} + \frac{5c^2}{2(b-c)(c-a)} - \frac{5b^2}{2(b-a)(c-a)}, & I_4 > b^2. \end{cases} \tag{25}$$

The values of the piecewise constants for the symmetric triangular distribution are

$$A^*(I_4) = \begin{cases} 0, & I_4 < a^2, \\ -\frac{2a^2}{(b-a)^2}, & a^2 \leqslant I_4 \leqslant \left(\frac{a+b}{2}\right)^2, \\ \frac{(b^2-a^2+2ab)}{(b-a)^2}, & \left(\frac{a+b}{2}\right)^2 < I_4 \leqslant b^2, \\ -1, & I_4 > b^2, \end{cases} \tag{26}$$

$$B^*(I_4) = \begin{cases} 0, & I_4 < a^2, \\ \frac{4a\log a}{(b-a)^2}, & a^2 \leqslant I_4 \leqslant \left(\frac{a+b}{2}\right)^2, \\ \frac{4a\log a}{(b-a)^2} - \frac{4(b+a)}{(b-a)^2}\log\left(\frac{a+b}{2}\right), & \left(\frac{a+b}{2}\right)^2 < I_4 \leqslant b^2, \\ \frac{4a\log a}{(b-a)^2} + \frac{4b\log b}{(b-a)^2} - \frac{4(b+a)}{(b-a)^2}\log\left(\frac{a+b}{2}\right), & I_4 > b^2, \end{cases} \tag{27}$$

$$C^*(I_4) = \begin{cases} 0, & I_4 < a^2, \\ \frac{2}{(b-a)^2}, & a^2 \leqslant I_4 \leqslant \left(\frac{a+b}{2}\right)^2, \\ -\frac{2}{(b-a)^2}, & \left(\frac{a+b}{2}\right)^2 < I_4 \leqslant b^2, \\ 0, & I_4 > b^2, \end{cases} \tag{28}$$

$$D^*(I_4) = \begin{cases} 0, & I_4 < a^2, \\ -\frac{4a}{(b-a)^2}, & a^2 \leqslant I_4 \leqslant \left(\frac{a+b}{2}\right)^2, \\ \frac{4b}{(b-a)^2}, & \left(\frac{a+b}{2}\right)^2 < I_4 \leqslant b^2, \\ 0, & I_4 > b^2. \end{cases} \tag{29}$$

$$G^*(I_4) = \begin{cases} 0, & I_4 < a^2, \\ \frac{2a^2\log a}{(b-a)^2} - \frac{5a^2}{(b-a)^2}, & a^2 \leqslant I_4 \leqslant \left(\frac{a+b}{2}\right)^2, \\ \frac{2a^2\log a}{(b-a)^2} - \frac{(a+b)^2\log\left(\frac{a+b}{2}\right)}{(b-a)^2} - \frac{5a^2}{(b-a)^2} + \frac{5(a+b)^2}{2(b-a)^2}, & \left(\frac{a+b}{2}\right)^2 \leqslant I_4 \leqslant b^2, \\ \frac{2a^2\log a}{(b-a)^2} - \frac{(a+b)^2\log\left(\frac{a+b}{2}\right)}{(b-a)^2} + \frac{2b^2\log b}{(b-a)^2} - \frac{5a^2}{(b-a)^2} + \frac{5(a+b)^2}{2(b-a)^2} - \frac{5b^2}{(b-a)^2}, & I_4 > b^2. \end{cases} \tag{30}$$

B Approximate Bayesian Computation

Before we used RWM MCMC, we tried to study this problem with a statistical technique called *Approximate Bayesian Computation* (ABC). A likelihood function is not used in ABC. Instead, parameter vectors are proposed by sampling from the prior distribution, inserting the parameter vector into the model, and measuring the closeness between the model's output and the observed, experimental data through a distance criterion. For example, the distance criterion we used was the L_2-norm, that is, the Euclidean distance, between the Ankersen *et al.* data set and the predicted stress-strain vector created by inserting the proposed parameter vector into the SEF. If the distance criterion is satisfied, the parameter vector is retained, and if the distance criterion is not satisfied, the parameter vector is discarded. At the conclusion of the algorithm, the retained parameter vectors are used to estimate the posterior distribution of the parameters.

ABC, therefore, is applied to problems where a likelihood cannot be determined, or is computationally expensive to work out for each proposed parameter vector in an algorithm. For soft tissue modelling, we erroneously believed, at first, that the likelihood could not be derived for the deterministic models that we use. However, we just needed to introduce IID noise to the system. With the introduction of noise, we derived the likelihood function for this problem and were able to use standard MCMC instead of ABC. This is preferable because MCMC assigns some probability of being accepted to any proposed parameter vector, regardless of the quality of fit to data, assuming that the proposed parameters lie in the support of the prior distributions. This enables the tails of the posterior distributions to be explored within the algorithm and full characterisation of the posterior to take place. In ABC, these parameter vectors will fail the distance criterion, or if not, the distance criterion may be too lenient. Furthermore, the models used in this chapter are highly non-linear, and so relatively small changes in their proposed values may lead to relatively large changes in the model's output, that is, the simulated data set. Therefore, there may be parameter vectors that satisfy the distance criterion, but nearby vectors in the parameter space may not satisfy the criterion. In that case, the algorithm may only propose new acceptable parameter vectors very slowly. It is, therefore, preferable to not have a distance criterion that may become stuck in the simulation and which requires fine-tuning to find the right balance between accepting too many parameter vectors and accepting too few parameter vectors.

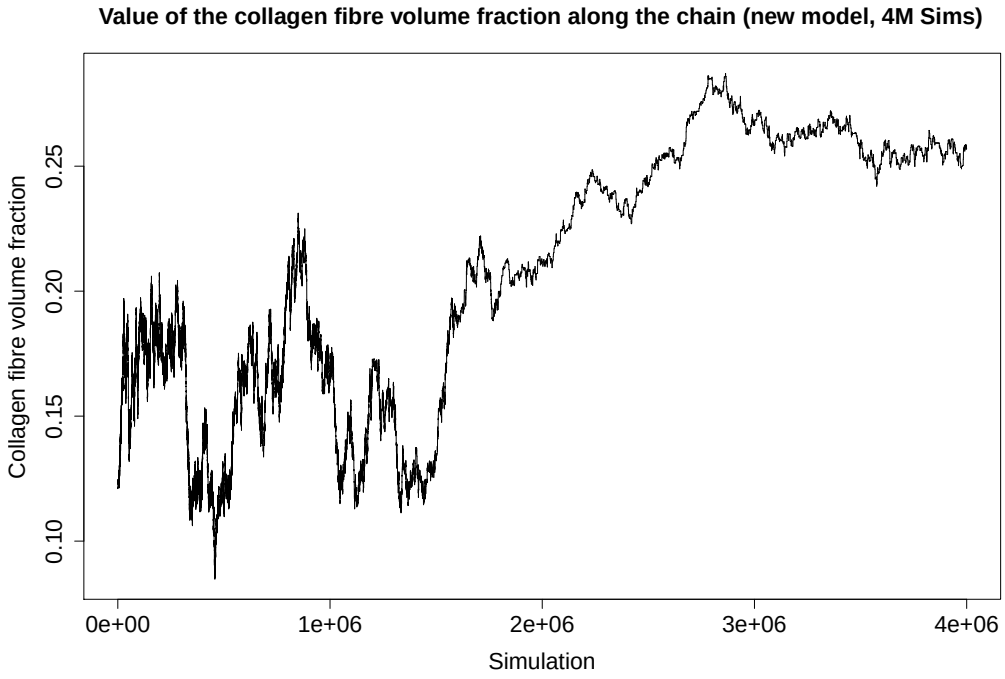

(a)

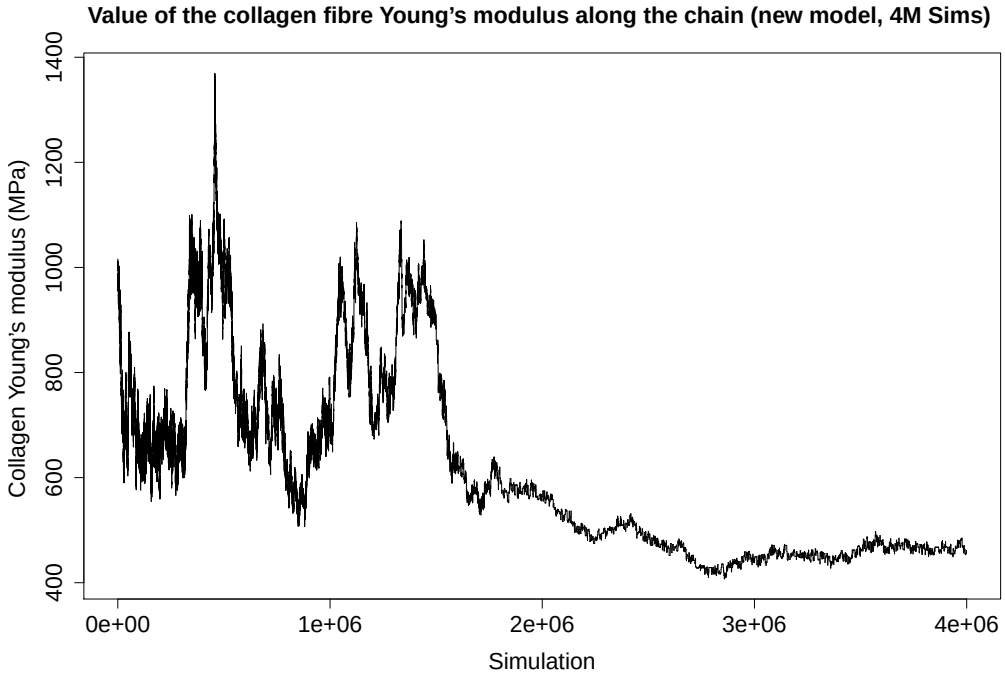

(b)

Figure 13: Trace plots of the values of (a) ϕ and (b) E. These trace plots seem to be correlated, with the value of one parameter likely to increase if the other decreases. This provides good evidence for combining the parameters into one, ϕE, to improve the efficiency of our RWM algorithm.

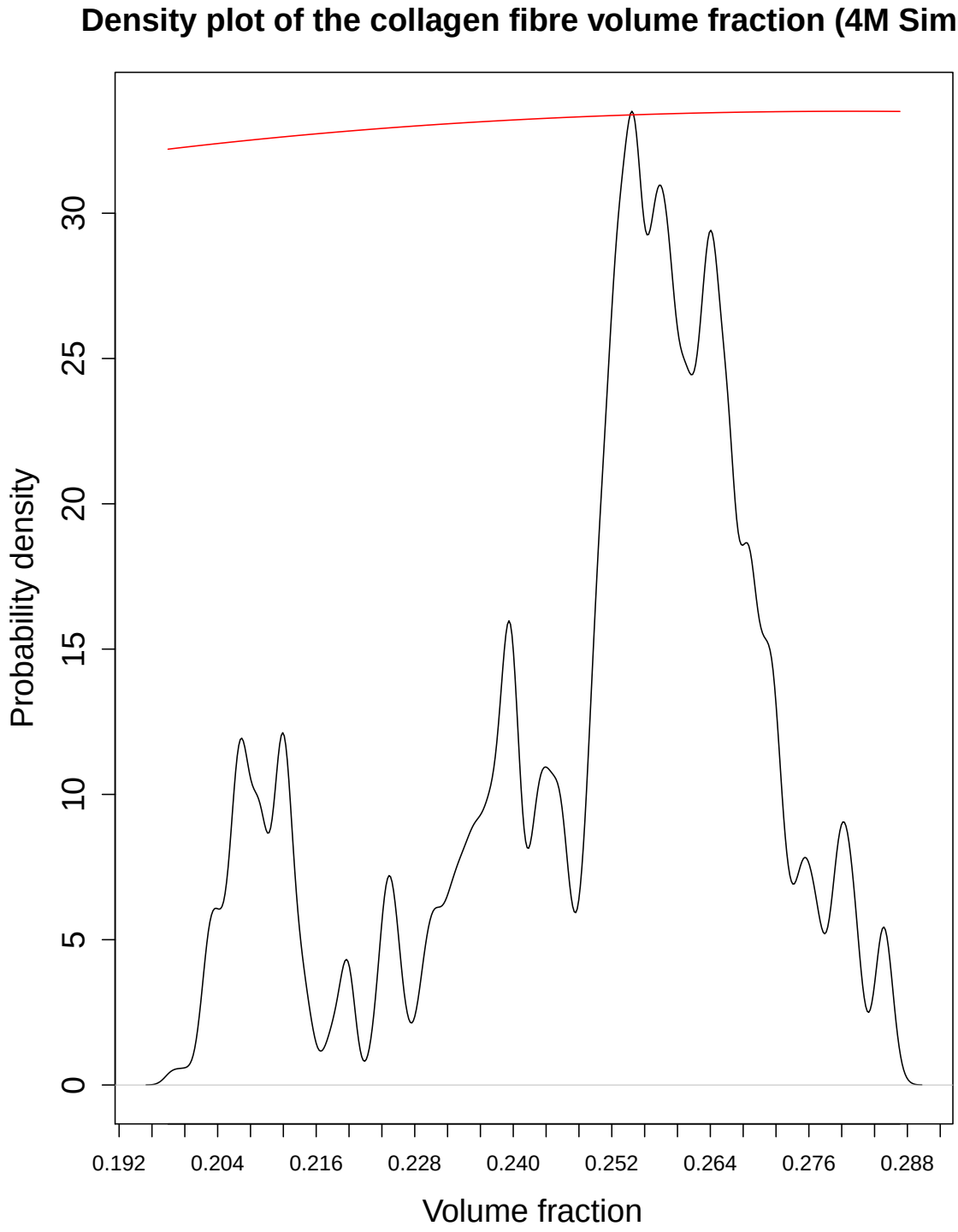

Figure 14: The posterior distribution of ϕ. The red line represents the prior distribution of ϕ, normalised to the height of the posterior (in order for the prior line to be visible on the graph). We did this in order to compare the overall form of the estimated posterior distribution to the prior. In actuality, however, the estimated posterior is not well-defined.

To demonstrate the problems with ABC, we present Figure 13, which contains trace plots of the values of firstly ϕ and E over four million simulations in ABC, and Figure 14, which consists of an estimated posterior distribution for ϕ based on the four million simulations. Firstly, the sampling in Figure 13 is slow to move around the parameter space, with only small moves in the parameter space being accepted. In better, more efficient sampling, the posterior parameter space would be covered in much fewer simulations than this ABC algorithm would take. This makes the ABC process computationally expensive, negating one potential advantage of ABC. We can see the effect that slow, inefficient sampling has on the estimated parameter posteriors with the posterior shown in Figure 14. In contrast to the posteriors found when fitting to synthetic data in the RWM algorithm or the data set from Ankersen *et al.*, Figures 7 and 9, the posterior in Figure 14 is not well-defined and is likely not to represent the true range of probable values for the parameter because of the aforementioned inefficient sampling. It should be noted, however, that these figures were created in 2019. Since then, there will have been improvements that we have made to our understanding of sampling from the posterior parameter space that will have benefited our RWM algorithm. However, MCMC is still a much more appropriate technique to use for this problem for the aforementioned reasons. As the plots were created in 2019, they do not look similar to the rest of the plots in this chapter.

References

[1] P. A. Payne, "Measurement of properties and function of skin," *Clinical Physics and Physiological Measurement*, vol. 12, no. 2, pp. 105–129, May 1991. DOI: 10.1088/0143-0815/12/2/001. [Online]. Available: https://doi.org/10.1088/0143-0815/12/2/001.

[2] S. Vijayavenkataraman, W. Lu, and J. Fuh, "3d bioprinting of skin: A state-of-the-art review on modelling, materials, and processes," *Biofabrication*, vol. 8, no. 3, p. 032 001, 2016.

[3] T. Lee, S. Y. Turin, A. K. Gosain, I. Bilionis, and A. Buganza Tepole, "Propagation of material behavior uncertainty in a nonlinear finite element model of reconstructive surgery," *Biomechanics and Modeling in Mechanobiology*, vol. 17, no. 6, pp. 1857–1873, Dec. 2018, ISSN: 1617-7940. DOI: 10.1007/s10237-018-1061-4. [Online]. Available: https://doi.org/10.1007/s10237-018-1061-4.

[4] E. McLafferty, C. Hendry, and A. Farley, "The integumentary system: Anatomy, physiology and function of skin," English, *Nursing Standard (through 2013)*, vol. 27, no. 3, pp. 35–42, Sep. Sep 19, CODEN - NSTAEU, ISSN: 00296570. [Online]. Available: https://manchester.idm.oclc.org/login?url=https://www.proquest.com/scholarly-journals/integumentary-system-anatomy-physiology-function/docview/1081981576/se-2?accountid=12253.

[5] Z. Zaidi and S. W. Lanigan, "Skin: Structure and function," in *Dermatology in Clinical Practice*. London: Springer London, 2010, pp. 1–15, ISBN: 978-1-84882-862-9. DOI: 10.1007/978-1-84882-862-9_1. [Online]. Available: https://doi.org/10.1007/978-1-84882-862-9_1.

[6] F. H. Silver, J. W. Freeman, and D. DeVore, "Viscoelastic properties of human skin and processed dermis," *Skin Research and Technology*, vol. 7, no. 1, pp. 18–23, 2001. DOI: https://doi.org/10.1034/j.1600-0846.2001.007001018.x. eprint: https://onlinelibrary.wiley.com/doi/pdf/10.1034/j.1600-0846.2001.007001018.x. [Online]. Available: https://onlinelibrary.wiley.com/doi/abs/10.1034/j.1600-0846.2001.007001018.x.

[7] A. Delalleau, G. Josse, J.-M. Lagarde, H. Zahouani, and J.-M. Bergheau, "A nonlinear elastic behavior to identify the mechanical parameters of human skin in vivo," *Skin Research and Technology*, vol. 14, no. 2, pp. 152–164, 2008. DOI: https://doi.org/10.1111/j.1600-0846.2007.00269.x. eprint: https://onlinelibrary.wiley.com/doi/pdf/10.1111/j.1600-0846.2007.00269.x. [Online]. Available: https://onlinelibrary.wiley.com/doi/abs/10.1111/j.1600-0846.2007.00269.x.

[8] F. Khatyr, C. Imberdis, P. Vescovo, D. Varchon, and J.-M. Lagarde, "Model of the viscoelastic behaviour of skin in vivo and study of anisotropy," *Skin Research and Technology*, vol. 10, no. 2, pp. 96–103, 2004. DOI: https://doi.org/10.1111/j.1600-0846.2004.00057.x. eprint: https://onlinelibrary.wiley.com/doi/pdf/10.1111/j.1600-0846.2004.00057.x. [Online]. Available: https://onlinelibrary.wiley.com/doi/abs/10.1111/j.1600-0846.2004.00057.x.

[9] F. H. Silver, G. P. Seehra, J. W. Freeman, and D. DeVore, "Viscoelastic properties of young and old human dermis: A proposed molecular mechanism for elastic energy storage in collagen and elastin," *Journal of Applied Polymer Science*, vol. 86, no. 8, pp. 1978–1985, 2002.

[10] W. Wong, T. Joyce, and K. Goh, "Resolving the viscoelasticity and anisotropy dependence of the mechanical properties of skin from a porcine model," *Biomechanics and modeling in mechanobiology*, vol. 15, no. 2, pp. 433–446, 2016.

[11] V. R. Sherman, Y. Tang, S. Zhao, W. Yang, and M. A. Meyers, "Structural characterization and viscoelastic constitutive modeling of skin," *Acta Biomaterialia*, vol. 53, pp. 460–469, 2017, ISSN: 1742-7061. DOI: https://doi.org/10.1016/j.actbio.2017.02.011. [Online]. Available: https://www.sciencedirect.com/science/article/pii/S1742706117301174.

[12] Y.-c. Fung, *Biomechanics: mechanical properties of living tissues*. Springer Science & Business Media, 2013.

[13] G. A. Holzapfel, T. C. Gasser, and R. W. Ogden, "A new constitutive framework for arterial wall mechanics and a comparative study of material models," *Journal of elasticity and the physical science of solids*, vol. 61, no. 1, pp. 1–48, Jul. 2000, ISSN: 1573-2681. DOI: 10.1023/A:1010835316564. [Online]. Available: https://doi.org/10.1023/A:1010835316564.

[14] T. Shearer, "A new strain energy function for the hyperelastic modelling of ligaments and tendons based on fascicle microstructure," *J. Biomech*, vol. 48, no. 2, pp. 290–297, 2015, ISSN: 0021-9290. DOI: https://doi.org/10.1016/j.jbiomech.2014.11.031. [Online]. Available: https://www.sciencedirect.com/science/article/pii/S0021929014006198.

[15] A. Ní Annaidh, K. Bruyère, M. Destrade, M. D. Gilchrist, and M. Otténio, "Characterization of the anisotropic mechanical properties of excised human skin," *Journal of the Mechanical Behavior of Biomedical Materials*, vol. 5, no. 1, pp. 139–148, 2012, ISSN: 1751-6161. DOI: https://doi.org/10.1016/j.jmbbm.2011.08.016. [Online]. Available: https://www.sciencedirect.com/science/article/pii/S1751616111002219.

[16] A. V. Rawlings, "Ethnic skin types: Are there differences in skin structure and function?1," *International Journal of Cosmetic Science*, vol. 28, no. 2, pp. 79–93, 2006. DOI: https://doi.org/10.1111/j.1467-2494.2006.00302.x. eprint: https://onlinelibrary.wiley.com/doi/pdf/10.1111/j.1467-2494.2006.00302.x. [Online]. Available: https://onlinelibrary.wiley.com/doi/abs/10.1111/j.1467-2494.2006.00302.x.

[17] J. S. Graham, A. N. Vomund, C. L. Phillips, and M. Grandbois, "Structural changes in human type i collagen fibrils investigated by force spectroscopy," *Experimental Cell Research*, vol. 299, no. 2, pp. 335–342, 2004, ISSN: 0014-4827. DOI: https://doi.org/10.1016/j.yexcr.2004.05.022. [Online]. Available: https://www.sciencedirect.com/science/article/pii/S0014482704003052.

[18] N. Sasaki and S. Odajima, "Stress-strain curve and young's modulus of a collagen molecule as determined by the x-ray diffraction technique," *Journal of Biomechanics*, vol. 29, no. 5, pp. 655–658, 1996, ISSN: 0021-9290. DOI: https://doi.org/10.1016/0021-9290(95)00110-7. [Online]. Available: https://www.sciencedirect.com/science/article/pii/0021929095001107.

[19] Y. Lanir and Y. Fung, "Two-dimensional mechanical properties of rabbit skin—ii. experimental results," *Journal of biomechanics*, vol. 7, no. 2, 171IN9175–174 182, 1974.

[20] J. Ankersen, A. E. Birkbeck, R. D. Thomson, and P. Vanezis, "Puncture resistance and tensile strength of skin simulants," *Proceedings of the Institution of Mechanical Engineers, Part H: Journal of Engineering in Medicine*, vol. 213, no. 6, pp. 493–501, 1999, PMID: 10635698. DOI: 10.1243/0954411991535103. eprint: https://doi.org/10.1243/0954411991535103. [Online]. Available: https://doi.org/10.1243/0954411991535103.

[21] C. Gunner, W. Hutton, and T. Burlin, "The mechanical properties of skin in vivo—a portable hand-held extensometer," *British Journal of Dermatology*, vol. 100, no. 2, pp. 161–163, 1979.

[22] M. G. Dunn, F. H. Silver, and D. A. Swann, "Mechanical analysis of hypertrophic scar tissue: Structural basis for apparent increased rigidity," *Journal of Investigative Dermatology*, vol. 84, no. 1, pp. 9–13, 1985.

[23] M. Jiang, Z. T. Lawson, V. Erel, *et al.*, "Clamping soft biologic tissues for uniaxial tensile testing: A brief survey of current methods and development of a novel clamping mechanism," *Journal of the Mechanical Behavior of Biomedical Materials*, vol. 103, p. 103 503, 2020, ISSN: 1751-6161. DOI: https://doi.org/10.1016/j.jmbbm.2019.103503. [Online]. Available: https://www.sciencedirect.com/science/article/pii/S1751616119310628.

[24] C. Edwards and R. Marks, "Evaluation of biomechanical properties of human skin," *Clinics in dermatology*, vol. 13, no. 4, pp. 375–380, 1995.

[25] H. Miyazaki and K. Hayashi, "Tensile tests of collagen fibers obtained from the rabbit patellar tendon," *Biomedical Microdevices*, vol. 2, no. 2, pp. 151–157, 1999.

[26] F. Silver and W. Landis, "Viscoelasticity, energy storage and transmission and dissipation by extracellular matrices in vertebrates," in *Collagen: Structure and Mechanics*, P. Fratzl, Ed. Boston, MA: Springer US, 2008, pp. 133–154, ISBN: 978-0-387-73906-9. DOI: 10.1007/978-0-387-73906-9_6. [Online]. Available: https://doi.org/10.1007/978-0-387-73906-9_6.

[27] P. P. Purslow, "The shear modulus of connections between tendon fascicles," in *2009 IEEE Toronto International Conference Science and Technology for Humanity (TIC-STH)*, IEEE, 2009, pp. 134–136.

[28] K. L. Goh, D. F. Holmes, H.-Y. Lu, *et al.*, "Ageing Changes in the Tensile Properties of Tendons: Influence of Collagen Fibril Volume Fraction," *J. Biomech. Eng.*, vol. 130, no. 2, Mar. 2008, 021011, ISSN: 0148-0731. DOI: 10.1115/1.2898732. eprint: https://asmedigitalcollection.asme.org/biomechanical/article-pdf/130/2/021011/5489672/021011_1.pdf. [Online]. Available: https://doi.org/10.1115/1.2898732.

[29] A. Gautieri, S. Vesentini, A. Redaelli, and R. Ballarini, "Modeling and measuring visco-elastic properties: From collagen molecules to collagen fibrils," *International Journal of Non-Linear Mechanics*, vol. 56, pp. 25–33, 2013, Soft Matter: a nonlinear continuum mechanics perspective, ISSN: 0020-7462. DOI: https://doi.org/10.1016/j.ijnonlinmec.2013.03.012. [Online]. Available: https://www.sciencedirect.com/science/article/pii/S0020746213000590.

Chapter 6

Conclusions

6.1 Introduction

We have two aims for the concluding chapter of this thesis. In the first part of the conclusion, we analyse the work that has been completed. To do this, we look at the topics covered in each chapter and relate them to one another in order to define what has been accomplished and to ascertain whether the physical and mathematical motivations developed in the initial chapters have been successfully applied to the research. Then, we briefly describe some future areas of research that would both build upon the progress made and introduce novel mathematics that would advance the field of soft tissue modelling.

6.2 Summary of the thesis

In Chapter 1 of this thesis, we introduced fibrous soft tissues and their constituents. We started by describing some of the complex macroscopic phenomena we observe when soft tissues are deformed and explaining why the microstructure accounts for these complex macroscale behaviours. We provided further evidence of the close relationship between the microscale and macroscale in soft tissues by describing how changes to the microstructure, caused by natural processes such as ageing or damage, affect the mechanics of tissues on larger length scales. Having established that the microstructure influences tissue behaviour on the macroscale, we then examined the constituents that are frequently found in fibrous soft tissues in more depth. We described how they aggregate and are structured in a tissue, what their functions are, and what properties they themselves exhibit. Through this, we determined that collagen, because it is much stiffer than the other components of the extracellular matrix, is the constituent that confers stiffness to soft tissues. We then introduced the field of soft tissue modelling, using our understanding of the importance of the microstructure to explain why it is advantageous to incorporate soft tissue microstructure into models of macroscopic mechanical behaviour. Finally, we explained why advances in soft tissue modelling have a beneficial impact on wider society. Therefore, this introductory chapter provided motivation for the research done in the rest of this thesis. It answered both why we want to study soft tissue behaviour and why we want to account directly for microstructural phenomena when modelling soft tissues.

In Chapter 2 of this thesis, we described the mathematical preliminaries that we use to de-

velop hyperelastic microstructural strain-energy functions (SEFs) and quantify uncertainty in the estimates of our parameter values. We first defined the mathematical terminology needed to describe the bulk properties of continua and quantitatively describe a deformation applied to a solid. We then derived the balance and conservation laws that all materials, including deformed objects, must adhere to. We used this collection of laws to show why a material-specific constitutive law is necessary to describe completely the mechanics of a deformed soft tissue. Having determined the need for a constitutive equation to describe soft tissue deformation fully, we then used the properties of SEFs and the symmetry properties of materials to derive the constitutive equations for isotropic materials, transversely isotropic materials, and orthotropic materials. Then, we explained the usefulness of accounting for uncertainty in this modelling problem and introduced Bayesian statistical methods. We defined the fundamental rule of Bayesian statistics, the prior and posterior probability distributions, and the likelihood function, three quantities of particular importance in Bayesian statistics. We then introduced some statistical techniques that allow inference to be performed on posterior distributions for which the exact form of the distribution is not known. In these introductions, we also explained why we would infer the values of model parameters using Markov chain Monte Carlo (MCMC) methods later in the thesis. Therefore, the work in this chapter provided us with the understanding, and motivated our use, of the mathematical expressions and techniques we would use later in the thesis to study soft tissue behaviour and calculate uncertainty in the values of model parameters.

In Chapter 3 of this thesis, we reviewed the history of soft tissue modelling in the literature. Too many models have been created to discuss each one in detail, so we studied a representative subset that elucidates the results of different modelling approaches. We started by examining phenomenological models of soft tissues, identifying that they cannot provide us with information on the relationship between the microstructure and the macroscale tissue due to their use of parameters that do not have a physical basis for inclusion in the model. However, we also ascertained that these models are tractable, ease to use, and are able to fit experimental data well. Next, we discussed semi-structural models, determining that microstructural considerations are key to the overall form of semi-structural SEFs, but these SEFs possess phenomenological parameters that limit our understanding of tissue microstructure. We then examined structural models and their use of parameters that possess a physical basis for inclusion. We described how these models have the potential to improve our understanding of tissue microstructure through the macroscopic behaviour they describe, and predict. However, we also demonstrated the need to choose the phenomena incorporated in the tissue and make careful assumptions of tissue behaviour in order for microstructural SEFs to retain their tractability. Finally, we showcased the versatility of Bayesian statistical methods by introducing some of the fields that these methods have been applied to in order to investigate uncertainty in model parameters. The work in this chapter reinforced the viability and usefulness of our stated direction of research. This chapter also provided insights into how to proceed with creating a new microstructural model that is easy to use and how to expand upon the work that has previously been described in the literature.

In Chapter 4, we derived two versions of our microstructural model, the versions differing in the form of the triangular distribution used to model the variation in recruitment stretch in the collagen fibrils, and a random walk Metropolis Markov chain Monte Carlo (RWM MCMC) algorithm that could find probable values for the parameters and construct credible intervals around them. We used the introductory chapter and the literature review to motivate the construction of the new model, which, due to simplifying but realistic assumptions about the tissue constituents, produced, for both versions of the microstructural model, a tractable SEF that contained only physical parameters. Both versions of the model fit experimental tendon data well, performing favourably in comparison to a semi-structural, widely used SEF and a microstructural SEF developed to fit tendon data. This was true for both low-resolution and high-resolution data sets. We introduced independently and identically distributed noise to the experimental data and, from this, derived the likelihood function. We were then able to find an expression for the posterior distribution, up to a normalisation constant, where the dependence of the posterior on the variance of the noise was integrated out, thanks to the choice of a conjugate prior for the variance of the noise. After transforming the model parameters so that their support extended over the real axis, and accounting for this transformation, sampling in the algorithm was efficient, especially for high-resolution data, and we found realistic values for the model parameters. In this chapter, we applied the motivations we received from the work we performed in Chapter 1 and Chapter 3 and the mathematical framework we developed in Chapter 2 to create a microstructural model that is tractable, contains physically relevant parameters, and can experimental tendon data well. Furthermore, our choice of Bayesian statistics to describe uncertainty was vindicated by the ability to integrate out the dependence of the noise parameter we introduced to account for the uncertainty. Thus, we could focus on inferring the model parameters.

In Chapter 5, we extended the use of our model to fit uniaxial tensile test data on skin samples. We showed that both versions of the microstructural model fit experimental data on a second soft tissue well and that efficient sampling can still occur in the RWM MCMC algorithm when mechanical skin data is fitted. Furthermore, we showed that the algorithm still works even for the noisier skin data, where the stress-strain values that were fitted were calculated indirectly rather than being taken from a data file uploaded by the authors of the research. Finally, we used our understanding of the structure of fibrous soft tissues from Chapter 1 to determine how the material covered in the chapter needs to be expanded upon. We identified, using existing literature models that we reviewed earlier in the thesis, how we could incorporate these required extensions into the model microstructurally.

6.3 Future work

Having summarised the work we have completed in this thesis, we can now describe in more detail ways to potentially expand upon it. Throughout, we have attempted to relate our research to the fundamentals of microstructural soft tissue modelling, continuum mechanics, and Bayesian statistics that we analysed in the first three chapters. Consequently, in this

section of the chapter, we also relate the areas of expansion to the key features of these mathematical fields.

6.3.1 Furthering the complexity of the model

We have fit a microstructural transversely isotropic model that assumes collagen fibrils are co-aligned with one another to uniaxial tensile data on tendons and skin. We have achieved close fits to data that compare favourably to fits achieved by a couple of other models that have previously been described and used in the literature. However, for more general deformations of some soft tissues, such as the skin, for example, a transversely isotropic model would not be able to adequately describe the observed behaviour. For instance, if we stretch the skin in one direction and assume the collagen fibrils co-align with the direction of stretch, then stretch in a direction perpendicular to the first direction, the current model predicts that the collagen fibrils contract and the skin is linearly elastic and compliant. This does not occur in actuality. Skin may be more compliant in certain directions, but it still stiffens when stretched far enough. Therefore, we would need to increase the complexity of the current model to account for multi-axial tissue behaviour. For a microstructural model, it would be ideal to directly incorporate phenomena that confers non-linear elastic behaviour in an arbitrary direction, and there are ways to achieve this.

By assuming that there exists one family of collagen fibrils, where the fibrils are aligned with respect to one another, and that the non-collagenous matrix is isotropic, we have produced a transversely isotropic model, where the preferred direction aligns with the orientation of the collagen fibrils. However, we could introduce a more complicated level of anisotropy, while still retaining the other assumptions that we made for the transversely isotropic model, by introducing at least one more family of collagen fibrils that possesses a different orientation to the first family. We have discussed models that assume multiple fibril families in the literature review, and the modifications to the constitutive equation required for a second fibril family have been covered in the literature also. The additional fibril family, or families, could be modelled using the same SEF as the first family of collagen fibrils or not. By assuming in the model that there are collagen fibrils oriented in multiple directions, we increase the number of directions where the modelled tissue can be stretched with at least some initially crimped collagen fibrils elongating and eventually tautening. It is this feature of collagen fibrils that accounts, in the model we have developed in this thesis, for the non-linear elastic behaviour. Imaging of tissues such as skin and arteries has shown that collagen fibrils are not all oriented in the same direction, so assuming that there are multiple families of fibrils in the tissue would be an extension to the model that is justified biologically.

Treating collagen fibrils as being situated in multiple families, with each family of fibrils oriented in a distinct direction, is not the only way that we can model the fact that fibrils are splayed in some biological soft tissues. We can also explicitly model the dispersion of fibril orientations with, say, a probability distribution. This would also allow for more general deformations to be studied, with some fibrils straightening, according to a model that accounts

for dispersion, for more deformations than in the non-dispersed transversely isotropic model. By making simplifying assumptions about the nature of dispersion in a tissue, we can retain a transversely isotropic model. For example, fibril dispersion could be modelled using a Von Mises distribution, with fibrils exhibiting rotational symmetry around the mean fibril direction. However, in the literature review, we identified shortcomings in the Generalised Structure Tensor approach to modelling dispersion that was described in the GOH model. The Latorre-Montans model attempted to fix the tension-compression switch of the GOH model, but discontinuities in the stress were identified. The Holzapfel-Ogden model contains a tension-compression switch that allows for fibril dispersion to be described in a single parameter that changes the pseudoinvariant I_4 and, thus, features in the SEF. This tension-compression switch, however, is only tractable for particular deformations, an example being a uniaxial stretch along the mean fibril direction, with the fibril dispersion governed by the Von Mises distribution. Therefore, to account for dispersion within a single family of fibrils, the more computationally expensive *Angular Integration* (AI) approach can be applied to a general deformation. Especially for the RWM MCMC algorithm, code will need to be heavily optimised to run the algorithm for many simulations when the AI approach to dispersion is included in the microstructural model.

6.3.2 More advanced Bayesian statistical methods

In this thesis, we have developed an RWM MCMC algorithm that enables uncertainty in the parameters of a model of soft tissue deformation to be estimated. We have been able to sample efficiently in the algorithm for certain tendon and skin data sets, producing clearly defined marginal posteriors for which the majority of the probability mass is situated in a narrow region. Furthermore, two-dimensional contour plots have largely shown the correlation structure between parameters. This MCMC method is guaranteed to eventually converge on the target distribution, that is, the posterior probability distribution for the parameters. That convergence, however, can be slow. Especially for higher-resolution data sets, the form of the marginal posterior, which is focused on a narrow range of values with smooth estimated curves, suggests that convergence has been reached for sampling after the burn-in phase has ended. The adaptive methods we employ in the burn-in phase, along with the large length of the burn-in phase, help to ensure that the samples we obtain are from the target distribution. However, in other Monte Carlo methods, we can change the proposal distribution from a Gaussian centred on the current position of the Markov chains to one that is more efficient. Namely, the Metropolis-Adjusted Langevin Algorithm (MALA) and the Hamiltonian Monte Carlo (HMC) algorithm have been developed through physical analogues, and they efficiently sample from the target posterior distribution because they use the gradient of the log-posterior to inform proposal distributions. By introducing information about the posterior into the choice of proposed vectors, MALA and HMC will spend more simulations, for a given number of simulations, in regions of high posterior probability than RWM MCMC. However, an iteration of MALA or HMC is more computationally intensive than RWM MCMC because proposals have to be created using discrete-time methods such as, in

HMC, the leapfrog algorithm. Complicating things further, MALA and HMC also contain parameters that need tuning correctly for the algorithm to run properly.

Outside of employing a more efficient algorithm to sample the posterior probability space, there are other ways that we can apply other Bayesian statistical techniques to the analysis of soft tissue modelling. In particular, the RWM MCMC algorithm that we have used in this thesis only samples the posterior distribution of one model at a time. Reversible Jump MCMC is an established technique that enables models which contain different numbers of unknown parameters to be compared against one another when it comes to fitting to a particular data set. In this approach, not only can posteriors for model parameters be accurately estimated, but we can study the relative effectiveness of a group of models in fitting to the observed data. More generally, Bayes' factors are quantities that analyse the probability of two different models being the correct model to explain a particular data set. With the variety of soft tissue models that have been described in the literature, plus with more models being created as time goes on, model comparisons seem a logical avenue for future research.

6.3.3 Collaboration with experimentalists

Finally, throughout this thesis, we have discussed how accurate microstructural models of tissue behaviour could potentially be used in a wider array of situations than phenomenological models. This is because microstructural models are intimately connected to properties that can be measured independently via experiments. It is important, therefore, to test this potential. If microstructural models were found to be good predictors, after the microstructural parameters of the model have been calculated experimentally and then inserted into the model, of physical stress-strain behaviour then it would have ramifications in any real-life situation where it would be desirable to estimate the behaviour of *in vivo* tissue samples. Although, we have to note that differences are likely to exist between skin mechanics *in vivo* and *ex vivo*. Further, independent imaging would be a good test for the validity of the assumptions of our model. For example, is a triangle distribution, either symmetric or general, a good approximation to the distribution of recruitment stretches amongst the collagen fibrils in a tissue sample? Would distributions such as the *log* distribution, the *step* distribution, or the *trapezium* distribution, which would also produce tractable microstructural SEFs if the other model assumptions remained the same, be a better approximation to the real distribution? For these reasons, closer collaboration between model creators, mechanical experimental scientists, and imaging (or non-destructive) experimental scientists working on the same set of soft tissue samples would likely be a productive undertaking.

References

[1] M. Kim, G. Pons-Moll, S. Pujades, S. Bang, J. Kim, M. J. Black, and S.-H. Lee, "Data-driven physics for human soft tissue animation," *ACM Trans. Graph.*, vol. 36, no. 4, Jul. 2017, ISSN: 0730-0301. DOI: 10.1145/3072959.3073685. [Online]. Available: https://doi.org/10.1145/3072959.3073685.

[2] H. Jayabal, N. N. Dingari, and B. Rai, "A linear viscoelastic model to understand skin mechanical behaviour and for cosmetic formulation design," *International Journal of Cosmetic Science*, vol. 41, no. 3, pp. 292–299, 2019. DOI: https://doi.org/10.1111/ics.12535. eprint: https://onlinelibrary.wiley.com/doi/pdf/10.1111/ics.12535. [Online]. Available: https://onlinelibrary.wiley.com/doi/abs/10.1111/ics.12535.

[3] N. Famaey, E. Verbeken, S. Vinckier, B. Willaert, P. Herijgers, and J. V. Sloten, "In vivo soft tissue damage assessment for applications in surgery," *Medical Engineering & Physics*, vol. 32, no. 5, pp. 437–443, 2010, ISSN: 1350-4533. DOI: https://doi.org/10.1016/j.medengphy.2010.04.002. [Online]. Available: https://www.sciencedirect.com/science/article/pii/S1350453310000767.

[4] W. F. Larrabee Jr., "A finite element model of skin deformation. i. biomechanics of skin and soft tissue: A review," *The Laryngoscope*, vol. 96, no. 4, pp. 399–405, 1986. DOI: https://doi.org/10.1288/00005537-198604000-00012. eprint: https://onlinelibrary.wiley.com/doi/pdf/10.1288/00005537-198604000-00012. [Online]. Available: https://onlinelibrary.wiley.com/doi/abs/10.1288/00005537-198604000-00012.

[5] J. H. T. Bates and B. Ma, "A progressive rupture model of soft tissue stress relaxation," *Annals of Biomedical Engineering*, vol. 41, no. 6, pp. 1129–1138, Jun. 2013, ISSN: 1573-9686. DOI: 10.1007/s10439-013-0789-3. [Online]. Available: https://doi.org/10.1007/s10439-013-0789-3.

[6] M. Safadi and M. Rubin, "Modeling rate-independent hysteresis in large deformations of preconditioned soft tissues," *International Journal of Solids and Structures*, vol. 51, no. 18, pp. 3265–3272, 2014, ISSN: 0020-7683. DOI: https://doi.org/10.1016/j.ijsolstr.2014.05.025. [Online]. Available: https://www.sciencedirect.com/science/article/pii/S0020768314002194.

[7] D. Hulmes, "Collagen diversity, synthesis and assembly," in *Collagen: Structure and Mechanics*, P. Fratzl, Ed. Boston, MA: Springer US, 2008, pp. 15–47, ISBN: 978-0-387-73906-9. DOI: 10.1007/978-0-387-73906-9_2. [Online]. Available: https://doi.org/10.1007/978-0-387-73906-9_2.

[8] N. Sasaki and S. Odajima, "Stress-strain curve and young's modulus of a collagen molecule as determined by the x-ray diffraction technique," *Journal of Biomechanics*, vol. 29, no. 5, pp. 655–658, 1996, ISSN: 0021-9290. DOI: https://doi.org/10.1016/0021-9290(95)00110-7. [Online]. Available: https://www.sciencedirect.com/science/article/pii/0021929095001107.

[9] M. Brennan and P. F. Davison, "Influence of the telopeptides on type i collagen fibrillogenesis," *Biopolymers*, vol. 20, no. 10, pp. 2195–2202, 1981. DOI: https://doi.org/10.1002/bip.1981.360201012. eprint: https://onlinelibrary.wiley.com/doi/pdf/10.1002/bip.1981.360201012. [Online]. Available: https://onlinelibrary.wiley.com/doi/abs/10.1002/bip.1981.360201012.

[10] M. J. Buehler, "Molecular architecture of collagen fibrils: A critical length scale for tough fibrils," *Current Applied Physics*, vol. 8, no. 3, pp. 440–442, 2008, AMN-3 (Third International Conference on Advanced Materials and Nanotechnology), ISSN: 1567-1739. DOI: https://doi.org/10.1016/j.cap.2007.10.058. [Online]. Available: https://www.sciencedirect.com/science/article/pii/S1567173907002283.

[11] K. Gelse, E. Pöschl, and T. Aigner, "Collagens—structure, function, and biosynthesis," *Advanced Drug Delivery Reviews*, vol. 55, no. 12, pp. 1531–1546, 2003, Collagen in drug delivery and tissue engineering, ISSN: 0169-409X. DOI: https://doi.org/10.1016/j.addr.2003.08.002. [Online]. Available: https://www.sciencedirect.com/science/article/pii/S0169409X03001820.

[12] V. Ottani, M. Raspanti, and A. Ruggeri, "Collagen structure and functional implications," *Micron*, vol. 32, no. 3, pp. 251–260, 2001, ISSN: 0968-4328. DOI: https://doi.org/10.1016/S0968-4328(00)00042-1. [Online]. Available: https://www.sciencedirect.com/science/article/pii/S0968432800000421.

[13] J. S. Graham, A. N. Vomund, C. L. Phillips, and M. Grandbois, "Structural changes in human type i collagen fibrils investigated by force spectroscopy," *Experimental Cell Research*, vol. 299, no. 2, pp. 335–342, 2004, ISSN: 0014-4827. DOI: https://doi.org/10.1016/j.yexcr.2004.05.022. [Online]. Available: https://www.sciencedirect.com/science/article/pii/S0014482704003052.

[14] A. Gautieri, S. Vesentini, A. Redaelli, and R. Ballarini, "Modeling and measuring visco-elastic properties: From collagen molecules to collagen fibrils," *International Journal of Non-Linear Mechanics*, vol. 56, pp. 25–33, 2013, Soft Matter: a nonlinear continuum mechanics perspective, ISSN: 0020-7462. DOI: https://doi.org/10.1016/j.ijnonlinmec.2013.03.012. [Online]. Available: https://www.sciencedirect.com/science/article/pii/S0020746213000590.

[15] J.-Y. Exposito, U. Valcourt, C. Cluzel, and C. Lethias, "The fibrillar collagen family," *International Journal of Molecular Sciences*, vol. 11, no. 2, pp. 407–426, 2010, ISSN: 1422-0067. DOI: 10.3390/ijms11020407. [Online]. Available: https://www.mdpi.com/1422-0067/11/2/407.

[16] D. Hulmes, "Collagen diversity, synthesis and assembly," in *Collagen: Structure and Mechanics*, P. Fratzl, Ed. Boston, MA: Springer US, 2008, pp. 15–47, ISBN: 978-0-387-73906-9. DOI: 10.1007/978-0-387-73906-9_2. [Online]. Available: https://doi.org/10.1007/978-0-387-73906-9_2.

[17] H. L. Ansorge, X. Meng, G. Zhang, G. Veit, M. Sun, J. F. Klement, D. P. Beason, L. J. Soslowsky, M. Koch, and D. E. Birk, "Type xiv collagen regulates fibrillogenesis," *Journal of Biological Chemistry*, vol. 284, no. 13, pp. 8427–8438, 2009.

[18] G. Zhang, B. Young, Y. Ezura, M. Favata, L. Soslowsky, S. Chakravarti, D. E. Birk, *et al.*, "Development of tendon structure and function: Regulation of collagen fibrillogenesis," *J Musculoskelet Neuronal Interact*, vol. 5, no. 1, pp. 5–21, 2005.

[19] D. A. D. Parry, G. R. G. Barnes, A. S. Craig, and D. C. Phillips, "A comparison of the size distribution of collagen fibrils in connective tissues as a function of age and a possible relation between fibril size distribution and mechanical properties," *Proceedings of the Royal Society of London. Series B. Biological Sciences*, vol. 203, no. 1152, pp. 305–321, 1978. DOI: 10.1098/rspb.1978.0107. eprint: https://royalsocietypublishing.org/doi/pdf/10.1098/rspb.1978.0107. [Online]. Available: https://royalsocietypublishing.org/doi/abs/10.1098/rspb.1978.0107.

[20] J. Halper and M. Kjaer, "Basic components of connective tissues and extracellular matrix: Elastin, fibrillin, fibulins, fibrinogen, fibronectin, laminin, tenascins and thrombospondins," in *Progress in Heritable Soft Connective Tissue Diseases*, J. Halper, Ed. Dordrecht: Springer Netherlands, 2014, pp. 31–47, ISBN: 978-94-007-7893-1. DOI: 10.1007/978-94-007-7893-1_3. [Online]. Available: https://doi.org/10.1007/978-94-007-7893-1_3.

[21] C. T. Thorpe and H. R. C. Screen, "Tendon structure and composition," in *Metabolic Influences on Risk for Tendon Disorders*, P. W. Ackermann and D. A. Hart, Eds. Cham: Springer International Publishing, 2016, pp. 3–10, ISBN: 978-3-319-33943-6. DOI: 10.1007/978-3-319-33943-6_1. [Online]. Available: https://doi.org/10.1007/978-3-319-33943-6_1.

[22] J. Halper, "Proteoglycans and diseases of soft tissues," in *Progress in Heritable Soft Connective Tissue Diseases*, J. Halper, Ed. Dordrecht: Springer Netherlands, 2014, pp. 49–58, ISBN: 978-94-007-7893-1. DOI: 10.1007/978-94-007-7893-1_4. [Online]. Available: https://doi.org/10.1007/978-94-007-7893-1_4.

[23] R. Shadwick, "Mechanical design in arteries," *Journal of Experimental Biology*, vol. 202, no. 23, pp. 3305–3313, Dec. 1999, ISSN: 0022-0949. DOI: 10.1242/jeb.202.23.3305. eprint: https://journals.biologists.com/jeb/article-pdf/202/23/3305/1235968/3305.pdf. [Online]. Available: https://doi.org/10.1242/jeb.202.23.3305.

[24] F. Silver and W. Landis, "Viscoelasticity, energy storage and transmission and dissipation by extracellular matrices in vertebrates," in *Collagen: Structure and Mechanics*, P. Fratzl, Ed. Boston, MA: Springer US, 2008, pp. 133–154, ISBN: 978-0-387-73906-9. DOI: 10.1007/978-0-387-73906-9_6. [Online]. Available: https://doi.org/10.1007/978-0-387-73906-9_6.

[25] P. P. Purslow, T. J. Wess, and D. W. Hukins, "Collagen orientation and molecular spacing during creep and stress-relaxation in soft connective tissues.," *Journal of Experimental Biology*, vol. 201, no. 1, pp. 135–142, Jan. 1998, ISSN: 0022-0949. DOI: 10.1242/jeb.201.1.135. eprint: https://journals.biologists.com/jeb/article-pdf/201/1/135/1108098/135.pdf. [Online]. Available: https://doi.org/10.1242/jeb.201.1.135.

[26] Y.-c. Fung, *Biomechanics: mechanical properties of living tissues*. Springer Science & Business Media, 2013.

[27] J. Diamant, A. Keller, E. Baer, M. Litt, R. G. C. Arridge, and F. C. Frank, "Collagen; ultrastructure and its relation to mechanical properties as a function of ageing," *Proceedings of the Royal Society of London. Series B. Biological Sciences*, vol. 180, no. 1060, pp. 293–315, 1972. DOI: 10.1098/rspb.1972.0019. eprint: https://royalsocietypublishing.org/doi/pdf/10.1098/rspb.1972.0019. [Online]. Available: https://royalsocietypublishing.org/doi/abs/10.1098/rspb.1972.0019.

[28] A. Ní Annaidh, K. Bruyère, M. Destrade, M. D. Gilchrist, and M. Otténio, "Characterization of the anisotropic mechanical properties of excised human skin," *Journal of the Mechanical Behavior of Biomedical Materials*, vol. 5, no. 1, pp. 139–148, 2012, ISSN: 1751-6161. DOI: https://doi.org/10.1016/j.jmbbm.2011.08.016. [Online]. Available: https://www.sciencedirect.com/science/article/pii/S1751616111002219.

[29] J. Kastelic, I. Palley, and E. Baer, "A structural mechanical model for tendon crimping," *Journal of Biomechanics*, vol. 13, no. 10, pp. 887–893, 1980, ISSN: 0021-9290. DOI: https://doi.org/10.1016/0021-9290(80)90177-3. [Online]. Available: https://www.sciencedirect.com/science/article/pii/0021929080901773.

[30] J. Zabrzyński, Ł. Łapaj, Ł. Paczesny, A. Zabrzyńska, and D. Grzanka, "Tendon — function-related structure, simple healing process and mysterious ageing," *Folia Morphologica*, vol. 77, no. 3, pp. 416–427, 2018, ISSN: 1644-3284. DOI: 10.5603/FM.a2018.0006. [Online]. Available: https://journals.viamedica.pl/folia_morphologica/article/view/FM.a2018.0006.

[31] M. Franchi, A. Trirè, M. Quaranta, E. Orsini, and V. Ottani, "Collagen structure of tendon relates to function," *TheScientificWorldJOURNAL*, vol. 7, p. 132 725, Jan. 1900, ISSN: 2356-6140. DOI: 10.1100/tsw.2007.92. [Online]. Available: https://doi.org/10.1100/tsw.2007.92.

[32] D. Jaiswal, L. Yousman, M. Neary, E. Fernschild, B. Zolnoski, S. Katebifar, S. Rudraiah, A. D. Mazzocca, and S. G. Kumbar, "Tendon tissue engineering: Biomechanical considerations," vol. 15, no. 5, p. 052 001, Jul. 2020. DOI: 10.1088/1748-605x/ab852f. [Online]. Available: https://doi.org/10.1088/1748-605x/ab852f.

[33] J. Price, G. Njus, and T. Conway, "Ultrastructural properties of rat tail tendon," in *Proceedings of the 1996 Fifteenth Southern Biomedical Engineering Conference*, 1996, pp. 456–459. DOI: 10.1109/SBEC.1996.493275.

[34] C. T. Thorpe, H. L. Birch, P. D. Clegg, and H. R. Screen, "Chapter 1 - tendon physiology and mechanical behavior: Structure–function relationships," in *Tendon Regeneration*, M. E. Gomes, R. L. Reis, and M. T. Rodrigues, Eds., Boston: Academic Press, 2015, pp. 3–39, ISBN: 978-0-12-801590-2. DOI: https://doi.org/10.1016/B978-0-12-801590-2.00001-6. [Online]. Available: https://www.sciencedirect.com/science/article/pii/B9780128015902000016.

[35] M. Mardani-Kivi, M. Karimi-Mobarakeh, A. Mirbolook, S. Keyhani, K. Saheb-Ekhtiari, K. Hashemi-Motlagh, and P. Porteghali, "Predicting the hamstring tendon diameter using anthropometric parameters," eng, *The archives of bone and joint surgery*,

vol. 4, no. 4, pp. 314–317, Oct. 2016, PMC5100445[pmcid], ISSN: 2345-4644. [Online]. Available: https://pubmed.ncbi.nlm.nih.gov/27847842.

[36] P. Malliaras and J. Cook, "Changes in anteroposterior patellar tendon diameter support a continuum of pathological changes," *British Journal of Sports Medicine*, vol. 45, no. 13, pp. 1048–1051, 2011, ISSN: 0306-3674. DOI: 10.1136/bjsm.2010.082180. eprint: https://bjsm.bmj.com/content/45/13/1048.full.pdf. [Online]. Available: https://bjsm.bmj.com/content/45/13/1048.

[37] H. R. C. Screen, D. L. Bader, D. A. Lee, and J. C. Shelton, "Local strain measurement within tendon," *Strain*, vol. 40, no. 4, pp. 157–163, 2004. DOI: https://doi.org/10.1111/j.1475-1305.2004.00164.x. eprint: https://onlinelibrary.wiley.com/doi/pdf/10.1111/j.1475-1305.2004.00164.x. [Online]. Available: https://onlinelibrary.wiley.com/doi/abs/10.1111/j.1475-1305.2004.00164.x.

[38] P. Sharma and N. Maffulli, "Basic biology of tendon injury and healing," *The Surgeon*, vol. 3, no. 5, pp. 309–316, 2005, ISSN: 1479-666X. DOI: https://doi.org/10.1016/S1479-666X(05)80109-X. [Online]. Available: https://www.sciencedirect.com/science/article/pii/S1479666X0580109X.

[39] L. K. Smalls, R. Randall Wickett, and M. O. Visscher, "Effect of dermal thickness, tissue composition, and body site on skin biomechanical properties," *Skin Research and Technology*, vol. 12, no. 1, pp. 43–49, 2006. DOI: https://doi.org/10.1111/j.0909-725X.2006.00135.x. eprint: https://onlinelibrary.wiley.com/doi/pdf/10.1111/j.0909-725X.2006.00135.x. [Online]. Available: https://onlinelibrary.wiley.com/doi/abs/10.1111/j.0909-725X.2006.00135.x.

[40] D. J. Tobin, "Biochemistry of human skin—our brain on the outside," *Chem. Soc. Rev.*, vol. 35, pp. 52–67, 1 2006. DOI: 10.1039/B505793K. [Online]. Available: http://dx.doi.org/10.1039/B505793K.

[41] Y. Lee and K. Hwang, "Skin thickness of korean adults," *Surgical and Radiologic Anatomy*, vol. 24, no. 3, pp. 183–189, Jan. 2002, ISSN: 1279-8517. DOI: 10.1007/s00276-002-0034-5. [Online]. Available: https://doi.org/10.1007/s00276-002-0034-5.

[42] S. Girardeau, S. Mine, H. Pageon, and D. Asselineau, "The caucasian and african skin types differ morphologically and functionally in their dermal component," *Experimental Dermatology*, vol. 18, no. 8, pp. 704–711, 2009. DOI: https://doi.org/10.1111/j.1600-0625.2009.00843.x. eprint: https://onlinelibrary.wiley.com/doi/pdf/10.1111/j.1600-0625.2009.00843.x. [Online]. Avail-

able: https://onlinelibrary.wiley.com/doi/abs/10.1111/j.1600-0625.2009.00843.x.

[43] A. Baroni, E. Buommino, V. De Gregorio, E. Ruocco, V. Ruocco, and R. Wolf, "Structure and function of the epidermis related to barrier properties," *Clinics in Dermatology*, vol. 30, no. 3, pp. 257–262, 2012, Epidermal Barrier Function: Clinical Implications and Therapeutic Relevance, ISSN: 0738-081X. DOI: https://doi.org/10.1016/j.clindermatol.2011.08.007. [Online]. Available: https://www.sciencedirect.com/science/article/pii/S0738081X11002112.

[44] Z. Zaidi and S. W. Lanigan, "Skin: Structure and function," in *Dermatology in Clinical Practice*. London: Springer London, 2010, pp. 1–15, ISBN: 978-1-84882-862-9. DOI: 10.1007/978-1-84882-862-9_1. [Online]. Available: https://doi.org/10.1007/978-1-84882-862-9_1.

[45] F. Ginhoux, F. Tacke, V. Angeli, M. Bogunovic, M. Loubeau, X.-M. Dai, E. R. Stanley, G. J. Randolph, and M. Merad, "Langerhans cells arise from monocytes in vivo," *Nature Immunology*, vol. 7, no. 3, pp. 265–273, Mar. 2006, ISSN: 1529-2916. DOI: 10.1038/ni1307. [Online]. Available: https://doi.org/10.1038/ni1307.

[46] S. Maksimovic, M. Nakatani, Y. Baba, A. M. Nelson, K. L. Marshall, S. A. Wellnitz, P. Firozi, S.-H. Woo, S. Ranade, A. Patapoutian, and E. A. Lumpkin, "Epidermal merkel cells are mechanosensory cells that tune mammalian touch receptors," *Nature*, vol. 509, no. 7502, pp. 617–621, May 2014, ISSN: 1476-4687. DOI: 10.1038/nature13250. [Online]. Available: https://doi.org/10.1038/nature13250.

[47] F. H. Silver, J. W. Freeman, and D. DeVore, "Viscoelastic properties of human skin and processed dermis," *Skin Research and Technology*, vol. 7, no. 1, pp. 18–23, 2001. DOI: https://doi.org/10.1034/j.1600-0846.2001.007001018.x. eprint: https://onlinelibrary.wiley.com/doi/pdf/10.1034/j.1600-0846.2001.007001018.x. [Online]. Available: https://onlinelibrary.wiley.com/doi/abs/10.1034/j.1600-0846.2001.007001018.x.

[48] L. C. U. Junqueira, G. S. Montes, J. E. C. Martins, and P. P. Joazeiro, "Dermal collagen distribution," *Histochemistry*, vol. 79, no. 3, pp. 397–403, Sep. 1983, ISSN: 1432-119X. DOI: 10.1007/BF00491775. [Online]. Available: https://doi.org/10.1007/BF00491775.

[49] C. Lovell, K. Smolenski, V. Duance, N. Light, S. Young, and M. Dyson, "Type i and iii collagen content and fibre distribution in normal human skin during ageing," *British Journal of Dermatology*, vol. 117, no. 4, pp. 419–428, 1987. DOI: https://doi.org/10.1111/j.1365-2133.1987.tb04921.x. eprint: https://onlinelibrary.

wiley.com/doi/pdf/10.1111/j.1365-2133.1987.tb04921.x. [Online]. Available: https://onlinelibrary.wiley.com/doi/abs/10.1111/j.1365-2133.1987.tb04921.x.

[50] F. Xu, T. Lu, *et al.*, *Introduction to skin biothermomechanics and thermal pain*. Springer, 2011.

[51] M. Ventre, F. Mollica, and P. A. Netti, "The effect of composition and microstructure on the viscoelastic properties of dermis," *Journal of Biomechanics*, vol. 42, no. 4, pp. 430–435, 2009, ISSN: 0021-9290. DOI: https://doi.org/10.1016/j.jbiomech.2008.12.004. [Online]. Available: https://www.sciencedirect.com/science/article/pii/S002192900800626X.

[52] J. Zimoch, D. Zielinska, K. Michalak-Micka, D. Rütsche, R. Böni, T. Biedermann, and A. S. Klar, "Bio-engineering a prevascularized human tri-layered skin substitute containing a hypodermis," *Acta Biomaterialia*, vol. 134, pp. 215–227, 2021, ISSN: 1742-7061. DOI: https://doi.org/10.1016/j.actbio.2021.07.033. [Online]. Available: https://www.sciencedirect.com/science/article/pii/S1742706121004712.

[53] J. E. Lai-Cheong and J. A. McGrath, "Structure and function of skin, hair and nails," *Medicine*, vol. 41, no. 6, pp. 317–320, 2013, Dermatology Part 1 of 2, ISSN: 1357-3039. DOI: https://doi.org/10.1016/j.mpmed.2013.04.017. [Online]. Available: https://www.sciencedirect.com/science/article/pii/S1357303913001114.

[54] Y. Wang, R. Xu, W. He, Z. Yao, H. Li, J. Zhou, J. Tan, S. Yang, R. Zhan, G. Luo, and J. Wu, "Three-dimensional histological structures of the human dermis," *Tissue Engineering Part C: Methods*, vol. 21, no. 9, pp. 932–944, 2015, PMID: 25781868. DOI: 10.1089/ten.tec.2014.0578. eprint: https://doi.org/10.1089/ten.tec.2014.0578. [Online]. Available: https://doi.org/10.1089/ten.tec.2014.0578.

[55] J. Manne, M. Markova, L. D. Siracusa, and S. A. Jimenez, "Collagen content in skin and internal organs of the tight skin mouse: An animal model of scleroderma," *Biochemistry Research International*, vol. 2013, p. 436 053, Oct. 2013, ISSN: 2090-2247. DOI: 10.1155/2013/436053. [Online]. Available: https://doi.org/10.1155/2013/436053.

[56] P. H. Byers and M. L. Murray, "Heritable collagen disorders: The paradigm of the ehlers—danlos syndrome," *Journal of Investigative Dermatology*, vol. 132, E6–E11, Nov. 2012, ISSN: 0022-202X. DOI: 10.1038/skinbio.2012.3. [Online]. Available: https://doi.org/10.1038/skinbio.2012.3.

[57] A. Ortiz and S. A. Grando, "Smoking and the skin," *International Journal of Dermatology*, vol. 51, no. 3, pp. 250–262, 2012. DOI: https://doi.org/10.1111/j.1365-4632.2011.05205.x. eprint: https://onlinelibrary.wiley.com/doi/pdf/10.1111/j.1365-4632.2011.05205.x. [Online]. Available: https://onlinelibrary.wiley.com/doi/abs/10.1111/j.1365-4632.2011.05205.x.

[58] N. D. Evans, R. O. Oreffo, E. Healy, P. J. Thurner, and Y. H. Man, "Epithelial mechanobiology, skin wound healing, and the stem cell niche," *Journal of the Mechanical Behavior of Biomedical Materials*, vol. 28, pp. 397–409, 2013, ISSN: 1751-6161. DOI: https://doi.org/10.1016/j.jmbbm.2013.04.023. [Online]. Available: https://www.sciencedirect.com/science/article/pii/S1751616113001550.

[59] E. Cerda, "Mechanics of scars," *Journal of Biomechanics*, vol. 38, no. 8, pp. 1598–1603, 2005, ISSN: 0021-9290. DOI: https://doi.org/10.1016/j.jbiomech.2004.07.026. [Online]. Available: https://www.sciencedirect.com/science/article/pii/S0021929004003793.

[60] M.-A. Y. Abyaneh, R. Griffith, L. Falto-Aizpurua, and K. Nouri, "Famous Lines in History: Langer Lines," *JAMA Dermatology*, vol. 150, no. 10, pp. 1087–1087, Oct. 2014, ISSN: 2168-6068. DOI: 10.1001/jamadermatol.2014.659. eprint: https://jamanetwork.com/journals/jamadermatology/articlepdf/1912372/dnn140017.pdf. [Online]. Available: https://doi.org/10.1001/jamadermatol.2014.659.

[61] J. A. Bush, M. W. Ferguson, T. Mason, and D. A. McGrouther, "Skin tension or skin compression? small circular wounds are likely to shrink, not gape," *Journal of Plastic, Reconstructive & Aesthetic Surgery*, vol. 61, no. 5, pp. 529–534, 2008, ISSN: 1748-6815. DOI: https://doi.org/10.1016/j.bjps.2007.06.004. [Online]. Available: https://www.sciencedirect.com/science/article/pii/S1748681507003233.

[62] D. Laiacona, J. Cohen, K. Coulon, Z. Lipsky, C. Maiorana, R. Boltyanskiy, E. Dufresne, and G. German, "Non-invasive in vivo quantification of human skin tension lines," *Acta Biomaterialia*, vol. 88, pp. 141–148, 2019, ISSN: 1742-7061. DOI: https://doi.org/10.1016/j.actbio.2019.02.003. [Online]. Available: https://www.sciencedirect.com/science/article/pii/S1742706119301072.

[63] M. J. Blair, J. D. Jones, A. E. Woessner, and K. P. Quinn, "Skin structure–function relationships and the wound healing response to intrinsic aging," *Advances in Wound Care*, vol. 9, no. 3, pp. 127–143, 2020. DOI: 10.1089/wound.2019.1021. eprint:

https://doi.org/10.1089/wound.2019.1021. [Online]. Available: https://doi.org/10.1089/wound.2019.1021.

[64] F. Irgens, *Continuum Mechanics*, eng. Berlin, Heidelberg: Springer Berlin Heidelberg, 2008, ISBN: 9783540742982.

[65] A. J. M. Spencer, *Continuum mechanics*. Courier Corporation, 2004.

[66] R. W. Ogden, *Non-linear elastic deformations*. Courier Corporation, 1997.

[67] J. Murphy, "Transversely isotropic biological, soft tissue must be modelled using both anisotropic invariants," *European Journal of Mechanics - A/Solids*, vol. 42, pp. 90–96, 2013, ISSN: 0997-7538. DOI: https://doi.org/10.1016/j.euromechsol.2013.04.003. [Online]. Available: https://www.sciencedirect.com/science/article/pii/S0997753813000466.

[68] G. A. Holzapfel, R. W. Ogden, and S. Sherifova, "On fibre dispersion modelling of soft biological tissues: A review," *Proceedings of the Royal Society A: Mathematical, Physical and Engineering Sciences*, vol. 475, no. 2224, p. 20 180 736, 2019. DOI: 10.1098/rspa.2018.0736. eprint: https://royalsocietypublishing.org/doi/pdf/10.1098/rspa.2018.0736. [Online]. Available: https://royalsocietypublishing.org/doi/abs/10.1098/rspa.2018.0736.

[69] G. Holzapfel, *Nonlinear Solid Mechanics. A Continuum Approach for Engineering*, English, second print. John Wiley & Sons, 2001.

[70] T. Kibble and F. H. Berkshire, *Classical mechanics*. world scientific publishing company, 2004.

[71] T. C.-t. Ting and T. C.-t. Ting, *Anisotropic elasticity: theory and applications*, 45. Oxford University Press on Demand, 1996.

[72] P. C. Chou, *Elasticity : tensor, dyadic, and engineering approaches*, eng, ser. Dover books on engineering. New York: Dover Publications, 1992 - 1967, ISBN: 9781628708196.

[73] T. G. Sitharam, *Theory of elasticity*, eng. Singapore: Springer, 2021, ISBN: 9789813346505.

[74] R. van de Schoot, S. Depaoli, R. King, B. Kramer, K. Märtens, M. G. Tadesse, M. Vannucci, A. Gelman, D. Veen, J. Willemsen, and C. Yau, "Bayesian statistics and modelling," *Nature Reviews Methods Primers*, vol. 1, no. 1, p. 1, Jan. 2021, ISSN: 2662-8449. DOI: 10.1038/s43586-020-00001-2. [Online]. Available: https://doi.org/10.1038/s43586-020-00001-2.

[75] T. Bayes and n. Price, "Lii. an essay towards solving a problem in the doctrine of chances. by the late rev. mr. bayes, f. r. s. communicated by mr. price, in a letter to john canton, a. m. f. r. s," *Philosophical Transactions of the Royal Society of London*, vol. 53, pp. 370–418, 1763. DOI: 10.1098/rstl.1763.0053. eprint: https://royalsocietypublishing.org/doi/pdf/10.1098/rstl.1763.0053. [Online]. Available: https://royalsocietypublishing.org/doi/abs/10.1098/rstl.1763.0053.

[76] H. Jeffreys, "An invariant form for the prior probability in estimation problems," *Proceedings of the Royal Society of London. Series A. Mathematical and Physical Sciences*, vol. 186, no. 1007, pp. 453–461, 1946. DOI: 10.1098/rspa.1946.0056. eprint: https://royalsocietypublishing.org/doi/pdf/10.1098/rspa.1946.0056. [Online]. Available: https://royalsocietypublishing.org/doi/abs/10.1098/rspa.1946.0056.

[77] J. C. Spall, "Monte carlo computation of the fisher information matrix in nonstandard settings," *Journal of Computational and Graphical Statistics*, vol. 14, no. 4, pp. 889–909, 2005. DOI: 10.1198/106186005X78800. eprint: https://doi.org/10.1198/106186005X78800. [Online]. Available: https://doi.org/10.1198/106186005X78800.

[78] R. E. Kass and L. Wasserman, "The selection of prior distributions by formal rules," *Journal of the American Statistical Association*, vol. 91, no. 435, pp. 1343–1370, 1996. DOI: 10.1080/01621459.1996.10477003. eprint: https://www.tandfonline.com/doi/pdf/10.1080/01621459.1996.10477003. [Online]. Available: https://www.tandfonline.com/doi/abs/10.1080/01621459.1996.10477003.

[79] A. Gelman, "Bayes, jeffreys, prior distributions and the philosophy of statistics," *Statistical Science*, vol. 24, no. 2, pp. 176–178, 2009, ISSN: 08834237, 21688745. [Online]. Available: http://www.jstor.org/stable/25681293.

[80] D. van Ravenzwaaij, P. Cassey, and S. D. Brown, "A simple introduction to markov chain monte–carlo sampling," *Psychonomic Bulletin & Review*, vol. 25, no. 1, pp. 143–154, Feb. 2018, ISSN: 1531-5320. DOI: 10.3758/s13423-016-1015-8. [Online]. Available: https://doi.org/10.3758/s13423-016-1015-8.

[81] G. O. Roberts and J. S. Rosenthal, "Optimal scaling for various metropolis-hastings algorithms," *Statistical science*, vol. 16, no. 4, pp. 351–367, 2001.

[82] M. K. Cowles and B. P. Carlin, "Markov chain monte carlo convergence diagnostics: A comparative review," *Journal of the American Statistical Association*, vol. 91, no. 434, pp. 883–904, 1996. DOI: 10.1080/01621459.1996.10476956. eprint: https:

//www.tandfonline.com/doi/pdf/10.1080/01621459.1996.10476956. [Online]. Available: https://www.tandfonline.com/doi/abs/10.1080/01621459.1996.10476956.

[83] S. Chib and E. Greenberg, "Understanding the metropolis-hastings algorithm," *The American Statistician*, vol. 49, no. 4, pp. 327–335, 1995. DOI: 10.1080/00031305.1995.10476177. eprint: https://www.tandfonline.com/doi/pdf/10.1080/00031305.1995.10476177. [Online]. Available: https://www.tandfonline.com/doi/abs/10.1080/00031305.1995.10476177.

[84] J. E. Griffin and S. G. Walker, "On adaptive metropolis–hastings methods," *Statistics and Computing*, vol. 23, no. 1, pp. 123–134, Jan. 2013, ISSN: 1573-1375. DOI: 10.1007/s11222-011-9296-2. [Online]. Available: https://doi.org/10.1007/s11222-011-9296-2.

[85] A. Gelman, W. R. Gilks, and G. O. Roberts, "Weak convergence and optimal scaling of random walk Metropolis algorithms," *The Annals of Applied Probability*, vol. 7, no. 1, pp. 110–120, 1997. DOI: 10.1214/aoap/1034625254. [Online]. Available: https://doi.org/10.1214/aoap/1034625254.

[86] A. E. Brockwell and J. B. Kadane, "Identification of regeneration times in mcmc simulation, with application to adaptive schemes," *Journal of Computational and Graphical Statistics*, vol. 14, no. 2, pp. 436–458, 2005. DOI: 10.1198/106186005X47453. eprint: https://doi.org/10.1198/106186005X47453. [Online]. Available: https://doi.org/10.1198/106186005X47453.

[87] M. Zhu, "Sample adaptive mcmc," in *Advances in Neural Information Processing Systems*, H. Wallach, H. Larochelle, A. Beygelzimer, F. d'Alché-Buc, E. Fox, and R. Garnett, Eds., vol. 32, Curran Associates, Inc., 2019. [Online]. Available: https://proceedings.neurips.cc/paper/2019/file/2cfa8f9e50e0f510ede9d12338a5f564-Paper.pdf.

[88] G. O. Roberts and J. S. Rosenthal, "Examples of adaptive mcmc," *Journal of Computational and Graphical Statistics*, vol. 18, no. 2, pp. 349–367, 2009. DOI: 10.1198/jcgs.2009.06134. eprint: https://doi.org/10.1198/jcgs.2009.06134. [Online]. Available: https://doi.org/10.1198/jcgs.2009.06134.

[89] A. Buchholz, N. Chopin, and P. E. Jacob, "Adaptive Tuning of Hamiltonian Monte Carlo Within Sequential Monte Carlo," *Bayesian Analysis*, vol. 16, no. 3, pp. 745–771, 2021. DOI: 10.1214/20-BA1222. [Online]. Available: https://doi.org/10.1214/20-BA1222.

[90] C. Naesseth, F. Lindsten, and T. Schon, "Nested sequential monte carlo methods," in *Proceedings of the 32nd International Conference on Machine Learning*, F. Bach and D. Blei, Eds., ser. Proceedings of Machine Learning Research, vol. 37, Lille, France: PMLR, Jul. 2015, pp. 1292–1301. [Online]. Available: https://proceedings.mlr.press/v37/naesseth15.html.

[91] P. Del Moral, A. Doucet, and A. Jasra, "Sequential monte carlo samplers," *Journal of the Royal Statistical Society: Series B (Statistical Methodology)*, vol. 68, no. 3, pp. 411–436, 2006. DOI: https://doi.org/10.1111/j.1467-9868.2006.00553.x. eprint: https://rss.onlinelibrary.wiley.com/doi/pdf/10.1111/j.1467-9868.2006.00553.x. [Online]. Available: https://rss.onlinelibrary.wiley.com/doi/abs/10.1111/j.1467-9868.2006.00553.x.

[92] M. Betancourt, *A conceptual introduction to hamiltonian monte carlo*, 2017. DOI: 10.48550/ARXIV.1701.02434. [Online]. Available: https://arxiv.org/abs/1701.02434.

[93] S. Vasishth, "Using approximate bayesian computation for estimating parameters in the cue-based retrieval model of sentence processing," *MethodsX*, vol. 7, p. 100 850, 2020, ISSN: 2215-0161. DOI: https://doi.org/10.1016/j.mex.2020.100850. [Online]. Available: https://www.sciencedirect.com/science/article/pii/S2215016120300698.

[94] T. Toni, D. Welch, N. Strelkowa, A. Ipsen, and M. P. Stumpf, "Approximate bayesian computation scheme for parameter inference and model selection in dynamical systems," *Journal of The Royal Society Interface*, vol. 6, no. 31, pp. 187–202, 2009. DOI: 10.1098/rsif.2008.0172. eprint: https://royalsocietypublishing.org/doi/pdf/10.1098/rsif.2008.0172. [Online]. Available: https://royalsocietypublishing.org/doi/abs/10.1098/rsif.2008.0172.

[95] P. Marjoram, J. Molitor, V. Plagnol, and S. Tavaré, "Markov chain monte carlo without likelihoods," *Proceedings of the National Academy of Sciences*, vol. 100, no. 26, pp. 15 324–15 328, 2003. DOI: 10.1073/pnas.0306899100. eprint: https://www.pnas.org/doi/pdf/10.1073/pnas.0306899100. [Online]. Available: https://www.pnas.org/doi/abs/10.1073/pnas.0306899100.

[96] Y. Fung, "Elasticity of soft tissues in simple elongation," *American Journal of Physiology-Legacy Content*, vol. 213, no. 6, pp. 1532–1544, 1967, PMID: 6075755. DOI: 10.1152/ajplegacy.1967.213.6.1532. eprint: https://doi.org/10.1152/ajplegacy.1967.213.6.1532. [Online]. Available: https://doi.org/10.1152/ajplegacy.1967.213.6.1532.

[97] P. Tong and Y.-C. Fung, "The stress-strain relationship for the skin," *Journal of Biomechanics*, vol. 9, no. 10, pp. 649–657, 1976, ISSN: 0021-9290. DOI: https://doi.org/10.1016/0021-9290(76)90107-X. [Online]. Available: https://www.sciencedirect.com/science/article/pii/002192907690107X.

[98] C. J. Chuong and Y. C. Fung, "Three-Dimensional Stress Distribution in Arteries," *Journal of Biomechanical Engineering*, vol. 105, no. 3, pp. 268–274, Aug. 1983, ISSN: 0148-0731. DOI: 10.1115/1.3138417. eprint: https://asmedigitalcollection.asme.org/biomechanical/article-pdf/105/3/268/5765387/268_1.pdf. [Online]. Available: https://doi.org/10.1115/1.3138417.

[99] Y. C. Fung, K. Fronek, and P. Patitucci, "Pseudoelasticity of arteries and the choice of its mathematical expression," *American Journal of Physiology-Heart and Circulatory Physiology*, vol. 237, no. 5, H620–H631, 1979, PMID: 495769. DOI: 10.1152/ajpheart.1979.237.5.H620. eprint: https://doi.org/10.1152/ajpheart.1979.237.5.H620. [Online]. Available: https://doi.org/10.1152/ajpheart.1979.237.5.H620.

[100] P. J. Blatz, B. Mae Chu, and H. Wayland, "On the mechanical behavior of elastic animal tissue," *Transactions of the Society of Rheology*, vol. 13, no. 1, pp. 83–102, 1969. DOI: 10.1122/1.549157. eprint: https://doi.org/10.1122/1.549157. [Online]. Available: https://doi.org/10.1122/1.549157.

[101] R. N. Vaishnav, J. T. Young, J. S. Janicki, and D. J. Patel, "Nonlinear anisotropic elastic properties of the canine aorta," *Biophysical Journal*, vol. 12, no. 8, pp. 1008–1027, 1972, ISSN: 0006-3495. DOI: https://doi.org/10.1016/S0006-3495(72)86140-X. [Online]. Available: https://www.sciencedirect.com/science/article/pii/S000634957286140X.

[102] M. D. Ridge, "The rheology of skin: A bio-engineering study of the mechanical properties of human skin in relation to its structure," Ph.D. dissertation, University of Leeds, 1964.

[103] M. Ridge and V. Wright, "Mechanical properties of skin: A bioengineering study of skin structure.," *Journal of applied physiology*, vol. 21, no. 5, pp. 1602–1606, 1966.

[104] ——, "The directional effects of skin: A bio-engineering study of skin with particular reference to langer's lines*," *Journal of Investigative Dermatology*, vol. 46, no. 4, pp. 341–346, 1966, ISSN: 0022-202X. DOI: https://doi.org/10.1038/jid.1966.54. [Online]. Available: https://www.sciencedirect.com/science/article/pii/S0022202X15470964.

[105] G. Limbert and J. Middleton, "A polyconvex anisotropic strain energy function. application to soft tissue mechanics," in *ASME Summer Bioengineering Conf., Vail, CO, 22–26 June*, 2005.

[106] M. Itskov, A. E. Ehret, and D. Mavrilas, "A polyconvex anisotropic strain–energy function for soft collagenous tissues," *Biomechanics and Modeling in Mechanobiology*, vol. 5, no. 1, pp. 17–26, Mar. 2006, ISSN: 1617-7940. DOI: 10.1007/s10237-005-0006-x. [Online]. Available: https://doi.org/10.1007/s10237-005-0006-x.

[107] J. E. Bischoff, E. M. Arruda, and K. Grosh, "Finite element simulations of orthotropic hyperelasticity," *Finite Elements in Analysis and Design*, vol. 38, no. 10, pp. 983–998, 2002, 2001 Robert J. Melosh Medal Competition, ISSN: 0168-874X. DOI: https://doi.org/10.1016/S0168-874X(02)00089-6. [Online]. Available: https://www.sciencedirect.com/science/article/pii/S0168874X02000896.

[108] R. Lapeer, P. Gasson, and V. Karri, "Simulating plastic surgery: From human skin tensile tests, through hyperelastic finite element models to real-time haptics," *Progress in Biophysics and Molecular Biology*, vol. 103, no. 2, pp. 208–216, 2010, Special Issue on Biomechanical Modelling of Soft Tissue Motion, ISSN: 0079-6107. DOI: https://doi.org/10.1016/j.pbiomolbio.2010.09.013. [Online]. Available: https://www.sciencedirect.com/science/article/pii/S0079610710000817.

[109] K. Romanov, "The drucker stability of a material," *Journal of Applied Mathematics and Mechanics*, vol. 65, no. 1, pp. 155–162, 2001, ISSN: 0021-8928. DOI: https://doi.org/10.1016/S0021-8928(01)00017-X. [Online]. Available: https://www.sciencedirect.com/science/article/pii/S002189280100017X.

[110] O. H. Yeoh, "Some Forms of the Strain Energy Function for Rubber," *Rubber Chemistry and Technology*, vol. 66, no. 5, pp. 754–771, Nov. 1993, ISSN: 0035-9475. DOI: 10.5254/1.3538343. eprint: https://meridian.allenpress.com/rct/article-pdf/66/5/754/1942809/1_3538343.pdf. [Online]. Available: https://doi.org/10.5254/1.3538343.

[111] G. A. Holzapfel, T. C. Gasser, and R. W. Ogden, "A new constitutive framework for arterial wall mechanics and a comparative study of material models," in *Cardiovascular soft tissue mechanics*, Springer, 2001, pp. 1–48.

[112] S. Chen, A. Ní Annaidh, and S. Roccabianca, "A microstructurally inspired constitutive model for skin mechanics," *Biomechanics and Modeling in Mechanobiology*, vol. 19, no. 1, pp. 275–289, Feb. 2020, ISSN: 1617-7940. DOI: 10.1007/s10237-

019-01210-9. [Online]. Available: https://doi.org/10.1007/s10237-019-01210-9.

[113] T. Shearer, "A new strain energy function for the hyperelastic modelling of ligaments and tendons based on fascicle microstructure," *Journal of Biomechanics*, vol. 48, no. 2, pp. 290–297, 2015, ISSN: 0021-9290. DOI: https://doi.org/10.1016/j.jbiomech.2014.11.031. [Online]. Available: https://www.sciencedirect.com/science/article/pii/S0021929014006198.

[114] M. A. Zulliger, P. Fridez, K. Hayashi, and N. Stergiopulos, "A strain energy function for arteries accounting for wall composition and structure," *Journal of Biomechanics*, vol. 37, no. 7, pp. 989–1000, 2004, ISSN: 0021-9290. DOI: https://doi.org/10.1016/j.jbiomech.2003.11.026. [Online]. Available: https://www.sciencedirect.com/science/article/pii/S0021929003004391.

[115] W. Yang, V. R. Sherman, B. Gludovatz, E. Schaible, P. Stewart, R. O. Ritchie, and M. A. Meyers, "On the tear resistance of skin," *Nature Communications*, vol. 6, no. 1, p. 6649, Mar. 2015, ISSN: 2041-1723. DOI: 10.1038/ncomms7649. [Online]. Available: https://doi.org/10.1038/ncomms7649.

[116] J. Schoeftner, "Extension of castigliano's method for isotropic beams," *Acta Mechanica*, vol. 231, no. 11, pp. 4621–4640, Nov. 2020, ISSN: 1619-6937. DOI: 10.1007/s00707-020-02762-z. [Online]. Available: https://doi.org/10.1007/s00707-020-02762-z.

[117] A. D. Freed and K. R. Rajagopal, "A promising approach for modeling biological fibers," *Acta Mechanica*, vol. 227, no. 6, pp. 1609–1619, Jun. 2016, ISSN: 1619-6937. DOI: 10.1007/s00707-016-1583-8. [Online]. Available: https://doi.org/10.1007/s00707-016-1583-8.

[118] A. R. Babu, A. G. Byju, and N. Gundiah, "Biomechanical Properties of Human Ascending Thoracic Aortic Dissections," *Journal of Biomechanical Engineering*, vol. 137, no. 8, Aug. 2015, 081013, ISSN: 0148-0731. DOI: 10.1115/1.4030752. eprint: https://asmedigitalcollection.asme.org/biomechanical/article-pdf/137/8/081013/6093068/bio_137_08_081013.pdf. [Online]. Available: https://doi.org/10.1115/1.4030752.

[119] A. D. Freed and T. C. Doehring, "Elastic Model for Crimped Collagen Fibrils," *Journal of Biomechanical Engineering*, vol. 127, no. 4, pp. 587–593, Feb. 2005, ISSN: 0148-0731. DOI: 10.1115/1.1934145. eprint: https://asmedigitalcollection.asme.org/biomechanical/article-pdf/127/4/587/5769500/587_1.pdf. [Online]. Available: https://doi.org/10.1115/1.1934145.

[120] P. Aparício, M. S. Thompson, and P. N. Watton, "A novel chemo-mechano-biological model of arterial tissue growth and remodelling," *Journal of Biomechanics*, vol. 49, no. 12, pp. 2321–2330, 2016, Cardiovascular Biomechanics in Health and Disease, ISSN: 0021-9290. DOI: https://doi.org/10.1016/j.jbiomech.2016.04.037. [Online]. Available: https://www.sciencedirect.com/science/article/pii/S0021929016305425.

[121] G. Martufi and T. C. Gasser, "Turnover of fibrillar collagen in soft biological tissue with application to the expansion of abdominal aortic aneurysms," *Journal of The Royal Society Interface*, vol. 9, no. 77, pp. 3366–3377, 2012. DOI: 10.1098/rsif.2012.0416. eprint: https://royalsocietypublishing.org/doi/pdf/10.1098/rsif.2012.0416. [Online]. Available: https://royalsocietypublishing.org/doi/abs/10.1098/rsif.2012.0416.

[122] J. Lu and L. Zhang, "Physically motivated invariant formulation for transversely isotropic hyperelasticity," *International Journal of Solids and Structures*, vol. 42, no. 23, pp. 6015–6031, 2005, ISSN: 0020-7683. DOI: https://doi.org/10.1016/j.ijsolstr.2005.04.014. [Online]. Available: https://www.sciencedirect.com/science/article/pii/S0020768305002295.

[123] T. C. Gasser, R. W. Ogden, and G. A. Holzapfel, "Hyperelastic modelling of arterial layers with distributed collagen fibre orientations," *Journal of The Royal Society Interface*, vol. 3, no. 6, pp. 15–35, 2006. DOI: 10.1098/rsif.2005.0073. eprint: https://royalsocietypublishing.org/doi/pdf/10.1098/rsif.2005.0073. [Online]. Available: https://royalsocietypublishing.org/doi/abs/10.1098/rsif.2005.0073.

[124] M. Latorre and F. J. Montáns, "On the tension-compression switch of the gasser–ogden–holzapfel model: Analysis and a new pre-integrated proposal," *Journal of the Mechanical Behavior of Biomedical Materials*, vol. 57, pp. 175–189, 2016, ISSN: 1751-6161. DOI: https://doi.org/10.1016/j.jmbbm.2015.11.018. [Online]. Available: https://www.sciencedirect.com/science/article/pii/S1751616115004361.

[125] G. A. Holzapfel and R. W. Ogden, "On fiber dispersion models: Exclusion of compressed fibers and spurious model comparisons," *Journal of Elasticity*, vol. 129, no. 1, pp. 49–68, Dec. 2017, ISSN: 1573-2681. DOI: 10.1007/s10659-016-9605-2. [Online]. Available: https://doi.org/10.1007/s10659-016-9605-2.

[126] Y. Lanir, "Constitutive equations for fibrous connective tissues," *Journal of Biomechanics*, vol. 16, no. 1, pp. 1–12, 1983, ISSN: 0021-9290. DOI: https://doi.org/10.

1016/0021-9290(83)90041-6. [Online]. Available: https://www.sciencedirect.com/science/article/pii/0021929083900416.

[127] C. Flynn, M. B. Rubin, and P. Nielsen, "A model for the anisotropic response of fibrous soft tissues using six discrete fibre bundles," *International Journal for Numerical Methods in Biomedical Engineering*, vol. 27, no. 11, pp. 1793–1811, 2011. DOI: https://doi.org/10.1002/cnm.1440. eprint: https://onlinelibrary.wiley.com/doi/pdf/10.1002/cnm.1440. [Online]. Available: https://onlinelibrary.wiley.com/doi/abs/10.1002/cnm.1440.

[128] N. Metropolis and S. Ulam, "The monte carlo method," *Journal of the American Statistical Association*, vol. 44, no. 247, pp. 335–341, 1949, PMID: 18139350. DOI: 10.1080/01621459.1949.10483310. eprint: https://www.tandfonline.com/doi/pdf/10.1080/01621459.1949.10483310. [Online]. Available: https://www.tandfonline.com/doi/abs/10.1080/01621459.1949.10483310.

[129] N. Metropolis, A. W. Rosenbluth, M. N. Rosenbluth, A. H. Teller, and E. Teller, "Equation of state calculations by fast computing machines," *The Journal of Chemical Physics*, vol. 21, no. 6, pp. 1087–1092, 1953. DOI: 10.1063/1.1699114. eprint: https://doi.org/10.1063/1.1699114. [Online]. Available: https://doi.org/10.1063/1.1699114.

[130] W. K. Hastings, "Monte Carlo sampling methods using Markov chains and their applications," *Biometrika*, vol. 57, no. 1, pp. 97–109, Apr. 1970, ISSN: 0006-3444. DOI: 10.1093/biomet/57.1.97. eprint: https://academic.oup.com/biomet/article-pdf/57/1/97/23940249/57-1-97.pdf. [Online]. Available: https://doi.org/10.1093/biomet/57.1.97.

[131] D. S. Reis and J. R. Stedinger, "Bayesian mcmc flood frequency analysis with historical information," *Journal of Hydrology*, vol. 313, no. 1, pp. 97–116, 2005, Palaeofloods, hystorical data & climate variability: Applications in flood risk assessment, ISSN: 0022-1694. DOI: https://doi.org/10.1016/j.jhydrol.2005.02.028. [Online]. Available: https://www.sciencedirect.com/science/article/pii/S0022169405000314.

[132] R. E. Ogunsakin and L. Siaka, "Bayesian inference on malignant breast cancer in nigeria: A diagnosis of mcmc convergence," eng, *Asian Pacific journal of cancer prevention : APJCP*, vol. 18, no. 10, pp. 2709–2716, Oct. 2017, PMC5747394[pmcid], ISSN: 2476-762X. [Online]. Available: https://pubmed.ncbi.nlm.nih.gov/29072396.

[133] Y. Huang, D. Liu, and H. Wu, "Hierarchical bayesian methods for estimation of parameters in a longitudinal hiv dynamic system," *Biometrics*, vol. 62, no. 2, pp. 413–423, 2006. DOI: https://doi.org/10.1111/j.1541-0420.2005.00447.x. eprint: https://onlinelibrary.wiley.com/doi/pdf/10.1111/j.1541-0420.2005.00447.x. [Online]. Available: https://onlinelibrary.wiley.com/doi/abs/10.1111/j.1541-0420.2005.00447.x.

[134] V. Acquaviva, E. Gawiser, and L. Guaita, "Sed fitting with mcmc: Methodology and application to large galaxy surveys," *Proceedings of the International Astronomical Union*, vol. 7, no. S284, pp. 42–45, 2011. DOI: 10.1017/S1743921312008691.

[135] I. Bray, "Application of markov chain monte carlo methods to projecting cancer incidence and mortality," *Journal of the Royal Statistical Society: Series C (Applied Statistics)*, vol. 51, no. 2, pp. 151–164, 2002. DOI: https://doi.org/10.1111/1467-9876.00260. eprint: https://rss.onlinelibrary.wiley.com/doi/pdf/10.1111/1467-9876.00260. [Online]. Available: https://rss.onlinelibrary.wiley.com/doi/abs/10.1111/1467-9876.00260.

[136] B. Mathew, A. M. Bauer, P. Koistinen, T. C. Reetz, J. Léon, and M. J. Sillanpää, "Bayesian adaptive markov chain monte carlo estimation of genetic parameters," *Heredity*, vol. 109, no. 4, pp. 235–245, Oct. 2012, ISSN: 1365-2540. DOI: 10.1038/hdy.2012.35. [Online]. Available: https://doi.org/10.1038/hdy.2012.35.

[137] P. Mehta, M. Kuttolamadom, and L. Mears, "Mechanistic force model for machining process—theory and application of bayesian inference," *The International Journal of Advanced Manufacturing Technology*, vol. 91, no. 9, pp. 3673–3682, Aug. 2017, ISSN: 1433-3015. DOI: 10.1007/s00170-017-0064-0. [Online]. Available: https://doi.org/10.1007/s00170-017-0064-0.

[138] G. Baele, P. Lemey, A. Rambaut, and M. A. Suchard, "Adaptive MCMC in Bayesian phylogenetics: an application to analyzing partitioned data in BEAST," *Bioinformatics*, vol. 33, no. 12, pp. 1798–1805, Feb. 2017, ISSN: 1367-4803. DOI: 10.1093/bioinformatics/btx088. eprint: https://academic.oup.com/bioinformatics/article-pdf/33/12/1798/25416866/btx088.pdf. [Online]. Available: https://doi.org/10.1093/bioinformatics/btx088.

[139] B. Everitt and A. Skrondal, *The Cambridge dictionary of statistics*. Cambridge University Press Cambridge, 2002, vol. 106.

Appendices

Appendix A

Reynolds Transport Theorem

Suppose that we want to calculate the material derivative of the quantity $\Phi(\mathbf{x}, t)$, which is defined by the 'Φ-density field' $\phi(\mathbf{x}, t)$. We must determine, therefore,

$$\frac{\mathrm{D}}{\mathrm{D}t} \iiint_V \phi(\mathbf{x}, t) \mathrm{d}V. \tag{A.1}$$

To calculate the rate of change of Φ in a volume V at a time t, we must consider both the change of ϕ associated with the material instantaneously in V at a time t and the influx of $\phi\mathbf{v}$ across the surface of V, S. Therefore, (A.1) is equal to

$$\frac{D}{Dt} \iiint_V \phi(\mathbf{x}, t) \mathrm{d}V = \iiint_V \frac{\partial(\phi(\mathbf{x}, t))}{\partial t} \mathrm{d}V + \iint_S \phi(\mathbf{x}, t)\mathbf{v} \cdot \mathbf{n} \mathrm{d}S, \tag{A.2}$$

$$= \iiint_V \left(\frac{\partial(\phi(\mathbf{x}, t))}{\partial t} + \boldsymbol{\nabla} \cdot (\phi(\mathbf{x}, t)\mathbf{v}) \right) \mathrm{d}V, \tag{A.3}$$

by the divergence theorem, which relates surface and volume integrals to one another. Rewriting (A.3) in terms of the material derivative of $\phi(\mathbf{x}, t)$, we get

$$\frac{D}{Dt} \iiint_V \phi(\mathbf{x}, t) \mathrm{d}V = \iiint_V \left[\frac{\mathrm{D}\phi(\mathbf{x}, t)}{\mathrm{D}t} + \phi(\mathbf{x}, t)(\boldsymbol{\nabla} \cdot \mathbf{v}) \right] \mathrm{d}V. \tag{A.4}$$

Appendix B

Von Mises Distribution

The von Mises distribution is a circular distribution of the form [124], assuming that the mean direction is zero,

$$\rho(\theta) = 2\sqrt{\frac{2r}{\pi}}\frac{1}{\text{erfi}(\sqrt{2r})}\exp(2r\cos^2\theta),$$

where r is the concentration parameter and erfi denotes the imaginary error function. The Von Mises distribution is the circular analogue to the normal distribution [139].